

2

**MATERIALS FOR ADAPTIVE STRUCTURAL  
ACOUSTIC CONTROL**

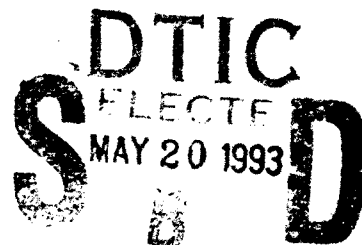
**AD-A264 622**



Period February 1, 1992 to January 31, 1993

Annual Report

VOLUME IV



**OFFICE OF NAVAL RESEARCH  
Contract No. N00014-92-J-1510**

**APPROVED FOR PUBLIC RELEASE - DISTRIBUTION UNLIMITED**

Reproduction in whole or in part is permitted for any purpose  
of the United States Government

L. Eric Cross

**PENNSTATE**



**THE MATERIALS RESEARCH LABORATORY  
UNIVERSITY PARK, PA**

**93 5 19 06 2**

**93-11219**





## ABSTRACT

This report documents work carried out in the Materials Research Laboratory of the Pennsylvania State University over the first year of a new ONR sponsored University Research Initiative (URI) entitled "Materials for Adaptive Structural Acoustic Control." For this report the activities have been grouped under the following topic headings:

1. General Summary Papers.
2. Materials Studies.
3. Composite Sensors.
4. Actuator Studies.
5. Integration Issues.
6. Processing Studies.
7. Thin Film Ferroelectrics.

In material studies important advances have been made in the understanding of the evaluation of relaxor behavior in the PLZT's and of the order disorder behavior in lead scandium tantalate:lead titanate solid solutions and of the Morphotropic Phase Boundary in this system. For both composite sensors and actuators we have continued to explore and exploit the remarkable versatility of the flextensional moonie type structure. Finite element (FEA) calculations have given a clear picture of the lower order resonant modes and permitted the evaluation of various end cap metals, cap geometries and load conditions. In actuator studies multilayer structures have been combined with flextensional moonie endcaps to yield high displacement (50  $\mu$  meter) compact structures. Electrically controlled shape memory has been demonstrated in lead zirconate stannate titanate compositions, and used for controlling a simple latching relay. Detailed study of fatigue in polarization switching compositions has highlighted the important roles of electrodes, grain size, pore structures and microcracking and demonstrated approaches to controlling these problems. For practical multilayer actuators a useful lifetime prediction can be made from acoustic emission analysis.

New modelling of 2:2 and 1:3 type piezoceramic:polymer composites has given more exact solutions for the stress distribution and good agreement with ultradilatometer measurements of local deformations. Composites with 1:3 connectivity using thin wall ceramic tubes appear to offer excellent hydrostatic sensitivity, unusual versatility for property control and the possibility to use field biased electrostrictors in high sensitivity configurations. Processing approaches have continued to use reactive calcining and have supplied the group with the wide range of ceramics used in these studies. For lead magnesium niobate:lead

**ABSTRACT** (continued)

titanate solid solutions grain size effects in samples of commercial purity have been traced to a thin (~20 n meter) glassy layer at the grain boundary. In parallel with the ONR URI the laboratory has extensive DARPA and Industry sponsored research on ferroelectric thin films, a very short selection of most relevant papers has been included for the convenience of users.

Approved For	SECRET
NTIS	
DTIC	
Library	
Dist	
Approved For Release	
Approved For Release	
Approved For Release	
Dist	A-1

**MATERIALS FOR ADAPTIVE STRUCTURAL  
ACOUSTIC CONTROL**

Period February 1, 1992 to January 31, 1993

Annual Report

**VOLUME IV**

**OFFICE OF NAVAL RESEARCH  
Contract No. N00014-92-J-1510**

**APPROVED FOR PUBLIC RELEASE - DISTRIBUTION UNLIMITED**

Reproduction in whole or in part is permitted for any purpose  
of the United States Government

**L. Eric Cross**

**PENNS**STATE



---

**THE MATERIALS RESEARCH LABORATORY  
UNIVERSITY PARK, PA**

## TABLE OF CONTENTS

ABSTRACT .....	6
INTRODUCTION .....	7
1.0 GENERAL SUMMARY PAPERS .....	10
2.0 MATERIALS STUDIES .....	10
3.0 SENSOR STUDIES .....	12
4.0 ACTUATOR STUDIES .....	13
5.0 INTEGRATION ISSUES .....	14
6.0 PROCESSING STUDIES .....	14
7.0 THIN FILM FERROELECTRICS .....	15
8.0 HONORS AND AWARDS .....	15
9.0 APPRENTICE PROGRAM .....	17
10.0 PAPERS PUBLISHED IN REFEREED JOURNALS .....	18
11.0 INVITED PAPERS PRESENTED AT NATIONAL AND INTERNATIONAL MEETINGS .....	21
12.0 INVITED PRESENTATIONS AT UNIVERSITY, INDUSTRY AND GOVERNMENT LABORATORIES .....	23
13.0 CONTRIBUTED PAPERS AT NATIONAL AND INTERNATIONAL MEETINGS .....	24

## APPENDICES

### *General Summary of Papers*

1. R. E. Newnham, "Memories of Arthur Von Hippel," *Ferroelectrics* 137, 17 (1992).
2. C. Rosen, B. V. Hiremath and R. E. Newnham, "Piezoelectricity," American Inst. of Physics, New York (1991).
3. R. E. Newnham, "Ferroelectric Sensors and Actuators Smart Electroceramics," *Ferroelectric Ceramics*, Editor N. Setter, Proc. of Summer School on Ferroelectrics, Ascona (1991).
4. R. E. Newnham, "Smart Electroceramics in the 1990's and Beyond," *J. European Ceramic Soc.* (1992).
5. V. Sundar and R. E. Newnham, "Electrostriction and Polarization," *Ferroelectrics* 135, 431 (1992).

### **Materials Studies**

6. J. R. Giniewicz, A. S. Bhalla and L. E. Cross, "Identification of the Morphotropic Phase Boundary in Lead Scandium Tantalate-Lead Titanate Solid Solution System."
7. J. R. Giniewicz, A. S. Bhalla and L. E. Cross, "Variable Structure Ordering in Lead Scandium Tantalate-Lead Titanate Materials."
8. J. R. Giniewicz, A. S. Bhalla and L. E. Cross, "Lead Scandium Tantalate:Lead Titanate Materials for Field Stabilized Pyroelectric Device Applications," *Ferroelectrics Letters* **14**, 21 (1992).
9. A. S. Bhalla, R. Guo, L. E. Cross, G. Burns, F. H. Dacol and R. R. Neurgaonkar, "Glassy Polarization in the Ferroelectric Tungsten Bronze (BaSr) Nb<sub>2</sub>O<sub>6</sub>," *J. Appl. Phys.* **71** (11), 5591 (1992).
10. J. S. Yoon, V. S. Srikanth and A. S. Bhalla, "The Electrical Properties of Antiferroelectric Lead Zirconate-Ferroelectric Lead Zinc Niobate Ceramics with Lanthanum," *Proc. ISAF 1992*, Greenville, South Carolina, pp. 556.
11. E. F. Alberta, D. J. Taylor, A. S. Bhalla and T. Takenaka, "The DC Field Dependence of the Piezoelectric, Elastic and Dielectric Constants for a Lead Zirconate Based Ceramic," *Proc. ISAF 1992*, Greenville, South Carolina, pp. 560.
12. W. Cao and L. Eric Cross, "The Ratio of Rhombohedral and Tetragonal Phases at the Morphotropic Phase Boundary in Lead Zirconate Titanate," *Japan Journal of Applied Physics* **31** (Pt. 1, No. 5A), 1399 (1992).
13. C. A. Randall, M. G. Matsko, W. Cao and A. S. Bhalla, "A Transmission Electron Microscope Investigation of the R3m - R3c Phase Transition in Pb(ZrTi)O<sub>3</sub> Ceramics," *Solid State Comm.* **85** (3), 193 (1993).
14. Shaoping Li, Chi Yeun Huang, A. S. Bhalla and L. E. Cross, "90° Domain Reversal in Pb(Zr<sub>x</sub>Ti<sub>1-x</sub>)O<sub>3</sub> Ceramics," *Proc. ISAF 1992*, Greenville, South Carolina.
15. Shaoping Li, Jyh Sheen, Q. M. Zhang, Sei-Joo Jang, A. S. Bhalla and L. E. Cross, "Quasi Lumped Parameter Method for Microwave Measurements of Dielectric Dispersion in Ferroelectric Ceramics," *Proc. ISAF 1992*, Greenville, South Carolina.
16. H. Wang, Q. M. Zhang, L. E. Cross and A. O. Sykes, "Piezoelectric Dielectric and Elastic Properties of Poly (Vinylidene Fluoride/Trifluoroethylene)."
17. H. Wang, Q. M. Zhang, L. E. Cross and A. O. Sykes, "Clamping Effect on Piezoelectric Properties of Poly (Vinylidene Fluoride/Trifluoroethylene) Copolymers."

### **Composite Sensors**

18. Ki-Young Oh, Yutaka Saito, Atsushi Furuta and Kenji Uchino, "Piezoelectricity in the Field Induced Ferroelectric Phase of Lead Zirconate Based Antiferroelectrics," *J. Amer. Ceram. Soc.* **75** (4), 795 (1992).

### *Composite Sensors (continued)*

19. R. E. Newnham, Q. C. Xu, K. Onitsuka and S. Yoshikawa, "A New Type of Flextensional Transducer," Proc. 3<sup>rd</sup> Int. Mtg. on Transducers for Sonics and Ultrasonics (May 1992).
20. C. A. Randall, D. V. Miller, J. H. Adair and A. S. Bhalla, "Processing of Electroceramic-Polymer Composites Using the Electrorheological Effect," J. Mat. Res. **8** (4), 1 (1993).
21. C. A. Randall, S. Miyazaki, K. L. More, A. S. Bhalla and R. E. Newnham, "Structural-Property Relations in Dielectrophoretically Assembled BaTiO<sub>3</sub> Nanocomposites," Materials Letters **15**, 26 (1992).
22. C. A. Randall, S. F. Wang, D. Laubscher, J. P. Dougherty and W. Huebner, "Structure Property Relations in Core-Shell BaTiO<sub>3</sub>:LiF Ceramics," J. Mat. Res. (in press).
23. C. A. Randall, G. A. Rossetti and W. Cao, "Spatial Variations of Polarization in Ferroelectrics and Related Materials."
24. Jayu Chen, Qi Chang Xu, M. Blaszkiewicz, R. Meyer, Jr. and R. E. Newnham, "Lead Zirconate Titanate Films on Nickel-Titanium Shape Memory Alloys: SMARTIES," J. Amer. Ceram. Soc. **75** (10), 2891 (1992).

### *Actuator Studies*

25. D. Damjanovic and R. E. Newnham, "Electrostrictive and Piezoelectric Materials for Actuator Applications," J. Intell. Mat. Syst. and Struct. **3**, 190 (1992).
26. Y. Sugawara, K. Onitsuka, S. Yoshikawa, Q. C. Xu, R. E. Newnham and K. Uchino, "Metal-Ceramic Composite Actuators," J. Amer. Ceram. Soc. **75** (4), 996 (1992).
27. Q. C. Xu, A. Dogan, J. Tressler, S. Yoshikawa and R. E. Newnham, "Ceramic-Metal Composite Actuators," Ferroelectrics Special Issue.
28. K. Uchino, "Piezoelectric Ceramics in Smart Actuators and Systems," Proc. 1<sup>st</sup> European Conference on Smart Structures and Materials.
29. A. Furuta, Ki-Young Oh and K. Uchino, "Shape Memory Ceramics and Their Application to Latching Relays," Sensors and Materials **3** (4), 205 (1992).
30. K. Uchino and A. Furuta, "Destruction Mechanisms in Multilayer Ceramic Actuators," Proc. ISAF 1992, Greenville, South Carolina, pp. 195.
31. Q. Jiang, Wenwu Cao and L. E. Cross, "Electric Fatigue Initiated by Surface Contamination in High Polarization Ceramics," Proc. ISAF 1992, Greenville, South Carolina, pp. 107.
32. Q. Jiang, Wenwu Cao and L. E. Cross, "Electric Fatigue in PLZT Ceramics."

### ***Integration Issues***

33. Wenwu Cao, Q. M. Zhang and L. E. Cross, "Theoretical Study on the Static Performance of Piezoelectric Ceramic-Polymer Composite with 1-3 Connectivity," *J. Appl. Phys.* **72** (12), 5814 (1992).
34. Q. M. Zhang, Wenwu Cao, H. Wang and L. E. Cross, "Characterization of the Performance of 1-3 Type Piezocomposites for Low Frequency Applications," *J. Appl. Phys.* **73** (3), 1403 (1993).
35. Q. M. Zhang, Wenwu Cao, H. Wang and L. E. Cross, "Strain Profile and Piezoelectric Performance of Piezocomposites with 2-2 and 1-3 Connectivities," *Proc. ISAF 1992, Greenville, South Carolina*, pp. 252.
36. Q. M. Zhang, H. Wang and L. E. Cross, "Piezoelectric Tubes and 1-3 Type Tubular Composites as Tunable Actuators and Sensors."
37. Q. M. Zhang, H. Wang and L. E. Cross, "Piezoelectric Tubes and Tubular Composites for Actuator and Sensor Applications."

### ***Processing Studies***

38. Thomas R. ShROUT and Scott L. Swartz, "Processing of Ferroelectric and Related Materials: A Review."
39. G. A. Rossetti, D. J. Watson, R. E. Newnham and J. H. Adair, "Kinetics of the Hydrothermal Crystallization of the Perovskite Lead Titanate," *J. Crystal Growth* **116**, 251 (1992).
40. A. V. Prasadarao, U. Selvaraj, S. Komarneni and A. S. Bhalla, "Sol-Gel Synthesis of  $\text{Ln}_2(\text{Ln} = \text{La}, \text{Nd}) \text{Ti}_2\text{O}_7$ ," *J. Mat. Res.* **7** (10), 2859 (1992).
41. A. V. Prasadarao, U. Selvaraj, S. Komarneni and A. S. Bhalla, "Sol Gel Synthesis of Strontium Pyroniobate and Calcium Pyroniobate," *J. Amer. Ceram. Soc.* **75** (10), 2697 (1992).
42. A. V. Prasadarao, U. Selvaraj, S. Komarneni and A. S. Bhalla, "Fabrication of  $\text{La}_2\text{Ti}_2\text{O}_7$  Thin Films by A Sol-Gel Technique," *Ferroelectrics Letters* **14**, 65 (1992).
43. S. F. Wang, U. Kumar, W. Huebner, P. Marsh, H. Kankel and C. G. Oakley, "Grain Size Effects on the Induced Piezoelectric Properties of 0.9 PMN-0.1PT Ceramic," *Proc. ISAF 1992, Greenville, South Carolina*, pp. 148.
44. C. A. Randall, A. D. Hilton, D. J. Barber and T. R. ShROUT, "Extrinsic Contributions to the Grain Size Dependence of Relaxor Ferroelectric  $\text{Pb}(\text{Mg}_{1/3}\text{Nb}_{2/3})\text{O}_3:\text{PbTiO}_3$  Ceramics," *J. Mat. Res.* **8** (4) (1993).
45. B. V. Hiremath, R. E. Newnham and L. E. Cross, "Barrier Layer Capacitor Using Barium Bismuth Plumbate and Barium Plumbate," *J. Amer. Ceram. Soc.* **75** (11), 2953 (1992).
46. U. Kumar, S. F. Wang, S. Varanasi and J. P. Dougherty, "Grain Size Effects on the Dielectric Properties of Strontium Barium Titanate," *Proc. ISAF 1992, Greenville, South Carolina*, pp. 55.

*Processing Studies (continued)*

47. U. Kumar, S. F. Wang and J. P. Dougherty, "Preparation of Dense Ultra-Fine Grain Barium Titanate-Based Ceramics," Proc. ISAF 1992, Greenville, South Carolina, pp. 70

*Thin Film Ferroelectrics*

48. J. Chen, K. R. Udayakumar, K. G. Brooks and L. E. Cross, "Dielectric Behavior of Ferroelectric Thin Films at High Frequencies," Proc. ISAF 1992, Greenville, South Carolina, pp. 182.
49. K. Uchino, N-Y. Lee, T. Toba, N. Usuki, H. Aburatani and Y. Ito, "Changes in the Crystal Structure of RF-Magnetron Sputtered BaTiO<sub>3</sub> Thin Films," J. Chem. Soc. Japan 100 (9), 1091 (1992).
50. R. E. Newnham, K. R. Udayakumar and S. Trolier-McKinstry, "Size Effects in Ferroelectric Thin Films," *Chemical Processing of Advanced Materials*, Edited by Larry L. Hench and Jon K. West, John Wiley and Sons, Inc. (1992).
51. S. Trolier-McKinstry, H. Hu, S. B. Krupanidhi, P. Chindaudom, K. Vedam and R. E. Newnham, "Spectroscopic Ellipsometry Studies on Ion Beam Sputter Deposited Pb(Zr, Ti)O<sub>3</sub> Films on Sapphire and Pt-Coated Silicon Substrates."

# **PROCESSING- STUDIES**

**APPENDIX 38.**

# Processing of Ferroelectric and Related Materials: A Review

Thomas R. Shrout<sup>†</sup> and Scott L. Swartz<sup>\*</sup>

<sup>†</sup>Materials Research Laboratory  
The Pennsylvania State University  
University Park, PA 16802

<sup>\*</sup>Battelle Memorial Institute  
Columbus, OH 43201

## ABSTRACT

The objective of this article is to present a synopsis of recent, ongoing, and future evolutionary developments pertaining to the fabrication/processing of ferroelectric materials, with an emphasis on polycrystalline ceramics. The basis for the review was derived from relevant literature over the last dozen years, including the responses from a worldwide questionnaire. This survey addressed issues such as chemical synthesis methods vs. conventional processes and anticipated future developments in processing and their impact on new applications, if any. The survey participants were scientists and engineers, both academic and industrial, involved in research and development of ferroelectrics and related materials. The primary conclusion of this survey revealed that evolutionary advancements in the processing of ferroelectric ceramics will continue to impact commercial production over the next ten years.

## I. INTRODUCTION

Ferroelectric and related materials continue to be exploited for numerous applications, including recent concepts of "smart" or intelligent systems, whereby multifunctional components are required.<sup>(1-4)</sup> In recent years, substantial research and development has been devoted to ferroelectric materials in the form of single crystals, polymers, composites, and especially, thin films. References are provided for these important topics, but the primary focus of this paper pertains to polycrystalline materials. The most widely used and researched ferroelectric structural types, compositions, applications, and their state of development are presented in Table 1. Although the materials and ceramic fabrication methods for the ferroelectric materials described had their origin decades ago, this paper attempts to review evolutionary advances in the processing and fabrication of ferroelectric ceramics. The data presented is based on the compilation of responses to a questionnaire from more than 100 international scientists and engineers, of both academic and industrial backgrounds. In addition, recent processing developments and novel fabrication schemes, their future impact on new applications, if any, are discussed.

## II. MATERIALS AND APPLICATIONS

As presented in Table 1, the most widely used ferroelectrics are found in the perovskite family general formula  $ABO_3$ , which includes hundreds of compositional modifications (e.g., solid solution substitutions and/or dopants). In addition to ceramic materials, ferroelectric polymers, including PVF<sub>2</sub> and other copolymers, are well established in the market place. Perhaps the most significant development comes not from monolithic materials but in the tailoring of physical properties using the nature of composites. Through the concept of phase connectivity<sup>(5-7)</sup>, properties can be engineered to give orders of magnitude performance enhancement. Specifically, piezoelectric composites are finding increasing use in applications such as ultrasonic transducers for bio-medical imaging<sup>(8-9)</sup> and towed-array hydrophones.<sup>(10)</sup>

The ability to fabricate known ferroelectric materials in thin-film form offers applications such as non-volatile memories and DRAMs, both soon to be commercial realities. Furthermore, thin-film offers the potential of engineered crystallographic technology, thus allowing the exploitation of non-centrosymmetric materials such as ZnO and AlN, which in polycrystalline form cannot be made piezoelectrically active.<sup>(11,12)</sup>

Overall, however, in the field of ferroelectric polycrystalline ceramics, No new materials are foreseen that will provide revolutionary impact to new applications. Instead, evolutionary advances in the processing of ferroelectric ceramics will lead to improvements in existing commercial applications and to a gradual implementation of existing materials in new applications. For example, although ceramic materials such as relaxor ferroelectrics have been known for some forty years, progress in their commercialization for MLC capacitors and actuators has resulted from recent enhancements in their processing and fabrication.<sup>(13-16)</sup>

## III. FABRICATION/PROCESSING OF FERROELECTRIC CERAMICS

Fabrication technologies for all electronic ceramic materials have the same basic process steps as presented in Figure 1, regardless of the application: powder preparation, powder processing, green forming, and densification.

### A. Powder Preparation

The goal in the preparation of ferroelectric powders is to achieve a ceramic powder which, after consolidation, yields a product satisfying specified performance standards. A secondary goal is to produce a powder that can be consolidated/densified at lower temperatures. The most important commercialized powder preparation methods for ferroelectric ceramics include: mixing/calcination, coprecipitation from solvents, metal organic decomposition and hydrothermal processing. The trend in powder preparation is towards powders having particle sizes less than 1  $\mu$ m and little or no agglomerates for enhanced reactivity and uniformity. Such powder qualities allow for the development of fine-grained microstructures with enhanced mechanical and electrical properties. Most importantly, fine particulates are critical for the continuing miniaturization of electro-ceramic devices. Examples of the four basic methods are presented in Table 2 for the preparation of BaTiO<sub>3</sub> powder. References relevant to processing advancements, particularly in regard to multilayer capacitor applications, including review articles<sup>(18,43)</sup>, are given at the end of this paper.

Specific examples of significant developments in mixing/calcination processes are given for the PbO-based relaxor-based materials  $Pb(Mg_{1/3}Nb_{2/3})O_3$  [PMN] in Table 3. The primary limitation for the development of ferroelectric relaxors has been in the consistent synthesis of phase-pure perovskite powders and ceramics. However, this problem has been successfully addressed through an improved understanding of the surface properties of the constituent oxides, crystal chemistry of PMN, and overall kinetics of the synthesis reaction. Specifically, the "B-site precursor" method, whereby the B-site oxides are prereacted to form a columbite phase, allows enhanced dispersion and favors formation of the perovskite phase in contrast to lead-niobate pyrochlores.

Note, many of the advances in mixing/calcination have come through the better understanding of process-structure-property relationships. For example, knowledge of the underlying physiochemical behavior of Pb-based perovskites, also including pyrochlores and Bi-layer structures, allows for controlled morphological developments during calcination or "soft agglomeration," whereupon high reactive materials can be readily prepared.

**Coprecipitation** is a chemical method whereby insoluble compounds (e.g., hydroxides or oxalates, etc.) are precipitated from a solution of metal salts (e.g., chlorides), and the precipitated product is calcined to form the desired oxide powder. The advantage of this technique over calcination of mixed oxides is that intimate mixing of the precursors (in the solution phase) leads to lower calcination temperatures and the preparation of high-purity and fine-particle-size powders, see Table 3. Limitations are that the calcination step may once again result in agglomeration of fine particulates and the need for milling. An additional problem is that contaminants from the coprecipitation process (e.g., chlorides, carbonates, etc.) may linger in the powder after calcination. For example, commercially available, high-purity BaTiO<sub>3</sub> powder prepared by the well-known oxalate process, whereby a Ba-Ti chloride solution is precipitated by oxalic acid and the resulting precipitate is calcined. However, the sintering performance of these high-purity BaTiO<sub>3</sub> powders is hindered by the presence of BaCO<sub>3</sub>, which is formed during calcination.

**Metal organic decomposition (MOD)**, often referred to as sol-gel processing, in which metal-containing organic chemicals (e.g. alkoxides) react with water in a non-aqueous solvent to produce a metal hydroxide or hydrous oxide, or in special cases, an anhydrous metal oxide. Powders typically require calcination to obtain the desired phase. A major advantage of the MOD method is the control over purity and stoichiometry that can be achieved with powder crystallite size on the order of 5-50 nm. However, powder processing methods for nano-sized particulates have not been developed to take full advantage of such fine powders.

The advantage of this technique over mixing/calcination is exemplified by multilayer capacitors fabricated using alkoxide-derived relaxor based dielectrics. Capacitors produced with this powder have lower sintering temperatures and submicron grain sizes, thus allowing thinner layers and enhanced dielectric breakdown strength. Such benefits, however, are contrasted by expensive chemicals and processing methods.

**Hydrothermal synthesis** uses hot (above 100°C) water under pressure to produce crystalline oxides<sup>(62)</sup> and is widely used in the formation of Al<sub>2</sub>O<sub>3</sub> (Bayer Process). The major advantage of the hydrothermal technique is that crystalline powders of the desired stoichiometry and phases can be prepared at temperatures significantly below those required for calcination. Another advantage is that the solution phase can be used to keep the particles separated and thus minimize agglomeration. The major limitation of hydrothermal processing is the need for the feedstocks to react in a closed system to maintain pressure and prevent boiling of the solution. Currently, Sakai Chemical and Cabot Corporation offer commercially available BaTiO<sub>3</sub>-based powders, with PZT materials from Morgan Matroc in the late stages of development.

Laboratory research has shown the considerable benefits of hydrothermally-synthesized powders, e.g. Ba:Ti homogeneity, lower sintering temperatures, etc. However, these powders perform dramatically differently in post processing and sintering behavior requiring further developments for successful commercialization. As an example of their unique behavior, the intrinsic nature of OH-bonding in hydrothermally derived BaTiO<sub>3</sub> powders is thought to greatly influence densification<sup>(63)</sup>, particularly when accompanied by a Bi<sub>2</sub>O<sub>3</sub>-based flux, whereby densification could be achieved at temperatures less than 800°C.<sup>(64)</sup>

### Hybrid Synthesis

A wide spectrum of ferroelectric ceramic powders may also be produced by the hybrid process involving both chemical synthesis and conventional powder processing steps. For example, promising results have been reported for PZT ceramics derived from powders prepared from the conventional processing of a mixture of PbO and a hydrothermal zirconium titanate precursor.<sup>(60,65)</sup> The use of chemical synthesis methods to

Table 1. Ferroelectric Materials and Applications<sup>(17-23)</sup>

Structural Family	Composition	Application	Development Stage
Perovskite	BaTiO <sub>3</sub>	Capacitors	Commercialized
	(Ba,Sr)TiO <sub>3</sub>	IR Detectors	Development <sup>(24)</sup>
	(Ba,Sr)TiO <sub>3</sub> (doped)	PTCR Thermistors	Commercialization
	Pb(Zr,Ti)O <sub>3</sub> (PZT)	Transducers	Commercialization
		Actuators	Development <sup>(25)</sup>
	Pb,La(Zr,Ti)O <sub>3</sub> (PLZT)	Electro-optics	Commercialization
	Ca-doped PbTiO <sub>3</sub>	Transducers	Development/Commercialization <sup>(26,27)</sup>
	Sm-doped PbTiO <sub>3</sub>	(hydrophones)	
	Pb(Sc,Ta)O <sub>3</sub>	IR Detectors	Development <sup>(28)</sup>
	(Na,Bi)TiO <sub>3</sub>	Transducers (Pb-free)	Research <sup>(29)</sup>
Tungsten-Bronze	Pb(Mg,Nb)O <sub>3</sub> (Relaxors)	Capacitors	Commercialization <sup>(30,31)</sup>
		Actuators	Development <sup>(32,33)</sup>
		Electro-optics	Research <sup>(34,35)</sup>
	Ba(Zn,Ta)O <sub>3</sub>	Microwave Resonators	Commercialization
Bismuth-Bronze	PbNb <sub>2</sub> O <sub>6</sub>	Transducers (hydrophones)	Commercialization
	(Sr,Ba)Nb <sub>2</sub> O <sub>6</sub>	Electro-optics	Research/Development <sup>(36)</sup>
Bismuth-Layer Structure	Bi <sub>4</sub> Ti <sub>3</sub> O <sub>12</sub> , Bi <sub>2</sub> WO <sub>6</sub>	Transducers (accelerometers)	Commercialization
Perovskite-Layer Structure	Sr <sub>2</sub> Nb <sub>2</sub> O <sub>7</sub>	Transducers	Research <sup>(37)</sup>
	La <sub>2</sub> Ti <sub>2</sub> O <sub>7</sub>	(high-temperature)	
	Bi <sub>2</sub> (Zn,Ni,Nb)O <sub>2</sub>	Capacitors	Development <sup>(38)</sup> /Commercialization <sup>(39)</sup>
Composites	PZT/Polymer	Transducers	Development <sup>(9,10)</sup>
Polymers	PVF <sub>2</sub> , Co-polymers	Transducers	Development/Commercialization <sup>(40-42)</sup>
Miscellaneous	Li <sub>2</sub> B <sub>4</sub> O <sub>7</sub> and AlPO <sub>4</sub> (Crystals)	Transducers	Development
	ZnO films	(high-frequency)	Commercialized
	AlN films		Research <sup>(11)</sup>

Note: Development stage may refer to limited commercial introduction specific to certain geographical regions.

uniformly distribute dopants to conventionally prepared powders of BaTiO<sub>3</sub> for capacitors is another way to combine the performance advantages of chemical synthesis and cost effectiveness of conventional processing.<sup>(61)</sup>

## B. Powder Processing

A basic guideline of powder manufacturing is to do as little processing as possible to achieve the targeted performance standards. Ceramic powder fabrication is an iterative process during which undesirable contaminants and defects can enter into the materials at any stage. Therefore, it is best to keep the powder processing scheme as simple as possible to maintain flexibility. Uncontrollable factors such as changes in characteristics of as-received powders must be accommodated to achieve reproducibility in the processing from batch to batch of material. Keeping the processing simple is not always possible for ferroelectric ceramics, based simply on their complex nature, e.g. the need for precise stoichiometry control and dopants.

A fundamental requirement in powder processing and perhaps key to the continued performance enhancement is characterization of the as-received or synthesized powders.<sup>(66)</sup>

Information on tap and pour density, particle size distribution, specific surface areas, and chemical and phase analysis are critical. Uniaxial compaction behavior, in particular, is easily measured and provides data on the nature of the agglomerates in a powder.

Milling is required for most powders, either to reduce particle size or to aid in the mixing of component powders. Commonly employed types of comminution include ball milling, vibratory, attrition, and jet milling, each possessing its own advantages and disadvantages. For example, ball milling is well suited for mixing, but not for comminution, unless varying media sizes and long milling times are used. Vibratory milling is well suited for comminution, but extreme care in dispersion/rheological behavior must be considered, whereas attrition milling, though very effective, is generally more expensive. Example of advances in terms of powder processing are given in Table 4. As presented, attrition milling allows for the preparation of extremely fine particulates, generally are achievable by chemical synthesis methods. Along with the introduction of high performance milling media, e.g. partially stabilized zirconia (PSZ), minimizing contamination, attrition milling is finding growing usage for the processing of electronic ceramics.

Figure 1. Schematic of iterative processing of ferroelectric ceramics and key characterization methods. "Key to performance and reliability lies in the understanding of precursor-process-structure property relationships."

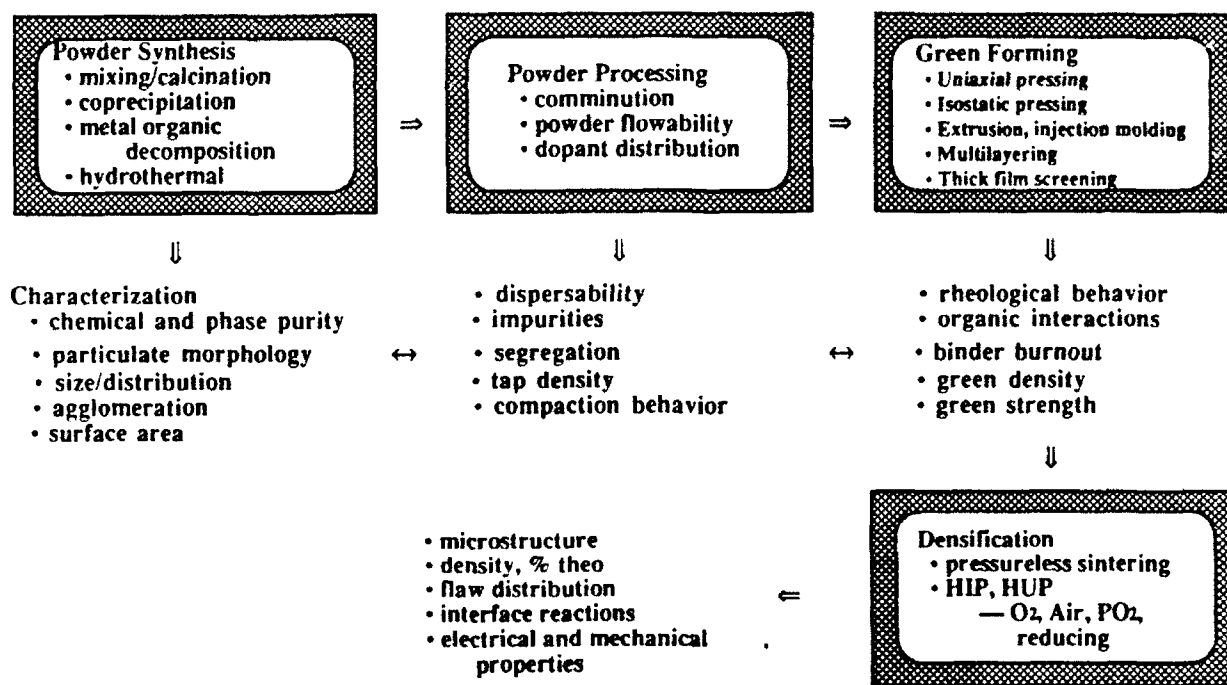


Table 2. Methods Used to Prepare BaTiO<sub>3</sub> Electronic Ceramic Powders

Method	Reaction	Particle Size
Mixing/calcination	$BaCO_3 + TiO_2 \xrightarrow{\Delta T} BaTiO_3 + CO_2 \uparrow$	1 $\mu$ m to 100 $\mu$ m
Coprecipitation	$Ba^{2+} + TiO_2^{2+} + 2 C_2O_4^{2-} \xrightarrow{\frac{2}{4} H_2O} BaTi(C_2O_4)_2 \cdot 4H_2O \xrightarrow{\Delta T}$	0.5 $\mu$ m (after calcining and milling)
Hydrothermal	$Ba(OH)_2 + Ti(OH)_4 + \xrightarrow[\Delta T, P]{H_2O, pH} BaTiO_3 + 2H_2O$	Nanosize to 5 $\mu$ m
Metal organic (Alkoxide)	$Ba(OR)_2 + Ti(OR)_4 + \xrightarrow[\text{solvent}]{H_2O, \Delta T} BaTi(OR)_6 \xrightarrow{\Delta T} BaTiO_3 + 6R$	5.0-50.0 nm, (crystallite size) [agglomerate size larger]

Progress in understanding the surface chemistry of component and reacted materials has allowed the wide spread usage of aqueous processing as well as the ability to disperse fine particulates through surface passivation.<sup>(67)</sup> With growing environmental concerns related to the use and/or disposal of hazardous solvents, aqueous processing will continue to become important in the future.

"With the advances presented above and the overall control of incoming raw materials, e.g. morphology, purity, etc., high performance ceramics are generally achievable without the implementation of expensive chemical methodologies, making the mixing/calcination process the method of choice for most ferroelectric materials well into the future." However, continued development of powder processing methods for fine-particle size powders will allow future commercialization of chemical methods if the cost of their advanced powders can be reduced.

### C. Green Forming

Green forming is one of the most critical steps in the fabrication of ferroelectric ceramics. The choice of green forming technique depends on the ultimate geometry required for a specific application. There are many different ways to form green ceramics, several of which are summarized in Table 5. Perhaps, of all the methods, the most significant advances in processing have been in the realm of multilayer fabrication, which includes: piezoelectric/electrostrictive capacitors (>50 billion units/year), piezoelectric/electrostrictive actuators, and varistors, as well as several in non-ferroelectric applications (e.g. ceramic packaging).<sup>(69,70)</sup>

Table 6 summarizes recent developments in MLC fabrication. Naturally, the enhanced performance arises from the corresponding development in binders, dispersants, and overall organics and their role in sheet formation. In addition, ultra-thin MLCs have led to the need for correspondingly thin metallization. Of particular significance in the fabrication of MLCs is that based on

magnetic tape fabrication technology, whereupon thin sheets can be formed >600 ft./min., while being simultaneously electroded.<sup>(71)</sup>

Recent developments in the fabrication of piezoelectric-polymer composites, primarily for bio-medical ultrasound and towed array transducers, are given in Table 7. In addition to achieving fine-scale composites, current emphasis lies in the ability to economically fabricate large areas (>meter-square).

### D. Densification

Densification of ferroelectric materials generally requires high temperature and atmosphere control (O<sub>2</sub>, PbO, vacuum, etc.) to minimize the porosity in consolidated ceramics. Heat-controlled cycles are critical to microstructural development and grain size control. Techniques such as fast firing and rate controlled sintering have been utilized to inhibit or eliminate undesirable sintering mechanisms. Hot isostatic pressing (HIP), which employs a gaseous pressure at high temperature, has found more commercialization in contrast to hot uniaxial pressing, which is limited to relatively simple shapes. The HIP process has been shown to greatly enhance the dielectric breakdown strength (DBS) of multilayer ceramics and actuators and can be used to prepare transparent materials, including PLZTs and PMN. Advancements in HIP processing of PbO-based ferroelectrics have also been made with the introduction of oxygen atmosphere compatible systems (see Table 8).

Work continues to find economical densification processes by which macro-defect free ceramics with near theoretical densities can be achieved, allowing one to approach the maximum properties allowable in ferroelectric ceramics. Much of the progress in this direction, however, will be made through advances in the powder synthesis, processing, and forming methods.

Table 3. Advances in Synthesis of Ferroelectric Materials

Advancement	Material	Demonstrated Benefits
<b>Conventional (Mixing/Calcination) Powder Synthesis</b>		
Pre-reaction of B-site precursors (Columbite method)	Pb(Mg,Nb)O <sub>3</sub>	Improved perovskite phase purity <sup>(44)</sup>
Modification of surface chemistry (pH control) to optimize dispersion	Pb(Mg,Nb)O <sub>3</sub>	Improved perovskite phase purity <sup>(14)</sup>
Crystal chemical engineering (doping with BaTiO <sub>3</sub> , SrTiO <sub>3</sub> )	Pb(Zn,Nb)O <sub>3</sub>	Improved perovskite phase purity <sup>(45,46)</sup>
Reactive calcination (optimization of calcination conditions)	PMN, PZT	Improved sintering reactivity <sup>(47)</sup>
<b>Advanced Powder Synthesis Methods</b>		
Alkoxide Synthesis	Pb-based relaxors	Fine-particle-size powders <sup>(31,49)</sup> Thin-layer MLCs
Pechiney Method (Citrate decomposition)	BaTiO <sub>3</sub> Ba,SrTiO <sub>3</sub> ,PZT	Fine-particle-size powders <sup>(50,51,52)</sup> High purity
Oxalate Coprecipitation	BaTiO <sub>3</sub>	Fine-particle-size powders <sup>(53,54)</sup> High purity, stoichiometry
Hydrothermal Synthesis	BaTiO <sub>3</sub> , PZT	Fine-particle-size powders <sup>(55,56,57,58,59)</sup> Lower sintering temperatures
<b>Hybrid Methods</b>		
PbO + hydrothermal (Zr,Ti)O <sub>4</sub>	PZT	Improved compositional uniformity <sup>(60)</sup> Fine grain size
Chemical methods for dopant addition "nanoheterogeneity"	BaTiO <sub>3</sub>	Uniform dopant incorporation <sup>(61)</sup> (X7R dielectrics)

Table 4. Advances in Powder Processing

Concept	Benefit
<ul style="list-style-type: none"> <li>High energy mil. s e.g. attrition <math>PbO+MgO+Nb_2O_5 \rightarrow PMN</math></li> </ul>	<ul style="list-style-type: none"> <li>Submicron powders<sup>(47,68)</sup></li> <li>Dispersion<sup>(14)</sup></li> </ul>
<ul style="list-style-type: none"> <li>PSZ media</li> </ul>	<ul style="list-style-type: none"> <li>Minimal contamination</li> </ul>
<ul style="list-style-type: none"> <li>Aqueous processing</li> </ul>	<ul style="list-style-type: none"> <li>Non-toxic solvent</li> <li>Low cost</li> </ul>
<ul style="list-style-type: none"> <li>Surface powder chemistry understanding e.g. "Passivation - <math>BaTiO_3</math>"</li> </ul>	<ul style="list-style-type: none"> <li>Rheological control (dispersability)</li> </ul>

IV. SUMMARY

The primary conclusion of this review is that the fabrication of ferroelectric ceramic materials will continue to see evolutionary advances, primarily in the areas of synthesis and processing. The implementation of recent improvements in processing methods for conventional powders (e.g. attrition milling, dispersion, etc.) will extend the performance of ferroelectric ceramics. However, there will be a need for advanced powder synthesis methods and associated handling and consolidation procedures for the high-performance end of certain applications, e.g. cryogenic actuators for space. Without revolutionary advances, the primary focus of development will be on reducing cost of advanced powder synthesis methods, such as hydrothermal synthesis and coprecipitation. If these cost issues can be addressed, advanced synthesis methods will significantly enhance existing materials (e.g.,  $BaTiO_3$ -based dielectric ceramics and PZT-based piezoelectric ceramics). Although the discovery of new ferroelectric materials is not anticipated, continued improvements in the processing of emerging ferroelectric ceramics, such as  $PbO$ -based relaxors, will lead to their increased use in existing applications (capacitors and actuators), and enable their development for emerging applications (e.g., E-field tunable transducers for sonar and bio-medical ultrasound).<sup>(97)</sup>

Table 5. Green Forming Procedures for Ferroelectric Ceramics

Green Forming Method	Geometries	Applications
Uniaxial Pressing	Disks, toroids, plates	Disk capacitors, piezo transducers, igniters, inch-worm actuators
Cold Isostatic Pressing	Complex and simple	High-frequency ultrasonic transducers
Colloidal Casting	Complex shapes	Transducers
Extrusion	Thin sheets (>80 $\mu m$ ) rods, tubes, honeycombs, substrates	Igniters PTC thermister heaters
Injection Molding	Complex shapes	PZT-composites
Multilayer Fabrication	Thin sheets/multicomponent	Capacitors, actuators Varistors

Table 6. Advances in MLC Manufacturing

Advances	Benefits	Development Stage
Ultra-thin MLCs • $\leq 10\mu$	<ul style="list-style-type: none"> <li>Cap. Vol. Eff.</li> <li>High energy storage<sup>(73)</sup> (replace tantalum &amp; electrolytics)</li> </ul>	Commercialized <sup>(31,72)</sup>
• $\leq 6\mu$		Research/Development <sup>(74)</sup>
• Fine Metallization		Development <sup>(75)</sup>
• High Speed Fabrication	<ul style="list-style-type: none"> <li>Low cost (&gt;600 ft/min.)</li> </ul>	Development <sup>(71)</sup>
• Low-Fire — Ag:Pd electrodes	<ul style="list-style-type: none"> <li>Low cost</li> </ul>	Commercialized
• Material/Dielectrics —High K >5000 X7R	<ul style="list-style-type: none"> <li>Cap. Vol. Eff.</li> </ul>	Development <sup>(76)</sup> /Commercialized
—Relaxors, e.g. PMN-based	<ul style="list-style-type: none"> <li>Cap. Vol. Eff.</li> </ul>	Commercialized
—Varistors (ZnO)	<ul style="list-style-type: none"> <li>Surface Mount Chip Integration</li> </ul>	Commercialized
—PZTs, PMN	<ul style="list-style-type: none"> <li>Actuators</li> </ul>	Commercialized

## V. SURVEY RESULTS

Prior to conducting this review, a worldwide survey was conducted of scientists and engineers involved in ferroelectric materials research, from both academic and industrial organizations. This survey addressed significant recent and anticipated developments of ferroelectric materials, and the question of whether conventional fabrication methods for ferroelectric materials will be sufficient for future applications requirements. Responses were categorized by geographical region (North America, Europe, and the Far East). Results of this survey are summarized below:

- The field of ferroelectric films, although outside the scope of this review, was recognized as an area where significant recent developments were achieved, and where an even larger number of future developments and applications were anticipated. The importance of ferroelectric films was recognized by the largest percentage of respondents, regardless of geographical region.
- Multilayer ceramics, both actuators and capacitors, were identified as an application area where significant recent developments, particularly in terms of ultra-thin layers and the incorporation of relaxor ferroelectrics, have been made, especially by respondents from the Far East
- Advances in conventional processing was cited as an area of significant recent achievement, although there was little confidence that conventional processing would see additional advances in the future. Chemical synthesis of ceramic powders, by sol-gel and coprecipitation methods, was recognized as important to future development of existing and emerging applications, but strides must be made to achieve economical feasibility, perhaps being achievable through combined methodologies, i.e. hybrid processes.

- Areas identified as seeing significant recent developments included hot-pressing and HIP techniques and piezoelectric composites, whereas research topics identified as important to future applications include thick film processing for multicomponent packaging, assemble of nano-composites for electro-optics and ferro-fluids, relaxor ferroelectrics, smart materials, and optoelectronic materials.

## ACKNOWLEDGEMENTS

The authors wish to thank all those who took time out from their busy schedules to answer our questionnaire. The following is a partial list of industries, universities, and government laboratories from which the responses came:

### Companies

Toshiba, Sakai Chemical, Denka, NEC, Sumitomo Metals, Matsushita Electric, Murata, Nippon Soda, Mitsubishi Mining and Cement (Materials), Kyocera, Hitachi, TDK, AT&T, DuPont, Battelle, Martin Marietta, BM Hi-Tech, Piezo Systems, Alcoa, MRA Laboratories, Centre Engineering, Acoustic Imaging, Krautkramer Branson, Hewlett Packard, Alliant Ceramics, Cleveland Crystals, ITEK Optical, IBM, Vitramon, Army (Fort Monmouth), Siemens, Philips, GEC Marconi, Ferroperm, CNET/France Telecom, ISMRA Lab CRTSMAT, Toshiba Tungalloy, Morgan Matroc

Shonan Institute of Tech, National Defense Academy, Science University at Tokyo, Nagoya, Kyushu Institute of Tokyo, Penn State, Texas A&M, Office of Naval Research, Florida University, Montana State, Naval Research Lab, Institute of Physics-Rostov, Ben-Curion University, University des Saarlandes, Ecole Polytechnique de Lausanne, National Institute in Inorganic Materials, Hachinohe Institute of Technology, Institute of Crystallography (Moscow), Indian Institute of Science, Osaka University

A special thanks to JoAnn Mantz for her help in putting together the questionnaire and this manuscript.

Table 7. Advances in the Fabrication of PiezoPolymer Composites

Advances	Benefits	Development Stage
Extrusion	≤100 micron PZT rods ≤10 micron	Development <sup>(77)</sup> Research <sup>(78)</sup>
Pick and Place (Weaving)	Large Area (> meter-squared)	Development <sup>(79)</sup>
Lost Mould Method	10 μ - 100 scale	Development <sup>(80,82)</sup>
Injection Molding	Low cost	Development <sup>(83)</sup>
Fill and Dice	Simplistic	Commercialized

Table 8. Advances in the Densification of Ferroelectric Materials

Advances	Benefit	Development Stage
• Pressureless sintering — Vacuum/atmosphere control — Rate-controlled densification	• Transparent PLZT • Lower Firing Temp PZTs	Development <sup>(84,84)</sup> Research <sup>(86)</sup>
• Hot uniaxial pressing (HUP)	• PZTs (pyroelectric ~10 μ wafers • Transparent PMN, SBN,	Commercialized Research <sup>(87,88)</sup>
• Hot isostatic pressing (HIP)	• Complex shapes • Multilayer capacitors — fatigue reduction • Multilayer actuators • Transparent PMN, PLZT	Research/Development <sup>(89,91)</sup> Commercialized <sup>(88-91)</sup>
• Hot forging	• Grain orientation e.g. Bi <sub>4</sub> Ti <sub>3</sub> O <sub>12</sub>	Research <sup>(29,37,92)</sup>
• Mixed sintering	• Flat T.C.C. MLCs	Research <sup>(93,94)</sup>
• Fluxes (liquid phase) e.g. lithium oxide & fluorides	• Low firing temps	Research/Development <sup>(95,96)</sup>

†Temperature coefficient of capacitors.

## REFERENCES

1. R.E. Newnham and G. R. Ruschau, "Smart Electroceramics," *J. Amer. Cer. Soc.*, 74, pp. 463-479 (1991).
2. R.E. Newnham, "The Golden Age of Electroceramics," *Adv. Ceram. Mater.*, 3, 12-16 (1988).
3. H. Yanagida, "Intelligent Materials--A New Frontier," *Angew. Chem.*, 100, 1443-46 (1988).
4. C.A. Rogers, "From the Editor," *Journal of Intelligent Material Systems and Structures*, 1,3 (1990).
5. R.E. Newnham, "Composite Electroceramics," *J. Mater. Educ.*, 7, 605-51 (1985).
6. R.E. Newnham, et al., "Connectivity and Piezoelectric-Pyroelectric Composites," *Mater. Res. Bull.*, Vol. 13, No. 5, pp. 525-536, 1978.
7. H. Banno and S. Saito, "Piezoelectric and Dielectric Properties of Composites of Synthetic Rubber and  $\text{PbTiO}_3$  or PZT," *Ann. N.Y. Acad. Sci.*, Vol. 22, Suppl. 22-2, pp. 67-69 (1983).
8. H. Masuzawa, Y. Ito, Nakaya, et al., "Electrostrictive Materials for Ultrasonic Probes in the  $\text{Pb}(\text{Mg}_{1/3}\text{Nb}_{2/3})\text{O}_3$ - $\text{PbTiO}_3$  System," *Japanese Journal of Applied Physics*, Vol. 28, Supplement 28-2, pp. 101-104 (1989).
9. Wallace A. Smith, "New Opportunities in Ultrasonic Transducers Emerging From Innovations in Piezoelectric Materials," *Proc. 1992 SPIE Int'l Symp. New Developments in Ultrasonic Transducers and Transducer Systems*, July 1992.
10. R.Y. Ting, "Evaluation of New Piezoelectric composite Materials for Hydrophone Applications," *Ferroelectrics*, Vol. 67, pp. 143-157 (1986).
11. N.D. Patel and P.S. Nicholson, "High Frequency, High Temperature Ultrasonic Transducers," *NDT International* 23 (5) pp. 262-266 (1990).
12. Y. Ito, K. Kushida, H. Kanda, H. Takeuchi, and K. Sugawara, "Thin-Film  $\text{AlN}$  Ultrasonic Transducer Arrays for Operation at 100 MHz," *Ferroelectrics* in press (1992). Presented at the Second European Conference on the Application of Polar Dielectrics, London, United Kingdom, 12-15 April 1992.
13. T.R. Shrout and A. Halliyal, "Preparation of Lead-Based Ferroelectric Relaxors for Capacitors," *Am. Ceram. Soc. Bull.*, Vol. 66, No. 4, pp. 704-711 (1987).
14. T.R. Shrout, et al., "Enhanced Processing of Perovskite  $\text{Pb}(\text{Mg}_{1/3}\text{Nb}_{2/3})\text{O}_3$  Relaxors through Understanding of the Surface Chemistry of the Component Powders," in *Ceramic Powder Science, Ceramic Transactions*, Vol. 1, ed. by G.L. Messing, et al., American Ceramic Society, Westerville, OH, pp. 519-527 (1988).
15. M. Lejeune and J.P. Boilot, "Low-Firing Dielectrics Based on Lead Magnesium Niobate," *Mater. Res. Bull.*, Vol. 20, pp. 493-499 (1985).
16. Joseph P. Dougherty, "Fifth U.S.: Japan Workshop on Dielectric and Piezoelectric Materials," *Office of Naval Research Report N66005* (1990)
17. T. Shiosaki, "Recent Developments in Piezoelectric Materials," *Ferroelectrics*, 91, pp. 39-51 (1989).
18. S.L. Swartz, "Topics in Electronic Ceramics," *IEEE Trans. Electr. Insul. Digest on Dielectrics* 25, 935-987 (Oct. 1990).
19. L.L. Hench and J.K. West (Eds.), *Principles of Electronic Ceramics*, John Wiley & Sons, Inc., New York, 1990.
20. J.M. Herbert, *Ferroelectric Transducers and Sensors*, Gordon and Breach Science Publishers, Inc., New York (1982).
21. G.H. Haertling, "Piezoelectric and Electrooptic Ceramics," in *Ceramic Materials for Electronics: Processing, Properties, and Applications*, ed. by R.C. Buchanan, Marcel-Dekker, Inc., New York, pp. 139-225 (1986).
22. R.C. Pohanka, P.L. Smith, and G.H. Haertling, "Recent Advances in Piezoelectric Ceramics," in *Electronic Ceramics: Properties, Devices, and Applications*, ed. by L.M. Levinson, Marcel Dekker, Inc., New York, pp. 45-145 (1988).
23. Helmut Thomann, "Piezoelectric Ceramics," *Advanced Materials*, 2, pp. 458-463 (1990).
24. B.M. Kulwicki, A. Amin, H.R. Beratan and C.M. Hanson, "Pyroelectric Imaging," (to be published, Proc. 8th Int'l Symp. on Application of Ferroelectrics (1992)).
25. S. Takahashi, "Recent Developments in Multilayer Piezoelectric Ceramic Actuators and Their Applications," *Ferroelectrics*, 91, 293 (1989).
26. Y. Yamashita, et al., " $(\text{Pb,Ca})((\text{Co}_{1/2}\text{W}_{1/2}),\text{Ti})\text{O}_3$  Piezoelectric Ceramics and Their Applications," *Jpn. J. Appl. Phys.*, Vol. 20, Suppl. 20-4, pp. 183-187 (1981).
27. H. Takeuchi, et al., "Electromechanical Properties of  $(\text{Pb,Ln})(\text{Ti,Mn})\text{O}_3$  Ceramics," *J. Acoustic Soc. Amer.*, Vol. 72, No. 4, pp. 1114-1120 (1982).
28. R.W. Whatmore, P.C. Osbond, N.M. Shorrocks, "Ferroelectric Materials for Thermal IR Detectors," *Ferroelectrics*, Vol. 76, pp. 351 (1987).
29. T. Takenaka and K. Sakata, "Grain Oriented and Mn-Doped  $(\text{NaBi})(1-x)/2\text{Ca}_x\text{Bi}_4\text{Ti}_4\text{O}_{15}$  Ceramics for Piezo- and Pyrosensor Materials," *Sensors and Materials* 1 pp. 35-46 (1988).
30. T.R. Shrout and J.P. Dougherty, "A World Review on Lead Based  $(\text{Pb}(\text{B}_1\text{B}_2)\text{O}_3)$  Relaxors Versus  $\text{BaTiO}_3$  Dielectrics for Multilayer Ceramic Capacitors," Proc. Symp. on Ceramic Dielectrics, H.C. Ling (ed.), Am. Ceram. Soc. (1989).
31. Masatomo Yonezawa, Kazuaki Utsumi, Atsushi Ochi, and Toru Mori, "Research and Development of Relaxor Ceramics at NEC," *Proc. 7th IEEE Int'l Symp. on Applications of Ferroelectrics*, pp. 159-164 (1990).
32. R. Aldrich, "Requirements for Piezoelectric Materials for Deformable Mirrors," *Ferroelectrics* 27, 19-25 (1986).
33. K. Uchino, "Electrostrictive Actuators: Materials and Applications," *Am. Ceram. Soc. Bull.*, Vol. 65, No. 4, pp. 647-652 (1986).
34. N.C. Kim, D.A. McHenry, S.J. Jang, and T.R. Shrout, "Fabrication of Optically Transparent Lanthanum Modified  $\text{Pb}(\text{Mg}_{1/3}\text{Nb}_{2/3})\text{O}_3$  Using Hot Isostatic Pressing," *J. Amer. Ceram. Soc.*, 73, 923-928 (1990).
35. D.A. McHenry, J.R. Giniewicz, S.J. Jang, T.R. Shrout, and A.S. Bhalla, "Optical and Electro-Optical Properties of Lead Magnesium Niobate-Lead Titanate," *Ferroelectrics* 107, 45-46 (1990).
36. S. Musikant, *Optical Materials, An Introduction to Selection and Applications*, Marcel-Dekker, Inc., New York, 1985.
37. P.A. Fuierer and R.E. Newnham, " $\text{La}_2\text{Ti}_2\text{O}_7$  Ceramics," *J. Am. Ceram. Soc.* 75 (11) pp. 2876-81 (1991).
38. M.F. Yan, H.C. Ling, and W.W. Rhodes, "Low-Firing, Temperature-stable Dielectric Compositions Based on Bismuth Nickel Zinc Niobates," *J. Am. Ceram. Soc.*, 73, 1106-117 (1990).
39. Xiao Yi: private communication.
40. T.T. Wang, J.M. Herbert, and A.M. Glass, editors, *The Applications of Ferroelectric Polymers*, Blackie, Glasgow, United Kingdom (1987).
41. H. Ohigashi, K. Koga, M. Suzuki, T. Nakanishi, K. Kimura, and N. Hashimoto, "Piezoelectric and Ferroelectric Properties of  $\text{P}(\text{VDF-TrFE})$  Copolymers and Their Application to Ultrasonic Transducers," *Ferroelectrics* 60, 263-276 (1984).
42. T. Furukawa, "Piezoelectricity and Pyroelectricity in Polymers," *IEEE Transactions on Electrical Insulation* 24, 375-394 (1989).
43. J.H. Adair, et al., "A Review of the Processing of Electronic Ceramics with an Emphasis on Multilayer Capacitor Fabrication," *J. Mater. Ed.*, Vol. 9, No. 1-2, pp. 71-118 (1987).

44. L. Swartz and T.R. ShROUT, "Fabrication of Perovskite Lead Magnesium Niobate," Mat. Res. Bull., 17, 1245-50 (1982).
45. A. Halliyal, et al., "Stabilization of Perovskite Phase and Dielectric Properties of Ceramics in the  $Pb(Zn_{1/3}Nb_{2/3})O_3$ - $BaTiO_3$  System," Am. Ceram. Soc. Bull., Vol. 66, pp. 571-676 (1987).
46. O. Furukawa, Y. Yamashita, M. Harata, T. Takahashi, and K. Inagaki, "Dielectric Properties of Modified Lead Zinc Niobate Ceramic," Jpn. J. Appl. Phys., 24, 96-99 (1985).
47. T.R. ShROUT, P. Papet, S. Kim, and G.S. Lee, "Conventionally Prepared Submicron Lead-Based Perovskite by Reactive Calcination," Journal of the American Ceramic Society 73, 1862-1867 (1990).
48. S. Kim, G.S. Lee, S. Venkataramani, and T.R. ShROUT, "Fabrication of Fine Grain Piezoelectric Ceramics Using Reactive Calcination and Milling," Journal of Materials Science 26, 1141 (1991).
49. F. Chaput and J.P. Boilot, "Alkoxide-Hydroxide Route to Synthesize Barium Titanate Based Powders," J. Am. Ceram. Soc., 73, p. 942 (1990).
50. B.J. Mulder, "Preparation of  $BaTiO_3$  and Other Ceramic Powder by Coprecipitation of Citrates from Alcohol," Am. Cer. Soc. Bull., 49 [11], 990-993 (1970).
51. P.C. Osbond, N.I. Payne, N.M. Shorrocks, R.W. Whatmore, and R. W. Ainger, "Dielectric and Microstructural Properties of Barium Strontium Titanate Ceramics Prepared from Citrate Precursors," Sixth IEEE Int'l Symp. on Applications of Ferroelectrics, pp. 748-51 (1986).
52. Maria A. Zaghete, Carlos O. Poirá Santos, José A. Varela, Elson Longo, and Yvonne P. Mascarenhas, "Phase Characterization of Lead Zirconate Titanate Obtained from Organic Solutions of Citrates," J. Amer. Ceram. Soc., 75 [8] 2088-93 (1992).
53. K. Osseo-Asare, F.J. Arriagada, and J.H. Adair, "Solubility Relationships in the Coprecipitation Synthesis of Barium Titanate: Heterogeneous Equilibria in the  $Ba$ - $Ti$ - $C_2O_4$ - $H_2O$  System," in G. L. Messing, E.R. Fuller, Jr., and Hans Hausin, eds., Ceramic Powder Science, Vol. 2, 1987, pp. 47-53.
54. J.M. Criado, F.J. Gotor, C. Real, F. Jimenez, S. Ramos, and J. Del Cerro, "Application of the Constant Rate Thermal Analysis Technique to the Microstructure Control of  $BaTiO_3$  Yielded From Coprecipitated Oxalate," Ferroelectrics, 115, pp. 43-48 (1991).
55. W.J. Dawson and S.L. Swartz, "Process for Producing Sub-Micron Ceramic Powders of Perovskite Compounds with Controlled Stoichiometry and Particle Size," U.S. Patent 5,112,433, 12 May 1992.
56. W.J. Dawson, "Hydrothermal Synthesis of Advanced Ceramic Powders," Am. Ceram. Soc. Bull., Vol. 67, No. 10, pp. 1673-1678 (1988).
57. K. Abe, et al., "Process for Producing a Composition which Includes Perovskite Compounds," U.S. Patent #4,643,984 (1987).
58. J. Menashi, et al., "Barium Titanate Based Dielectric Compositions," U.S. Patent #4,832,939 (1989).
59. K. Fukai, K. Hidaka, M. Aoko, and K. Abe, "Preparation and Properties of Uniform Fine Perovskite Powders by Hydrothermal Synthesis," Ceramics International, 16 pp. 285-290 (1990).
60. Takashi Yamamoto, "Optimum Preparation Methods for Piezoelectric Ceramics and Their Evaluation," Ceramic Bull., 71, pp. 978-985 (1992).
61. D. Swanson, S.A. Bruno, I. Burn, K. Sasaki, and H.E. Bergna, "Advanced Dielectric Powders for Improved Capacitor Reliability," Proc. Multilayer Ceramic Reliability, 68-86, The Pennsylvania State University (1991).
62. E.P. Stambaugh and J.F. Miller, "Hydrothermal Precipitation of High Quality Inorganic Oxides," in S. Somiya, ed., Proceedings of First International Symposium on Hydrothermal Reactions, Gakujutsu Bunken Fukyu-kai (c/o Tokyo Institute of Technology), Tokyo, Japan, pp. 859-872 (1983).
63. D. Hennings and S. Schreinemaker, "Characterization of Hydrothermal Barium Titanate," J. Euro. Ceram. Soc., 9, 41-46 (1992).
64. U. Kumar, S.F. Wang, and J.P. Dougherty, "Preparation of Dense Ultra-Fine Grain Barium Titanate-Based Ceramics," (to be published).
65. T. Takagi, K. Anetami, and K. Shimizo, "Lead-containing Oxide Powder," U.S. Patent #4,812,426 (1989).
66. K.K. Verna and A. Roberts in G.Y. Onoda, Jr., and L.L. Hench, eds., Ceramic Processing Before Firing, John Wiley & Sons, Inc., New York, pp. 391-407 (1978).
67. James H. Adair and Thomas R. ShROUT, "Surface Passivation of Perovskite Compounds in Aqueous Suspension," (to be patented).
68. P. Papet, J.P. Dougherty, and T.R. ShROUT, "Particle and Grain Size Effects on the Dielectric Behavior of the Relaxor Ferroelectric  $Pb(Mg_{1/3}Nb_{2/3})O_3$ ," J. Mat. Res., 5, 1-8 (1990).
69. K. Utsumi, Y. Shimada, and H. Takamizawa, "Monolithic Multicomponent Ceramic (MMC) Substrate," in K.A. Jackson, R.C. Pohanka, D.R. Uhlmann, and D.R. Ulrich, eds., Electronic Packaging Materials Science, Materials Research Society, Pittsburgh, PA, pp. 15-26 (1986).
70. H.T. Sawhill and co-workers, "Low Temperature Co-Firable Ceramics with Co-Fired Resistors," International Society of Hybrid Microelectronics Proceedings, p. 473-480 (1986).
71. Joe Rainwater, Vistatech Corporation, Dallas, Texas (private communication).
72. Dettler Hennings, Mareike Klee, and Rainer Waser, "Advanced Dielectrics: Bulk Ceramics and Thin Films," Advanced Materials, 3 p. 334-340 (1990).
73. G.R. Love, "Energy Storage in Ceramic Dielectrics," J. Am. Ceram. Soc., 73 323-328 (1989).
74. G.H. Maher, "MLC Capacitors with 6 Microns Active Dielectric and X7R Electrical Characteristics," presented at the 91st Am. Cer. Soc. Meeting, Indianapolis, IN (1988).
75. A. Burer, MMC Tech. Co. (private communication).
76. T.T. Srinivasan, Ferro Corp. (private communication).
77. H. Park, CPS, Inc. (private communication).
78. Shoko Yoshikawa, The Pennsylvania State University (private communication).
79. Dean Bathol, Fiber Materials, Inc. (private communication).
80. K. Lubitz, A. Wolff, G. Preu, R. Stoll, and B. Schulmeyer, "New Piezoelectric Composites for Ultrasonic Transducers," Ferroelectrics in press (1992). Presented at the Second European Conference of the Application of Polar Dielectrics, London, United Kingdom, 12-15 April 1992.
81. Ulrich Bast, Dieter Cramer, and Andreas Wolff, "A New Technique for the Production of Piezoelectric Composites with 1-3 Connectivity," Ceramics Today-Tomorrow's Ceramics; Materials Science Monographs, 66C, Ed., P. Vincenzini, Elsevier Publishing, Proc. of the 7th Int'l Meeting on Modern Ceramics Tech., Montecatini Fermi, Italy, 2 June (1990).
82. G. Preu, A. Wolff, D. Cramer, and U. Bast, "Microstructuring of Piezoelectric Ceramic," ECERS (European Ceramic Soc.), Augsburg, Germany (Sept. 1991).
83. L. Bowen, Materials Systems, Inc. (private communication).
84. K. Nagata, et al., "Vacuum Sintering of Transparent Piezo-Ceramics," Ceram. Int., Vol. 3, No. 2, pp. 53-56 (1977).
85. G.S. Snow, "Fabrication of Transparent Electrooptic PLZT Ceramics by Atmosphere Sintering," J. Am. Ceram. Soc., Vol. 56, No. 2, pp. 91-96 (1973).
86. K. Lubitz, H. Hellebrand, D. Cramer, and I. Probst, "Low Sintering PZT for Multilayer Actuators," Proc. ECERS, Augsburg, Germany (Sept. 1991).

87. Nobuko, S. Van Damme, Audrey E. Sutherland, Lori Jones, Keith Bridges, and Stephen R. Winzer, "Fabrication of Optically Transparent and Electrooptic Strontium Barium Niobate Ceramics," *J. Amer. Ceram. Soc.*, 74, pp. 1785-1792 (1991).
88. J.R. Giniewicz, D.A. McHenry, S.J. Jang, T.R. Shrout, A. Bhalla, and F. Ainger, "Characterization of  $(1-x)\text{Pb}(\text{Mg}_{1/3}\text{Nb}_{2/3})\text{O}_3$ - $(x)\text{PbTiO}_3$  and  $\text{Pb}(\text{Sc}_{1/2}\text{Ta}_{1/2})\text{O}_3$  Transparent Ceramics by Uniaxial Hot-Pressing," *Ferroelectrics*, 109, 167-172 (1990).
89. L.J. Bowen, W.A. Schulze, and J.V. Biggers, "Hot Isostatic Pressing of PZT," *Powder Metallurgy Int.*, 12 [2], 42-96 (1980).
90. M. Takata, S. Kawahara, K. Kayeyama, and S. Toyota, "The HIP Treatment of Magnetic and Piezoelectric Ceramics," *Proc. of Int'l Conf. Hot Isostatic Pressing/Lulea*, 11, 399-401, 15-17 June (1987).
91. Mituhiro Takata and Keisuki Koyeyama, "The High Frequency Transducer of HIP-Densified Piezoelectric Ceramics," *Jap. J. of Appl. Physics*, 22 Supplement 22-2, pp. 148-149 (1983).
92. H. Watanabe, T. Kimura, and T. Yamaguchi, "Particle Orientation During Tape Casting in the Fabrication of Grain-Oriented Bismuth Titanate," *J. Am. Ceram. Soc.*, 72 [2] pp. 289-93 (1989).
93. J. Belsick, Y. Yamashita, and M. Harata, "Ceramic/Ceramic Composite for Multilayer Capacitor Application," *Proc. IEEE 7th Int'l Symp. Application of Ferroelectrics*, 44-47 (1990)
94. Brahim Boufrou, Filbert Desgardin, and Bernard Raveau, "Tetragonal Tungsten Bronze Niobate,  $\text{K}_{0.2}\text{Sr}_{0.4}\text{NbO}_3$ : A New Material for Capacitors with Flat Dielectric Curves," *J. Am. Ceram. Soc.*, 74, pp. 2804-2814 (1991).
95. J.M. Haussanne, O. Regreng, J. Lostec, G. Desgardin, M. Halmi, and B. Raveau, "Sintering of Various Perovskites with Lithium Salts," *Proc. 6th CIMTEC, Milan, Italy* (1986).
96. G. Desgardin, I. Meg, and B. Raveau, "BaLiF<sub>3</sub>-A New Sintering Agent for BaTiO<sub>3</sub>-Based Capacitors," *Ceramic Bulletin*, 64, pp. 564-570 (1985).
97. T.R. Shrout and J. Fielding, Jr., "Relaxor Ferroelectric Materials," *Proceedings of the 1990 IEEE Ultrasonics Symposium* 711-720 (1990).

**APPENDIX 39**

## Kinetics of the hydrothermal crystallization of the perovskite lead titanate

G.A. Rossetti, Jr., D.J. Watson<sup>1</sup>, R.E. Newnham and J.H. Adair<sup>2</sup>

*Materials Research Laboratory, The Pennsylvania State University, University Park, Pennsylvania 16802, USA*

Received 21 March 1991; manuscript received in final form 16 October 1991

The hydrothermal crystallization kinetics for the perovskite  $\text{PbTiO}_3$  have been investigated under autogenous conditions at temperatures in the range of 225–250°C and feedstock concentrations of 0.1–1.0 M. At these temperatures, crystalline perovskite particles were obtained in approximately 4–7 h. Transmission electron microscopy (TEM) of the product oxides showed nanometer sized crystallites with an elongated morphology. The crystallization kinetics were monitored using X-ray powder diffraction on samples extracted from the reaction mixture at various times. The crystallization rate data were analyzed according to a generalized solid-state kinetic treatment which, along with microstructural evidence, suggest that the  $\text{PbTiO}_3$  formation reaction proceeds via a dissolution–recrystallization mechanism. It is proposed that the precursor amorphous hydrous oxides of lead and titanium dissolve and recrystallize to form the perovskite phase. The relative rates of dissolution and recrystallization were found to be strongly temperature dependent within the range examined. At all temperatures, the recrystallization kinetics appeared to obey a zero-order rate law. An apparent activation energy of 7.2 kcal/mol was estimated for the hydrothermal  $\text{PbTiO}_3$  formation reaction.

### 1. Introduction

Hydrothermal particle synthesis involves the treatment of aqueous solutions or suspensions of precursor particles at elevated temperatures and pressures. The reactions occurring in hydrothermally treated solutions of inorganic compounds can produce fine, high purity, and homogeneous particles of single and multicomponent metal oxides under the appropriate conditions [1–8]. Furthermore, particle sizes from nanometer to centimeter ranges can be synthesized depending on the configuration of the hydrothermal equipment. However, the reaction sequences in hydrothermal systems are complex, and at the present time there is scant information regarding the reaction kinetics and underlying mechanisms [9]. Hydrothermal reactions are analogous to solid-state

reactions, but with correspondingly enhanced diffusion rates [9]. The reaction mechanisms and sequences that can lead to crystalline particle formation therefore include dissolution or transformation of any solid precursor phase(s), diffusion in solution, adsorption at the solid–liquid interface, surface diffusion, incorporation of solute material into the lattice, and crystal growth steps [8–12]. Unfortunately, the relatively high temperatures and pressures for hydrothermal syntheses (e.g., 100–500°C and 0.1–14 MPa, respectively) prohibit in most cases the use of in-situ systems to monitor the course of the reactions leading to product particle formation. Consequently, meaningful data relating to particle formation can at present often be obtained only by studying the solid-state nature of the reaction.

In the present work, we have evaluated the hydrothermal formation of the binary lead titanium oxide,  $\text{PbTiO}_3$ . The solution speciation and phase equilibria for this relatively complex, but technologically important, system have not been studied. However, there have been several studies

<sup>1</sup> Currently with IBM Fishkill, Hopewell Junction, New York 12533, USA.

<sup>2</sup> Currently with Material Science and Engineering, University of Florida, Gainesville, Florida 32611, USA.

verifying that lead titanate is the stable compound under a wide range of hydrothermal reaction temperatures and pressures [2-8]. Furthermore, studies that preceded the work currently being reported have demonstrated that a range from pH 9 to pH 10 is suitable to produce stoichiometric  $\text{PbTiO}_3$  with the perovskite crystal structure [6]. The objective of this study was to obtain kinetic data on this system to better understand the particle formation mechanisms for the complex binary oxides and, in particular, the perovskite family of materials.

## 2. Materials and methods

The hydrothermal synthesis of particulate lead titanate employed a solution crystallization process carried out at relatively modest temperatures and pressures (225-250°C and 1.38-5.17 MPa, respectively) [6]. The preparation of the feedstock materials was conducted according to the flowchart shown in fig. 1. Experiments were performed in a 1 liter 316 stainless steel autoclave equipped with a magnetically driven stirring unit (Model 4521, Parr Instruments Co., Moline, IL).

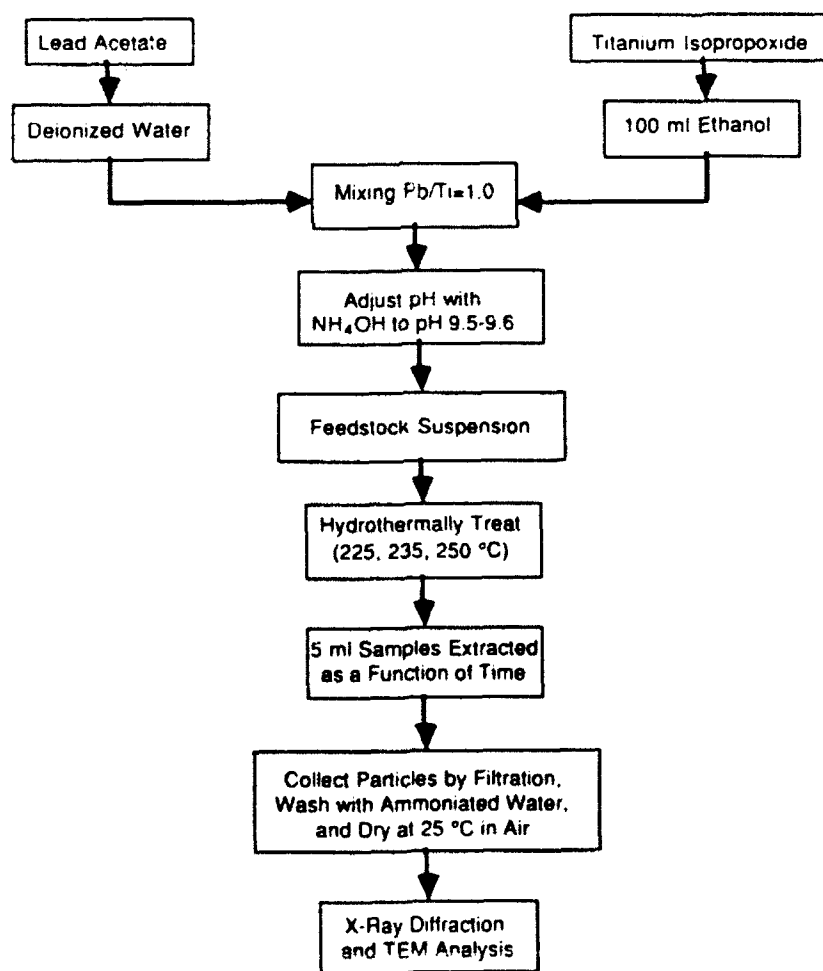


Fig. 1. Flow chart for the hydrothermal synthesis of  $\text{PbTiO}_3$  designed to collect crystallization data as a function of time.

Samples of 5 ml size were extracted under isothermal conditions at various times during the crystallization process. The extraction of these relatively small samples was accompanied by minimal reactor pressure losses ( $\sim 0.014\text{--}0.034$  MPa). The solid portion was immediately separated from the extracted suspensions by filtration and/or centrifugation depending on particle size. The solids were then washed with deionized water whose pH had been previously adjusted to pH 9.5 with ammonium hydroxide, filtered again, and air dried at room temperature. It was observed in preliminary studies that washing the powders with a solution near the pH for the minimum solubility of lead oxide and lead titanate was necessary to limit incongruent dissolution of the lead from the hydrothermally treated powders. X-ray powder diffraction patterns for the extracted samples were obtained using an automated diffractometer employing  $\text{Cu K}\alpha$  radiation. The degree of crystallinity of the solids was assessed by integrated intensity analysis of the (101) reflection [13]. Bright field transmission electron micrographs (TEM) were obtained on selected samples and used to estimate the mean particle size. The surface areas of the powders were determined by an automated nitrogen adsorption technique (Monosorb, Quantachrome Corp., Syosset, NY).

### 3. Results and discussion

#### 3.1. Materials characterization

Typical X-ray powder diffraction patterns for the  $\text{PbTiO}_3$  crystallization sequence as a function of hydrothermal reaction time are shown in fig. 2 for samples from a 0.33 molar feedstock solution at  $225^\circ\text{C}$ . As shown in the figure, the starting feedstocks were amorphous and became increasingly crystalline with time. Under these conditions, no change in crystallinity was detected by X-ray diffraction after hydrothermal treatment for  $\sim 7$  h. TEM micrographs corresponding to these samples are shown in fig. 3. The amorphous feedstock particles were 20 nm in diameter, equiaxed, and could be clearly distinguished from the product  $\text{PbTiO}_3$  particles, which crystallized

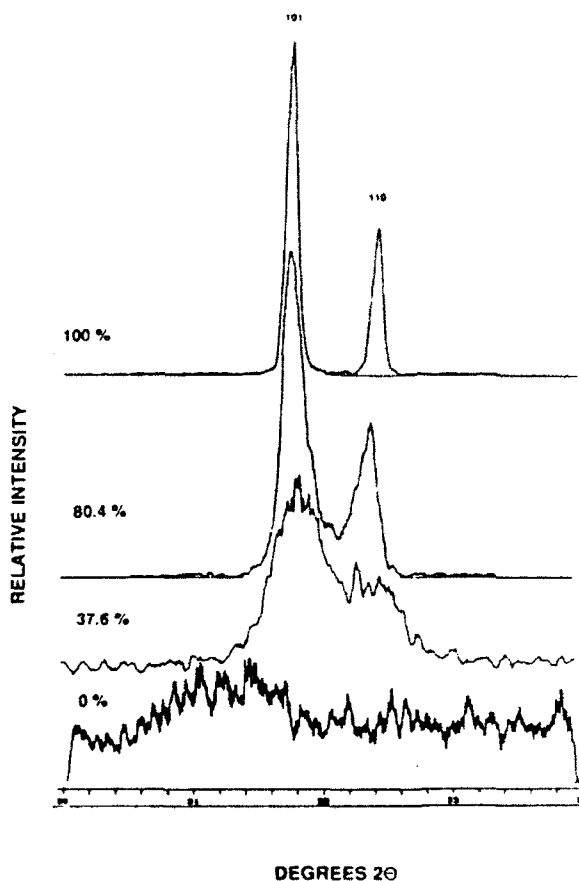


Fig. 2. Examples of X-ray diffraction patterns showing the typical change in crystallinity as a function of reaction time for hydrothermally treated  $\text{PbTiO}_3$ . Data are for 0.33M feedstock hydrothermally treated at  $225^\circ\text{C}$  for 0 time (0% crystallinity), and 37.6%, 80.4%, and 100% crystallinity.

with a relatively uniform, acicular morphology. The influence of feedstock concentration on particle size and surface area for the  $\text{PbTiO}_3$  crystallized at  $225^\circ\text{C}$  is shown in table 1. Particle size increases with feedstock concentration as judged by direct observation from the TEM micrographs and specific surface area measurements.

#### 3.2. Crystallization kinetics

The kinetics of  $\text{PbTiO}_3$  crystallization from a 0.33 molar feedstock suspension are shown at three temperatures in fig. 4. Qualitatively, the crystallization process may be divided into three

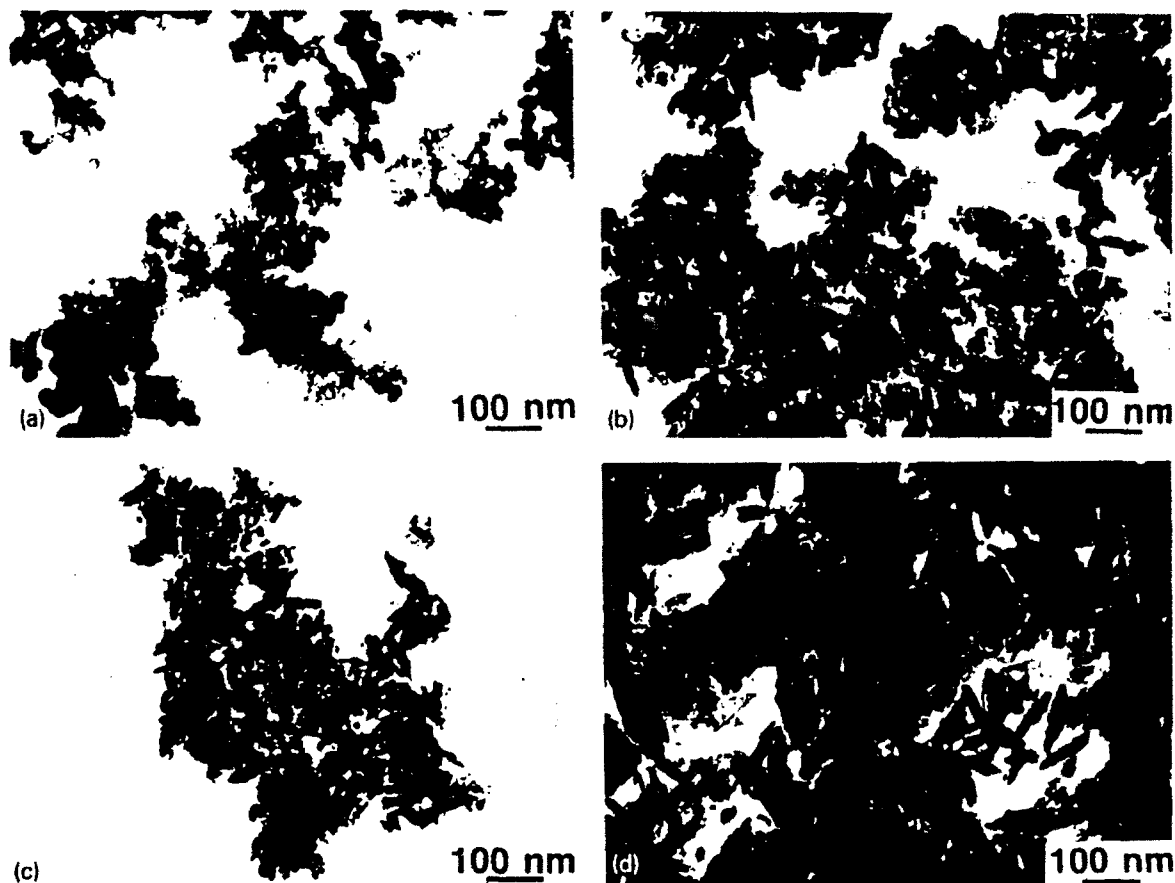


Fig. 3. Examples of transmission electron micrographs of some typical particle samples extracted from a 0.33M feedstock at 225°C as a function of reaction time: (a) 0%, (b) 37.6%, (c) 80.4%, and (d) 100% crystallinity.

distinct kinetic regimes. At relatively short reaction times there is a temperature-dependent induction time with no measurable crystallization taking place, followed by an initial period of rapid crystallization at intermediate times, and,

last, a second period of crystallization at a lower rate than during the intermediate regime. The transition between the two periods of crystalliza-

Table 1  
Crystallite sizes and specific surface areas for the  $\text{PbTiO}_3$  particles hydrothermally synthesized at 225°C to 100% crystallinity as a function of feedstock concentration

Feedstock concentration (mol/l)	Crystallite size <sup>a</sup> (length/diameter) (nm)	Specific surface area ( $\text{m}^2/\text{g}$ )
1.00	750/220	7.8
0.50	560/160	13
0.33	280/90	22
0.10	70/20	33

<sup>a</sup> Estimated from TEM photomicrographs.

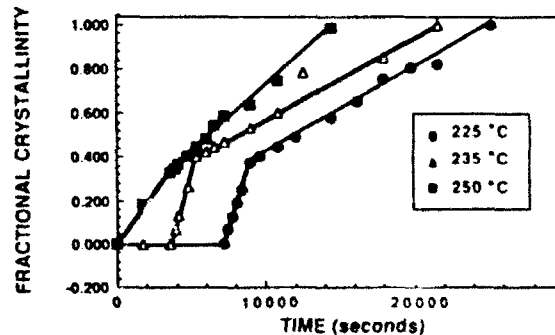


Fig. 4. Fractional  $\text{PbTiO}_3$  crystallinity as a function of time for 0.33M feedstocks hydrothermally treated at 225, 235, and 250°C.

tion occurred at approximately 30–40% crystallinity for all temperatures.

In order to gain further insight into the factors controlling the hydrothermal formation of crystalline PbTiO<sub>3</sub>, the rate data in fig. 4 were analyzed according to the generalized solid-state kinetic treatment of Hancock and Sharp [14]. This method was originally applied to isothermal solid-state transformations such as the dehydroxylation of brucite [14] and has also been successfully applied to more complex heterogeneous reaction sequences in both oxide [15] and non-oxide [16] systems. Care must be exercised, however, to ensure that a literal interpretation is not assigned to the rate constants or rate laws determined in this way from the simple regression analyses. Even when precise statistical data sets are available, best-fit rate constants obtained from regression analyses can be substantially in error [17]. Despite these reservations, careful application of simple kinetic treatments is often helpful in developing a qualitative understanding of the dominant processes in complex solid-state reaction systems, particularly when corroborated by microstructural evidence and other data.

Recognizing these limitations, and considering only the solid-state nature of the transformation, a kinetic analysis was applied based on the Johnson-Mehl-Avrami equation [18,19]:

$$f = 1 - \exp(-rt^m), \quad (1)$$

or, in linear form,

$$-\ln \ln(1-f) = \ln(r) + m \ln(t), \quad (2)$$

where  $f$  is the fraction crystallized isothermally at time  $t$ ,  $r$  is a constant that partially depends on nucleation frequency and rate of grain growth, and  $m$  is a constant that varies with the system geometry. Hancock and Sharp have shown that for reactions obeying a single theoretical rate expression, plots of  $-\ln \ln(1-f)$  against  $\ln(t)$  over  $f = 0.15-0.50$  yield approximately straight lines with slopes  $m$  having a value falling within a range characteristic of three distinct reaction mechanisms. When  $m = 0.54-0.62$ , a diffusion controlled mechanism is indicated, while a zero-order, first-order, or phase boundary controlled mechanism is indicated for  $m = 1.0-1.24$ . A mechanism involving nucleation and growth control is indicated when  $m = 2.0-3.0$ . Values of  $m$  lying outside the specified ranges have no obvious mechanistic interpretation, but can sometimes be indicative of competing processes [14]. The various standard solid-state reaction rate equations and associated values of  $m$  are summarized in table 2. It is not possible to distinguish the most appropriate rate law within a given group solely on the basis of the value of  $m$ . Instead, the individual rate laws must be tested and compared over the complete conversion range [20].

In fig. 5, plots of  $-\ln \ln(1-f)$  against  $\ln(t)$  over  $f = 0.15-0.50$  for the data in fig. 4 are presented. For PbTiO<sub>3</sub> crystallization at 225 and 235°C, it is shown in figs. 5a and 5b that the kinetics are described by a two-stage rate law. In each case, the kinetics of the first stage are characterized by a large  $m$  exponent ( $m > 5$ ) followed by a sharp transition at  $f = 0.3-0.4$  to a second

Table 2  
Solid-state reaction rate equations (from ref. [14])

Function	Implied mechanism	Equation	$m$
$D_1(f)$	Diffusion controlled	$f^2 = kt$	0.62
$D_2(f)$	Diffusion controlled	$(1-f) \ln(1-f) + f = kt$	0.57
$D_3(f)$	Diffusion controlled	$[1 - (1-f)^{1/3}]^2 = kt$	0.54
$D_4(f)$	Diffusion controlled	$1 - 2f/3 - (1-f)^{2/3} = kt$	0.57
$I_1(f)$	First order	$-\ln(1-f) = kt$	1.00
$R_2(f)$	Phase boundary	$1 - (1-f)^{1/2} = kt$	1.11
$R_3(f)$	Phase boundary	$1 - (1-f)^{1/3} = kt$	1.07
$Z_1(f)$	Zero order	$f = kt$	1.24
$A_2(f)$	Nucleation and growth	$[-\ln(1-f)]^{1/2} = kt$	2.00
$A_3(f)$	Nucleation and growth	$[-\ln(1-f)]^{1/3} = kt$	3.00

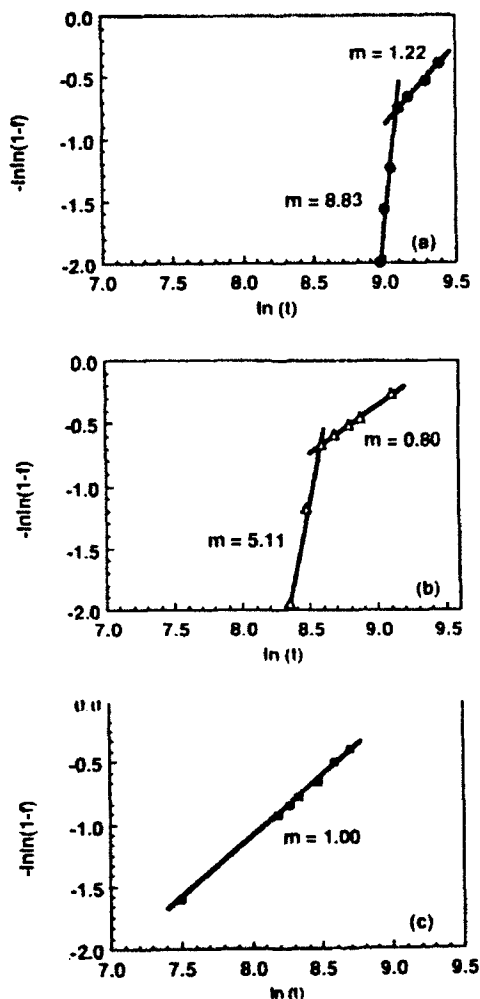


Fig. 5. Plots based on the Johnson-Mehl-Avrami analyses of the kinetic data from fig. 4.

stage characterized by an  $m$  value close to unity. The  $m$  exponent for the first stage decreases rapidly with increasing temperature, so that for crystallization at  $250^\circ\text{C}$ , the first stage is not obvious and the kinetics may apparently be described in terms of a single rate law, as shown in fig. 5c.

In figs. 5a and 5b, the  $m$  exponent of the first stage ( $m = 8.83$  and  $5.11$ , respectively) reflects the initial period of rapid crystallization in the early portions of the corresponding curves of fig. 4. Comparison of these  $m$  exponents with the theoretical values presented in table 2 shows that the kinetics of the initial stage of crystallization

cannot be simply described by any of the ten standard solid-state reaction rate equations.

On the other hand, the  $m$  exponent of the second-stage crystallization in figs. 5a and 5b, along with the single  $m$  value of fig. 5c ( $m = 1.22$ ,  $0.80$ , and  $1.00$ , respectively), suggest a reaction mechanism best described in terms of zero-order, first-order, or phase boundary controlled rate expressions. Consequently, the rate expressions for zero-order, first-order and phase boundary controlled mechanisms were tested over the second-stage crystallization ranges indicated by the  $m$  values of fig. 5. The first-order and phase boundary controlled rate equations gave poor fits of the raw kinetic data when continued to complete crystallization ( $f = 1.0$ ). In accordance with a zero-order rate law, however, fig. 4 shows that the second-stage ( $f > 0.3-0.4$ ) plots of  $f$  against  $t$  for  $\text{PbTiO}_3$  crystallization at  $225$  and  $235^\circ\text{C}$  are in fact linear. Fig. 4 indicates that the  $\text{PbTiO}_3$  crystallization kinetics at  $250^\circ\text{C}$  are also linear for  $f > 0.3-0.4$ . Over the specified crystallization ranges, therefore, the zero-order rate expression is most appropriate to describe the apparent crystallization kinetics. In fig. 4, the slight nonlinearity in the crystallization kinetics at  $250^\circ\text{C}$  for  $f < 0.3-0.4$  is contrary to the expectation from fig. 5c that only a single rate expression should be obeyed. However, it is likely that the crystallization kinetics at  $250^\circ\text{C}$  also conform to a two-stage rate law, but that first-stage crystallization was not detected due to the rapid initial rates at the higher temperature.

An Arrhenius plot for the hydrothermal  $\text{PbTiO}_3$  formation reaction is given in fig. 6. Using a method similar to that of Culfaz and Sand [21], the values plotted along the ordinate in fig. 6 represent the instantaneous rate determined at 50% crystallinity. This method was chosen because it makes no assumption regarding the underlying reaction mechanisms and associated rate laws. Even in the crystallization regime where the reaction is apparently isokinetic (i.e.,  $f > 0.4$ ), the rate data were used in preference to rate constants in constructing the plot because the error in the zero-order fits, as well as the extent to which the initial rapid crystallization at various temperatures affects the subsequent

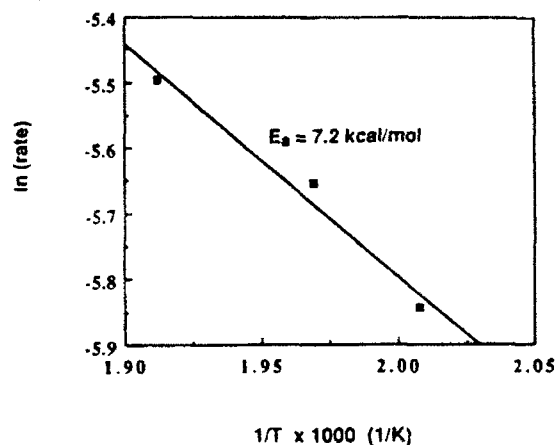


Fig. 6. Arrhenius plot for the hydrothermally crystallized  $\text{PbTiO}_3$ . The apparent activation energy for hydrothermal crystallization of  $\text{PbTiO}_3$  from the plot is 7.2 kcal/mol.

zero-order rate, is uncertain. The apparent activation energy obtained in this way is 7.2 kcal/mol.

### 3.3. Mechanistic interpretation

The microstructural and kinetic data presented above provide some insight into the mechanism of the hydrothermal formation of crystalline  $\text{PbTiO}_3$ . Based on the microstructural data of fig. 3, a mechanism involving a liquid assisted solid-state transformation [22–24] is deemed unlikely. The crystalline material in the micrographs of Fig. 3 does not appear to have grown out of the amorphous precursor. Furthermore, at no stage in the crystallization is there any evidence of partially or poorly crystalline material, as would be expected during the progress of a solid-state transformation. Similarly, the morphologies of the particles in the micrographs of fig. 3 would not be expected for a material precipitated via a classical nucleation and growth mechanism [11,12]. The particles are seen to be nearly the same size with similar acicular morphologies. A larger size distribution is expected if particles are precipitated from a heterogeneous, locally supersaturated solution [11]. In contrast, a narrow size distribution is more typical of particles precipitated from homogeneous solution [25–28]. Moreover, the particle size and surface area data of table 1 show that the average particle size decreases with decreas-

ing feedstock concentration. Such a result is not supported by a classical nucleation and growth model, which would predict higher supersaturation conditions and smaller particles at higher feedstock concentrations [11].

Alternatively, the generation of reacting species by the process generally known as precipitation from homogeneous solution (PFHS) [26–28] is often observed in systems where temperature is used to thermally decompose precursor reactants [24–27]. It is generally acknowledged that a major limitation in the PFHS reaction scheme is that relatively low concentrations of precursor species must be used to avoid continuous nucleation throughout the particle formation process. In the current work, the microstructural data strongly support the contention that PFHS is taking place in the  $\text{Pb-Ti-H}_2\text{O}$  system under hydrothermal conditions. However, in this system, a sparingly soluble precursor hydrous oxide was used to generate the reacting species. Under these conditions, a high yield of product powder is potentially attainable using relatively concentrated precursor suspensions. Furthermore, the high concentration of feedstock is not expected to compromise the generation of nuclei as it does in classical PFHS because the reservoir of nutrient stored in the solid precursor does not influence solution factors such as supersaturation and ionic strength.

Consequently, with reference to the schematic solubility curves shown in fig. 7, it is proposed that as the hydrothermal temperature is increased, the dissolution of the precursor hydrous oxides dictates the supersaturation ( $S_{12}$ ) at which  $\text{PbTiO}_3$  crystallizes. Assuming normal solubility behavior, this is consistent with the temperature-dependent induction time observed in the kinetic data of fig. 4. When the hydrothermal temperature is increased to the range where the solubility of the precursor hydrous oxide ( $S_p$ ) is greater than that of the anhydrous oxide ( $S_{pm}$ ), crystallization of the latter will take place with the nutrient precursor material acting as a reservoir for the precipitating species. If the particle growth is not topotactic with the precursor particles, then nucleation of the  $\text{PbTiO}_3$  is required. It is believed that this corresponds to the rapid, first-

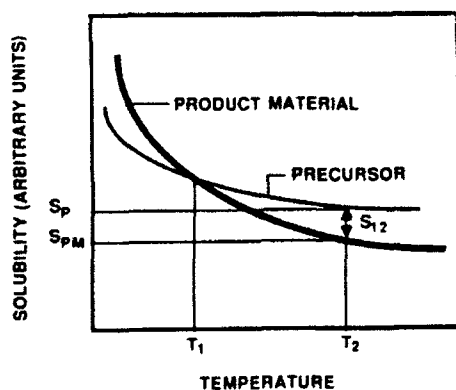


Fig. 7. Reaction scheme proposed for the hydrothermal crystallization of  $\text{PbTiO}_3$ . It is proposed that the difference in solubility of the precursor hydrous oxide and the product material,  $\text{PbTiO}_3$ , at the hydrothermal reaction temperature provides the driving force or supersaturation,  $S_{12}$ , necessary to nucleate and grow  $\text{PbTiO}_3$  particles via precipitation from homogeneous solution.

stage crystallization. As might be expected for a such a complex dissolution-recrystallization process, the  $m$  exponents for this stage of crystallization (fig. 5) did not correspond to any of the theoretical values for the standard solid-state reaction rate equations (table 2).

Once sufficient nuclei are formed, as dictated by the relative supersaturation at a particular temperature, growth will commence. It is believed that this corresponds to the sharp transition to a second-stage crystallization at  $f \approx 0.3$ – $0.4$  as observed in fig. 5. With the dissolution of a precursor solid providing the nutrient for the ultimate crystalline phase, uniformly shaped, nearly monosized particles are produced, provided that the dissolution or decomposition of the precursor material is the rate-limiting step. The zero-order kinetic dependence of the second-stage crystallization is consistent with this requirement. Zero-order kinetics imply that the reaction rate is independent of the concentration of the reactants, and are observed in systems where the rate is controlled by a large excess of one reactant, or is dictated by an external variable, such as the intensity of light in a photocatalyzed reaction [29]. In the mechanism proposed, crystallization can continue only so long as there is sufficient nutrient to maintain supersaturation.

When the nutrient is depleted to the point where this is no longer possible, the crystallization might be expected to end abruptly, with little premonitory diminution of the crystallization rate as 100% crystallinity is approached.

#### 4. Summary

Crystalline, nanometer sized  $\text{PbTiO}_3$  particles were synthesized under autogenous hydrothermal conditions at temperatures in the range of 225–250°C and feedstock concentrations of 0.1–1.0 molar. Under these conditions, the product particles crystallized with a relatively uniform acicular morphology. In contrast to expectations based on classical nucleation and growth models, the particle size was found to increase at higher feedstock concentrations. A simple solid-state analysis of the crystallization rate data showed that the kinetics could be characterized by three regimes corresponding to a temperature-dependent induction period, an initial period of rapid crystallization, and a second period of crystallization obeying a zero-order rate law. To account for these observations, a particle formation mechanism was proposed wherein an anhydrous oxide leading to the perovskite phase is precipitated from a homogeneous solution, the supersaturation condition of which is dictated by the solubility of a sparingly soluble amorphous hydrous oxide precursor. It is suggested that this reaction scheme may be useful in preparing uniform, monosized particles of complex oxides from high concentrations of nutrient and at high yields.

#### Acknowledgment

The authors would like to thank Dr. C.A. Randall of the Materials Research Laboratory for performing the transmission electron microscopy.

#### References

- [1] E.P. Stambaugh and R.A. Fox, US Patent #3,090,770, 1963.

- [2] T.R.N. Kutty and R. Balachandran, *Mater. Res. Bull.* 19 (1984) 1479.
- [3] M. Suzuki, S. Uedaira, H. Masuya and H. Tamura, in: *Ceramic Transactions, Ceramic Powder Science II* (Am. Ceram. Soc., 1987) p. 163.
- [4] K. Takai, S. Shoji, H. Naito and A. Sawaoka, in: *Proc. 1st Intern. Symp. on Hydrothermal Reactions*, Ed. S. Somiya (Gakujutsu Bunken Fukyo-kai, c/o Tokyo Inst. Technol., 1982) p. 877.
- [5] S. Kaneko and F. Imoto, *Bull. Chem. Soc. Japan* 51 (1978) 1739.
- [6] D.J. Watson, C.A. Randall, R.E. Newnham and J.H. Adair, in: *Ceramic Transactions, Ceramic Powder Science II* (Am. Ceram. Soc., 1987) p. 154.
- [7] I. Abe, M. Aoki, H. Rikimaru, T. Ito, K. Hidaka and K. Segawa, US Patent #4,643,984, 1987.
- [8] N.A. Ovramenko, L.I. Shvets, F.D. Ovcharenko and B.Yu. Kornilovich, *Inorgan. Mater.* 15 (1979) 1560.
- [9] V.A. Kuznetsov, *Kristallografiya* 9 (1963) 123.
- [10] A. Norlund Christensen, *Acta Chem. Scand.* 24 (1970) 2447.
- [11] A.E. Nielsen, *Kinetics of Precipitation* (Pergamon, Oxford, 1969).
- [12] A.G. Walton, *The Formation and Properties of Precipitates* (Krieger, 1979).
- [13] G.R. Fox, E. Brevet and R.E. Newnham, *J. Mater. Sci.* 26 (1991) 2566.
- [14] J.D. Hancock and J.H. Sharp, *J. Am. Ceram. Soc.* 55 (1972) 74.
- [15] R.A. Gardner, *J. Solid State Chem.* 9 (1974) 336.
- [16] G.A. Rossetti, Jr. and R.P. Denkwicz, Jr., *J. Mater. Sci.* 24 (1989) 3081.
- [17] A.H. Weiss, *Catal. Rev.* 5 (1971) 283.
- [18] M.J. Avrami, *J. Chem. Phys.* 7 (1939) 1103; 8 (1946) 212.
- [19] B.V. Erofe'ev, *Compt. Rend. Acad. Sci. URSS* 52 (1946) 511.
- [20] J.H. Sharp, G.W. Brindley and B.N.N. Achar, *J. Am. Ceram. Soc.* 49 (1966) 379.
- [21] A. Culfaz and L.B. Sand, *Advan. Chem. Ser.* 121 (1987) 41.
- [22] W.J. Dawson, *Am. Ceram. Soc. Bull.* 67 (1988) 1673.
- [23] J.H. Adair, R.P. Denkwicz, F.J. Arriagada and K. Osseo-Asare, in: *Ceramic Trans., Ceramic Powder Science, Vol. 1* (Am. Ceram. Soc., Westerville, OH, 1988) p. 135.
- [24] E. Tani, M. Yoshimura and S. Somiya, *J. Am. Ceram. Soc.* 66 (1983) 11.
- [25] L. Gordan, M.L. Salutsky and H.H. Willard, *Precipitation from Homogeneous Solution* (Wiley, New York, 1959).
- [26] H.H. Willard and N.K. Tang, *J. Am. Chem. Soc.* 59 (1937) 1190.
- [27] J.T.G. Overbeek, *Advan. Colloid Interface Sci.* 15 (1982) 251.
- [28] V.K. LaMer and R.H. Dinigar, *J. Am. Chem. Soc.* 72 (1950) 4847.
- [29] O. Levenspiel, *Chemical Reaction Engineering* (Wiley, New York, 1972) pp. 51-53.

**APPENDIX 40.**

# Sol-gel synthesis of $\text{Ln}_2(\text{Ln} = \text{La, Nd})\text{Ti}_2\text{O}_7$

A. V. Prasadarao,<sup>1)</sup> Ulagaraj Selvaraj, Sridhar Komarneni,<sup>2)</sup> and Amar S. Bhalla  
*Materials Research Laboratory, The Pennsylvania State University, University Park, Pennsylvania 16802*

(Received 4 October 1991; accepted 16 June 1992)

Lanthanum and neodymium titanates were prepared by a sol-gel route. Synthesis of  $\text{La}_2\text{Ti}_2\text{O}_7$  from pure alkoxide precursors yielded an intermediate perovskite type phase,  $\text{La}_{1-x}\text{Ti}_x\text{O}_3$ , which partially transformed to  $\text{La}_2\text{Ti}_2\text{O}_7$  on heating to 1500 °C. Substitution of the lanthanum acetylacetonate for alkoxide precursor yielded  $\text{La}_2\text{Ti}_2\text{O}_7$  without any intermediate phase at a very low temperature of 700 °C. Sintering of the  $\text{La}_2\text{Ti}_2\text{O}_7$  gel powder yielded a highly dense ceramic with ~97% theoretical density. Similar sintering treatment resulted in ~92% theoretical density for  $\text{Nd}_2\text{Ti}_2\text{O}_7$ .

## I. INTRODUCTION

Interest in lanthanide titanates with the general formula,  $\text{Ln}_2\text{Ti}_2\text{O}_7$ , arose as a result of the observation that they might be ferroelectric by analogy with  $\text{Cd}_2\text{Nb}_2\text{O}_7$ , which is a unique and unusual ferroelectric material at low temperatures.<sup>1</sup>  $\text{Cd}_2\text{Nb}_2\text{O}_7$  has a cubic structure of the mineral pyrochlore  $(\text{Na, Ca})(\text{Nb, Ta})\text{O}_6\text{F}$ . Roth was the first to synthesize and investigate a series of lanthanide titanates by solid-state reactions.<sup>2</sup> Among the rare earth titanates, those with  $\text{Ln} = \text{Sm}$  to  $\text{Lu}$  are isostructural to pyrochlore whereas lanthanum and neodymium titanates are monoclinic with a space group  $P2_1$ .<sup>3,4</sup> Further investigations revealed that both lanthanum and neodymium titanates are effective ferroelectric substances with both high Curie temperatures and coercive fields.<sup>5,6</sup> Their temperature stability and low dielectric loss at microwave frequencies make them good candidate materials for high frequency applications. Indeed,  $\text{La}_2\text{Ti}_2\text{O}_7$  and  $\text{Nd}_2\text{Ti}_2\text{O}_7$  are being used as major components in high K microwave dielectric formulations.<sup>7,8</sup> Also,  $\text{La}_2\text{Ti}_2\text{O}_7$  has been found to have good piezoelectric properties with possible use as a high temperature transducer material.<sup>9,10</sup> Nevertheless, studies on single crystals of these materials are limited because of their high melting points which make crystal growth difficult. The synthesis of single crystal fibers of these compounds by laser heated pedestal growth has recently been reported.<sup>11</sup> Though some methods for the synthesis of  $\text{La}_2\text{Ti}_2\text{O}_7$  and  $\text{Nd}_2\text{Ti}_2\text{O}_7$  in the polycrystalline form were reported based on coprecipitation of hydroxides,<sup>12,13</sup> thermal decomposition of nitrates,<sup>12</sup> liquid mix techniques,<sup>14</sup> and hydrothermal methods,<sup>15</sup> these ceramics are by far fabricated only by conventional solid state reactions of the oxides. However, for high quality products, pure powders consisting of uniform

particles are desirable for good sinterability and fine-grained microstructures.

In recent years, the sol-gel process has become a method of interest for the synthesis of nanocomposites and electroceramics.<sup>16</sup> The advantages of the sol-gel process compared to conventional methods for polycrystalline ceramics are better control of stoichiometry and homogeneity, lower reaction temperatures, less contamination, and ease of preparation of ultrafine powders, thin films, and fibers for device applications. Sol-gel synthesis of polycrystalline or thin film electroceramics is mostly based on the hydrolysis and subsequent polycondensation reactions of component alkoxides. Attempts on a similar basis with lanthanum and titanium isopropoxides as starting materials yielded a phase of  $\text{La}_{1-x}\text{Ti}_x\text{O}_3$  instead of the required phase  $\text{La}_2\text{Ti}_2\text{O}_7$ . However, by substituting one of the precursors (see below), phase pure  $\text{La}_2\text{Ti}_2\text{O}_7$  is obtained at a relatively low temperature. Also, the  $\text{La}_2\text{Ti}_2\text{O}_7$  precursor solution prepared by this method is useful for the formation of highly oriented thin films on different substrates.<sup>17</sup> This paper describes the first report on the sol-gel synthesis and sintering behavior of lanthanum and neodymium titanates.

## II. EXPERIMENTAL

The scheme for the synthesis of  $\text{Ln}_2\text{Ti}_2\text{O}_7$  is outlined in Fig. 1. Lanthanum/neodymium acetylacetonate [ $\text{Ln}(\text{acac})_3$  or  $\text{LnA}$ ] and titanium isopropoxide,  $\text{Ti}(\text{OPr}')_4$  (Aldrich Chemical Company, WI) were used as precursors and 2-methoxyethanol (MOE) was used as the solvent. 0.05 M of  $\text{La}(\text{acac})_3$  was added to 2 M MOE and dehydrated by distilling off the solvent at 120 °C. The resulting slurry was refluxed with MOE for 24 h in argon atmosphere keeping the molar ratio of MOE/ $\text{Ln}(\text{acac})_3$  around 80. The required amount of  $\text{Ti}(\text{OPr}')_4$  was then added to the above solution after cooling. The resultant mixture was again refluxed for 12 h, cooled, and the pH was adjusted from ~12.0 to

<sup>1)</sup>On leave from Andhra University, Visakhapatnam, India.

<sup>2)</sup>Also with the Department of Agronomy.

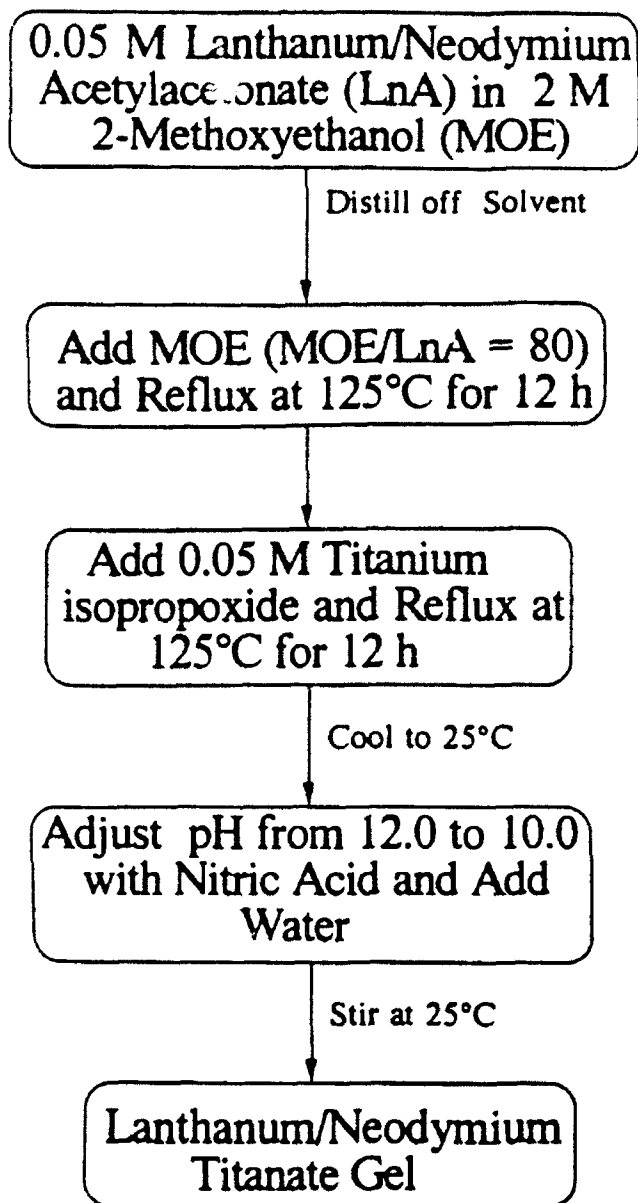


FIG. 1. Schematic outline of the preparation of lanthanum/neodymium titanate

10.0 with concentrated  $\text{HNO}_3$ . Four times the theoretical amount of water necessary for hydrolysis was added slowly under continuous stirring. The addition of water cleared the slight turbidity of the solution. The solution and the gel were air dried at  $60^\circ\text{C}$ .

Powdered gels were characterized by thermogravimetric (Delta Series TGA7, Perkin-Elmer, CT) and differential thermal (Model DTA 1700, Perkin-Elmer, CT) analyzers interfaced with computerized data acquisition and manipulation systems. Phase identification of the various heat treated samples was performed using a diffractometer (Model DMC 105, Scintag, CA) with Ni filtered  $\text{Cu K}_\alpha$  radiation. The  $\text{La}_2\text{Ti}_2\text{O}_7$  gel powder was calcined at  $800^\circ\text{C}$  for 1 h and pelletized using polyvinyl

alcohol (2 wt. %) as binder. The pellets were subjected to heat treatment at 1300, 1350, 1400, and  $1500^\circ\text{C}$  for 5 h to study their sintering behavior. Bulk densities were measured by the Archimedes method. A scanning electron microscope (ISI-DS 130, Akashi Beam Technology, Tokyo) was used for obtaining microstructures of the sintered ceramics.

### III. RESULTS AND DISCUSSION

As stated in the introduction, the synthesis based on pure alkoxide precursors resulted in the formation of a defect perovskite phase of composition close to  $\text{La}_{(1-x)}\text{TiO}_3$ . The thermal behavior of the gel powder obtained is shown in Fig. 2. X-ray diffraction (XRD) patterns of this sample heat treated at various temperatures are depicted in Fig. 3. The formation of such A-site deficient perovskite  $\text{La}_{(1-x)}\text{TiO}_3$ , where  $0 < x < 0.3$ , from ceramic oxides was reported earlier by Kestigan and Ward.<sup>18</sup> The phase of  $\text{La}_{0.66}\text{TiO}_3$  (corresponding to  $x = 0.33$ ) was also synthesized from a stoichiometric mixture of  $\text{La}_2\text{O}_3$  and  $\text{TiO}_2$  in the presence of a small amount of alkaline earth ion.<sup>18</sup> Abe and Uchino<sup>19</sup> reported the synthesis of  $\text{La}_{2/3}\text{TiO}_{3-\lambda}$  from pure oxides under  $\text{CO-H}_2$  mixed gas atmosphere. Based on XRD results, these authors concluded that the structure of  $\text{La}_{2/3}\text{TiO}_{3-\lambda}$  was dependent on  $\lambda$ : when  $\lambda$  is small the perovskite cell is distorted to orthorhombic symmetry, while a cubic perovskite phase is facilitated with the increase of  $\lambda$ . In the present case, the XRD pattern (Fig. 3) shows a cubic cell with lattice constant,  $a = 3.91 \text{ \AA}$ . Only partial transformation of  $\text{La}_{(1-x)}\text{TiO}_3$  into  $\text{La}_2\text{Ti}_2\text{O}_7$  occurred on heating to  $1500^\circ\text{C}$  for 6 h.

In order to modify the reactivity of molecular precursors, chemical additives, such as acetylacetonate and alkanolamine, are sometimes used.<sup>20,21</sup> These additives, primarily being chelating agents, modify the molecular

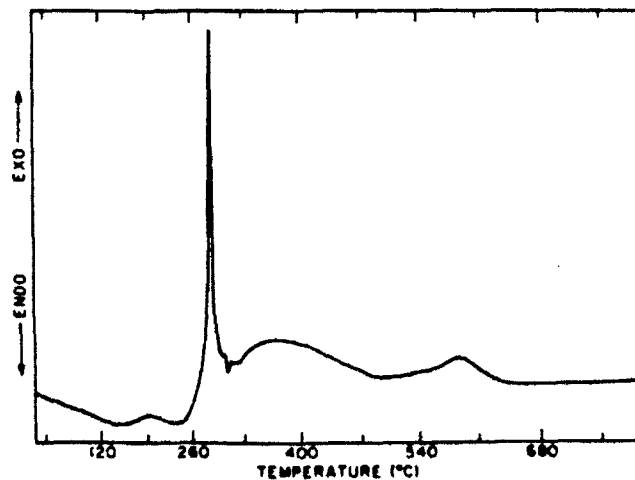


FIG. 2. DTA curve for the gel obtained from lanthanum and titanium isopropoxide precursors (heating rate  $10^\circ\text{C}/\text{min}$ )

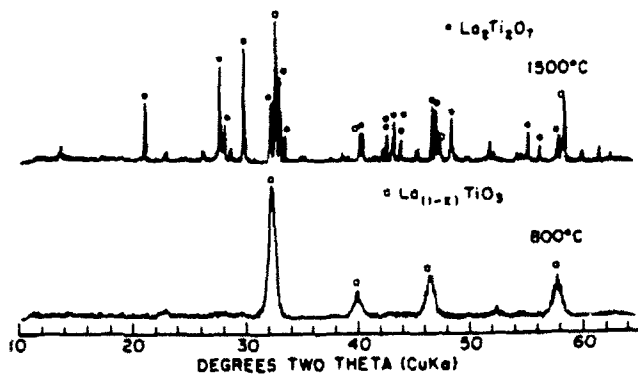


FIG. 3. XRD patterns of the gel powder obtained from lanthanum and titanium isopropoxide precursors and heat-treated at 800 and 1500 °C.

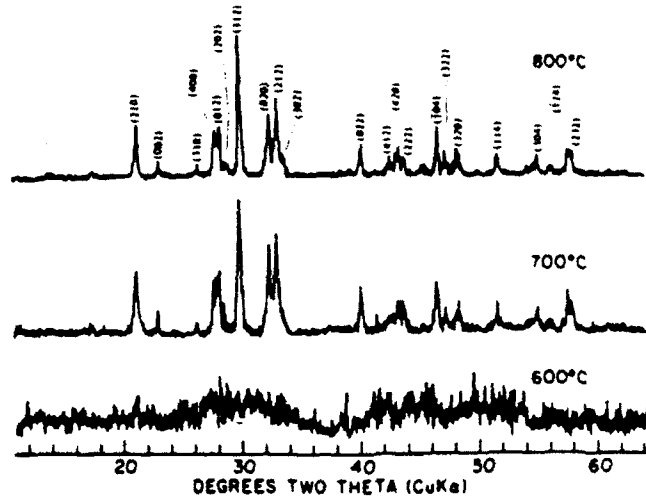


FIG. 6. XRD patterns for the gel powder obtained from lanthanum acetylacetonate and titanium isopropoxide precursors and heat-treated at different temperatures.

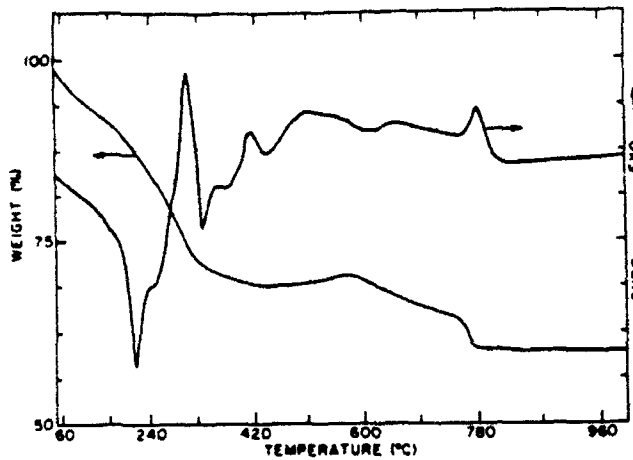


FIG. 4. TGA and DTA curves for the gel powder obtained from lanthanum acetylacetonate and titanium isopropoxide precursors (heating rate 10 °C/min).

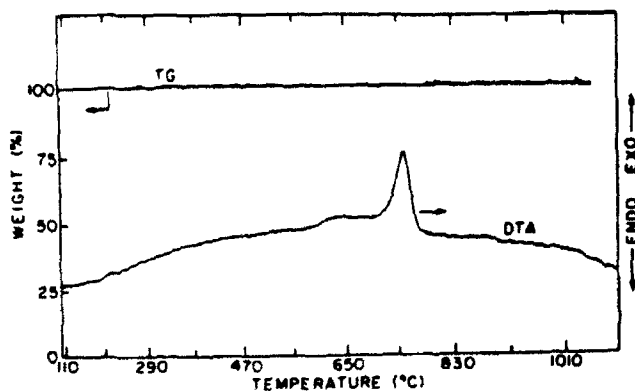


FIG. 5. TGA and DTA curves for the gel powder obtained from lanthanum acetylacetonate and titanium isopropoxide and heat-treated at 500 °C for 24 h (heating rate 10 °C/min).

precursor in such a way that its rate of hydrolysis is altered. The controlled rate of hydrolysis promotes homogeneous mixing of the resultant gel network. Instead of modifying lanthanum isopropoxide with acetylacetonate,

the lanthanum acetylacetonate itself was chosen as one of the precursors in this study. The change in lanthanum precursor facilitated the formation of  $\text{La}_2\text{T}_2\text{O}_7$  directly without any intermediate phase. The thermal behavior of air dried gel obtained from lanthanum acetylacetonate and titanium isopropoxide is depicted in Fig. 4. The thermogravimetric analysis (TGA) shows a continuous loss up to 350 °C and another loss in the range of 580 to 780 °C. The earlier loss is due to dehydration and decomposition of organics. Differential thermal analysis of the gel powder previously heat-treated at 500 °C for 24 h gave a sharp exotherm at 750 °C with no corresponding weight loss observed in TGA, as shown in Fig. 5. Ishizawa *et al.*<sup>22</sup> reported a phase transformation of monoclinic  $\text{La}_2\text{T}_2\text{O}_7$  to an orthorhombic form with

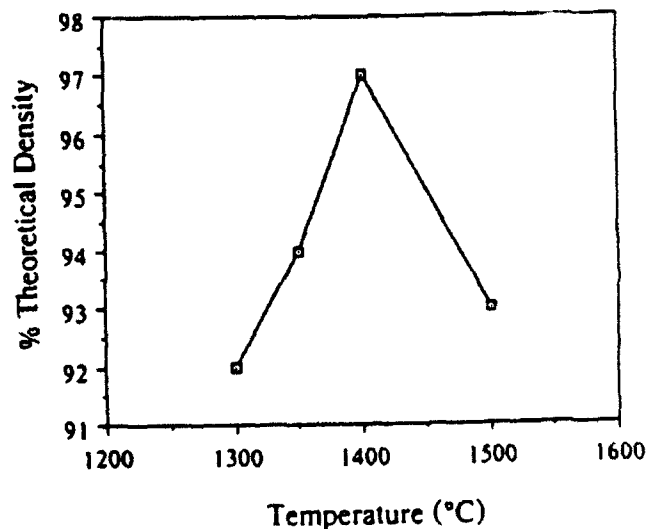


FIG. 7. Variation of density as a function of sintering temperature for  $\text{La}_2\text{T}_2\text{O}_7$ .

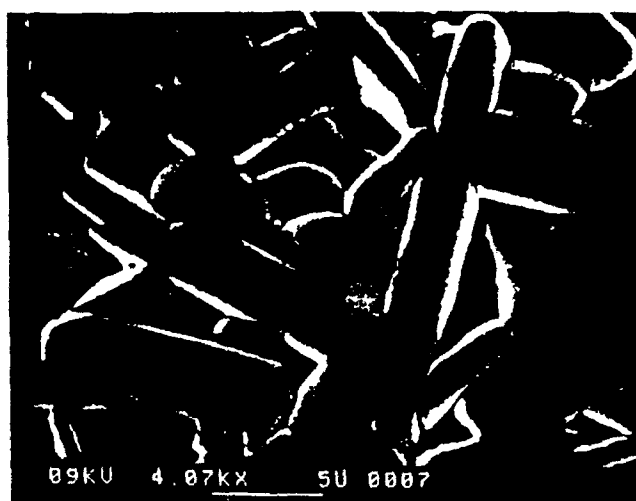
space group  $C_{mc2}$  at 780 °C. In order to verify whether the exotherm at 750 °C is due to crystallization or phase transformation of  $\text{La}_2\text{Ti}_2\text{O}_7$ , DTA cooling run was performed from 800 to 500 °C, which showed no peak in this region. This indicates that under the DTA setup conditions, it may not be possible to identify the monoclinic to orthorhombic transition. Hence, the above exotherm can be attributed to the crystallization of  $\text{La}_2\text{Ti}_2\text{O}_7$ . The phase identification was also followed by XRD for samples heat-treated at different temperatures. The sample was x-ray amorphous up to 600 °C. The XRD patterns (Fig. 6) clearly indicate the formation of  $\text{La}_2\text{Ti}_2\text{O}_7$  at 700 °C. As  $\text{TiO}_2$  crystallizes at temperatures less than 600 °C, the absence of  $\text{TiO}_2$  peaks suggests that  $\text{La}_2\text{Ti}_2\text{O}_7$  is formed directly. The phase formation was complete at temperatures  $\geq 800$  °C.

Figure 7 shows the densities of the sintered  $\text{La}_2\text{Ti}_2\text{O}_7$  samples as a function of sintering temperature. Maximum density was observed for the sample sintered at 1400 °C. For microstructural studies, sintered cross sections were prepared by polishing the surface followed by thermal etching at 1400 °C for 10 min. Figure 8 shows scanning electron micrographs (SEM) of  $\text{La}_2\text{Ti}_2\text{O}_7$  sintered at 1400 °C for 1, 3, and 5 h. The grain size increased with increasing heat treatment time (Fig. 8).

Thermal behavior of neodymium titanate gel shown in Fig. 9 is similar to that of lanthanum titanate gel powder. The phase formation followed by XRD (Fig. 10) indicated the formation of  $\text{Nd}_2\text{Ti}_2\text{O}_7$  at 800 °C. The phase formation was complete within 1000 °C. The optimum sintering conditions obtained for lanthanum titanate samples were adopted to the neodymium titanate



(a)



(b)



(c)

FIG. 8. SEM micrographs of  $\text{La}_2\text{Ti}_2\text{O}_7$  sintered at 1400 °C for (a) 1 h, (b) 3 h, and (c) 5 h.



**APPENDIX 41**

## Sol-Gel Synthesis of Strontium Pyroniobate and Calcium Pyroniobate

Alamanda V. Prasadarao,\* Ulagaraj Selvaraj,\* Sridhar Komarneni,\*† and Amar S. Bhalla\*

Materials Research Laboratory, The Pennsylvania State University, University Park, Pennsylvania 16802

Strontium and calcium pyroniobates were prepared by a sol-gel process, using strontium/calcium metal and niobium ethoxide as precursors. The formation of  $\text{Sr}_2\text{Nb}_2\text{O}_7$  occurred at  $750^\circ\text{C}$  via an intermediate perovskite phase of composition close to  $\text{Sr}_{1-x}\text{NbO}_3$ . The crystallization of  $\text{Ca}_2\text{Nb}_2\text{O}_7$  occurred at  $600^\circ\text{C}$  directly without any intermediate phases. Sintered  $\text{Sr}_2\text{Nb}_2\text{O}_7$  and  $\text{Ca}_2\text{Nb}_2\text{O}_7$  pellets showed a preferred grain orientation. Microstructural studies revealed an increase in grain growth and associated orientation with sintering temperature.

## I. Introduction

AMONG the ternary metallic oxides with the general formula  $\text{A}_2\text{B}_2\text{O}_7$ , compounds with layered perovskite-type structures exhibit interesting ferroelectric properties. The compounds where  $\text{A} = \text{Sr}, \text{Ca}$  and  $\text{B} = \text{Nb}, \text{Ta}$  have become the subject of some recent investigations.<sup>1-4</sup> Crystals of  $\text{Sr}_2\text{Nb}_2\text{O}_7$  are orthorhombic with space group  $Cmc_2$  at room temperature and the crystal structure is built up of slabs of distorted  $\text{NbO}_6$  octahedra and strontium atoms along the  $[010]$  axis.<sup>5</sup> Dielectric measurements on  $\text{Sr}_2\text{Nb}_2\text{O}_7$  single crystals revealed two ferroelectric transition temperatures, one at  $-156^\circ\text{C}$  and a second at  $1342^\circ\text{C}$ .<sup>6</sup> Also, the electric anomalies showed a normal to incommensurate phase transition at  $215^\circ\text{C}$ .<sup>7</sup> Refractive index, birefringence and lattice modulation properties of the incommensurate phase have also been investigated.<sup>8,9</sup> Besides being ferroelectric with a high Curie temperature,  $\text{Sr}_2\text{Nb}_2\text{O}_7$  exhibits excellent piezoelectric and electrooptic properties comparable to those of  $\text{LiTaO}_3$  and  $\text{Ba}_2\text{NaNb}_5\text{O}_{15}$  single crystals.<sup>1</sup>

$\text{Ca}_2\text{Nb}_2\text{O}_7$ , on the other hand, belongs to a monoclinic system with a space group  $P_2$  and is isostructural with  $\text{La}_2\text{Ti}_2\text{O}_7$ .<sup>10,11</sup> Early attempts to detect ferroelectricity in  $\text{Ca}_2\text{Nb}_2\text{O}_7$  were unsuccessful.<sup>10,11</sup> Nanamatsu and Kimura<sup>2</sup> reinvestigated the electrical properties of  $\text{Ca}_2\text{Nb}_2\text{O}_7$ . They reported a polarization reversal at very high applied fields and observed no dielectric anomaly from room temperature to  $1500^\circ\text{C}$ . The Curie temperature of  $\text{Ca}_2\text{Nb}_2\text{O}_7$  is therefore assumed to be higher than its melting point of  $1580^\circ\text{C}$ .  $\text{Ca}_2\text{Nb}_2\text{O}_7$  also exhibits remarkable piezoelectric and electrooptic properties when an electric field is applied along the polar axis.<sup>2</sup> All of the above studies have been performed with single crystals grown by float zone techniques. Single-crystal fibers of  $\text{Ca}_2\text{Nb}_2\text{O}_7$  and related materials were also prepared using laser-heated pedestal growth techniques.<sup>12</sup> Attempts to grow  $\text{Sr}_2\text{Nb}_2\text{O}_7$  and  $\text{Sr}_2\text{Ta}_2\text{O}_7$  fibers were unsuccessful. Since single crystals of these materials are impractical for most device applications because of excessive cost, low-temperature synthesis of polycrystalline or grain-oriented polycrystalline ceramics is desirable.

In recent years, sol-gel synthesis is found to have many advantages over conventional ceramic processing.<sup>13</sup> Because of

the mixing of the precursor solution at the molecular level, the sol-gel method offers homogeneity, reduced reaction temperatures, and ease of formation of thin films. We have recently reported the sol-gel synthesis of  $\text{La}_2\text{Ti}_2\text{O}_7$  and  $\text{Nd}_2\text{Ti}_2\text{O}_7$ .<sup>14</sup> In view of the above interesting properties outlined for  $\text{Sr}_2\text{Nb}_2\text{O}_7$  and  $\text{Ca}_2\text{Nb}_2\text{O}_7$ , synthesis of these phase-pure materials is undertaken by the sol-gel process. In fact, the sol-gel process produces single-phase materials, as opposed to the conventional processing methods, leading to the formation of second phases.<sup>15</sup>

## II. Experimental Procedure

The flow chart for the synthesis of  $\text{Sr}_2\text{Nb}_2\text{O}_7$  and  $\text{Ca}_2\text{Nb}_2\text{O}_7$  gel is outlined in Fig. 1. For the preparation of  $\text{Sr}_2\text{Nb}_2\text{O}_7$  gel, strontium metal and niobium ethoxide (Aldrich Chemical Co., Milwaukee, WI) were used as starting materials with 2-methoxyethanol (Aldrich) as a solvent. The required amount of strontium metal was slowly reacted with 2-methoxyethanol in a molar ratio of 1:5 under argon atmosphere. After the complete dissolution of the metal, the solution was refluxed under argon at  $125^\circ\text{C}$  for 4 h. Niobium ethoxide was refluxed separately with 2-methoxyethanol in a molar ratio of 1:27 under similar conditions.

A mixture of 0.1M strontium alkoxide solution, 0.2M acetylacetone (Aldrich), and 4.0M 2-methoxyethanol was refluxed under argon at  $125^\circ\text{C}$  for 4 h. After the solution was cooled, 0.1M niobium ethoxide solution was added and further refluxed under the same conditions. The resulting solution was cooled and the pH was adjusted from  $\sim 12.0$  to 10 with  $\text{HNO}_3$ .

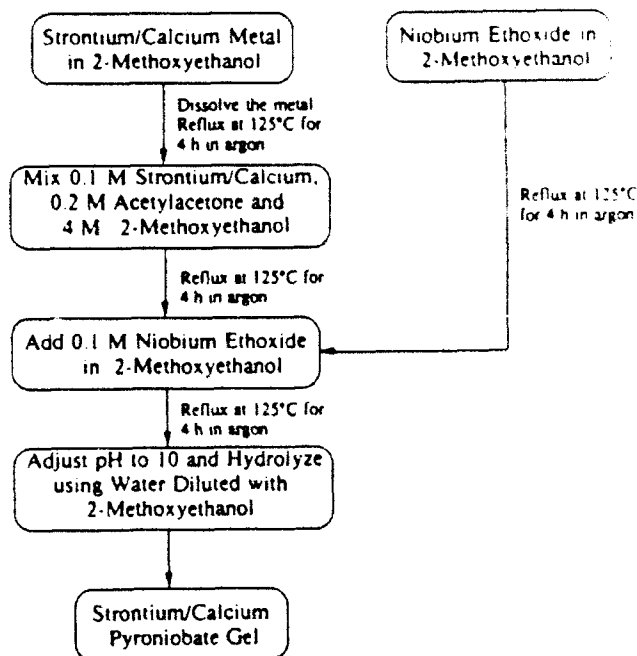


Fig. 1. Schematic outline of the preparation of  $\text{Sr}_2\text{Nb}_2\text{O}_7$  and  $\text{Ca}_2\text{Nb}_2\text{O}_7$  gels.

C. J. Brinker—contributing editor

Manuscript No. 196268. Received October 14, 1991; approved June 11, 1992.

\*Member, American Ceramic Society

†On leave from Andhra University

Also with the Department of Agronomy

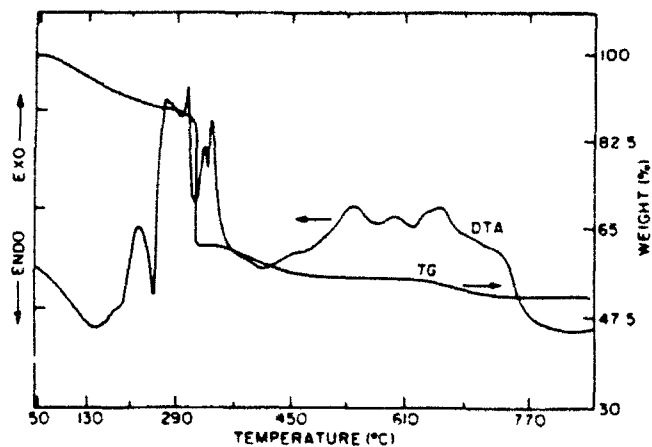


Fig. 2. TG and DTA curves for  $\text{SrNb}_2\text{O}_7$  gel (heating rate  $10^\circ\text{C}/\text{min}$ ).

Slow hydrolysis was initiated with the theoretical amount of water (diluted with 2-methoxyethanol) necessary for complete hydrolysis and the resulting gel was dried at  $60^\circ\text{C}$ . A similar procedure was followed for the synthesis of  $\text{Ca}_2\text{Nb}_2\text{O}_7$  gel with calcium metal (Aldrich) and niobium ethoxide as precursors. The gel powders of  $\text{Sr}_2\text{Nb}_2\text{O}_7$  and  $\text{Ca}_2\text{Nb}_2\text{O}_7$  were characterized by thermogravimetric (Delta Series TGA7, Perkin-Elmer, Norwalk, CT) and differential thermal (Model DTA 1700, Perkin-Elmer) analyzers interfaced with computerized data acquisition and manipulation systems. Phase identification of the various heat-treated samples was performed using a diffractometer (Model DMC 105, Scintag, Santa Clara, CA) with Ni-filtered  $\text{CuK}\alpha$  radiation. The gel powders, after the removal of carbon by heating at  $500^\circ\text{C}$ , were pressed into pellets with 2 wt% poly(vinyl alcohol) as a binder and sintered at different temperatures. The densities were measured by the Archimedes method.  $\text{Sr}_2\text{Nb}_2\text{O}_7$  and  $\text{Ca}_2\text{Nb}_2\text{O}_7$  sintered at  $1450^\circ\text{C}$  for 1 h showed 88%

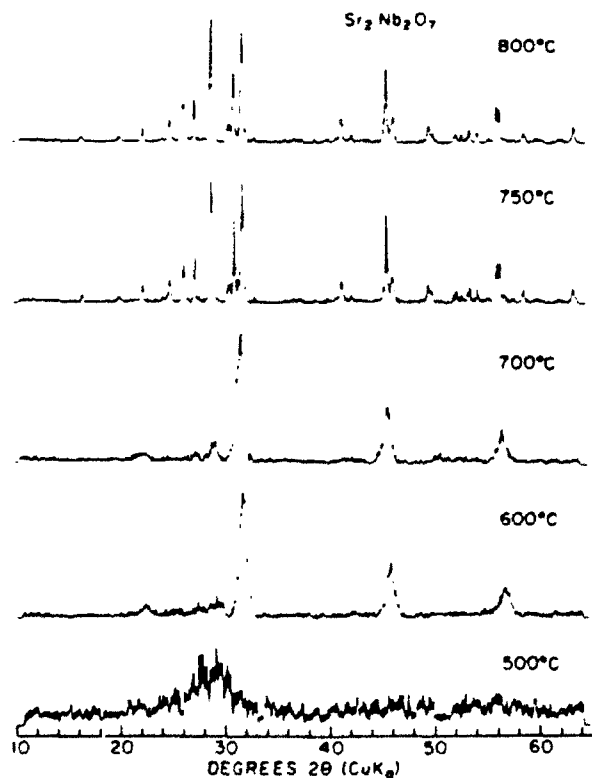


Fig. 3. XRD patterns of  $\text{Sr}_2\text{Nb}_2\text{O}_7$  gel powder heat-treated at different temperatures.

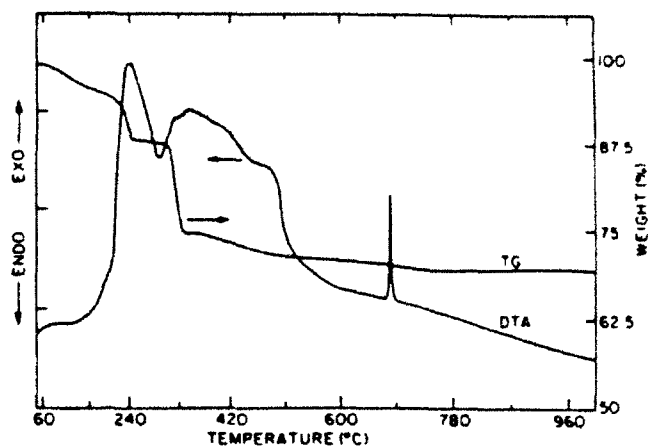


Fig. 4. TG and DTA curves for  $\text{Ca}_2\text{Nb}_2\text{O}_7$  gel powder (heating rate  $10^\circ\text{C}/\text{min}$ ).

and 92% of theoretical densities, respectively. The pellets sintered at different temperatures were polished and thermally etched for microstructural studies with a scanning electron microscope (ISI-DS 130, Akashi Beam Technology Corp., Tokyo, Japan).

### III. Results and Discussion

Figure 2 shows the DTA and TGA curves for  $\text{Sr}_2\text{Nb}_2\text{O}_7$  gel in the temperature range of  $50^\circ$  to  $850^\circ\text{C}$ . As indicated by the TG curve, there is a sudden weight loss at about  $310^\circ\text{C}$  followed by a continuous weight loss in the range of  $580^\circ$  to  $680^\circ\text{C}$ . These two weight losses are separated by a plateau from  $450^\circ$  to  $580^\circ\text{C}$ . The DTA curve shows a series of exothermic peaks. The peaks below  $400^\circ\text{C}$  are due to the loss of water and organics, while the peaks above this temperature may be due to the crystallization and the oxidation of residual carbon. As there is no sharp exothermic peak indicative of crystallization, the phase formation is followed by X-ray diffraction of the gel powders heat-treated at different temperatures (Fig. 3). The gel powder heat-treated at  $500^\circ\text{C}$  was X-ray amorphous. However, it transformed to a perovskite phase at  $600^\circ\text{C}$ . The XRD pattern of this perovskite phase matched with  $\text{Sr}_{0.4}\text{NbO}_3$  (Joint Commission on Powder Diffraction Standards, File No. 9-79). Ceramics with the composition  $\text{Sr}_2\text{Nb}_2\text{O}_7$  have been known since

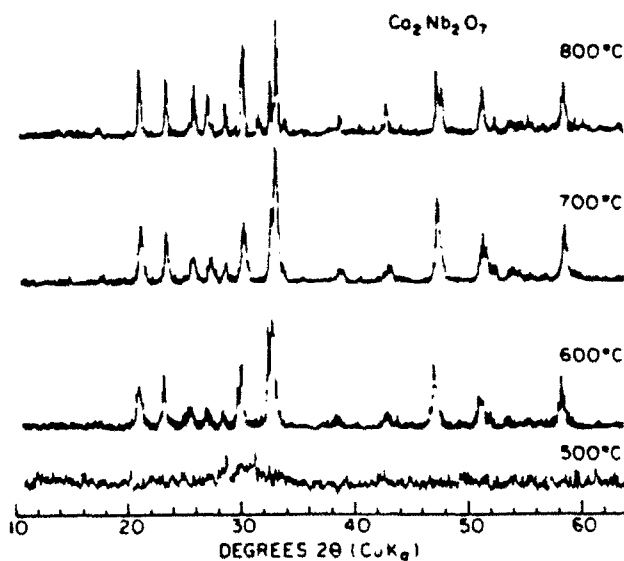


Fig. 5. XRD patterns of  $\text{Ca}_2\text{Nb}_2\text{O}_7$  gel powder heat-treated at different temperatures.

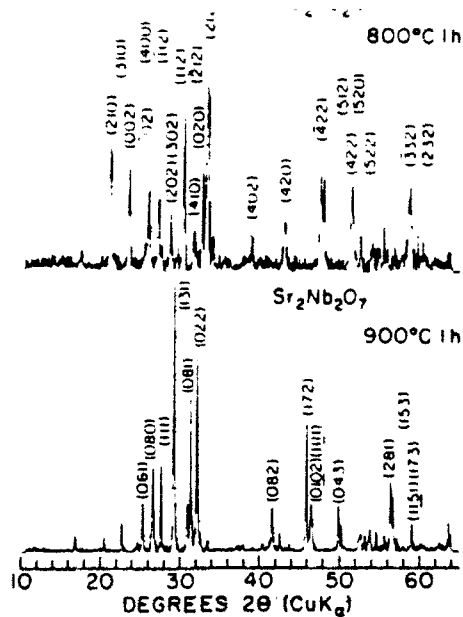


Fig. 6. XRD patterns of  $\text{Ca}_2\text{Nb}_2\text{O}_7$  and  $\text{Sr}_2\text{Nb}_2\text{O}_7$  gel powder calcined at 800° and 900°C for 1 h, respectively.

1950. It has been well established that for  $0.70 < x < 0.95$  the formation of a single-phase perovskite is favored.<sup>17,18</sup> Heat treatment of the gel powder at 750°C yielded phase-pure  $\text{Sr}_2\text{Nb}_2\text{O}_7$ . Samples of  $\text{Sr}_2\text{Nb}_2\text{O}_7$ , prepared from  $\text{SrCO}_3$  and  $\text{Nb}_2\text{O}_5$  by the conventional powder mixing method<sup>16</sup> were

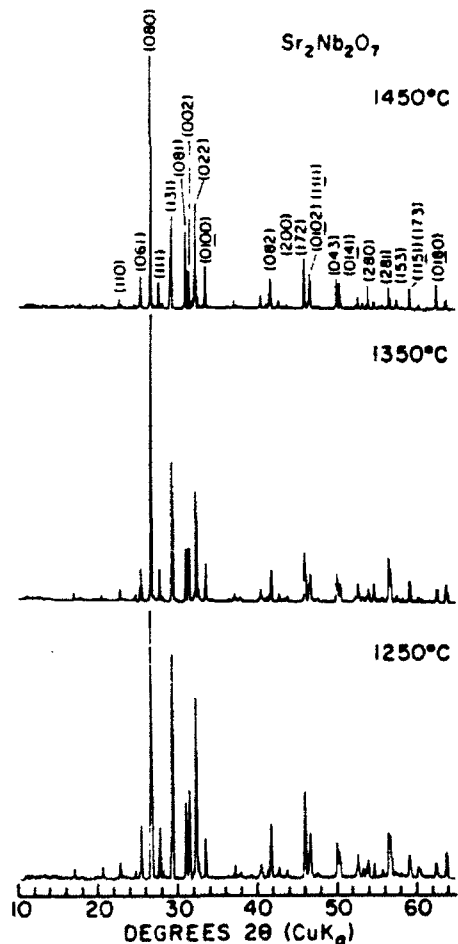


Fig. 7. XRD patterns of polished surfaces of  $\text{Sr}_2\text{Nb}_2\text{O}_7$  pellets sintered at 1250°, 1350°, and 1450°C.

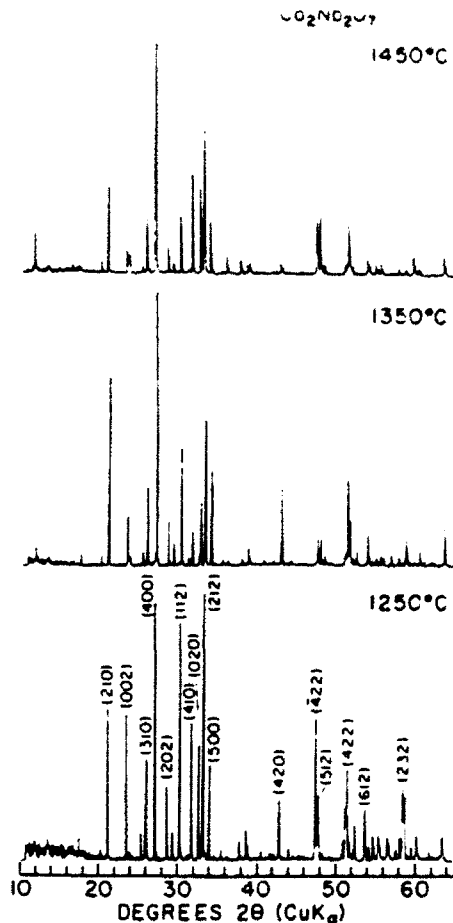


Fig. 8. XRD patterns of polished surfaces of  $\text{Ca}_2\text{Nb}_2\text{O}_7$  pellets sintered at 1250°, 1350°, and 1450°C.

reported to have a small amount of  $\text{Sr}_2\text{Nb}_2\text{O}_7$ , as impurity which was not observed in the present synthesis.

Figure 4 shows the DTA and TGA curves for  $\text{Ca}_2\text{Nb}_2\text{O}_7$  gel in the temperature range of 50° to 1000°C. There is a continuous weight loss shown in the TG curve up to about 500°C followed by a minute weight loss up to 650°C. As in the previous case, DTA peaks below 500°C are due to loss of water and decomposition of organics. Above 500°C DTA showed a sharp exotherm at 680°C, due to the crystallization of  $\text{Ca}_2\text{Nb}_2\text{O}_7$ . This was further confirmed by XRD of gel powders heat-treated at different temperatures (Fig. 5).

The XRD patterns for the calcined powders of  $\text{Ca}_2\text{Nb}_2\text{O}_7$  and  $\text{Sr}_2\text{Nb}_2\text{O}_7$  are shown in Fig. 6. The (212) and (131) reflections are the highest intensity peaks, respectively. However, when the pellets were sintered at different temperatures, the corresponding XRD patterns of polished surfaces showed (080) as the highest intensity peak for  $\text{Sr}_2\text{Nb}_2\text{O}_7$ , and (400) as the highest intensity peak for  $\text{Ca}_2\text{Nb}_2\text{O}_7$ , as shown in Figs. 7 and 8. This shift in intensities is attributed to a preferred grain orientation during sintering. A similar grain orientation was also observed for  $\text{La}_2\text{Ti}_2\text{O}_7$  and  $\text{Nd}_2\text{Ti}_2\text{O}_7$ .<sup>19</sup>  $\text{Ca}_2\text{Nb}_2\text{O}_7$ , being isostructural with  $\text{La}_2\text{Ti}_2\text{O}_7$ , showed a similar trend.  $\text{Sr}_2\text{Nb}_2\text{O}_7$ , on the other hand, is orthorhombic and the observed XRD intensities of the

Table I. Orientation Factors,  $f$ , for  $\text{Sr}_2\text{Nb}_2\text{O}_7$  and  $\text{Ca}_2\text{Nb}_2\text{O}_7$ .

Sintering temperature (°C)	Orientation factor, $f$	
	$\text{Sr}_2\text{Nb}_2\text{O}_7$	$\text{Ca}_2\text{Nb}_2\text{O}_7$
1250	0.14	0.06
1350	0.23	0.13
1450	0.21	0.20

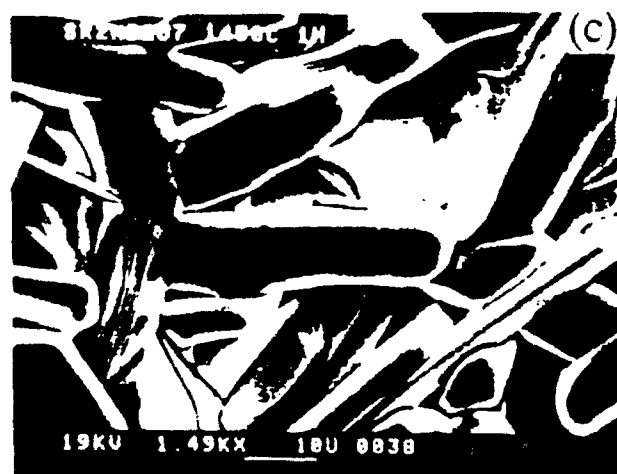
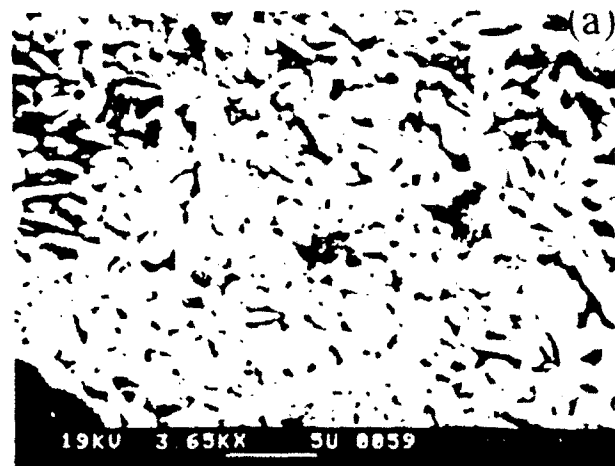


Fig. 9. SEM micrographs of polished and thermally etched pellet surfaces of Sr:Nb:O sintered at (a) 1250°, (b) 1350°, and (c) 1450°C.

Fig. 10. SEM micrographs of polished and thermally etched pellet surfaces of Ca:Nb:O sintered at (a) 1250°, (b) 1350°, and (c) 1450°C.

sintered pellets showed (080) reflection as the highest intensity peak (Fig. 8), which is in accordance with the ceramics prepared by the powder mixing method. The extent of preferred orientation is estimated in terms of the Lotgering orientation factor,  $f$ , which is defined as<sup>20</sup>

$$f = (P - P_0)/(1 - P_0)$$

where  $P = \sum I(080) / \sum I(hkl)$  for the Sr:Nb:O sintered pellet,  $P_0 = \sum I(080) / \sum I(hkl)$  for the Sr:Nb:O powder calcined at 900°C for 1 h,  $P = \sum I(400) / \sum I(hkl)$  for the Ca:Nb:O sintered pellet, and  $P_0 = \sum I(400) / \sum I(hkl)$  for the Ca:Nb:O powder calcined at 800°C for 1 h over 10° to 65° of  $2\theta$  values. For a non-

oriented sample,  $P$  becomes  $P_0$ , leading to  $f = 0$ . With an increasing degree of orientation from nonoriented sample to an oriented sample,  $P$  increases from the value  $P_0$  and correspondingly  $f$  increases from 0 to 1.0. The factor  $f$  is therefore a measure of the extent of orientation in a given set of samples. The values of  $f$  for Ca:Nb:O and Sr:Nb:O are shown in Table I. The degree of orientation is representative of the bulk of the sample because the  $f$  values measured at different pellet depths were almost identical.

The microstructures of the polished and thermally etched surfaces of the sintered pellets of Sr:Nb:O and Ca:Nb:O are shown in Figs. 9 and 10. The orientation of grains is clearly

significant increase in grain size is noticed with increasing sintering temperature

#### IV. Conclusions

Using strontium calcium metal and niobium ethoxide as precursors, phase-pure  $\text{Sr}_2\text{Nb}_2\text{O}_7$  and  $\text{Ca}_2\text{Nb}_2\text{O}_7$  were prepared by a sol-gel process. Unlike the samples prepared by conventional powder mixing methods, these materials did not show any impurities as second phase.  $\text{Sr}_2\text{Nb}_2\text{O}_7$  crystallized via an intermediate perovskite phase, while  $\text{Ca}_2\text{Nb}_2\text{O}_7$  crystallized directly at 600°C. Sintered pellets of  $\text{Sr}_2\text{Nb}_2\text{O}_7$  and  $\text{Ca}_2\text{Nb}_2\text{O}_7$  showed considerable grain orientation, which was further confirmed by SEM microstructure studies.

#### References

- <sup>1</sup>S. Nanamatsu, M. Kimura, K. Doi, and M. Takahashi, "Ferroelectric Properties of  $\text{Sr}_2\text{Nb}_2\text{O}_7$  Single Crystal," *J. Phys. Soc. Jpn.*, **30**, 300-301 (1971).
- <sup>2</sup>S. Nanamatsu and M. Kimura, "Ferroelectric Properties of  $\text{Ca}_2\text{Nb}_2\text{O}_7$  Single Crystals," *J. Phys. Soc. Jpn.*, **36**, 1495 (1974).
- <sup>3</sup>S. Nanamatsu, M. Kimura, and T. Kawamura, "Crystallographic and Dielectric Properties of Ferroelectric A<sub>2</sub>B<sub>2</sub>O<sub>7</sub> (A = Sr, B = Ta, Nb) Crystals and Their Solid Solutions," *J. Phys. Soc. Jpn.*, **38**, 817-24 (1975).
- <sup>4</sup>A. Ishitani and M. Kimura, "Single Crystal  $\text{Sr}_2\text{Nb}_2\text{O}_7$  Film Optical Waveguide Deposited by RF Sputtering," *Appl. Phys. Lett.*, **29**, 289-91 (1976).
- <sup>5</sup>N. Ishijawa and F. Marumo, "The Crystal Structure of  $\text{Sr}_2\text{Nb}_2\text{O}_7$ , a Compound with Perovskite Type Slabs," *Acta Crystallogr.*, **B31**, 1912-15 (1975).
- <sup>6</sup>Y. Akishige, M. Kobayashi, K. Ohi, and E. Sawaguchi, "Dielectric and Ferroelectric Properties in the Low-Temperature Phase of Strontium Niobate," *J. Phys. Soc. Jpn.*, **55**, 2270-77 (1986).
- <sup>7</sup>Y. Akishige, Y. Yonezawa, K. Ohi, and E. Sawaguchi, "Refractive Index and Birefringence of  $\text{Sr}_2\text{Nb}_2\text{O}_7$  Around the Incommensurate Phase Transition," *J. Phys. Soc. Jpn.*, **58**, 398-401 (1989).
- <sup>8</sup>N. Yamamoto and K. Ishizuka, "Analysis of the Incommensurate Structure in  $\text{Sr}_2\text{Nb}_2\text{O}_7$  by Electron Microscopy and Convergent Beam Electron Diffraction," *Acta Crystallogr.*, **B39**, 210-16 (1983).
- <sup>9</sup>A. A. Ballman, "Growth of Piezoelectric and Ferroelectric Materials by the Czochralski Technique," *J. Am. Ceram. Soc.*, **48**, 112-13 (1965).
- <sup>10</sup>N. Ishijawa, F. Marumo, S. Iwa, M. Kimura, and P. Kawamura, "Compounds with Perovskite Slabs III. The Structure of Monoclinic Modification of  $\text{Ca}_2\text{Nb}_2\text{O}_7$ ," *Acta Crystallogr.*, **B36**, 763-66 (1980).
- <sup>11</sup>F. Jona, G. Shirane, and R. Pepinsky, "Dielectric, X-ray and Optical Study of Ferroelectric  $\text{Cd}_2\text{Nb}_2\text{O}_7$  and Related Compounds," *Phys. Rev.*, **98**, 903-909 (1955).
- <sup>12</sup>J. Yamamoto, "Growth and Characterization of Ferroelectric Single Crystal Fiber Produced by the Laser Heated Pedestal Growth Technique," Ph.D. Thesis, Pennsylvania State University, University Park, PA (1990).
- <sup>13</sup>C. J. Brinker and G. H. Scherer, *The Physics and Chemistry of Sol-Gel Processing*, Academic Press, New York (1990).
- <sup>14</sup>A. V. Prasadarao, U. Selvaraj, S. Komarneni, and A. S. Bhalla, "Sol-Gel Synthesis of  $\text{Ln}_2\text{Ln}'_2\text{O}_7$  (Ln = La, Nd;  $\text{Ln}' = \text{O}$ )," *J. Mater. Res.*, in press.
- <sup>15</sup>M. Fukuhara, C. Y. Huang, A. S. Bhalla, and R. E. Newham, "Grain Orientation and Electrical Properties of  $\text{Sr}_2\text{Nb}_2\text{O}_7$  Ceramics," *J. Mater. Sci.*, **26**, 61-66 (1991).
- <sup>16</sup>D. Ridgley and R. Ward, "The Preparation of a Strontium-Niobium Bronze with the Perovskite Structure," *J. Am. Chem. Soc.*, **77**, 6132-35 (1955).
- <sup>17</sup>B. Hessen, S. A. Sunshine, T. Siegrist, and R. Jimenez, "Crystallization of Reduced Strontium and Barium Niobate Perovskite from Borate Fluxes," *Mater. Res. Bull.*, **26**, 85-90 (1991).
- <sup>18</sup>A. V. Prasadarao, U. Selvaraj, S. Komarneni, and A. S. Bhalla, "Grain Orientation in Sol-Gel Derived  $\text{Ln}_2\text{Ln}'_2\text{O}_7$  (Ln = La, Nd;  $\text{Ln}' = \text{O}$ ) Ceramics," *Mater. Lett.*, **12**, 306-10 (1991).
- <sup>19</sup>F. K. Lotgering, "Topotactical Reactions with Ferrimagnetic Oxides Having Hexagonal Crystal Structures—I," *J. Inorg. Nucl. Chem.*, **9**, 111-21 (1959).

**APPENDIX 42.**

## FABRICATION OF $\text{La}_2\text{Ti}_2\text{O}_7$ THIN FILMS BY A SOL-GEL TECHNIQUE

A. V. Prasadarao,\* U. Selvaraj, S. Komarneni<sup>†</sup> and A.S. Bhalla

Materials Research Laboratory, The Pennsylvania State University,  
University Park, Pennsylvania 16802, USA.

\*Permanent Address: Andhra University, Visakhapatnam, India.

<sup>†</sup>Also with the Department of Agronomy.

(Received for Publication March 9, 1992)

Sol-gel thin films of  $\text{La}_2\text{Ti}_2\text{O}_7$  were deposited on fused silica and Si(100) substrates by a spin-coating process. The  $\text{La}_2\text{Ti}_2\text{O}_7$  precursor solution for the spin-coating was prepared from lanthanum acetylacetonate and titanium iso-propoxide dissolved in 2-methoxyethanol. Crystalline and crack-free films of  $\sim 0.3 \mu\text{m}$  thickness were deposited on the above substrates using a single coating and followed by annealing at a temperature of 800 °C. Microstructural studies revealed that these films contained extremely fine grains of  $\sim 0.1 \mu\text{m}$ . Thin film X-ray diffraction patterns indicated the formation of grain oriented films along [100] direction on these substrates.

### INTRODUCTION

Much interest has been focused on the ferroelectric properties of layered perovskite compounds of the general formula  $\text{A}_2\text{B}_2\text{O}_7$ , because of their high Curie temperatures and thermal stability. In this category of compounds, A is a trivalent ion such as  $\text{La}^{3+}$ ,  $\text{Nd}^{3+}$  with B being  $\text{Ti}^{4+}$ , or, A is a divalent ion such as  $\text{Ca}^{2+}$ ,  $\text{Sr}^{2+}$  with B being  $\text{Nb}^{5+}$ ,  $\text{Ta}^{5+}$ . Among the layered perovskite compounds, lanthanum and neodymium titanates ( $\text{La}_2\text{Ti}_2\text{O}_7$  and  $\text{Nd}_2\text{Ti}_2\text{O}_7$ ) have high Curie

temperatures ( $\sim 1500^\circ\text{C}$ ) and high coercive fields.<sup>1,2</sup> Their high temperature stability combined with low dielectric loss at microwave frequencies make them good candidate materials for high frequency applications. In addition to being ferroelectric, these materials also exhibit excellent piezoelectric and electro-optic properties for possible use as high temperature transducers.<sup>2,3</sup>

The room temperature modification of  $\text{La}_2\text{Ti}_2\text{O}_7$  belongs to the monoclinic system with the space group,  $\text{P}2_1$ . The crystal structure is built up of layers of perovskite slabs running parallel to (100) plane, with the  $\text{TiO}_6$  octahedra bonded to each other by the interlayer  $\text{La}^{3+}$  ions.<sup>4</sup> A high temperature modification of  $\text{La}_2\text{Ti}_2\text{O}_7$  at  $\sim 780^\circ\text{C}$  with the orthorhombic space group,  $\text{Cmc}2_1$  has also been reported.<sup>5</sup>  $\text{La}_2\text{Ti}_2\text{O}_7$  has also been described as  $n = 3$  member of a homologous series of layered structures with the general formula  $\text{A}_{n+1}\text{B}_{n+1}\text{O}_{3n+5}$  [ $0 \leq n \leq \infty$ ].<sup>6</sup> Single crystal fibers of  $\text{La}_2\text{Ti}_2\text{O}_7$  and related materials have been synthesized by laser-heated pedestal growth technique.<sup>7</sup> The microwave dielectric properties and the piezoelectric properties of these single crystal fibers have also been investigated.<sup>8,9</sup>

The sol-gel method has been widely used to deposit many ferroelectric and dielectric thin films. When compared to vacuum based techniques such as chemical vapor deposition and sputtering, the sol-gel processing is a solution based technique of depositing thin films without any vacuum. The advantages of sol-gel method over other methods are precise control of composition, low processing temperature, better homogeneity, easier fabrication of thin films over large area on either one or both faces of the substrate and low cost. We have recently reported the preparation of some layered perovskite ceramics using sol-gel derived fine crystalline powders.<sup>10,11</sup> In this letter we present the first report on the fabrication of thin sol-gel films of  $\text{La}_2\text{Ti}_2\text{O}_7$ .

## EXPERIMENTAL

The precursor solution for  $\text{La}_2\text{Ti}_2\text{O}_7$  was prepared from lanthanum acetylacetonate hydrate [ $\text{La}(\text{acac})_3 \cdot x\text{H}_2\text{O}$ ] and titanium iso-propoxide [ $\text{Ti}(\text{OPri})_4$ ]

dissolved in the solvent 2-methoxyethanol (2-MOE). A mixture of 0.05 M of  $\text{La}(\text{acac})_3 \cdot x\text{H}_2\text{O}$  and 4 M of 2-MOE was distilled in argon to dehydrate water. To the resulting slurry, 2-MOE was added to maintain the above lanthanum acetylacetonate : 2-MOE ratio and refluxed in argon for 24 h. Stoichiometric quantity of  $\text{Ti}(\text{OPi})_4$  was then added and the mixture was refluxed for 12 h to achieve homogeneous mixing. The pH of the solution after cooling was adjusted from  $\sim 12.0$  to 10 with concentrated  $\text{HNO}_3$ . Hydrolysis was initiated by adding water which resulted in a very clear solution. This precursor solution was used for subsequent spin-coating. A portion of the solution was gelled separately and the gel powder heat treated at  $500^\circ\text{C}$  for 24 h was characterized by thermogravimetric (Delta Series TGA7, Perkin-Elmer, CT) and differential thermal (Model DTA 1700, Perkin-Elmer, CT) analysers interfaced with computerized data acquisition and manipulation systems. Phase identification of the gel powder heat treated at  $700$  and  $1000^\circ\text{C}$  was performed using a diffractometer (Model DMC 105, Scintag, CA) with Ni filtered  $\text{Cu K}\alpha$  radiation..

Fused silica and  $\text{Si}(100)$  were used as substrates. Prior to coating, the substrates were cleaned by standard semiconductor processing technique.<sup>12</sup>  $\text{La}_2\text{Ti}_2\text{O}_7$  precursor solution was deposited on these cleaned substrates using a spin-coater (Integrated Technologies P-600) operated at 2000 rotations per minute for 20 s. The resulting films were dried at room temperature and slowly heated to  $800^\circ\text{C}$  at a heating rate of  $2^\circ\text{C}/\text{min}$ . A thin film XRD (Scintag, Model DMICRO8) equipped with a set of angular divergence soller slits in front of the detector element for parallel beam geometry operation was used for the phase identification of the thin films. The fine structure and the film thickness were obtained by a scanning electron microscope (SEM, ISI- DS-130, Akashi Beam Technology, Tokyo, Japan). The thickness of a single layer film deposited on either fused silica or  $\text{Si}(100)$ , calculated from SEM micrograph, corresponded to  $\sim 0.3 \mu\text{m}$ .

## RESULTS AND DISCUSSION

The gel powder when heated to  $500^\circ\text{C}$  for 24 h was X-ray amorphous. DTA of this powder gave an exothermic peak at  $750^\circ\text{C}$  with no corresponding weight

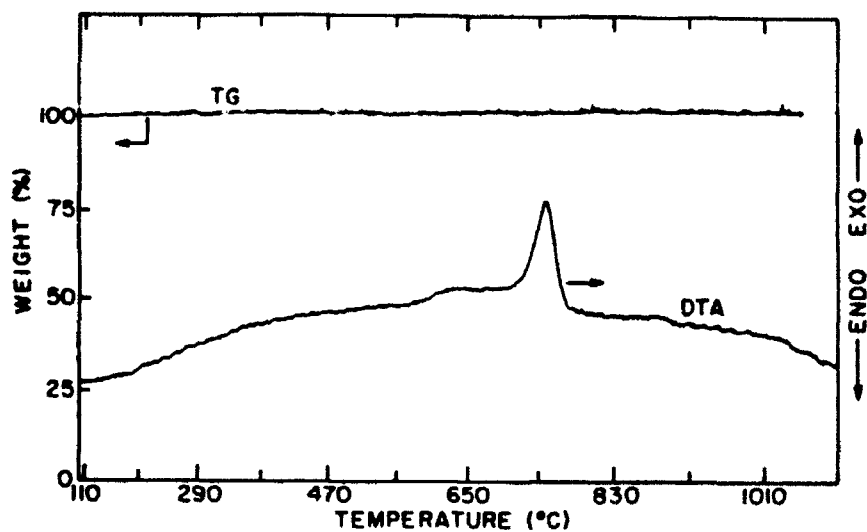


FIGURE 1. DTA and TG curves for  $\text{La}_2\text{Ti}_2\text{O}_7$  gel heat treated at  $500^\circ\text{C}$  for 24 h.

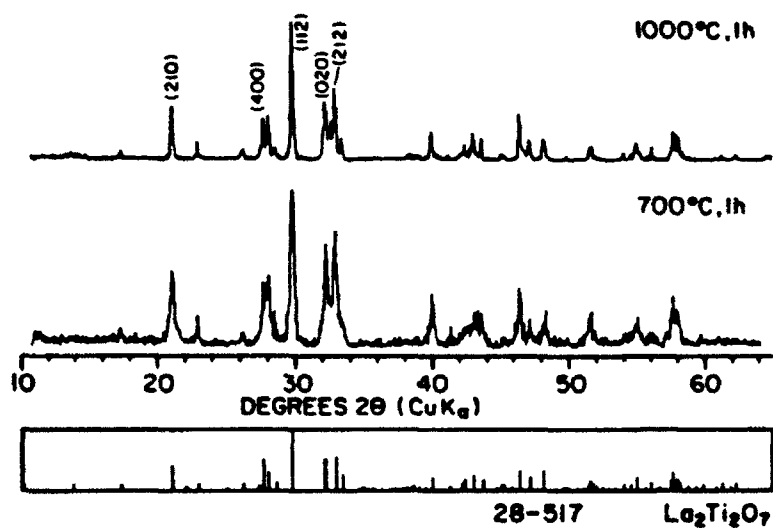


FIGURE 2. XRD patterns of  $\text{La}_2\text{Ti}_2\text{O}_7$  gel powder heat treated at  $700^\circ\text{C}$  and  $1000^\circ\text{C}$  for 1 h.

loss observed in TG as shown in Figure 1. This indicated that most of the carbon species present in the films would have been removed at temperatures below 500 °C. The exothermic peak in DTA can therefore be attributed to the crystallization of  $\text{La}_2\text{Ti}_2\text{O}_7$ . The XRD patterns of the gel powder heat treated at 700 and 1000 °C for 1 h are shown in Figure 2. As can be seen from the figure, phase formation of  $\text{La}_2\text{Ti}_2\text{O}_7$  occurs at temperature as low as 700 °C. Further increase in temperature altered the crystallite size only resulting in rather sharp peaks in the XRD pattern.

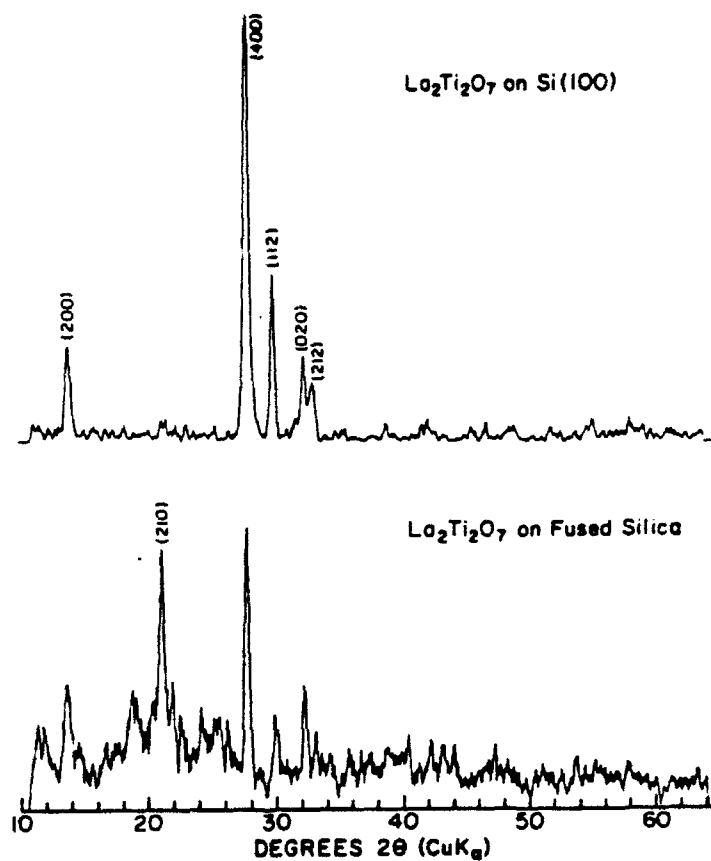


FIGURE 3. XRD patterns of  $\text{La}_2\text{Ti}_2\text{O}_7$  thin films on (a) fused silica and (b) Si(100) heat treated at 800°C for 1 h.

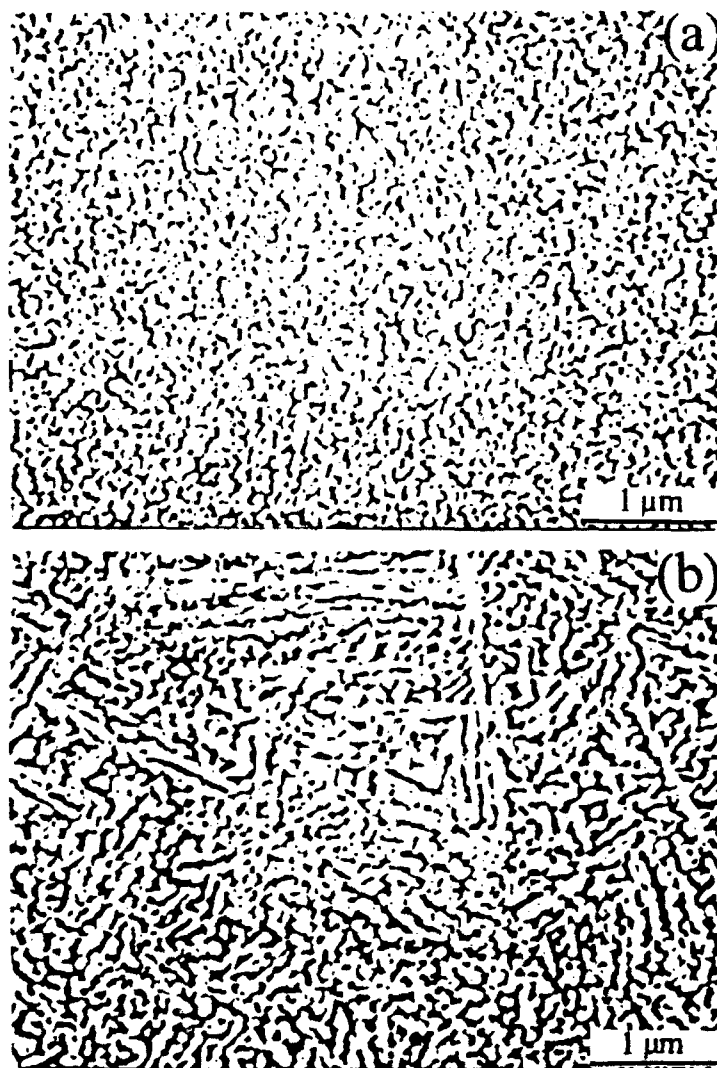


FIGURE 4. SEM micrographs of  $\text{La}_2\text{Ti}_2\text{O}_7$  thin films on (a) fused silica and (b) Si(100) heat treated at  $800^\circ\text{C}$  for 1 h.

Figure 3 shows the XRD patterns of  $\text{La}_2\text{Ti}_2\text{O}_7$  thin films spin-coated on fused silica and Si(100) and heat treated at  $800^\circ\text{C}$  for 1 h. The gel powder calcined at  $800^\circ\text{C}$  showed (112) reflection as the highest intense peak (Figure 2) which is in

agreement with the Joint commission on Powder Diffraction Standards (JCPDS) file no., 28-517.  $\text{La}_2\text{Ti}_2\text{O}_7$  sintered at  $1400^\circ\text{C}$ , however, displayed (400) as the highest intense peak, which indicated the existence of a considerable grain orientation in the ceramic.<sup>13</sup> For the  $\text{La}_2\text{Ti}_2\text{O}_7$  films heat treated at  $800^\circ\text{C}$ , the (400) peak appears to be more prominent as was observed for the sintered ceramic. As the structure of  $\text{La}_2\text{Ti}_2\text{O}_7$  is composed of perovskite  $\text{LaTiO}_3$  slabs of four  $\text{TiO}_6$  octahedra thick, bounded by shear in the perovskite {100} planes,<sup>6</sup> the observed grain orientation along [100] direction appears to be the preferred one for the sample to grow.

The microstructures of  $\text{La}_2\text{Ti}_2\text{O}_7$  films are shown in Figure 4, which reveal a very fine grain size of  $\sim 0.1 \mu\text{m}$ . The formation of needle shaped grains with visible orientation is evident in the film coated on Si(100). Since poling of  $\text{La}_2\text{Ti}_2\text{O}_7$  single crystals is considerably difficult due to high coercive field, the formation of thin films may be important for device applications. In this series of compounds,  $\text{Sr}_2\text{Nb}_2\text{O}_7$  single crystal films were reported on a b-plate  $\text{Sr}_2\text{Ta}_2\text{O}_7$  by RF sputtering for possible use as optical waveguide.<sup>14</sup>

### CONCLUSIONS

Thin films of  $\text{La}_2\text{Ti}_2\text{O}_7$  were deposited for the first time on fused silica and Si(100) at temperature as low as  $800^\circ\text{C}$  using a sol-gel technique. Thin film XRD and SEM results showed the formation of grain oriented films along [100] direction on these substrates. The present synthesis is simple and thin film of uniform thickness and good quality can be obtained on various substrates by this process. Ferroelectric and dielectric properties of these thin films are presently being investigated.

### REFERENCES

1. S. Nanamatsu, M. Kimura, K. Doi, S. Matsushita and N. Yamada, Ferroelectrics, **8**, 511 (1974).

2. M. Kimura, S. Nanamatsu, T. Kawamura and S. Matsushita, Jap. J. Appl. Phys., **13**, 1473 (1974).
3. M. Kimura, S. Nanamatsu, K. Doi, S. Matsushita and M. Takahashi, Jap. J. Appl. Phys. **11**, 904 (1972).
4. P.M. Gasperin, Acta Cryst. **B31**, 2129 (1975).
5. N. Ishizawa, F. Marumo, S. Iwai, M. Kimura and T. Kawamura, Acta Cryst. B **368** (1982).
6. T. Williams, H. Schmalte, A. Reller, F. Lightenberg, D. Widmer and G. Bednorz, J. Solid State Chem., **93**, 534 (1991).
7. J.K. Yamamoto, Growth and Characterization of Ferroelectric Single Crystal Fiber Produced by the Laser Heated Pedestal Growth Technique (Ph. D Thesis, The Pennsylvania State University, University Park, 1990).
8. J.K. Yamamoto and A.S. Bhalla, Mater. Lett., **10**, 497 (1991).
9. J.K. Yamamoto and A.S. Bhalla, J. Appl. Phys., **70**, 4469 (1991).
10. A.V. Prasadarao, U. Selvaraj, S. Komarneni and A.S. Bhalla, J. Mater. Res. (1992).
11. A.V. Prasadarao, U. Selvaraj, S. Komarneni and A.S. Bhalla, J. Am. Ceram. Soc., (1992).
12. U. Selvaraj, A.V. Prasadarao, S. Komarneni and R. Roy, J. Am. Ceram. Soc., (1992).
13. A.V. Prasadarao, U. Selvaraj, S. Komarneni and A.S. Bhalla, Mater. Lett., **12**, 306 (1991).
14. A. Ishitani and M. Kimura, Appl. Phys. Lett., **29**, 289 (1976).

**APPENDIX. 43.**

GRAIN SIZE EFFECT ON THE INDUCED PIEZOELECTRIC PROPERTIES  
OF 0.9PMN-0.1PT CERAMIC

S.F. Wang, U. Kumar, W. Huebner<sup>§</sup>, P. Marsh<sup>§§</sup>,  
H. Kankul<sup>§§§</sup> and C.G. Oakley<sup>§§§</sup>

Materials Research Laboratory, The Pennsylvania State University, University Park, PA 16802

<sup>§</sup> Department of Ceramic Engineering, University of Missouri-Rolla, MO 65401

<sup>§§</sup> Echo Ultrasound, R. D. 2, Box 118, Reedsville, PA 17084

<sup>§§§</sup> Tetrad Corporation, 12741 E. Caley Ave., Englewood, CO 80111

**Abstract:** Lead magnesium niobate ( $\text{Pb}(\text{Mg}_{1/3}\text{Nb}_{2/3})\text{O}_3$ -PMN)-lead titanate ( $\text{PbTiO}_3$ -PT) solid solutions are widely researched to produce devices that can be used in low and high electric field applications. For some applications, such as medical ultrasonic transducers, it is necessary to prepare the ceramic with high density and small average grain size. This paper describes the effect of grain size on the low and high field properties of 0.90PMN-0.10PT ceramics. To prepare highly dense ceramic, vibratory and attrition milled powders were sintered between 1000-1250°C. The average grain sizes of the sintered ceramics varied from 0.7 to 3.5  $\mu\text{m}$ . To understand the grain size effect, dielectric, pyroelectric, electrostrictive, and induced piezoelectric properties were studied.

### Introduction

Relaxor ferroelectric materials are widely studied for their dielectric, electrostrictive and induced piezoelectric properties. In the past decade, these materials were used in a variety of applications ranging from multi-layer capacitors to ultrasonic transducers[1,2]. Tabuchi et al.[2] investigated the effect of 0.90PMN-0.10PT ceramic for the medical imaging in the 1-3 configuration. Because of the high operating frequency, the dimensions of the 'cylindrical' ceramic posts are restricted to only a few tens of microns in all directions. To manufacture such posts reliably and reproducibly, it is necessary to use high density ceramic with small grain size.

The grain size effect on the low and high field properties of PMN-based ceramics has been investigated by several researchers[3-7]. In general, the properties degrade as the grain size is reduced. For example, in 0.93PMN-0.07PT ceramic, the peak dielectric constant drops from 25,000 to 5000 when the average grain size is reduced from 5  $\mu\text{m}$  to 0.3  $\mu\text{m}$ [5]. The size effects observed in these ceramics were attributed to the extrinsic and intrinsic effects such as pore volume, low-K grain boundary phase, and micropolar domain densities. From the literature survey, it appears that the properties of the fine grain ceramic can be improved by minimizing the effect of extrinsic variables and by improving the homogeneity.

In this paper, the effect of average grain size on the low and high electric field properties of 0.90PMN-0.10PT ceramic is reported. Ceramics with average grain sizes ranging from 0.7 to 3.5  $\mu\text{m}$  were prepared from vibratory and attrition milled powders. Low field properties such as dielectric constant and high field properties such as P-E hysteresis, pyroelectric, electrostrictive and a few of the electric field induced resonance properties were investigated as a function of grain size.

### Experimental

#### Preparation

To prepare the ceramic powder, a columbite precursor technique was adopted[7]. The niobium niobate precursor was prepared by calcining the appropriate mixture of MgO(J.T. Baker, Phillipsburg, NJ) and  $\text{Nb}_2\text{O}_5$ (Truselo, NJ) at 1000°C/5h and then at 1100°C/5h. The completion of reaction and the phase purity were

checked by comparing the XRD pattern with the JCPDS standard. The PMN-PT batches were prepared by calcining the appropriate mixture of PbO(Hammond, Pottstown, PA),  $\text{MgNb}_2\text{O}_6$ , and  $\text{TiO}_2$  (Whittake, Clark, and Daniel, South Plainfield, NJ) powders at 900°C/5h in a closed alumina crucible. To vary the initial average particle size, the calcined powder was subjected to the following grinding schedule. First, the powder was wet ball milled in alcohol in a mdfene bottle with  $\text{ZrO}_2$  grinding media for 24h. After drying, a portion of the powder was vibratory milled(Sweco) for 24h. For vibratory milling, a 30 vol% slurry was prepared with water and a few drops of Lanol 90H was used as a dispersant. To minimize contamination, small yttria stabilized  $\text{ZrO}_2$  spheres were used as milling media. To increase the surface area further, a small portion of the vibratory milled slurry was attrition milled(Reliance) for an additional 24h. The ball milled, vibratory milled, and attrition milled powders were named as batch A, B, and C, respectively. The  $\text{ZrO}_2$  contamination level, and the B.E.T. surface area of these powders are listed in Table I.

The dried powder was granulated with 5 wt% of Dupont 5200 binder in acetone media. After passing the mixture through a 100 mesh sieve, 1/2" dia. disks were cold pressed in a steel die with 30,000-35,000 psi uniaxial pressure. The binder from the disks was removed by a two stage heat treatment at 300°C/3h and then at 500°C/5h. These pellets were sintered in a closed alumina crucible at 1000-1250°C/1-5h. A small amount of  $\text{PbO}$ / $\text{ZrO}_2$  mixture was heated along with the pellets to control the lead oxide atmosphere inside the crucible. All the sintered samples were annealed at 950°C/2h to evaporate excess  $\text{PbO}$ . The weight losses during these preparation stages were monitored accurately.

#### Characterization

The bulk densities of the sintered specimens were calculated by measuring the weight change in Xylene. The grain size distribution was analyzed from the microstructures of fractured and polished surfaces. The microstructures were recorded using ISI-DS130 Secondary electron microscope.

Detailed experimental descriptions of dielectric, pyroelectric, P-E hysteresis, and electrostrictive measurements can be found in Ref.8. Dielectric measurements were made on gold sputtered discs.

Table I. Properties of Powder.

	A	B	C
$\text{ZrO}_2$ impurity (wt%)	0.67	0.71	1.04
B.E.T (m <sup>2</sup> /gm) Surface Area	1.20	3.17	15.46

while cooling from 100°C to -100°C at a rate of 2°C/min. For pyroelectric measurements, the electroded samples were cooled from 50°C to -75°C with an electric field of 10 kV/cm. After neutralizing the surface charge, the pyroelectric current was measured by heating the specimen to 50°C at 4°C/min. For P-E hysteresis and transverse electrostrictive measurements, an a.c. triangular field of  $\pm 10$  kV/cm was applied at a frequency of 0.1 Hz. The transverse strain measurements were made with a strain gauge technique. By differentiating E vs.  $s_2$  plots,  $-d_{31}^*$  values as a function of electric field were calculated.

AC impedance measurements were performed on circular disk samples of  $t < 0.3$  mm with sputtered silver electrodes. Resonance curves of conductance G, and resistance R of the samples at various biases were recorded with an HP 4194A impedance analyzer at 25°C. Series and parallel resonance frequencies  $f_s$  and  $f_p$  of thickness resonance mode were used to calculate  $k_t$  with the equation given in Ref 9.

### Results and Discussion

#### Physical Properties

The density and weight loss data of batch B and batch C samples are listed in Table 2. In general, samples sintered at lower temperatures show slightly higher density due to limited grain growth. Among the two batches, as the initial average particle size of C was lower, it sintered to comparatively higher densities. At higher sintering temperatures, as the grain growth mechanisms dominate, both batches sintered to similar densities. While batching the powders for calcination, to ensure the completion of reaction, 0.5 wt% excess PbO was added. But after sintering and annealing, higher weight losses were observed (Table 2). As reported by Wang and Scultz[6], our sample surfaces also showed a small number of pyrochlore grains. Since the pyrochlore is lead deficient in nature, excess PbO is evaporated while annealing.

The polished and fractured microstructures of a few of the sintered samples are reproduced in Fig. 1. The mean average grain sizes for all the samples are listed with standard deviation in Table 2.

Table 2. Physical Properties of the ceramic.

	Si. Tem °C/h	wt loss %	Density gm/cc	% Theo	Ave. g.s. ( $\mu$ m)
B1	1000/1		7.28 $\pm$ 0.04	89.24	
B2	1050/1	1.10	8.00 $\pm$ 0.02	98.06	1.1 $\pm$ 0.2
B3	1100/1	1.10	7.99 $\pm$ 0.01	97.94	1.2 $\pm$ 0.3
B4	1150/1	1.11	7.98 $\pm$ 0.02	97.84	1.3 $\pm$ 0.3
B5	1200/1	1.16	7.96 $\pm$ 0.03	97.57	1.7 $\pm$ 0.5
B6	1250/1	1.20	7.90 $\pm$ 0.02	96.84	2.2 $\pm$ 0.8
B7	1250/5	1.32	7.83 $\pm$ 0.03	95.98	3.3 $\pm$ 1.3
C1	1000/1	0.85	7.92 $\pm$ 0.03	97.08	0.7 $\pm$ 0.2
C2	1050/1	0.99	8.00 $\pm$ 0.03	98.08	1.0 $\pm$ 0.3
C3	1100/1	1.03	7.99 $\pm$ 0.02	97.94	1.4 $\pm$ 0.4
C4	1150/1	1.06	7.98 $\pm$ 0.02	97.82	1.5 $\pm$ 0.5
C5	1200/1	1.02	7.94 $\pm$ 0.02	97.33	1.9 $\pm$ 0.6
C6	1250/1	1.13	7.88 $\pm$ 0.03	96.59	2.4 $\pm$ 0.8
C7	1250/5	1.29	7.80 $\pm$ 0.03	96.51	3.6 $\pm$ 1.8

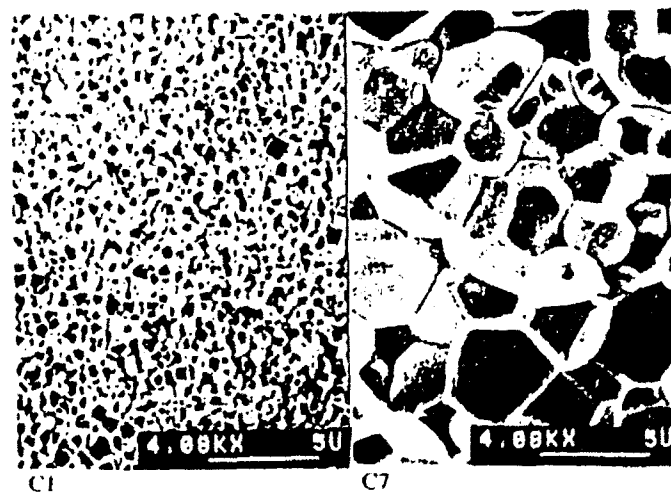


Fig. 1. Fractured surfaces of C1 and C7.

Table 3. Dielectric Properties of the ceramic

	g.s. $\mu$ m	Kmax	Tmax °C	Tan $\delta$ at 25°C	$\delta$ (°C)
B2	1.1	17800 $\pm$ 470	48	0.0582	40
B3	1.2	22250 $\pm$ 050	46	0.0686	38
B4	1.3	23750 $\pm$ 720	46	0.0718	34
B5	1.7	25300 $\pm$ 600	45	0.0765	31
B6	2.2	28850 $\pm$ 790	43	0.0829	27
B7	3.3	33000 $\pm$ 550	42	0.0922	
C1	0.7	13900 $\pm$ 300	48	0.0474	
C2	1.0	20800 $\pm$ 360	43	0.0725	33
C3	1.4	23350 $\pm$ 510	42	0.0792	32
C4	1.5	24700 $\pm$ 420	42	0.0803	32
C5	1.9	25450 $\pm$ 810	41	0.0795	30
C6	2.4	25800 $\pm$ 720	41	0.0850	29
C7	3.6	27450 $\pm$ 300	40	0.0891	

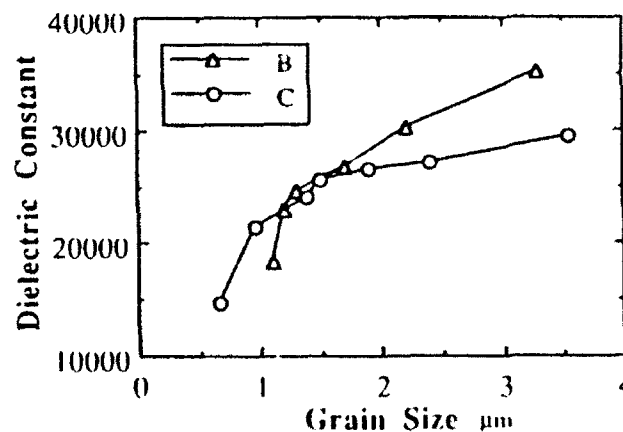


Fig. 2. Effect of average grain size on  $K_{max}$ . The dielectric constant was compensated for porosity with Weiner's rule.

### Low Electric Field Properties

The relevant dielectric properties are compared in Table 3. At least four samples were used to calculate the percentage change in the dielectric constant. The maximum dielectric constant ( $K_{max}$ ), after compensating for porosity with Weiner's equation [10], is plotted in Fig. 2, as a function of average grain size. Comparatively, the  $K_{max}$  of the samples from series B, changes as a strong function of grain size. In both batches,  $K_{max}$  reduces drastically when the grain size is  $< 1\mu m$ .

### High Electric Field Properties

The effect of grain size on the P vs. T behavior is compared in Fig. 3 and 4. To plot these figures, the polarization was calculated from the pyroelectric current. In relaxor ferroelectric materials, P vs. T behavior below the pyroelectric depolarization temperature,  $T_d$ , reflects the degree of cohesiveness among macrodomains. Below  $T_d$ , if the macrodomains are highly stable,  $\Delta P$  with respect to  $\Delta T$  will be small. When the material is heated, the stable macrodomains will convert into microdomains, over a narrow temperature interval around  $T_d$ . In our investigation, the samples sintered at higher temperatures show these behaviors very clearly. When the sintering temperature is reduced, increasingly large changes in P with respect to temperature is observed below  $T_d$ . Moreover, in these samples the macrodomains transform into microdomains over a wider temperature around  $T_d$ . Careful analysis of P vs. T behavior points out the importance of proper processing. In series C samples, as the grains were grown from finer particles, the grain size effect is minimized.

The induced polarization and the transverse strain characteristics of the fine grain samples from both batches show degradation of properties. This observation is clearly demonstrated by plotting  $-d_{31}^*$  vs. E field, as a function of grain size (Fig. 5 and 6). These measurements were made at 25°C. When the grain size is above 3  $\mu m$ , a maximum  $-d_{31}^*$  of about 500 pC/N is observed. When the grain size is reduced, the magnitude of maximum  $-d_{31}^*$  reduces with an increase in the corresponding electric field.

The piezoelectric thickness coupling coefficients calculated from the resonance curves observed at different d.c. biases are plotted in Fig. 7 and 8. These measurements were made at 25°C with increasing bias voltages. In both batches, coarse grained samples showed increased coupling at lower electric fields. The absolute values of coupling coefficients also increased as the grain size is increased.

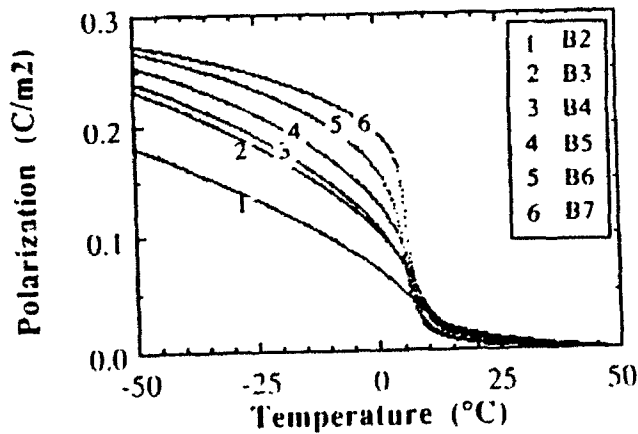


Fig. 3. Polarization vs. Temperature behavior of batch B samples.

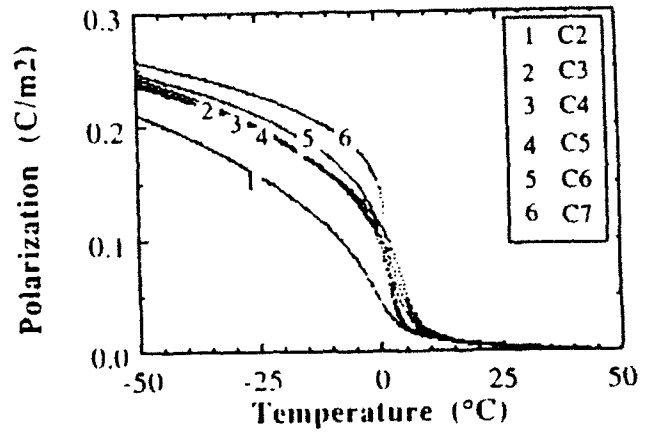


Fig. 4. Polarization vs. Temperature behavior of batch C samples

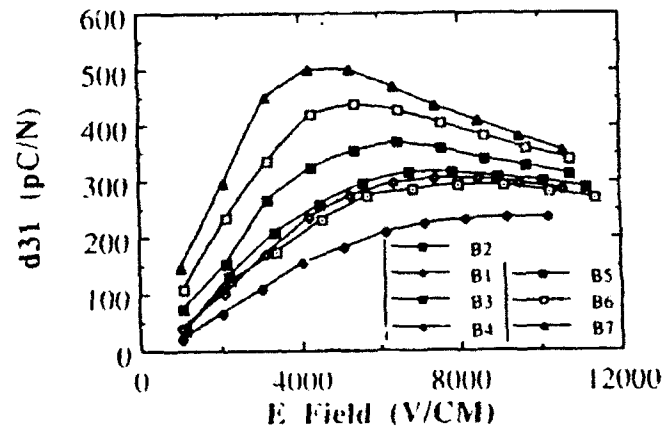


Fig. 5. Effective transverse piezoelectric d coefficients of batch B samples; calculated from electrostriction data

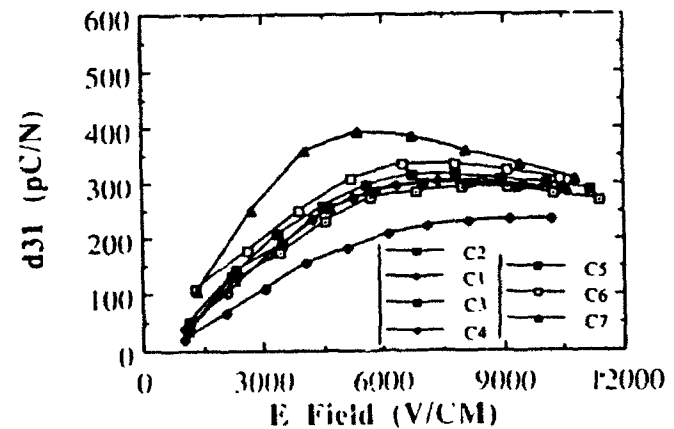


Fig. 6. Effective transverse piezoelectric d coefficients of batch C samples; calculated from electrostriction data.

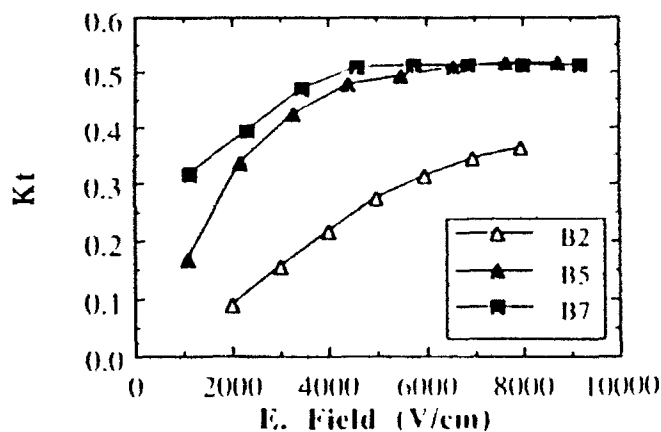


Fig. 7. Thickness coupling coefficients of batch B samples at different d. c. bias fields; calculated from resonance curves

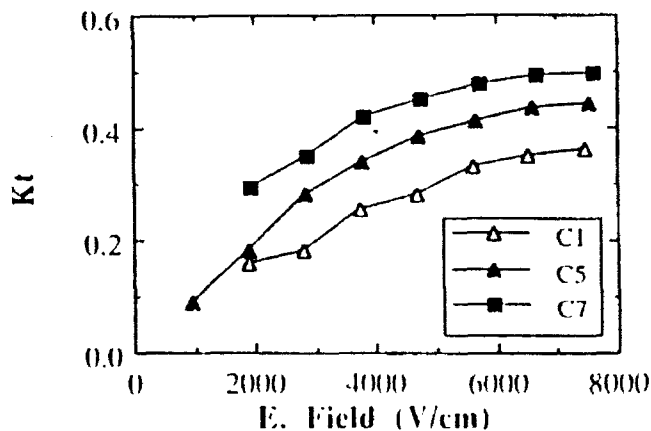


Fig. 8. Thickness coupling coefficients of batch C samples at different d. c. bias fields; calculated from resonance curves.

### Discussion

As mentioned in the introduction section, the grain size effect on the properties may be attributed to extrinsic and intrinsic variables. In the present samples, through careful annealing the effect of extrinsic variables are minimized. For example, B2, B3, B4 and C2, C3, C4 samples with similar weight losses and therefore with similar second phase volume at the grain boundary, show noticeable differences in the low and high electric field properties. As observed in all the properties, large grain samples with lower density show better properties as compared to fine grain samples with higher densities.

Careful analysis of the the low and high electric field properties show clear distinction between the properties of series B and series C samples. Slight depression of  $T_{max}$  and  $T_d$  in series C samples may be attributed to the higher concentration of  $Zr^{4+}$  ions as dopant[11]. Considering the average grain sizes of all these samples, ranging from approximately 0.7  $\mu m$  to only 3.5  $\mu m$ , it appears that the sintering temperature also influences the properties. From the surface area of the milled powders, the equivalent spherical diameter of the series B and series C powders are calculated as 0.23  $\mu m$ , and 0.047  $\mu m$ , respectively. Comparing the grain sizes, it is clear that the series C samples show at least 15 times growth during sintering. Because of this growth, it is hypothesized that these samples are more homogeneous as compared to series B samples. Hence, the lesser influence of the average grain size on the low and high field properties of series C samples may be attributed to higher degree of homogeneity.

### Conclusion

In this paper, the dielectric, pyroelectric, electrostrictive, and the induced piezoelectric properties of 0.90PMN-0.10PT ceramic are compared as a function of grain size. Comparatively, samples prepared from coarse particle compact show higher grain size dependence. When the average grain size is around 3.5  $\mu m$ , irrespective of the initial powder characteristics, the ceramic show similar high electric field properties. Through transverse strain measurements, a high  $-d_{31}^*$  of 500 pC/N at a d.c. bias of 4300 V/cm is observed. When the samples were prepared from very fine powders, the magnitudes of  $K_{max}$ ,  $-d_{31}^*$ , and  $k_t$  reduces only moderately as the grain size is reduced to 1.5  $\mu m$ . Since the effect of extrinsic variables such as density and the grain boundary phase are minimized through careful preparation, the observed grain size

Acknowledgements: Financial support from Echo Ultrasound of Reedsville, PA and The Ben Franklin Partnership Program of the commonwealth of PA and technical support from Mingfong Song are gratefully acknowledged.

### References

- [1] W. Y. Pan, W. Y. Gu, D. J. Taylor and L. E. Cross, "Large Piezoelectric effect induced by Direct Current Bias in PMN:PT Relaxor Ferroelectric," *Jpn. J. Appl. Phys.*, 4, p653 (1989)
- [2] H. Takeuchi, H. Masuzawa, C. Nakaya, and Y. Ito, "Relaxor Ferroelectric Transducers," 1990 IEEE Ultrasonic Symposium, Aomani, p697-705 (1990).
- [3] K. Uchino, M. Tatsumi, I. Hagashi, and H. Hayashi, *Jpn. J. Appl. Phys.*, 24, 733-735 (1985).
- [4] T. R. Shrout, U. Kumar, M. Megheri, N. Yang, and S. J. Jang, "Grain Size Dependence of Dielectric and Electrostriction of  $Pb(Mg_{1/3}Nb_{2/3})O_3$ -based ceramic," *Ferroelectrics*, 76, 479-85 (1987)
- [5] P. Peppet, J.P. Dougherty and T.R. Shrout, "Particle and Grain Size Effects on the Dielectric Behavior of the Relaxor Ferroelectric  $Pb(Mg_{1/3}Nb_{2/3})O_3$ ," *J. Mater. Res.*, 5[12], 2902-2909 (1990) (and the references there of).
- [6] H. C. Wang, and W. A. Schultze, "The role of excess magnesium oxide and lead oxide in determining the microstructure and the properties of lead magnesium niobate," *J. Am. Cer. Soc.*, 73[4] 825-32 (1990) (and the references there of).
- [7] S. Swartz and T. R. Shrout, "Fabrication of Perovskite Lead Magnesia Niobate," *Mat. Res. Bull.*, 17, 1245-1250 (1982)
- [8] U. Kumar, L. E. cross, and A. Halliyal, "Pyroelectric and electrostrictive properties of  $(1-x-y)PZN.xBT.yPT$  ceramic solid solution system," *J. Am. Ceram. Soc.*, 75[8], p-2155-64 (1992).
- [9] "IRE standards on piezoelectric crystals: Measurements of piezoelectric ceramic, 1961", *Proc. IRE*, 49, p-1161-1169 (1961)
- [10] D. F. Rushman, and M. A. Strivens, "The effective permittivity of two-phase systems," *Proc. Phys. Soc.* 59, p-1011-1016 (1947).
- [11] D. J. Voss, S. L. Swartz and T. R. Shrout, "Pyroelectric and Electrostrictive properties of B-site modifications on dielectric and electrostrictive properties of lead magnesium niobate ceramics," *Ferroelectrics*, 50, p-203-208 (1983).

**APPENDIX 44**

# Extrinsic contributions to the grain size dependence of relaxor ferroelectric $\text{Pb}(\text{Mg}_{1/3}\text{Nb}_{2/3})\text{O}_3:\text{PbTiO}_3$ ceramics

C. A. Randall

*Materials Research Laboratory, The Pennsylvania State University, University Park, Pennsylvania 16802*

A. D. Hilton and D. J. Barber

*Department of Physics, University of Essex, Wivenhoe Park, Colchester, Essex, United Kingdom*

T. R. Shtrout

*Materials Research Laboratory, The Pennsylvania State University, University Park, Pennsylvania 16802*

(Received 16 July 1990; accepted 24 November 1992)

This paper addresses the observed grain size dependence of the dielectric behavior for  $\text{Pb}(\text{Mg}_{1/3}\text{Nb}_{2/3})\text{O}_3:\text{PbTiO}_3$  ceramics grain sizes  $\geq 1.0 \mu\text{m}$ . A combined transmission electron microscopy (TEM) analysis and dielectric characterization are modeled with a modified brick wall approach. From this model, it is possible to extrapolate information such as single crystal values of dielectric maximum,  $K_{\text{max}}$ , the diffuseness coefficient,  $\delta$ , and the average intergranular thickness for relaxor ceramics. The calculated intergranular thickness agrees well with TEM observations,  $\approx 2.0 \text{ nm}$ . This semi-empirical method may be potentially useful in development work of relaxor ceramics to predict the optimized dielectric properties obtainable within microstructural restrictions.

## I. INTRODUCTION

Complex lead-based perovskites, with the general formula  $\text{Pb}(\text{B}_1\text{B}_2)\text{O}_3$ , exhibiting diffuse frequency dependent dielectric permittivities are commonly referred to as relaxor ferroelectrics. A typical example of a relaxor from this complex lead perovskite family is the  $\text{Pb}(\text{Mg}_{1/3}\text{Nb}_{2/3})\text{O}_3$  (PMN) compound. Solid solutions of relaxor PMN and the first order ferroelectric,  $\text{PbTiO}_3$  (PT), exhibit many attractive properties for dielectric and electrostrictive applications.<sup>1</sup> The high dielectric constants, over broad temperature ranges, close to room temperature, make systems like  $(1-x)\text{PMN}:x\text{PT}$  ( $x = 0.07$ ) very attractive for multilayer capacitor (MLC) and actuator applications. In several previous investigations for the dielectric properties, including  $K_{\text{max}}$  diffuseness (the effective width of the maxima) and aging, have been shown to be dependent on processing variations, in particular the role of grain size on these properties. These earlier investigations did not lead to simple interpretation, partly because of the presence of second phase pyrochlore.<sup>1</sup> The present paper successfully interprets the structure-property relations in  $(1-x)\text{PMN}:x\text{PT}$  ( $x = 0.07$ ) ceramics, using good processing control, dielectric characterization, and transmission electron microscopy techniques.

## II. EXPERIMENTAL

Polycrystalline ceramic disks with the relaxor composition,  $(1-x)\text{PMN}:x\text{PT}$  ( $x = 0.07$ ), were prepared via the B-site precursor method.<sup>2</sup> Both reagent grade and high purity powders were used in this study. In

processing the columbite precursor, the poor dispersion characteristics associated with magnesium carbonate powders were addressed using both steric hindrance (polyelectrolyte dispersant) and electrostatic repulsion (pH adjustment by ammonia) in conjunction with high energy milling. Upon calcination the appropriate amount of  $\text{PbO}$  was added followed by mixing in a dispersant and adjusting the pH to obtain minimum lead dissolution. Calcination at  $700^\circ\text{C}$  for 4 h produces the desired single phase perovskite powder. Uniformity and reactivity of PMN:PT powder were further enhanced by milling. Grain size variations in the PMN:PT ceramics were achieved by firing samples at different temperatures and times, as reported in Ref. 3. Significant grain growth through longer firing times was not found to be effective.

The dielectric measurements of ceramics were carried out on an automated Hewlett-Packard System. The dielectric constant and loss were measured on cooling at various frequencies (100 Hz, 1 KHz, 10 KHz, and 100 KHz) at a rate of  $4^\circ\text{C}/\text{min}$ .

Transmission electron microscopy (TEM) characterization was performed after dielectric characterization. Slices were cut from fired disks using a diamond saw followed by grinding to a thickness of  $\sim 30 \mu\text{m}$  using silicon carbide. A copper support grid was glued onto the surface of each polished specimen using epoxy resin. Electron transparent regions were obtained by ion-beam milling the samples with an Ion Tech argon beam thinner operating at an accelerating voltage of 5 kV and at an incidence angle of  $15\text{--}30^\circ$ . Finished TEM specimens were coated with a thin layer of carbon in order to prevent charging within the electron microscope.

TEM observations were made with a JEOL-200CX microscope and a Philips 420 STEM, both equipped with a LINK systems energy dispersive x-ray spectrometer (EDS).

### III. RESULTS

#### A. Physical and dielectric properties

The general characteristics of PMN:PT ceramic samples as a function of thermal history are summarized in Table I. All the samples possessed densities greater than 95% of the theoretical  $8.11 \text{ g/cm}^3$ . The weight loss during sintering was confined to the range of 0.5–1.5 wt. % with slightly higher losses occurring in samples processed at higher temperatures. Annealed samples and samples fired in  $\text{BaZrO}_3$  sand showed only marginal differences in weight loss. It should also be mentioned that x-ray analysis of PMN:PT ceramics were phase pure with no evidence of pyrochlore or  $\text{PbO}$  phases.

The magnitude of dielectric constant  $K_{\text{max}}$  (0.1 KHz) versus grain size (gs) is presented in Table I, and is shown in Fig. 1 (both from Ref. 3). For all ceramics studied, the  $K_{\text{max}}$  values are relatively high compared to those reported in the literature; this is believed to be owing to the overall care in processing. Clearly the value of  $K_{\text{max}}$  for a given frequency increases and the diffuseness of the dielectric temperature dependence decreases with increasing grain size.

#### B. Microstructural analysis

Intergranular boundaries examined in samples prepared in this study used standard TEM under focus/over focus bright field Fresnel fringe contrast and lattice fringe imaging techniques.<sup>4,5</sup> Under focus/over focus Fresnel images of the grain boundary are shown in

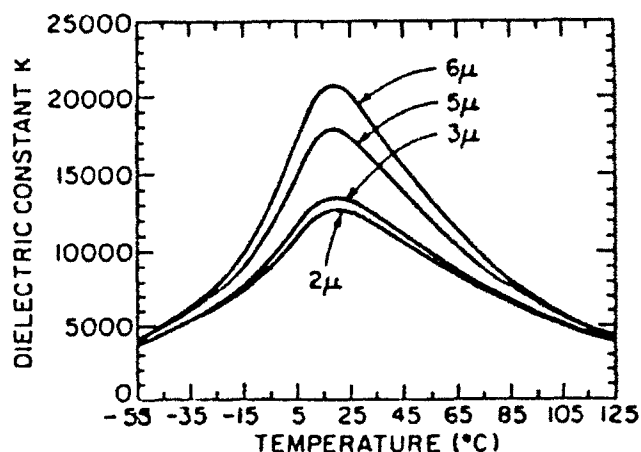


FIG. 1. Variation of the dielectric constant temperature dependence (100 Hz) with a grain size in PMN:PT (0.93:0.07) ceramics.

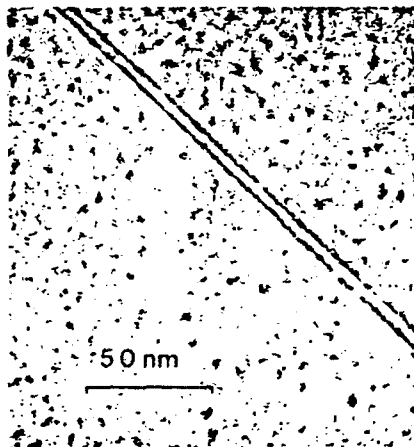
Figs. 2(a) and 2(b), respectively. A typical lattice firing image of the grain boundary phase in a coarse grain reagent grade sample is illustrated in Fig. 2(c). As shown,  $\{100\}$  planes (0.407 nm) have been imaged in adjacent edge-on grains, clearly showing a discontinuity between the two sets of lattice fringes. The thicknesses of those intergranular glassy phases were found to be approximately  $\sim 2 \pm 1 \text{ nm}$  with little measurable variations in thickness either along lengths of individual boundaries or throughout each sample. This was also found to be true for samples processed with excess  $\text{PbO}$  addition. It is important to point out that within the bonds of our processing variables a grain boundary phase was always found using these standard techniques. This includes the starting powder purity, namely from reagent grade to high purity powders ( $\geq 99.99\%$ ) and the firing of stoichiometrically batched PMN:PT under conventional and hot-pressing and also after annealing.

TABLE I. Processing conditions and general characteristics of 0.93 PMN:0.07 PT ceramics.

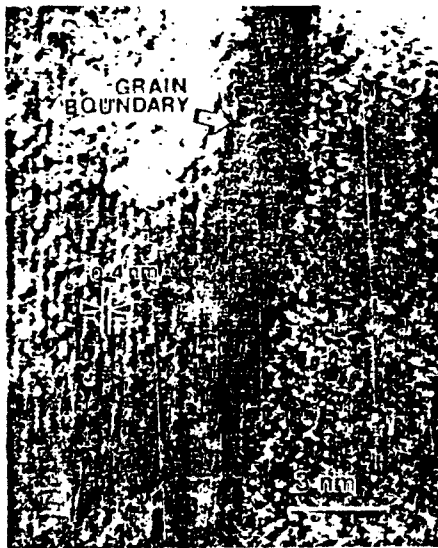
Firing condition	wt. loss %	$\rho$ ( $\text{g/cm}^3$ )	Grain size	$K_{\text{max}}$	$T_{\text{max}}$ °C	$\delta$ (°C)
950 °C	- 0.5 h	0.5	1.5 $\mu\text{m}$	11 500	24	58
	- 4 h	0.7	2.0 $\mu\text{m}$	13 000	22.8	50
	-48 h	0.6	2.0 $\mu\text{m}$	20 300	...	39
1050 °C (Zirconate sand)	- 0.5 h	0.8 (0.97)	2.0 $\mu\text{m}$	12 600 (14 800)	20.6	57 (47)
	- 4 h	0.5	3.0 $\mu\text{m}$	15 700	20.5	44
	-20 h	1.1	3.0 $\mu\text{m}$	18 800	22.2	43
1150 °C (Zirconate sand)	- 0.5 h	0.7 (0.87)	3.0 $\mu\text{m}$	13 500 (15 100)	19.7	48 (47)
	- 4 h	1.0	3.0 $\mu\text{m}$	17 800	...	43
	- 0.5 h	1.1	5.0 $\mu\text{m}$	17 500	...	44
1250 °C	- 4 h	1.2	6.5 $\mu\text{m}$	20 800	18.4	42
	-20 h	1.45	9.0 $\mu\text{m}$	22 800	17.9	39
	- 0.5 h	1.1	6.0 $\mu\text{m}$	21 000	18.7	41



(a)



(b)



(c)

FIG 2. (a), (b) Under-overfocus micrograph images of grain boundary phase in FMN:PT ceramics; reversal of contrast implies presence of grain boundary phases. (c) Lattice fringe image of grain boundary phase in PMN:PT ceramic.

A direct chemical analysis of the grain boundary phase could not be obtained owing to the small scale of the boundaries. However, the phases are most likely Pb-rich due to the low melting point of this constituent and the recent SIMS study (Secondary Ion Mass Spectroscopy) by Wang and Schulze.<sup>6</sup>

Second phases were found at all triple points in the coarse-grained materials prepared from reagent powders regardless of firing condition or composition (excess up to 2 at. wt. % PbO). A representative example of triple junction phase is shown in Fig. 3(a). The EDS analysis revealed that the second phase was rich in lead and contained impurity elements, Al, Si, P, and S, as shown in Fig. 3(b). This result is consistent with the finding of Gorton *et al.*<sup>7</sup> As the triple points are continuous with the grain boundaries, similar compositions are expected in the grain boundaries. Similar "dirty" triple junctions

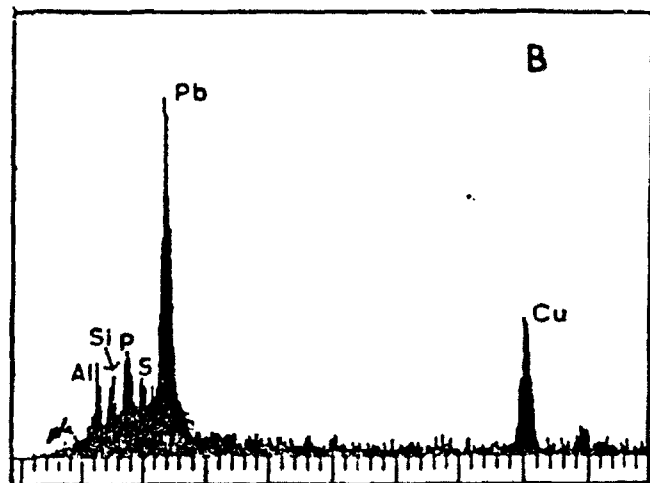
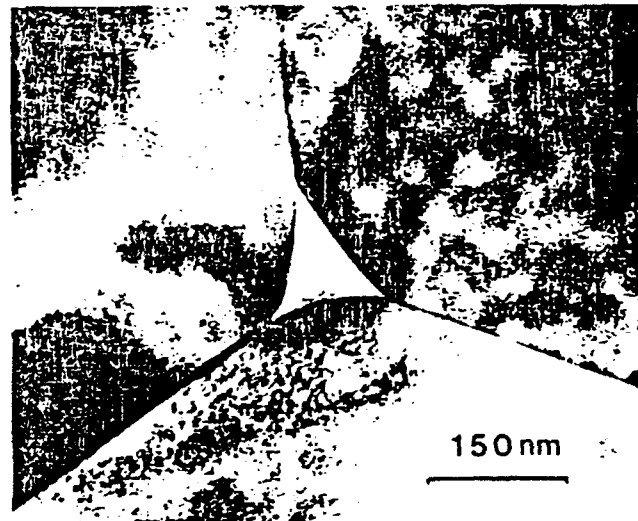


FIG 3. (A) Glassy phase found at triple point in reagent grade PMN:PT ceramics. (B) EDS spectrum from triple point in reagent grade PMN:PT.

were observed in all reagent grade ceramic samples. We draw attention to the rounded grain boundaries at the triple points, suggesting that a phase was liquid during sintering. Triple points of high purity ceramics were found to be clean and free of any second phase (Fig. 4).

#### IV. DISCUSSION

From the microstructural studies given here, we expect the observed continuous intergranular glassy phase of thickness  $\sim 2 \pm 1$  nm to reduce the dielectric constant of the  $0.93 \text{ Pb}(\text{Mg}_{1/3}\text{Nb}_{2/3})\text{O}_3 : 0.07 \text{ PbTiO}_3$  ceramics. There may be slight variations in the thickness of this grain boundary phase owing to different crystallographic orientations between adjacent grains, but there is no evidence of an inhomogeneous distribution of a glassy lead phase, as found in modified  $\text{Pb}(\text{Zr}, \text{Ti})\text{O}_3$  ceramics.<sup>3</sup>

In general, a ceramic microstructure is a mixture of parallel and series intergranular boundaries. The series boundaries in this system will dominate the dielectric constant owing to the small volume fraction of glassy phase existing and the amorphous nature, implying a low dielectric constant relative to ferroelectric grains.

Hence, a series mixing law can be applied to this problem in the form:

$$\frac{1}{K} = \frac{1}{K^g} + \frac{1}{RK^{gb}} \quad \text{where } R = \frac{\langle t^g \rangle}{\langle t^{gb} \rangle} \quad (1)$$

and where  $K^g$  = dielectric constant of grain,

$K^{gb}$  = dielectric constant of grain boundary,

$\langle t^g \rangle$  = mean grain size, and

$\langle t^{gb} \rangle$  = mean grain boundary thickness.

Qualitatively, we can expect a relative change of dielectric constant owing to the variation of the ratio  $R$  with grain size according to Eq. (1). However, to demonstrate

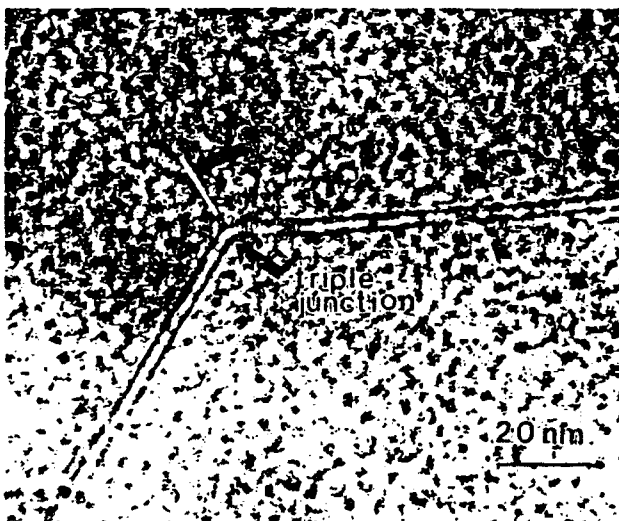


FIG. 4. Clear triple point in high purity PMN:PT ceramics.

the relative importance of this effect compared to other possible intrinsic effects, we need to consider the dielectric permittivity's temperature dependence at fixed frequencies, as this allows us to also account for the influence of both  $K_{\text{max}}$  and diffuseness with grain size in the relaxor systems.

In some ferroelectrics such as  $\text{BaTiO}_3$ , there is a spontaneous strain  $\sim 1\%$  at the phase transition. Within a ceramic each grain stresses at its neighbor at the transition and causes changes to the elastic boundary conditions of each grain. These self-induced stresses have an effect on the dielectric permittivity of the  $\text{BaTiO}_3$  grains. This is especially important in  $\text{BaTiO}_3$  ceramics with grain sizes  $\sim 1.0 \mu\text{m}$ , as discussed in detail in Refs. 9 and 10. In relaxor ferroelectrics there is very little spontaneous strain, and, hence, intergranular stresses are assumed to be negligible. So a relaxor single crystal dielectric permittivity is comparable to the individual grain electric permittivity for grains  $\geq 1.0 \mu\text{m}$ .

So  $K^g = K^x$  where  $K^x$  is the crystal dielectric constant. (2)

The temperature dependence of a relaxor single crystal dielectric at fixed frequency can be described by the semi-empirical relationship of Smolenskii<sup>11</sup>:

$$\frac{1}{K^x} = \frac{1}{K_{\text{max}}^x} + \frac{(T - T_{\text{max}})^2}{2\delta_x^2 K_{\text{max}}^x} \quad (3)$$

where  $K^x$  = dielectric constant of the single crystal relaxor,

$K_{\text{max}}^x$  = maximum dielectric constant of single crystal relaxor,

$T_{\text{max}}$  = temperature corresponding to dielectric constant maximum, and

$\delta_x$  = the diffuseness coefficient of single crystal relaxor.

The temperature dependence of the inverse dielectric constant in relaxor ferroelectrics does not follow the Curie-Weiss behavior in the region of the  $K_{\text{max}}$  in relaxors.<sup>10</sup>

Combining Eqs. (1), (2), and (3) allows us to model the average dielectric constant  $\bar{K}$  of the ceramic relaxor as a function of temperature:

$$\frac{1}{\bar{K}} = \left( \frac{1}{K_{\text{max}}^x} + \frac{1}{R K^{gb}} \right) + \left[ \frac{(T - T_{\text{max}})^2}{2\delta_x^2 K_{\text{max}}^x} \right] \quad (4)$$

By equating (3) and (4), we obtain the dielectric mixing law of the ceramic  $\bar{K}_{\text{max}}$  as a relationship between the series mixing of single crystal dielectric constant and grain boundary dielectric constants.

$$\frac{1}{\bar{K}_{\text{max}}} = \frac{1}{K_{\text{max}}^x} + \frac{1}{R K^{gb}} \quad (5)$$

In addition, we also note that there is a constant dependence of the diffuseness  $K_{\max}$  product for a given composition of relaxor ferroelectric at a constant density,

$$\delta_x^2 K_{\max}^x = \delta^2 \bar{K}_{\max}. \quad (6)$$

Hence  $\delta^2 K_{\max}$  is constant for all grain sizes ( $1/t_g$ ), provided the only variations in  $\delta$  and  $K_{\max}$  are owing to an extrinsic grain boundary phase. For the PMN:PT (0.07) ceramics studied here, we can observe in Fig. 5, that  $\delta^2 K_{\max}$  is constant for a broad range of grain sizes, suggesting grain boundary thickness and grain size dielectric constants extrinsically influence  $\delta^2 K_{\max}$ . Using a plot of this type, we can extrapolate the single crystal values of  $\delta_x^2 K_{\max}^x$ .

To complement these results plotting  $1/\bar{K}_{\max}$  vs  $1/\langle t_g \rangle$ , as in Fig. 6, additional information can be obtained from Eq. (5). The intercept of the y-axis gives  $1/K_{\max}^x$  and the slope corresponds to  $\langle t^{sb} \rangle / K_{gb}$ . Using typical values of lead glass for grain boundary dielectric constant  $K_{gb} \cong 20$  predicts an average grain boundary thickness  $\langle t_{gb} \rangle \cong 1.8$  nm. This theoretical prediction agrees very well with the TEM observations on these ceramic samples  $\sim 2.0$  nm  $\pm$  1.0 nm. Using the intercept of  $K_{\max}^x \cong 29000$  (at 100 Hz), we can predict a corresponding diffuseness coefficient  $\delta_x = 38$  for single crystal PMN:PT (0.07). No single crystal data of dielectric  $K_{\max}$  or  $\delta$  are known for single crystal PMN:PT (0.07).

A technique for characterizing  $\bar{K}_{\max}$ ,  $\delta$ , and  $\langle t^{sb} \rangle$  from dielectric data and grain size information is demonstrated for an important relaxor ferroelectric ceramic, PMN:PT ( $x = 0.07$ ). This methodology may be of use to the industrial ceramic processing engineer when optimizing the properties of a given relaxor system in which no single crystal data are available.

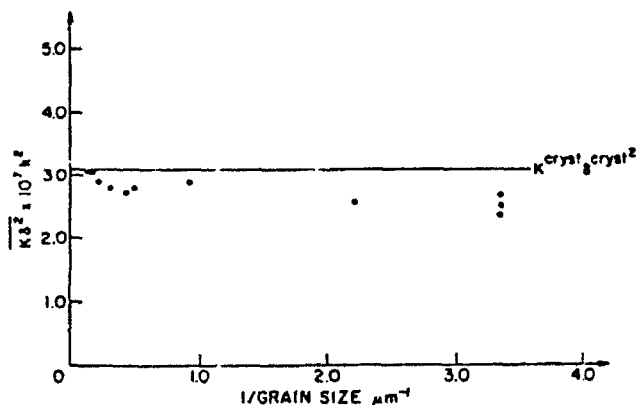


FIG. 5. Variation of  $\delta^2 K_{\max}$  and grain size for PMN:PT reagent grade ceramics.

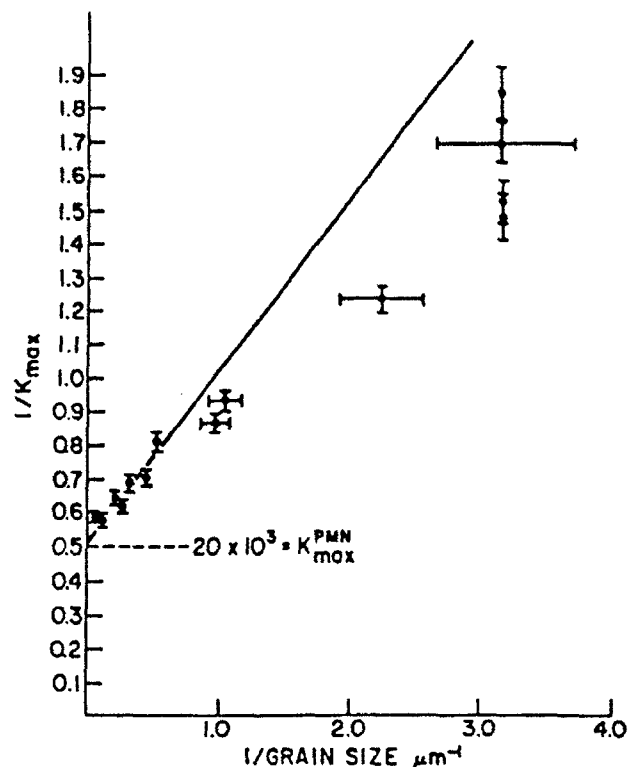


FIG. 6. Variations of  $1/K_{\max}$  and grain size for PMN:PT reagent grade ceramics.

## ACKNOWLEDGMENTS

We wish to thank JoAnn Mantz for typing this manuscript and Beth Jones for technical assistance. This was partly supported by the Office of Naval Research and the Center for Dielectric Studies at The Pennsylvania State University.

## REFERENCES

1. Thomas R. Shrout and Arvind Halliyal, *Am. Ceram. Soc. Bull.* **66** (4), 704 (1987).
2. S. L. Swartz and T. R. Shrout, *Mater. Res. Bull.* **XVIII**, 663-667 (1983).
3. T. R. Shrout, U. Kumar, M. Megherhi, W. Wang, and S. J. Jang, *Ferroelectrics* **76**, 474-487 (1989).
4. D. R. Clarke, *J. Appl. Phys.* **49**, (4) 2407 (1978).
5. O. L. Kraneek, T. M. Shaw, and G. Thomas, *J. Appl. Phys.* **50**, (6) 4223 (1979).
6. H. C. Wang and W. A. Schulze, *J. Am. Ceram. Soc.* **73** (4), 825 (1990).
7. A. J. Gorton, J. Chen, H. Chan, D. Smyth, and M. P. Harmer, *Proc. 6th IEEE Int. Symp. Appl. Ferroelec.*, 150-153 (1988).
8. C. A. Randall, D. J. Barber, and R. W. Whatmore, *J. Mater. Sci.* **21**, 925 (1987).
9. W. R. Buessem, L. E. Cross, and A. H. Goswami, *J. Am. Ceram. Soc.* **49**, 33 (1966).
10. G. Arlt, *Ferroelectrics* **104**, 217-227 (1990).
11. G. A. Smolenskii, *J. Phys. Soc. Jpn.* **28**, Suppl. 26 (1970).

**APPENDIX 45**

# Barrier Layer Capacitor Using Barium Bismuth Plumbate and Barium Plumbate

Basavaraj V. Hiremath\*

AT&T Bell Laboratories, Princeton, New Jersey 08542

Robert E. Newnham\* and Leslie E. Cross\*

Materials Research Laboratory, The Pennsylvania State University, University Park, Pennsylvania 16802

A new type of barrier layer capacitor is described utilizing thin glass layers on highly conducting ceramics of barium plumbate and barium bismuth plumbate. The frequency dispersion of the apparent dielectric constant has been explained using a modified version of the Maxwell-Wagner model. These capacitors have a low temperature coefficient of capacitance and a high dispersion frequency in the megahertz range. Simple processing conditions together with low firing temperature make it possible to produce the barrier layer capacitors inexpensively.

## I. Introduction

THE demand for capacitors of small size and large capacitance has increased recently because of the rapid miniaturization of electronic circuits. This trend is reflected in the development and widespread application of multilayer ceramic capacitors<sup>1</sup> and barrier layer capacitors.<sup>2</sup> Because of the lower operating voltage, barrier layer capacitors utilizing a thin dielectric layer have become feasible. A method of fabricating barrier layer capacitors with highly conducting ceramic grains is described in this paper.

Barrier layer ceramic capacitors are normally fabricated by forming an insulating layer on the surface of the grains of semiconducting ceramics such as barium titanate,<sup>3</sup> strontium titanate,<sup>4</sup> and modified compositions of the titanates described in this paper.<sup>5,6</sup> They have been widely used because of their large apparent dielectric constant ( $10^4$ ), small temperature coefficient of permittivity, and high dispersion frequency ( $10^6$  Hz).

In order to produce barrier layer capacitors having a large apparent permittivity, it is necessary to sinter ceramic materials so that the semiconducting ceramic contains grains ranging from 50 to 100  $\mu\text{m}$  in size.<sup>7</sup> To obtain disks of semiconducting ceramic, a two-step process is often used.<sup>8</sup> In the first step, a semiconducting ceramic composition is sintered and subsequently converted to a semiconducting state by heating in a reducing atmosphere. Then either the surface of the semiconducting disk is reoxidized, or an insulating oxide is diffused into the disk. The disk is then electroded and lead attached to form the finished capacitor product.

An important objective of the present work is to provide conducting ceramic compositions for barrier layer capacitors which have high permittivity, low loss factor, stable temperature coefficient of capacitance, high insulating resistance, and high cutoff frequency at relatively low cost. The conducting ceramics

selected for this investigation were barium plumbate and barium bismuth plumbate. These compounds belong to a family of conducting perovskites.<sup>9,10</sup>

It is clear from Maxwell-Wagner dispersion theory that a decrease of the grain interior resistivity will shift the capacitance dispersion in the direction of higher frequency.<sup>11</sup> Because the conductivity of semiconducting strontium titanate is higher than that of semiconducting barium titanate ceramics, the cutoff frequency of the barrier layer capacitors based on strontium titanate is 100 times higher than that of capacitors based on barium titanate.<sup>11</sup> The work described in this paper has shown that the cutoff frequency can be further improved in barrier layer capacitors fabricated from more conducting barium plumbate and barium bismuth plumbate compositions.

## (1) Sample Preparation

Barium carbonate (AR grade, J. T. Baker Chemical Co., Phillipsburg, NJ), lead oxide (100Y Litharge Hammond Lead Products Inc., Pottstown, PA), and bismuth oxide (AR grade, Fisher Scientific, Fairlawn, NJ) were used as starting materials to obtain various solid solutions in the series  $\text{Ba}(\text{Bi}_x\text{Pb}_{1-x})\text{O}_3$ , where  $0 \leq x \leq 0.25$ ; the composition  $\text{Ba}(\text{Bi}_{1-x}\text{Pb}_x)\text{O}_3$  is designated as BBP and  $\text{BaPbO}_3$  as BP. The batched materials were ball-milled for 10 h in a polyethylene jar using zirconia grinding media and deionized water. The slurry was dried at 110°C for 4 h. The dried powder was calcined in a flowing oxygen atmosphere for 12 h at 850°C as recommended by Gilbert.<sup>12</sup> Oxygen was allowed to flow in a tube furnace at the rate of 0.07 standard cubic meter per hour (SCMH) or 2.5 standard cubic feet per hour (SCFH). This powder was found to be single-phase by X-ray diffraction. The calcined powder was again milled in a polyethylene jar for 8 h and the slurry was dried. The dried powder was mixed with a polyvinyl binder and sieved through No. 100-mesh screen to obtain free flowing granules. The preweighed (about 1 g) granules were pressed into disks of  $1.4 \times 10^{-2}$  m diameter and  $1 \times 10^{-3}$  to  $2 \times 10^{-3}$  m thick. The average green density of these pellets was about 50% to 60% of the theoretical density. The green pellets were heated at about 550°C for 6 h to burn out the binder. The pellets were then sintered at 950°C for 30 min in an oxygen atmosphere with a flow rate of 0.07 SCMH or 2.5 SCFH using a heating rate of 100°C/h. Cooling was carried out by turning off the power to the furnace.

In order to form a barrier layer, several glasses (see Table I) were diffused over the major surfaces of disks. The glasses were powdered using a mortar and pestle and passed through a 325-mesh screen. The fine powder was then mixed with acetone to form a paste. The paste was brushed onto one side of the ceramic disks and dried in an oven at 100°C for 30 min to drive out the acetone. The glass-coated disks were then heated in a furnace at various temperatures in the range 400° to 900°C for periods ranging from 5 to 30 min. After diffusing glass on one major face of a disk, the other surface was also coated with glass powder and the process was repeated. Gold was sputtered

G. H. Haertling—contributing editor

Manuscript No. 196371 Received September 9, 1991; approved July 8, 1992.  
Supported by the Center for Dielectrics Studies, which is a consortium of leading manufacturers of ceramic capacitors in the United States.  
\*Member, American Ceramic Society.

**Table I. Melting Points of Various Glasses Used in the Fabrication of Barrier Layer Capacitors**

Composition	Melting point (°C)
Li <sub>2</sub> O-3B <sub>2</sub> O <sub>3</sub>	800
Li <sub>2</sub> O-5B <sub>2</sub> O <sub>3</sub>	900
Solder glass*	560
Pb <sub>2</sub> Ge <sub>3</sub> O <sub>11</sub>	750
EO <sup>†</sup>	750

\*Composition (wt%): PbO (66.0), B<sub>2</sub>O<sub>3</sub> (14.0), ZnO (10.5), Al<sub>2</sub>O<sub>3</sub> (3.5), Bi<sub>2</sub>O<sub>3</sub> (2.0), CuO (2.0), and SiO<sub>2</sub> (2.0). <sup>†</sup>Supplied by Corning Glass Works, Corning, NY, and approximate composition PbO-Ga<sub>2</sub>O-Bi<sub>2</sub>O.

onto the glass-covered disks to form electrodes on the major faces.

## (2) Measurements

The capacitance and dissipation factor of the barrier layer capacitors were measured over a wide range of temperatures (-55° to 150°C) and frequencies (10<sup>2</sup> to 10<sup>10</sup> Hz). To measure the capacitance and dissipation factor at low frequencies (<10<sup>6</sup> Hz), automated LCR bridges (HP4274A and HP4275A, Hewlett-Packard, San Diego, CA) were utilized. The lead wires of the sample were connected to a test fixture which was directly connected via a coaxial cable to the appropriate LCR bridges. The lead capacitance was compensated by calibrating the bridges under both the "shorted" and "open" conditions.

The fixture connected to the sample was placed in a copper container which both provided physical protection and acted as a heat sink. The temperature was controlled in an electrical resistance box oven (Delta design 2300) interfaced to a desktop computer (HP9816A, Hewlett-Packard) which controlled the rate of cooling by regulating the flow of liquid nitrogen into the oven. The same computer was used for on-line control of automatic measurements through a HP6904B multiprogrammer and an HP59500A multiprogrammer interface.

The dielectric constant and the dissipation factor for several barrier layer capacitors of composition BP and BBP were measured at high frequencies (10<sup>7</sup> to 10<sup>10</sup> Hz) using the reflection technique of an rf impedance analyzer (HP 4191A).<sup>13,14</sup> This method is based on the fact that an electromagnetic wave incident on a dielectric is partially reflected. A standing wave results from the interference of forward propagating and reflected waves, which can be related to the impedance of the sample. The dielectric constant and loss factor can be calculated from the impedance by a lumped or distributed circuit technique. The lumped impedance method assumes the electric field to be uniform throughout the sample. This is especially useful for low-K materials in which the wavelength of the electromagnetic wave is much larger than the sample thickness. The distributed impedance method accounts for a significant portion of the electromagnetic wave in the dielectric.

## II. Results and Discussion

In this section dielectric properties and their modeling for barrier layer capacitors of composition BP and BBP are discussed. A modified version of the Maxwell-Wagner model was applied to explain the behavior of the apparent dielectric constant and dissipation factor with frequency.

### (1) Barrier Layer Capacitor of Composition BP

The dielectric properties described here were measured on a disk barrier layer capacitor fabricated with solder glass (Table I). Intentionally, a thick layer of about 1 to 2 mm was coated on the barium plumbate ceramic as a conductor. The apparent dielectric constant and the dissipation factor at room temperature were 60 and 0.03, respectively, at 10 kHz measuring frequency. The variations of the apparent dielectric constant and the dissipation factor with temperature are shown in Figs. 1 and 2, respectively. The dielectric properties of the barrier layer capacitor of this composition are attributable to the diffused

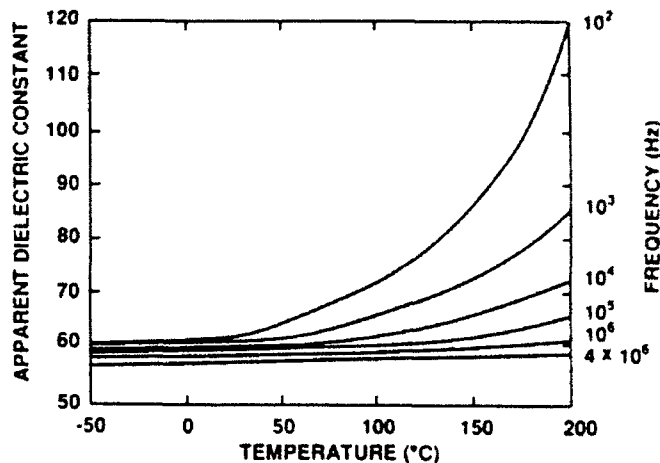


Fig. 1. Variation of the apparent dielectric constant with temperature and frequency of the disk barrier layer capacitor of composition BP.

glass. The variations shown in Figs. 1 and 2 are typical of the solder glass. At high temperature both the apparent dielectric constant and the dissipation factor increase because of the ionic conduction in the glass.

### (2) Model for the Barrier Layer Capacitor of Composition BP

The classical Maxwell-Wagner model is used to explain the variation of the apparent dielectric constant and the dissipation factor with respect to frequency at room temperature. As discussed by Von Hippel,<sup>10</sup> the real ( $K'$ ) and imaginary ( $K''$ ) parts of the dielectric constant are given by the following equations:

$$K' = K'_z \left( 1 + \frac{K}{1 + \omega^2 \tau^2} \right) \quad (1)$$

$$K'' = K'_z \left( \frac{\tau}{\omega \tau_1 \tau_2} + \frac{K \omega \tau}{1 + \omega^2 \tau^2} \right) \quad (2)$$

where

$$K = \frac{K'_z - K'_s}{K'_z} \quad (3)$$

The parameters listed in Eqs. (1) to (3) are defined in Table II where values were obtained from Fig. 3. These parameters were used to calculate the real part of the apparent dielectric constant of the barrier layer capacitor. The measured and calculated values of the real part of the apparent dielectric constant

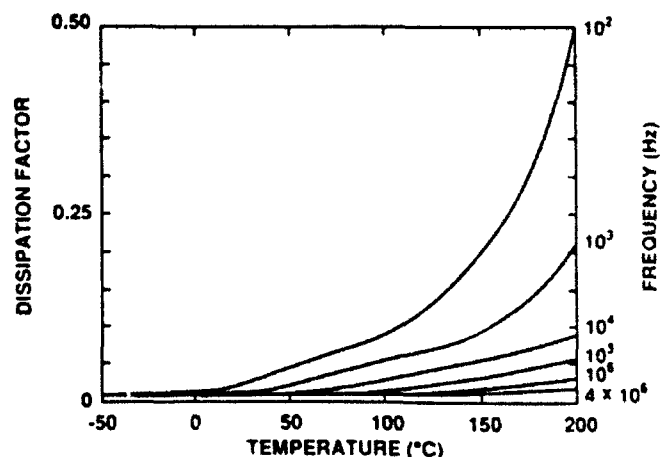


Fig. 2. Variation of the dissipation factor with temperature and frequency of the disk barrier layer capacitor of composition BP.

**Table II. Parameters of the Lumped Circuit for the Barrier Layer Capacitor of Composition BP**

Low-frequency apparent dielectric constant, $K'_1 = 60$
High-frequency apparent dielectric constant, $K'_2 = 30$
Cutoff frequency, $f_{\text{cutoff}} = 2 \times 10^7$ Hz
Relaxation time, $\tau = 7.95 \times 10^{-9}$ s
Relaxation time, $\tau_1 = 1.77 \times 10^{-11}$ s
Relaxation time, $\tau_2 = 9.15 \times 10^{-12}$ s

are plotted as a function of frequency in Fig. 3. There is a good agreement between the measured and calculated values. The increase of the real part of the apparent dielectric constant measured at frequencies greater than  $10^8$  Hz can be attributed to the measuring apparatus.

By assuming the known value of the imaginary part of the apparent dielectric constant ( $K''$ ) at the particular frequency, the relaxation time,  $\tau_2$ , is calculated. Using the known values for  $K'_1$ ,  $\tau_1$ ,  $\tau_2$ , and  $\tau_3$ , the dissipation factor  $\tan \delta$  was calculated using Eq. (4).

$$\tan \delta = \frac{K''}{K'} \quad (4)$$

The measured and calculated values of the dissipation factor are plotted against the frequency as shown in Fig. 4. Here also the calculated values agree very well with the measured values. Again the rise in the measured dissipation factor at high frequencies can be attributed to the instrumentation used.

### (3) Barrier Layer Capacitor of Composition BBP

Disk barrier layer capacitors of composition BBP were fabricated using the glass EO (Table I). Figures 5(a) and (b) are scanning electron micrographs of a sintered disk of composition BBP before and after glass diffusion. In Fig. 5(b), the dark-colored phases are the conducting grains and are surrounded by bright grain boundaries. The grain boundary is probably the glass phase and its thickness is estimated to be  $1 \mu\text{m}$ .

At room temperature, the apparent dielectric constant of the barrier layer capacitor at 1 kHz was about 3000 with a dissipation factor of 0.02. The apparent dielectric constant (3000) of the barrier layer capacitor was much higher than that of the barrier layer capacitor fabricated with composition BP. The variation of the change of capacitance with respect to room temperature is plotted against the temperature measured at 1 kHz in Fig. 6. As we observe from Fig. 6, the barrier layer capacitor has a very stable temperature coefficient of capacitance; the variation in the measured temperature range is less

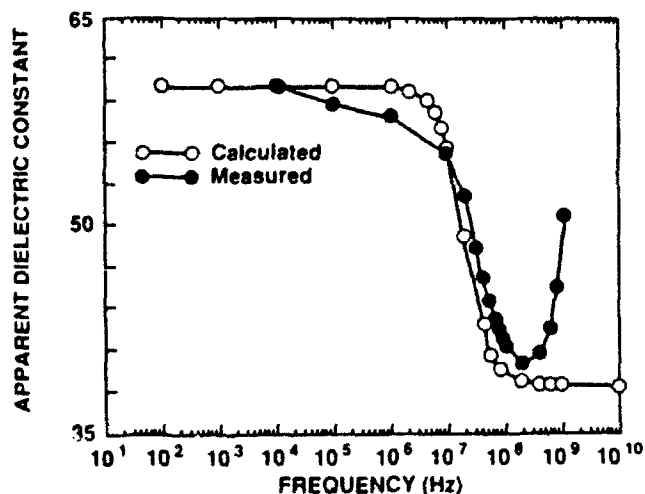


**Fig. 3.** Calculated and measured values of the apparent dielectric constant vs frequency at room temperature for the disk barrier layer capacitor of composition BP.

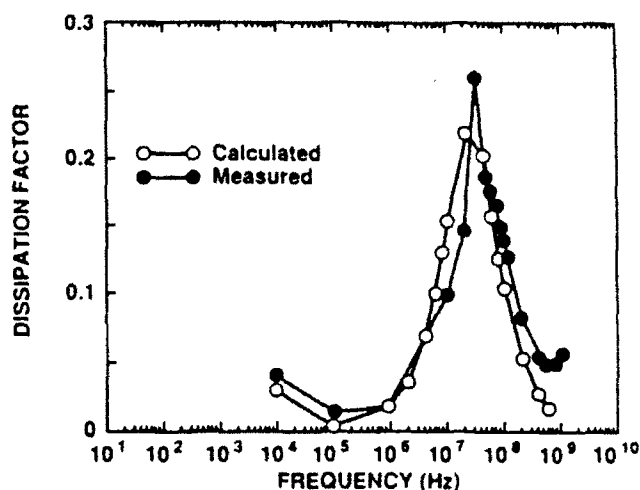


**Fig. 4.** Calculated and measured values of the dissipation factor vs frequency at room temperature for the disk barrier layer capacitor of composition BP.

than 1%. It is to be noted that the variation of capacitance with respect to temperature meets the requirement of Class I type dielectrics. The variation of the apparent dielectric constant with temperature is linear as in the case of the disk barrier layer capacitors made with composition BP, and is attributed to the diffused glass.

In an attempt to determine the reliability of BBP capacitors, the hot insulation resistance was measured at a temperature of  $85^\circ\text{C}$  by applying an electric field of  $100 \text{ V/m}$  for 10 h. The insulation resistance is plotted against temperature in Fig. 7. It is to be noted that the average resistance was  $10^7 \Omega$  for the duration of the measurement run (10 h). The insulation resistance of these barrier layer capacitors did not decrease as rapidly as that of the capacitors prepared from barium titanate ceramics. The dielectric properties exhibited by the barrier layer capacitors of composition BBP are those of the diffused glass.

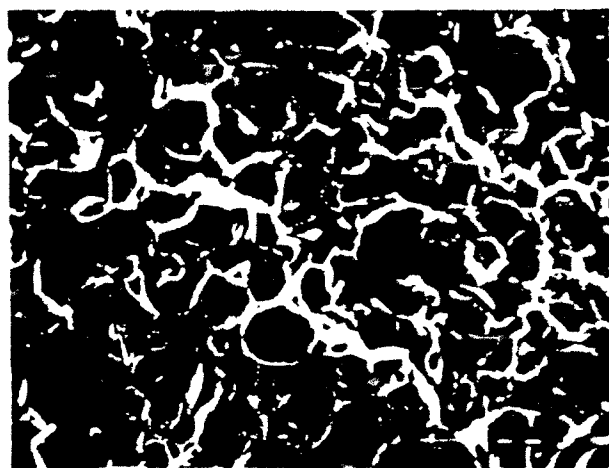
### (4) Model for the Disk Barrier Layer Capacitor of Composition BBP

As mentioned in the experimental procedure, several temperatures and periods of glass diffusion were used to fabricate the barrier layer capacitors. In order to estimate the thickness of the dielectric layer of the disk barrier layer capacitor, the two surfaces of the disk were polished gradually and their surface conductivities were measured using a multimeter (Micronta Digital Multimeter Model No. 22-1984, Fort Worth, TX). When approximately  $100\text{-}\mu\text{m}$  thickness of the surface disk was removed, the polished surface became conducting, as indicated on a multimeter by a short circuit. The other face also became conducting when approximately the same thickness was removed by polishing. This result suggests that the thickness of glass diffusion on either side of the disk barrier layer capacitor is about  $100 \mu\text{m}$ .

The scanning electron micrograph shown in Fig. 5(b) is a cross section of the dielectric layer which shows that the dark conducting grains of  $10\text{-}\mu\text{m}$  size are surrounded by  $1\text{-}\mu\text{m}$ -thick dielectric grain boundaries. Hence, in the disk barrier layer capacitor, we have two grain boundary dielectrics on either side of the disk separated by the conducting bulk ceramic of composition BBP. A schematic diagram of the barrier layer capacitor depicting the grain boundary and surface barrier layers is shown in Fig. 8. Equivalent circuits for a combination of two grain boundary barrier layers adjacent to two surface barrier layers which are separated by a conducting ceramic are shown in Figs. 9(a) and (b). Figure 9(b) is the equivalent lumped circuit diagram of the circuit shown in Fig. 9(a), in which the variable capacitance and resistor represent the dielectric phase of both the grain boundary and the surface barrier layers. The fixed



(a)



(b)

Fig. 5. Scanning electron micrograph of fractured disk of compression BHP capacitor showing grain boundary barrier.

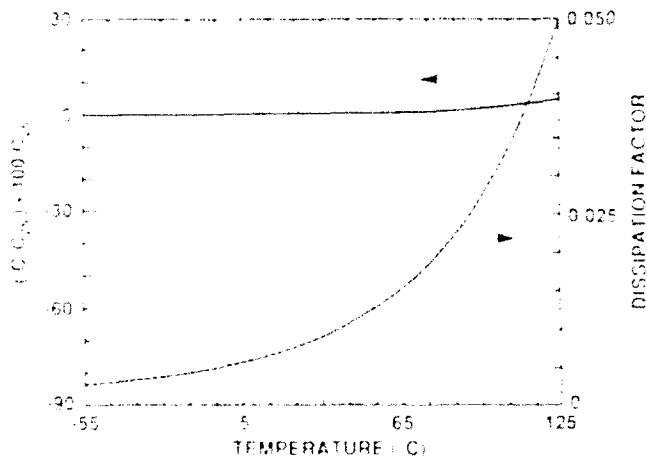


Fig. 6. Change in capacitance with respect to the capacitance and dissipation factor at 20°C vs. temperature at 1 kHz for the disk barrier layer capacitor of compression BHP.

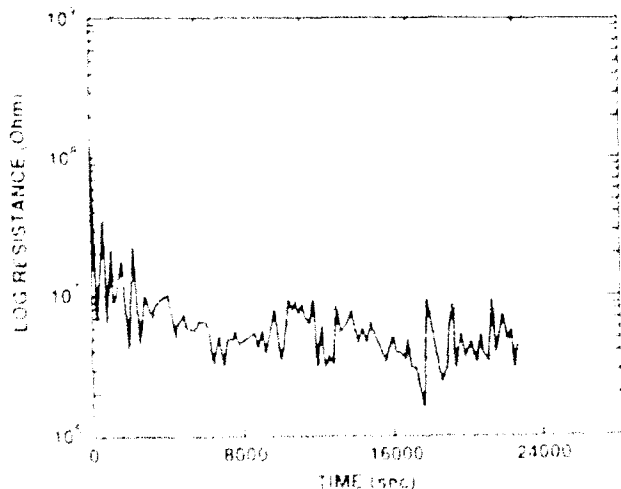


Fig. 7. Behavior of the barrier layer capacitor during the test of the barrier layer capacitor of compression BHP.

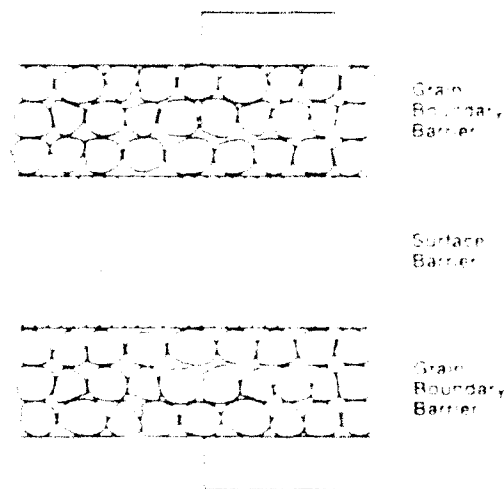


Fig. 8. Schematic diagram of a cross section of the disk barrier layer capacitor of BHP.

capacitor and resistor of Fig. 9(b) represent the conducting phase.

The apparent dielectric constant of the barrier layer capacitor at frequencies in the megahertz range is assumed to be approximately 30, about the same as that of the diffused phase. Because of the skin effect, a very small thickness (micrometers) of the barrier layer is effective in propagating an electrical signal. At moderate frequencies in the megahertz range, where the electrical signal can penetrate through a greater thickness, the grain boundary barrier layers become effective. At low frequencies in the kilohertz range, the capacitor behaves like a surface barrier layer with a dielectric thickness of about 100  $\mu\text{m}$  on each of the major faces of the disc.

According to the model discussed by Wernick,<sup>11</sup> the apparent dielectric constant ( $A$ ) of a barrier layer capacitor is given by

$$A = A_1 \frac{d}{l} + \epsilon$$

where  $A_1$  is the dielectric constant of the dielectric phase and  $l$  is the thickness of the conducting phase. The estimated grain size and the thickness of the grain boundaries are 0.1  $\mu\text{m}$  and 1  $\mu\text{m}$ , respectively. Assuming the dielectric constant of the dielectric

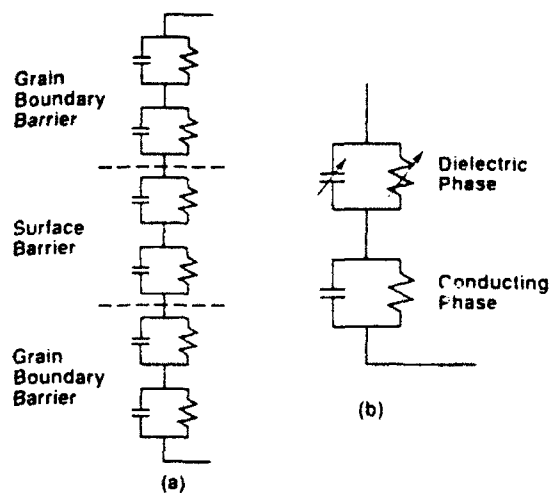


Fig. 9. (a) Equivalent circuit of the disk barrier layer capacitor and (b) its lumped circuit diagram.

phase is the same as that of glass (30) and considering only the contributions of grain boundaries, the apparent dielectric constant of the boundary layers can be calculated as 300 using Eq. (5).

At low frequency, the barrier layer capacitor behaves like a surface barrier layer with a dielectric thickness of 200  $\mu\text{m}$ , as explained earlier. Applying Eq. (5) and using  $d_c = 1800 \mu\text{m}$  and  $d_s = 700 \mu\text{m}$  and  $K_s = 300$ , the apparent dielectric constant at low frequency is calculated to be 2700, which agrees very well with the measured apparent dielectric constant shown in Fig. 10.

The calculated apparent dielectric constant and dissipation factor are plotted against frequency for the barrier layer capacitor in Fig. 11. Since the barrier layer capacitor has two contributions to the frequency response of the apparent dielectric constant and dissipation factor, it is suggested that the frequency response has two cutoff frequencies. The cutoff frequency can be calculated using

$$f_{\text{cutoff}} = \frac{\sigma_1 d_1}{2\pi\epsilon_0 K_s d_2} \quad (6)$$

where  $K_s$  is the dielectric constant of the dielectric medium,  $\epsilon_0$  is the permittivity of the free space,  $\sigma_1$  is the conductivity of the conducting medium, and  $d_1$  and  $d_2$  are the thicknesses of conducting and dielectric media, respectively. The cutoff frequency for the grain boundary barrier behavior at high frequency was calculated to be  $4.4 \times 10^9$  Hz using Eq. (4) and

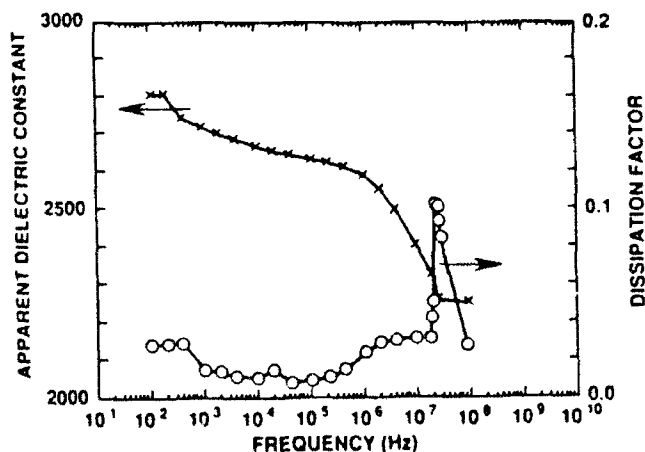


Fig. 10. Measured values of the apparent dielectric constant and dissipation factor vs frequency at room temperature for the disk barrier layer capacitor of composition BBP.

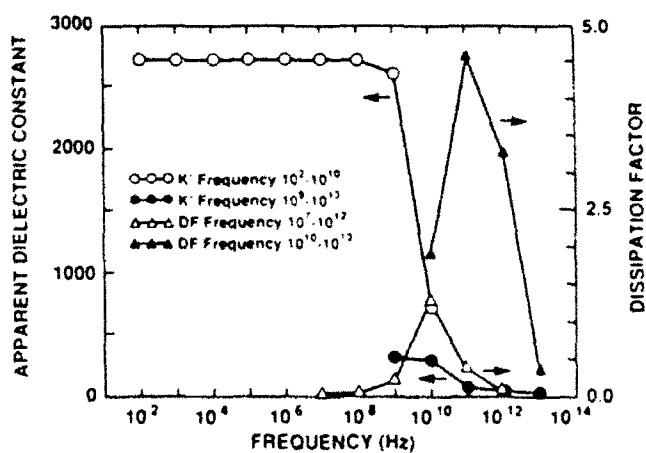


Fig. 11. Calculated values of the apparent dielectric constant and dissipation factor vs frequency at room temperature for the disk barrier layer capacitor of composition BBP.

assuming  $K_s = 30$ ,  $\sigma_1 = 6.67 (\Omega\text{-cm})^{-1}$ ,  $d_1 = 1 \mu\text{m}$ , and  $d_2 = 10 \mu\text{m}$ . Similarly, the cutoff frequency for the surface barrier layer at low frequency is calculated to be  $4.52 \times 10^{10}$  Hz by taking  $K_s = 300$ ,  $\sigma_1 = 6.67 (\Omega\text{-cm})^{-1}$ ,  $d_1 = 100 \mu\text{m}$ , and  $d_2 = 1800 \mu\text{m}$ .

The real part of the apparent dielectric constant for the barrier layer capacitor in the frequency range  $10^2$  to  $10^{10}$  Hz, in which the surface barrier layer behavior is assumed to be predominant, was calculated as a function of frequency using Eq. (2) assuming  $K_s = 2700$ ,  $K_s = 300$ , and  $\tau = 3.56 \times 10^{-11}$  s. Similarly, the real part of the apparent dielectric constant in the frequency range  $10^9$  to  $10^{11}$  Hz, in which the grain boundary barrier layer behavior is assumed to be contributing to the real part of apparent dielectric constant, was also calculated using Eq. (2) and assuming  $K_s = 300$ ,  $K_s = 30$ , and  $\tau = 3.95 \times 10^{-12}$  s.

The dissipation factor for both the grain boundary and the surface barrier layer is calculated as a function of frequency using Eq. (3) and parameters  $K_s$ ,  $K_s$ , and  $\tau$  specified earlier. The calculated apparent dielectric constant and dissipation factor are plotted as a function of frequency in Fig. 11. At a frequency of  $10^{10}$  Hz the contribution of the surface barrier layer to the apparent dielectric constant drops off and then, at a frequency of  $10^{11}$  Hz, the grain boundary barrier layer contribution drops off, leaving only the contribution of the diffused glass.

Figure 10 shows the measured values of the apparent dielectric constant and the dissipation factor for the barrier layer capacitors. Comparing Figs. 10 and 11, we find that at low frequency both the measured and calculated values agree very well. The difference between the measured and calculated values at high frequency can be explained as follows.

In our calculation, we assumed the dielectric constant of the barrier layer to be the same as the dielectric constant of the diffused glass ( $\sim 30$ ). The glass diffused in the barium bismuth plumbate ceramic may have a dielectric constant different from 30. Secondly, the conductivity of the conducting ceramic phase is assumed to be constant in both the surface and grain boundary barrier layers. When the conducting barium bismuth plumbate ceramic is subjected to the glass diffusion heat treatment, the conductivity may change. Thirdly, the inductance of the device becomes very important at high frequency ( $10^{10}$  Hz) especially when the reflectance method of measuring the dielectric constant is employed. In the Maxwell-Wagner model, the inductance of the device is not taken into consideration when calculating the real and imaginary parts of the apparent dielectric constant. In practice, even materials with dielectric constants as low as 150 exhibit enormous increases in dielectric constants at this frequency due to high inductance. One would expect this effect to be more prominent when measuring the dielectric properties of the device which has an apparent dielectric of 2780. The measured apparent dielectric

constant and dissipation factor shown in Fig. 10 increase enormously at high frequency ( $10^9$  Hz) as a result of this effect. The measured apparent dielectric constant does not decrease to a very low value (300) predicted by the model (Fig. 11). The considerable increase in the measured dielectric at high frequency ( $10^9$  Hz) may have affected the value at low frequency ( $10^7$  Hz). The peak in the measured dissipation factor (Fig. 10) may be attributed to the instrumentation used.

### III. Conclusion

This work showed that barrier layer capacitors can be fabricated using highly conducting ceramics barium plumbate and bismuth plumbate. These capacitors had a high frequency dispersion (megahertz) of the apparent dielectric constant, a low temperature coefficient of capacitance (TCC) (<1%), and maintained a high insulation resistance under accelerated reliability tests in which the capacitors were subjected to high temperature and high field simultaneously.

The frequency dependency of the capacitance was explained by the Maxwell-Wagner model and experimental data fitted fairly well with the predicted values. As predicted by the Maxwell-Wagner model, the dispersion frequency of the capacitors was in the megahertz range.

The simple processing and low firing temperatures make it possible to manufacture the barrier layer capacitors inexpensively. The high apparent dielectric constant and low TCC properties make these capacitors an alternative to conventional barium titanate low-TCC capacitors.

**Acknowledgments:** We would like to acknowledge the help of Paul Moses for the temperature coefficient measurements, Dean Anderson for the hot insulation resistance measurements, and Frank Steele for discussions of ceramic composition.

### References

- "Y. Bakabe, "Recent Progress on Multilayer Ceramic Capacitors", pp. 119-29 in Proceedings of the MRS International Meeting on Advanced Materials (Tokyo, Japan, May 31-June 1, 1988), Vol. 10, *Multilayers*, Edited by M. Doiama, S. Somya, R. P. H. Chang, R. Yamamoto, and T. Ohno, Materials Research Society, Pittsburgh, PA, 1989.
- "R. M. Glaister, "Barrier-Layer Dielectric," *Proc Inst Electr Eng, Part B*, **109B** (22) 423-31 (1961).
- "S. Waku, "Studies on the Boundary Layer Ceramic Capacitor," *Rev Electr Commun Lab*, **15**[9-10] 689-715 (1967).
- "M. Fujimoto and W. D. Kingery, "Microstructures of SrTiO<sub>3</sub> Internal Boundary Layer Capacitors During and After Processing and Resultant Electrical Properties," *J. Am Ceram Soc*, **64** [4] 171-73 (1985).
- "R. Wernicke, "Influence of Microstructure on the Electrical Properties of Intergranular Capacitors," *Ber Dtsch Keram Ges*, **55** [7] 356-58 (1978).
- "B. V. Hiremath, "Barrier Layer Ceramic Dielectric Capacitor Containing Barium Plumbate," U.S. Pat. No. 4,761,711, 1988.
- "H. D. Park and D. A. Payne, "Characterization of Internal Boundary Layer Capacitors", pp. 242-53 in *Advances in Ceramics*, Vol. 1, Edited by L. M. Levinson, American Ceramic Society, Columbus, OH, 1981.
- "R. R. Roup and C. E. Buler, U.S. Pat. No. 2,520,376, August 29, 1950.
- "F. Steele, "An Investigation of Barium Metaplumbate as a Ceramic Electrode for Ceramic Capacitors", M.S. Thesis, Pennsylvania State University, University Park, PA, 1985.
- "A. Von Hippel, *Dielectric Materials and Applications*, MIT Press, Cambridge, MA, 1966.
- "G. Goodman, "Capacitors Based on Ceramic Grain Boundary Barrier Layers—A Review", pp. 215-31 in *Advances in Ceramics*, Vol. 1, Edited by L. M. Levinson, American Ceramic Society, Columbus, OH, 1981.
- "L. R. Gilbert, "Bulk and Sputtered Thin Film Ba(Ph)O<sub>3</sub>—A Ceramic Superconductor", Ph.D. Thesis, Pennsylvania State University, University Park, PA, 1979.
- "T. W. Dakin, "Microwave Dielectric Measurements," *J. Appl. Phys*, **18** [4] 789-96 (1947).
- "M. A. Stuchly, "Permittivity Measurements at Microwave Frequencies Using Lumped Elements," *IEEE Trans. Instrum. Meas.*, **IM-23**, 56-62 (1974).
- "R. Wernicke, "Formation of Second-Phase Layers in SrTiO<sub>3</sub> Boundary Layer Capacitors", pp. 261-11 in *Advances in Ceramics*, Vol. 1, Edited by L. M. Levinson, American Ceramic Society, Columbus, OH, 1981.

**APPENDIX 46.**

# GRAIN SIZE EFFECT ON THE DIELECTRIC PROPERTIES OF STRONTIUM BARIUM TITANATE

U. Kumar, S. F. Wang, S. Varanasi, and J. P. Dougherty

Center for Dielectric Studies  
Materials Research Laboratory  
The Pennsylvania State University  
University Park, PA 16802

**Abstract:** In this paper, the grain size effect observed on the dielectric properties of  $\text{Sr}_{0.2}\text{Ba}_{0.8}\text{TiO}_3$  (SBT) ceramic is reported. For this study, SBT powder prepared by a hydrothermal procedure was used. A porous ceramic was prepared by sintering the powder compacts between  $1100^\circ\text{C}$ - $1350^\circ\text{C}/5\text{min}$ - $10\text{h}$ , either by conventional sintering or by 'fast firing'. When the average grain size of the ceramic was between  $0.75$ - $1.2\ \mu\text{m}$ , the room temperature dielectric constant peaks to  $5500$ - $6000$ . In porous fine grain ceramic also, classic P vs. E hysteresis behavior is observed.

## Introduction

Grain size effects on the dielectric properties of  $\text{BaTiO}_3$  has been an active area of research over three decades. Ever since, Kniekamp and Heywang [1] reported the observation of anomalously high room temperature dielectric constant in  $\text{BaTiO}_3$  ceramic with an average grain size of  $1\ \mu\text{m}$ , several research articles appeared in the literature. Careful literature review indicate that the observed grain size effect is a strong function of several external and a few internal variables. Effect of chemical purity, preparation procedure, initial particle size distribution of the powder, final grain size distribution, resistivity of the grains and the grain boundaries and the density of the ceramic etc., should be considered as external contributions to the dielectric anomaly. Through careful preparation it is possible to minimize the effect of external variables.

While discussing the intrinsic effect, it is necessary to consider the boundary conditions very carefully. Buessem et al. [2] prepared high density ceramic with varying grain sizes. SEM analysis of the fine grain ceramic showed fewer ferroelectric domains as compared to coarse grain ceramic. It is well known that in a coarse grain ceramic, the volume change associated with the cubic to tetragonal phase transition is minimized through domain formation. In fine grain ceramic, grains without multi-domains will induce stress of complex nature on other grains. Anomalous increases in the dielectric constant of fine grain ceramic are explained as a direct consequence of the stress.

Arlt et al., [3] on the other hand, observed that the domain size is a strong function of grain size. Through SEM and TEM observations, they observed an increase in the domain density when the average grain size of the ceramic was between  $1\ \mu\text{m}$  and  $10\ \mu\text{m}$ . Additionally, the domain size reduced as a function of grain size. They proposed that the increase in room temperature dielectric constant is at least partially due to the increase in domain wall density.

Shaikh et al., [4] observed similar anomaly in a porous ceramic. Effect of density on the magnitude of dielectric constant is discussed in a paper by wa Gachigi et al., [5] in this issue.

In fine grain  $\text{BaTiO}_3$  ceramic, the tetragonal to orthorhombic transition occurs nearer to  $25^\circ\text{C}$  instead of  $0.5^\circ\text{C}$ . Some of the observations, such as the difference in domain size, splitting of  $\langle 200 \rangle$  peak in XRD patterns are expected to be influenced by the presence of the orthorhombic phase.

To minimize the complications due to the orthorhombic phase, it is desirable to investigate the grain size effect in  $\text{BaTiO}_3$ -based solid solutions. Moreover, understanding the size effect in commercially important solid solutions such as  $\text{Sr}_{1-x}\text{Ba}_x\text{TiO}_3$ ,

$\text{Ba}(\text{Zr}_x\text{Ti}_{1-x})\text{O}_3$  etc., is essential to tailor the microstructure of fine grain thin layer MLCs and thin films. In this paper, we describe the grain size effect on the dielectric properties of  $\text{Sr}_{0.2}\text{Ba}_{0.8}\text{TiO}_3$  ceramic. We have used conventional and 'fast firing' schedules to prepare ceramics with differing densities. The size effects were studied through microstructure, XRD, dielectric, and P vs. E hysteresis behavior.

## Experimental

For this study,  $\text{Sr}_{0.2}\text{Ba}_{0.8}\text{TiO}_3$  powder, prepared by hydrothermal procedure, (Cabot Corporation, Boyertown, PA) was used. The B.E.T. surface area of the powder is  $14.6\ \text{m}^2/\text{gm}$ . The SEM micrograph of the powder (Fig. 1) clearly shows the size uniformity.

The powder was blended with appropriate amount of PVA solution and glycerol. Pellet preparation and binder evaporation procedures are elaborated in Ref. [6]. Binder removed pellets were sintered between  $1100^\circ\text{C}$  and  $1350^\circ\text{C}$  for  $5\text{min}$ - $10\text{h}$  in a clean furnace. For conventional firing, heating and cooling rates were maintained as  $400^\circ\text{C}/\text{h}$ . For 'fast firing', the samples were heated to  $950^\circ\text{C}$  at a rate of  $400^\circ\text{C}/\text{h}$ , and then to the soak temperature at  $1000^\circ\text{C}/\text{h}$ . They were cooled to room temperature with a similar schedule. Bulk density was measured only when the density of the sintered samples were greater than 90% theoretical. For the rest of the samples, geometrical densities are reported. Procedure for dielectric and P vs. E measurements are elaborated in Ref. [7].

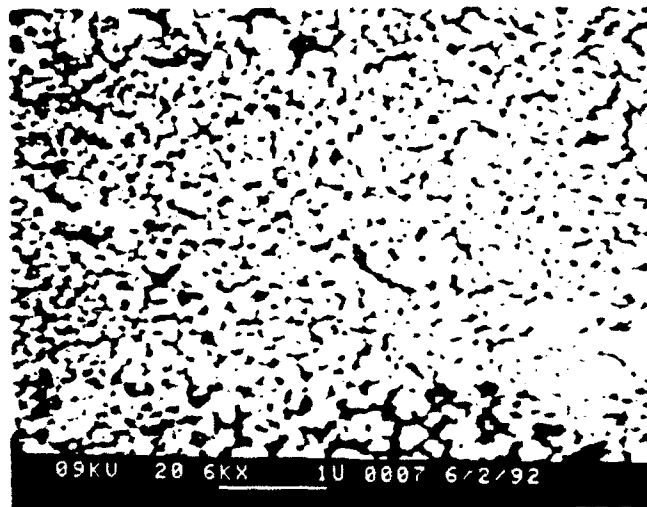


Fig. 1. SEM micrograph of 'as received' SBT powder.

## Results and Discussions

Densities of the sintered pellets are listed in Table 1. Typical microstructures of the samples sintered below 1250°C are shown in Fig. 2. As the particle size distribution of the starting powder was narrow, the grain size distribution of the sintered ceramic also remained narrow. But when the sintering temperature was raised beyond 1250°C, abnormal grain growth occurred. Thus it was not possible to prepare samples with uniform grain size in the range of 3-10 μm.

In Fig. 3, the temperature effect on the dielectric properties are compared. These K vs T plots are not compensated for porosity. Higher room temperature dielectric constant observed in samples sintered at 1200°C with an average grain size of 0.9 μm, and 87% of theoretical density (Table 1), clearly shows the existence of grain size effect in SBT very similar to that observed in pure BaTiO<sub>3</sub>. Dielectric constant values at room temperature and at T<sub>c</sub> of all the samples are compared in Table 1. To compensate the values for porosity, Botcher's equation was used

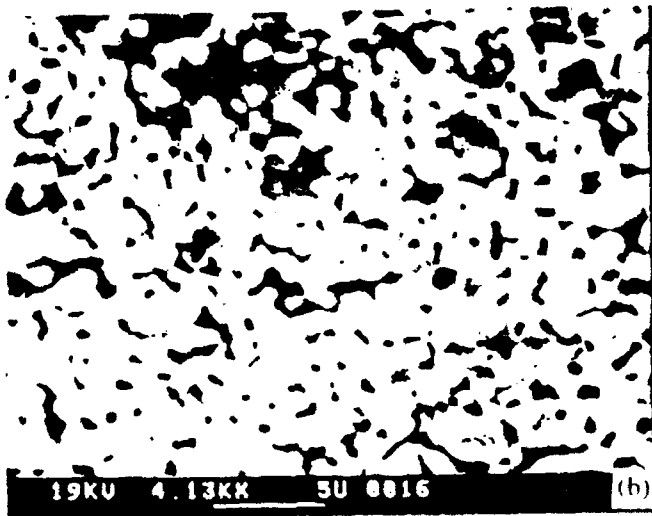
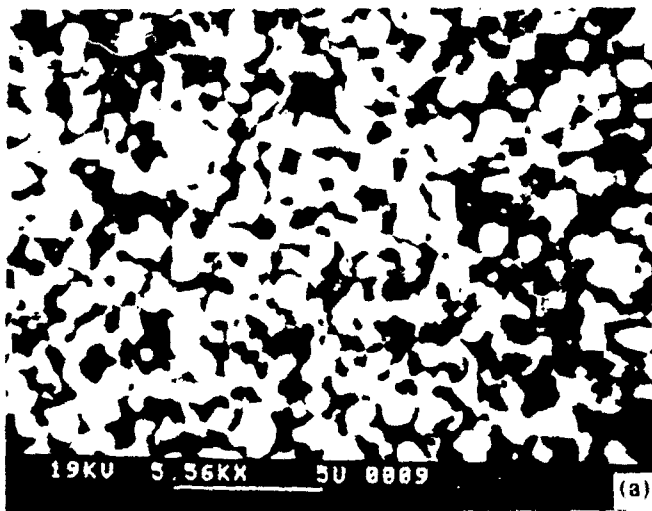


Fig. 2. Typical microstructure of SBT ceramic sintered at (a) 1100°C/10h and (b) 1200°C/2h.

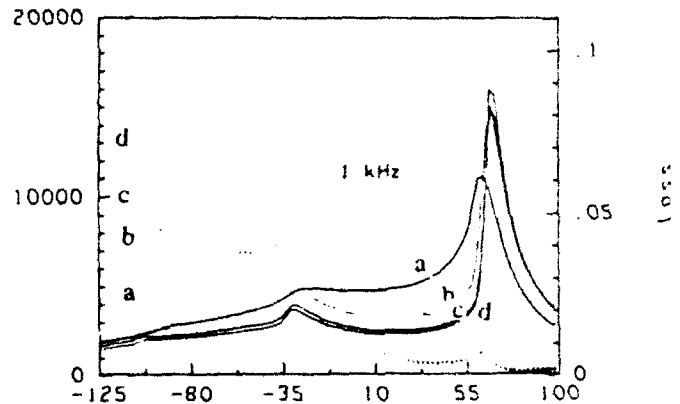


Fig. 3. Dielectric properties of SBT ceramic sintered at (a) 1200°C/2h, (b) 1300°C/2h, (c) 1350°C/2h and (d) 1350°C/10h. Solid lines are dielectric constant and dotted lines are dielectric loss data measured at 1 kHz.

Table 1. Physical and dielectric properties of SBT ceramic

Sint. Temp (°C/h)	Ave. gs (μm)	Dens (% theo)	K <sub>RT</sub> (obs.)	K <sub>RT</sub> (Cal.)	K <sub>at T<sub>c</sub></sub> (Obs.)	K <sub>at T<sub>c</sub></sub> (Cal.)	Curie Cons x 10 <sup>5</sup> °C	T <sub>c-t</sub> (°C)	T <sub>f-o</sub> (°C)	Pr (μC/cm <sup>2</sup> )	E <sub>c</sub> (KV/cm)
1100/4	0.7	65.87	2360	4840	4480	9180	1.56	61			
1100/6	0.75	68.26	2880	5500	5650	10800	1.73	63			
1100/10	1.25	69.45	3775	6260	7280	12080	1.54	62	-20	2.1	1080
1150/5	0.9	68.87	3095	5800	7720	14475	1.78	65	-24		
1175/0.5		74.64	3700	5970	7190	11600	1.47	61	-22	2.95	1700
1200/0.5	0.7	76.17	3850	5990	9800	13360	1.49	62	-19	1.98	1480
1200/2	0.9	87.17	4810	5970	11160	13800	1.40	63	-24	3.88	1125
1300/2	>8.0	96.34	5200	3390	14750	15600	1.51	67	-26	4.36	590
1350/2	>10.0	97.07	2480	2590	16000	18740	1.50	66	-28	4.70	530
1350/10	>10.0	97.19	2310	2890	15050	15700	1.47				
1255/(5mF)	1.0	72.53	3270	5570	8630	14680	1.70	64	-25		
1275/(5mF)	1.2	78.52	3580	5280	10075	14870	1.49	64	-25	2.44	870
1300/(5mF)	1.2	80.92	3660	5400	11580	16220	1.50	65	-25	3.44	840

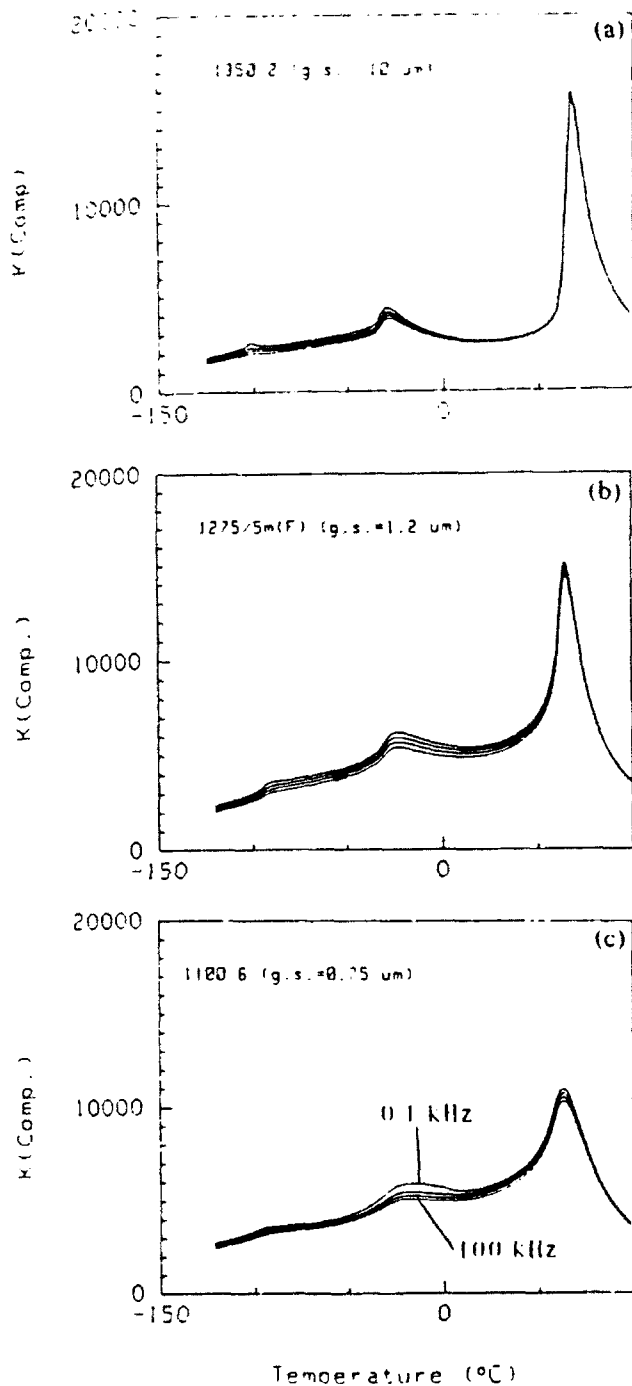


Fig. 4. Effect of measuring frequency on the dielectric properties of SBT ceramic sintered at (a) 1350°C/2h, (b) 1275°C/5min (Fast fired), and (c) 1100°C/6h; measuring frequencies were 0.1, 1, 10, and 100 kHz.

Comparing the porosity corrected values, it is clear that a peak room temperature dielectric constant of 5500-6000 is observed when the average grain size of the ceramic is between 0.75-1.2  $\mu\text{m}$ . In Fig. 4a,b, and c, the frequency effect on the dielectric constant of ceramic with differing grain sizes are plotted. Above  $T_c$ ,  $K$  vs  $T$  behavior is nearly independent of measuring frequency in all the cases. In Table 1, Curie constant of these samples are compared. As seen the magnitude falls within a narrow range of  $1.4-1.7 \times 10^5$  ( $^\circ\text{C}$ ). In Fig 4b and c, fine grain ceramic show smearing of dielectric peak at all three transition temperatures. In table 1, two of the transition temperatures are listed. When the average grain size of the ceramic is reduced from 10  $\mu\text{m}$  to 0.7  $\mu\text{m}$ , the cubic to tetragonal transition temperature decreases from 67 $^\circ\text{C}$  to 62 $^\circ\text{C}$ , whereas the tetragonal to orthorhombic transition temperature raises from -28 $^\circ\text{C}$  to -19 $^\circ\text{C}$ . Since the dielectric peak corresponding to the orthorhombic to rhombohedral transition occurs over a large temperature range in fine grain ceramic, these values are not tabulated.

In Fig 5, the  $P$  vs.  $E$  behavior of three samples is compared. As seen, in fine grain ceramics, the induced polarization reduces systematically. But, since the density of these samples are not the same, only the general behavior should be considered for comparison. Even in a fine grain porous ceramic, appearance of the classic  $P$  vs.  $E$  hysteresis is particularly noticeable. In Table 1,  $P_r$  and  $E_c$  values calculated from the hysteresis curves are listed.

In Fig 6 a and b, the polished and etched microstructures of two of the sintered ceramics are shown. The samples were polished slowly and carefully, so that the surface temperature of the samples are maintained always nearer to room temperature. To get a representative domain structure of the bulk, about 0.1-0.2 mm thick surface layer was removed before polishing. In Fig 6b, domains in the fine grain ceramic is very clearly seen. Since the density of the samples fired at temperatures below 1300 $^\circ\text{C}$  were low, it was not possible to polish them properly. At present even though the existence of multi-domains in fine grain ceramic is clearly demonstrated, it is necessary to prepare dense ceramic to quantify the domain size and the domain density as a function of grain size.

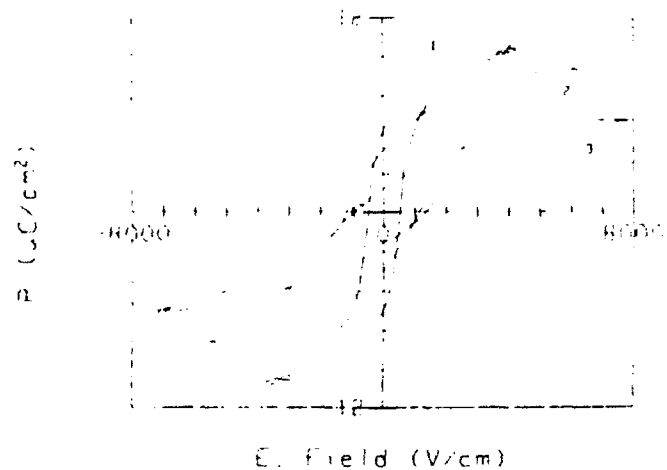


Fig. 5.  $P$  vs.  $E$  hysteresis behavior of SBT ceramic sintered at (1) 1350°C/10h, (2) 1200 $^\circ\text{C}$ , and (3) 1100°C/10h.

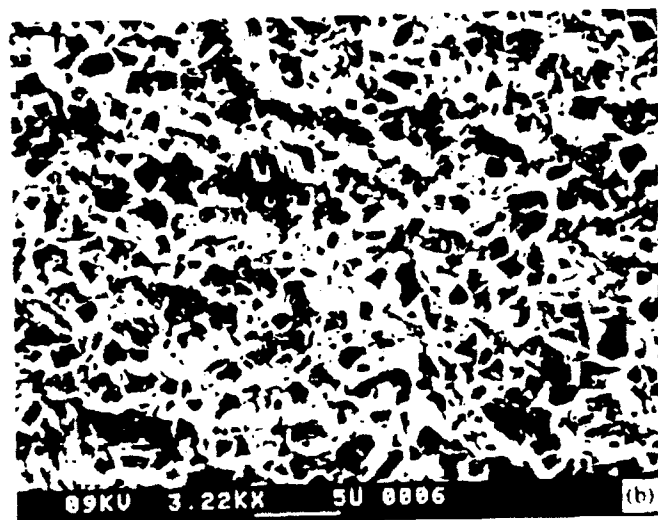


Fig. 6. Polished and etched microstructure of SBT ceramic sintered at (a) 1300°C/10h, and (b) 1300°C/10 min.

### Conclusions

Based on the experimental observations, the following conclusions are drawn:

1. When the grain size of the ceramic is between 0.75-1.2  $\mu\text{m}$ , the  $K_{RT}$  values peaks to 5500-6000.
2. The Curie constant of the ceramic is relatively independent of the grain size.
3. In fine grain ceramics, suppression of  $T_c$  and enhancement of low temperature transitions are clearly seen.
4. Fine grain ceramics also show classic P vs. E hysteresis behavior.
5. Etched and polished microstructure of fine grain porous ceramic show multi-domain characteristics.

To quantify the results, it is necessary to prepare dense ceramics with differing average grain sizes ranging from 0.1  $\mu\text{m}$  to 10  $\mu\text{m}$  with narrow distribution.

**Acknowledgements:** Authors gratefully acknowledge the financial support from Cabot Corporation of Boyertown, PA and the Ben Franklin Partnership Program of the Commonwealth of PA. Authors also acknowledges the technical support provided by Mingfeng Song.

### References

- [1] H. Kniekamp, and W. Heywang, "Depolarization effects in polycrystalline  $\text{BaTiO}_3$ ," *Z. Angew. Phys.*, Vol. 6, p.385-390, (1954).
  - [2] W. R. Buessem, L. E. Cross, and A. K. Goswami, *J. Am. Ceram. Soc.*, vol. 49, p. 33 (1966).
  - [3] G. Arlt, D. Hennings, and G. deWith, "Dielectric properties of fine grained  $\text{BaTiO}_3$ ," *J. Appl. Phys.*, Vol. 58, p.1619-1625 (1984).
  - [4] A.S. Shaikh, R. W. Vest, and G. M. Vest, "Dielectric properties of ultrafine grained ceramic," *IEEE Trans. on Ultrasonic, Ferroelectrics and Frequency Control*, Vol. 36, no.4, p.407-412 (1989).
  - [5] K. wa Gachigi, U. Kumar, and J. P. Dougherty, "Grain size effects on  $\text{BaTiO}_3$ ," this issue.
  - [6] U. Kumar, S. F. Wang, and J. P. Dougherty, "Preparation of dense ultra-fine grain barium titanate -based ceramics," this issue.
  - [7] S. F. Wang, U. Kumar, W. Huebner, P. Marsh, H. Kunkel, and C. Oakley, "Grain size effect on the induced piezoelectric properties of 0.90PMN-0.10PT ceramic," this issue.
- And the references in [1]-[7]

**APPENDIX 47**

PREPARATION OF DENSE ULTRA-FINE GRAIN  
BARIUM TITANATE-BASED CERAMICS

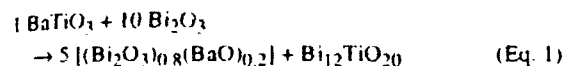
U. Kumar, S.F. Wang, and J.P. Dougherty

Materials Research Laboratory  
The Pennsylvania State University  
University Park, PA 16802

**Abstract.** Recently, we have sintered hydrothermal BaTiO<sub>3</sub> with 3-5 wt% Bi<sub>2</sub>O<sub>3</sub> to very high densities at 850°C. In this paper, new results on the effect of lower concentrations of Bi<sub>2</sub>O<sub>3</sub> on the densification and the dielectric properties of the BaTiO<sub>3</sub> ceramic are discussed. As an expansion of this work, hydrothermal Sr<sub>0.2</sub>Ba<sub>0.8</sub>TiO<sub>3</sub> was sintered with 0-5 wt% Bi<sub>2</sub>O<sub>3</sub> between 850-1250°C. When 5 wt% Bi<sub>2</sub>O<sub>3</sub> was added, the powder compacts sintered to a bulk density of >5.2 gms/cc, at 950°C. The room temperature dielectric constant of this ceramic was 1500, and K vs. T plot followed the ZSU industrial specification.

**Introduction**

In a recent paper [1], by comparing the effect of Bi<sub>2</sub>O<sub>3</sub> on the sintering behavior of high purity BaTiO<sub>3</sub> powders prepared by different procedures, good sinterability of hydrothermal BaTiO<sub>3</sub> at temperatures as low as 850°C was demonstrated. By performing XRD and DTA measurements on these mixtures, the following reaction sequence was identified:



As the reaction products melt at 717°C and 847°C respectively, good densification occurs at low temperatures through liquid phase sintering.

In a different paper [2], the effect of Bi<sub>2</sub>O<sub>3</sub> addition on the microstructural development and the dielectric properties of the sintered ceramic was discussed. For this work, hydrothermal BaTiO<sub>3</sub> powder compacts with 3, 5, and 7 wt% Bi<sub>2</sub>O<sub>3</sub> were sintered between 750°-950°C/2h.

In this paper, the results of the latest studies on the effect of Bi<sub>2</sub>O<sub>3</sub> addition on the densification, microstructure development, and the dielectric properties of the hydrothermal BaTiO<sub>3</sub> ceramic are explained. The result and discussion section of this paper is divided into four parts. In the first part, some of the physical and electrical characteristics of the ceramic are reviewed. In the second part, the effect of smaller quantities of Bi<sub>2</sub>O<sub>3</sub> on the densification and dielectric properties of the BT ceramics are discussed. In the third part, the effect of Bi-addition during the hydrothermal process on the microstructural development is discussed. In the final part, the effect of Bi<sub>2</sub>O<sub>3</sub> on the properties of Ba<sub>0.8</sub>Sr<sub>0.2</sub>TiO<sub>3</sub> is analyzed.

**Experimental**

The surface area of the as received hydrothermal powders (Cabot Corporation, Boyer Town, PA) were measured by BET technique. To prepare the pellets, the hydrothermal powders were mixed with 0-5wt% of Bi<sub>2</sub>O<sub>3</sub> (Johnson Matthey, Seabrook, NH) in an agate mortar and pestle. Several 1/2" disks were prepared in a steel die, by applying uniaxial pressure (30000-35000 psi) at room temperature. Pellets with about 53% green densities were prepared by using 1.5-1.7 wt% PVA and 1.5-2.0wt% glycerol as binder and plasticizer. After binder evaporation, the green pellets were sintered between 750-1250°C/0.5-2h in a closed crucible. The bulk density of the well sintered disks were measured by noting the weight loss in Xylene. Fractured microstructure of the ceramic was analyzed with an SEM (ISI-SKI 130, Akashi Beam Technology Corp., Tokyo, Japan). The dielectric properties of the ceramic disk samples were measured using a computer controlled LCR bridge (4274A, Hewlett Packard, CO) system.

**Results and Discussion**

Physical characteristics of the as received powders used for this study are listed in Table 1.

Table 1. The properties of BaTiO<sub>3</sub> Powders.

I.D.	Composition	Additions	S.A (m <sup>2</sup> /gm)	L.O.I (wt%)
BT1	BaTiO <sub>3</sub>	-----	8.54	1.8
BT2	BaTiO <sub>3</sub>	200ppm of Nb	7.96	1.4
BT3	BaTiO <sub>3</sub>	0.28wt% Bi <sub>2</sub> O <sub>3</sub>	7.59	-----
BT4	BaTiO <sub>3</sub>	3wt% Bi <sub>2</sub> O <sub>3</sub>	8.17	-----
BST20	Ba <sub>0.8</sub> Sr <sub>0.2</sub> TiO <sub>3</sub>	-----	14.5	0.9

**Part I:**

The hydrothermal BaTiO<sub>3</sub> sinters to high densities at low temperatures. In Fig. 1, the shrinkage profiles of hydrothermal and non-hydrothermal high purity BaTiO<sub>3</sub> powder compacts with 5 wt% Bi<sub>2</sub>O<sub>3</sub> are compared. In this figure, good densification of hydrothermal powder compacts is clearly seen to occur at about 750°C. Typical microstructures of the sintered compact are shown in Fig. 2. When the samples were sintered between 750-1250°C with 3, 5, and 7 wt% Bi<sub>2</sub>O<sub>3</sub>, irrespective of the sintering temperature and the flux concentration, the average grain size of the ceramic remained as 0.15-0.2 μm, which was also the initial particle size of BaTiO<sub>3</sub> powder. Typical dielectric properties of the sintered ceramics are given in Fig. 3. A broad transition at around 110°C, and the suppression of other lower temperature transitions are typical of this fine grain ceramic. Though the dielectric peak corresponding to cubic to tetragonal transition is clearly detected, room temperature XRD patterns of these ceramic did not show clear splitting in <200> peaks.

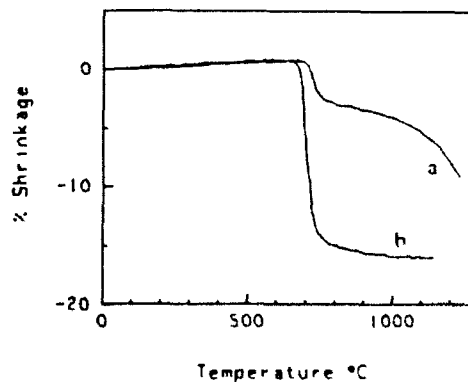


Fig. 1 Shrinkage profiles of (a) high purity BaTiO<sub>3</sub> (Transelco) + 5wt% Bi<sub>2</sub>O<sub>3</sub> and (b) BT2 + 5wt% Bi<sub>2</sub>O<sub>3</sub>

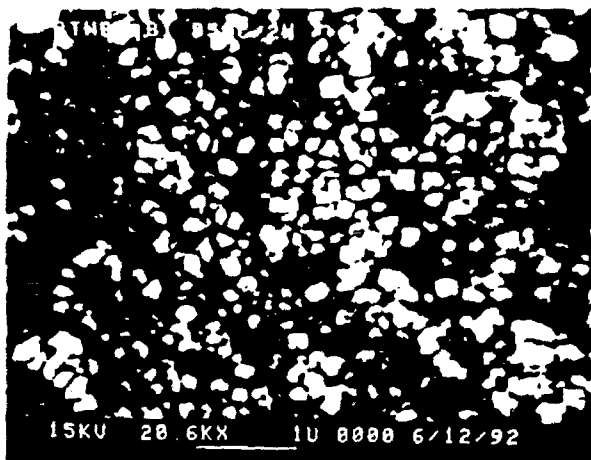


Fig. 2 Typical microstructure of BT sintered with  $\text{Bi}_2\text{O}_3$ . This microstructure represent the fracture surface of BT2 with 7wt%  $\text{Bi}_2\text{O}_3$  sintered at  $850^\circ\text{C}/2\text{h}$ .

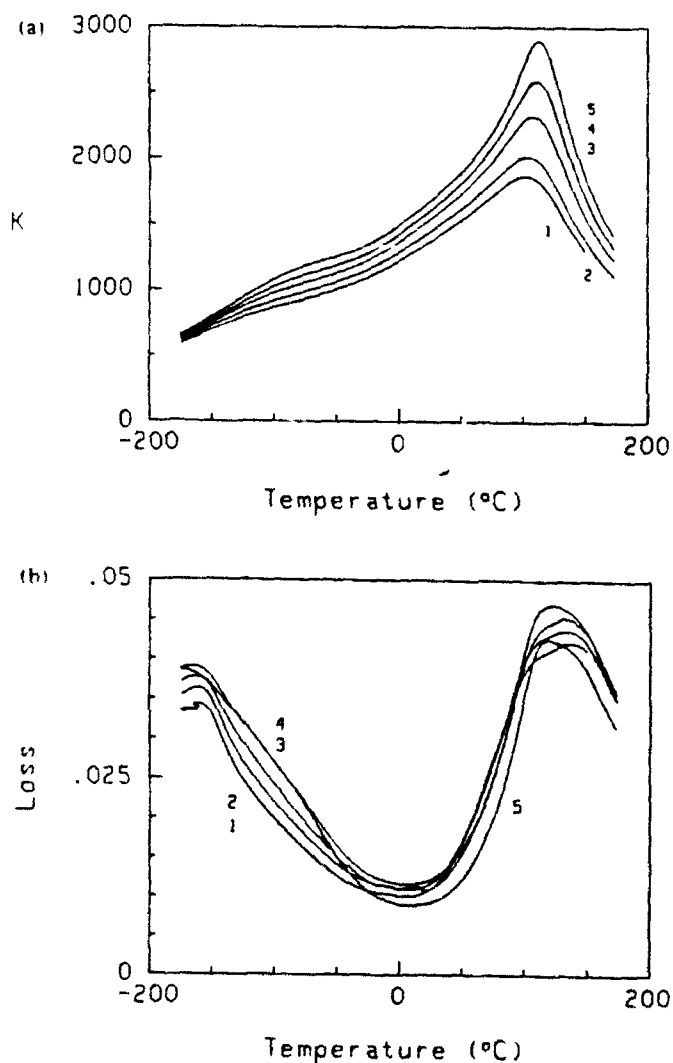


Fig. 3 The dielectric properties of BT2 ceramic with 5wt%  $\text{Bi}_2\text{O}_3$  sintered at various temperatures; (a)  $K$  vs  $T$  and (b)  $\tan \delta$  vs  $T$ ; the properties were measured at 1kHz. Sintering temperatures of ceramics are (1)  $750^\circ\text{C}$ , (2)  $800^\circ\text{C}$ , (3)  $850^\circ\text{C}$ , (4)  $900^\circ\text{C}$ , and (5)  $950^\circ\text{C}$ . The magnitudes are not corrected for porosity.

### Part 2.

In this section, the effect of smaller concentrations of  $\text{Bi}_2\text{O}_3$  on the properties of  $\text{BaTiO}_3$  ceramic is discussed. To achieve good densities in these ceramics, it was necessary to sinter the compacts at higher temperatures. Even after sintering at  $1250^\circ\text{C}$ , the microstructure of the ceramic looked very similar to that shown in Fig. 2. In Table 2, some of the physical and electrical characteristics of the sintered ceramic are listed. The dielectric properties of the ceramic showed qualitatively similar behavior as seen in Fig. 3. Since the liquid phase volume is low, higher  $T_c$  and  $K_{RT}$  are observed. In these ceramic also, the dielectric peaks corresponding to lower temperatures transitions are also suppressed.

Table 2. Physical and dielectric properties of BT1 and BT2 ceramic with 1 wt%  $\text{Bi}_2\text{O}_3$ .

I. D.	Sint. Temp ( $^\circ\text{C}/\text{h}$ )	wr. loss %	Bulk $\rho$ gm/cc $\pm 2\%$	$K_{\text{max}}$ @ 1kHz	$T_{\text{max}}$ ( $^\circ\text{C}$ )	$K_{RT}$	$\tan \delta$
BT1	1150/2	1.09	4.99	3185	127	1300	0.017
	1250/1	1.15	5.52	5820	127	2000	0.033
BT2	1150/2	1.43	5.61	5800	121	2340	0.013
	1250/2	1.50	5.79	7075	123	2650	0.019

### Part 3.

In two batches of  $\text{BaTiO}_3$ , Bi-ions were introduced during the hydrothermal processing. To introduce Bi-ions in the structure, an appropriate amount of Bismuth in the nitrate form was added during the formation of Titanium hydroxide[3]. To this mixture, Ba- solution was added for the  $\text{BaTiO}_3$  formation. Due to the complexity of the reaction, the nature of  $\text{Bi}^{3+}$  addition is unknown. In the XRD patterns of the reacted powder, few additional diffraction peaks other than the major  $\text{BaTiO}_3$  peaks were detected. These peaks with feable intensities could not be matched to any of the Bismuth Titanate or Barium Bismuth Titanium Oxide compounds, unambiguously. The concentration of Bi-ion listed in Table 1, was calculated through atomic absorption spectroscopy. The powder compacts were sintered between  $900^\circ\text{C}$ - $1250^\circ\text{C}/0.5-3\text{h}$ . The density and the weight loss data of the sintered compacts are listed in Table 3. It is necessary to increase the sintering temperature above  $1000^\circ\text{C}$  to achieve sufficiently good densities. When the samples were sintered over a platinum sheet, comparatively better densities were observed at lower temperatures. But the bottom surface of the ceramic, especially in BT4, was bright yellow in color, indicating the segregation of liquid phase. This observation indicates that the viscosity of the liquid is low.

The microstructure and the dielectric properties of 3 wt% Bi-added samples are very similar to that shown in Fig. 2 and Fig. 3. But the properties of 0.3 wt% Bi-containing samples showed marked differences. The microstructural evaluation as a function of sintering temperature is compared in Fig. 4a, b, c and d. When the samples were sintered beyond  $1050^\circ\text{C}$ , the average grain size of the ceramic increased to  $>10\mu\text{m}$ . In  $K$  vs  $T$  plots, dielectric peaks corresponding to three transitions could be detected very clearly. In Table 3, some of the dielectric properties are listed. The dielectric properties of these samples varied as a function of measuring frequencies at all temperatures. Careful analysis of the microstructure, density, and the dielectric properties of the ceramic as a function of sintering temperature and time indicate the grain growth mechanism is dominantly diffusion controlled in nature.

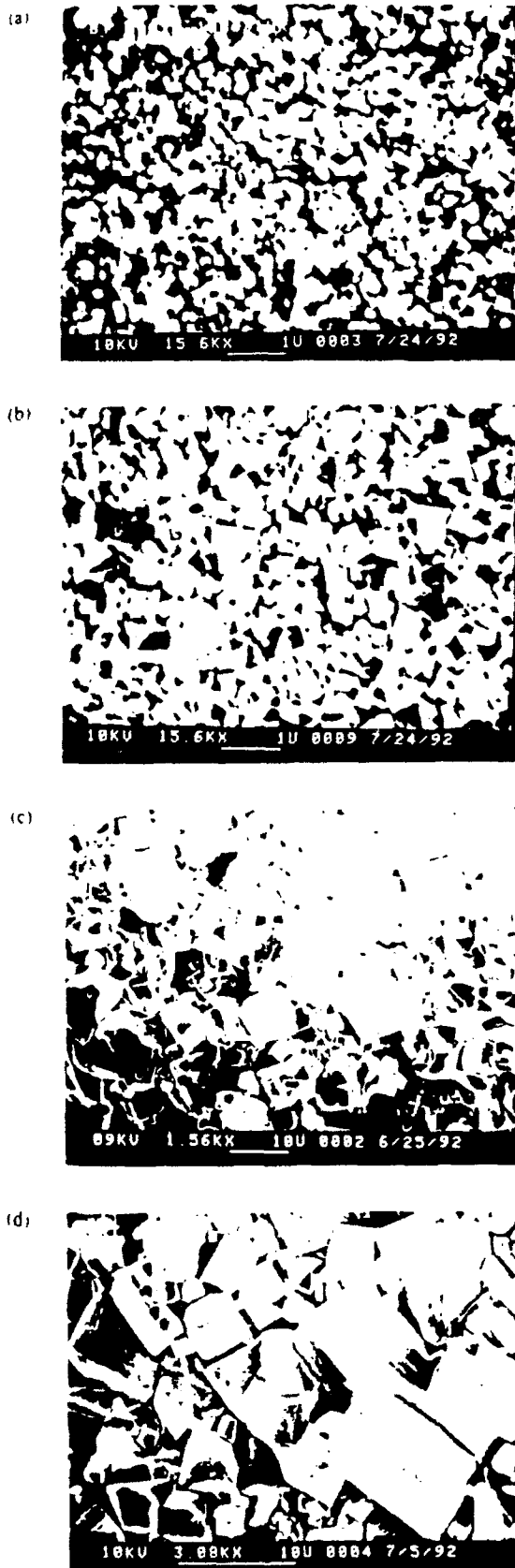


Fig. 4 Fractured microstructures of BT3 ceramics sintered at (a) 1000°C/1h, (b) 1050°C/1h, (c) 1100°C/1h, and (d) 1150°C/2h

Table 3: Physical properties of BT3 and BT4 ceramic

I. D.	Sint. Temp. °C/h	Setter	Wt. loss %	Bulk ρ gm/cc
BT3	1000/0.5	ZrO <sub>2</sub>	0.78	4.40
	1000/1	ZrO <sub>2</sub>	0.58	4.54
	1000/2	ZrO <sub>2</sub>	0.52	5.30
	1000/3	ZrO <sub>2</sub>	0.81	5.28
	1050/1	ZrO <sub>2</sub>	0.55	5.28
	1050/1.5	ZrO <sub>2</sub>	0.84	5.36
	1050/2	ZrO <sub>2</sub>	1.07	5.60
	1100/2	ZrO <sub>2</sub>	1.18	
	1150/2	ZrO <sub>2</sub>	1.17	5.65
	1200/2	ZrO <sub>2</sub>	1.37	5.68
1250/2	ZrO <sub>2</sub>	1.34	5.68	
BT4	850/2	Pt	0.6	4.59
	850/2	ZrO <sub>2</sub>	0.92	4.76
	900/2	Pt	0.63	4.98
	950/2	Pt	0.66	5.31
	1000/1	ZrO <sub>2</sub>	0.92	5.22
	1100/2	ZrO <sub>2</sub>	1.36	5.82
	1200/2	ZrO <sub>2</sub>	1.76	5.89
	1250/2	ZrO <sub>2</sub>	2.03	5.91

#### Part 4.

In the Ba<sub>0.8</sub>Sr<sub>0.2</sub>TiO<sub>3</sub> (BST) powder used for this investigation, small amount of carbonates were detected through XRD patterns. In a separate paper presented in this conference, the effect of grain size on the dielectric properties of pure porous ceramic is discussed. In that study, the smallest average grain size achieved through conventional sintering was 0.2 μm, and in this ceramic, dielectric peaks corresponding to three transitions are clearly identified.

The densification behavior of BST as a function of flux concentration and the sintering temperatures are represented in Fig. 5. Primarily because of the presence of strontium, it is necessary to sinter the ceramic with higher flux concentrations and at higher temperatures. K vs. T plots of the flux added ceramic are given in Fig. 6 and 7. Suppression of dielectric peaks at the transition temperatures are clearly seen. XRD patterns of these ceramic failed to show splitting in <200> peaks due to tetragonality.

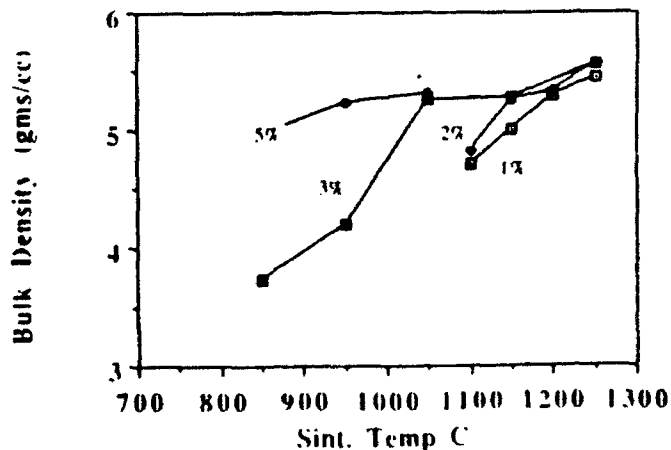


Fig. 5 Effect of flux concentration in the densification behavior of Sr<sub>0.2</sub>Ba<sub>0.8</sub>TiO<sub>3</sub>. These ceramics were sintered for 2hr

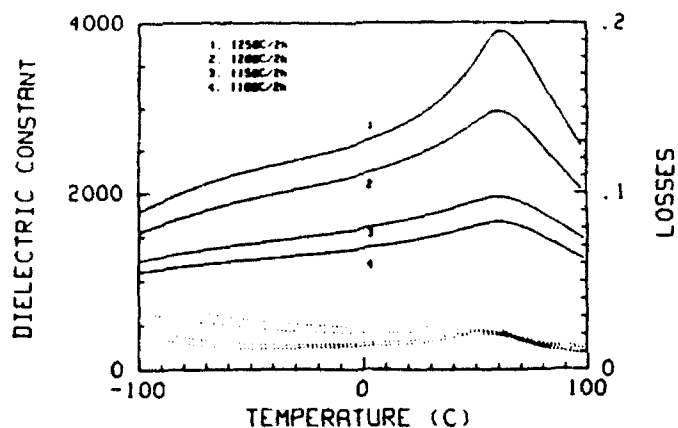


Fig 6 K vs T plots of SBT20 with 2wt%  $\text{Bi}_2\text{O}_3$ , which were measured at 1kHz. These ceramics were sintered at 1. 1250°C, 2. 1200°C, 3. 1150°C, and 4. 1100°C for 2hr.

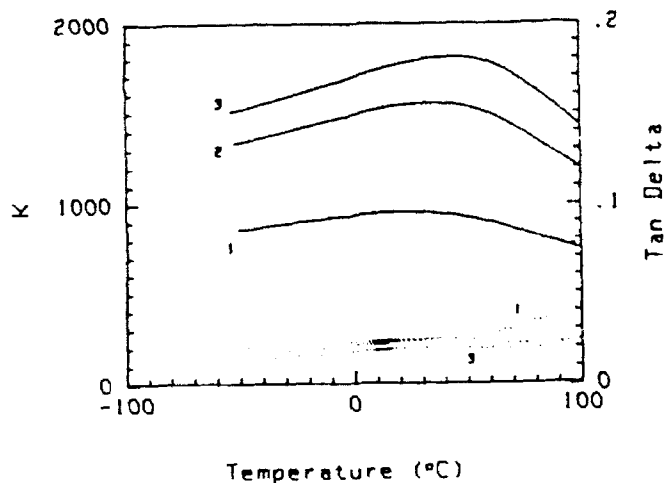


Fig 7 K vs T plots of SBT20 with 5wt%  $\text{Bi}_2\text{O}_3$ , which were measured at 1kHz. The ceramics were sintered at 1. 850°C, 2. 950°C and 3. 1050°C.

### Conclusions

1. When smaller amount of  $\text{Bi}_2\text{O}_3$  was added to hydrothermal  $\text{BaTiO}_3$ , to achieve high density, it was necessary to sinter the compact at higher temperatures.
2. Addition of  $\text{Bi}_2\text{O}_3$  during the hydrothermal preparation of  $\text{BaTiO}_3$ , produced an unidentifiable Bi-based second phase. To achieve high densities, even with 3 wt%  $\text{Bi}_2\text{O}_3$ , it was necessary to sinter the compacts beyond 1000°C. This observation indicates the importance of processing procedure.
3. When the  $\text{Bi}_2\text{O}_3$  concentration was reduced to 0.28 wt%, good densification, accompanied with grain growth, occurs beyond 1000°C. Careful consideration of weight loss observed during sintering, grain growth and the dielectric properties suggest that the densification is accomplished dominantly by grain boundary and bulk diffusion mechanisms.
4. When 5 wt%  $\text{Bi}_2\text{O}_3$  was added to  $\text{Sr}_{0.2}\text{Ba}_{0.8}\text{TiO}_3$  powders, the compacts sinter to bulk densities  $> 5.2$  gms/cc at 950°C. Percentage changes in TCC calculated from C vs. T plots of this ceramic show Z5U industrial specifications, with a room temperature dielectric constant of 1500. By changing the particle size and the concentration of the  $\text{Bi}_2\text{O}_3$ , it appears that it is possible to reduce the sintering temperature to 850°C, which is the typical thick film processing temperature.

**Acknowledgements:** Authors gratefully acknowledge the financial support from Cabot Corporation of Boyertown, PA and the Ben Franklin Partnership Program of the Commonwealth of PA. Authors also acknowledge the technical support provided by D Laubscher and Mingfong Song.

### References

- [1] U. Kumar, and J. P. Dougherty, "Sintering behavior of high purity  $\text{BaTiO}_3$  in the presence of  $\text{Bi}_2\text{O}_3$  as the liquid phase", Communicated to J. Am. Cer. Soc.
- [2] U. Kumar, and J. P. Dougherty, "Dielectric properties of fine grain hydrothermal  $\text{BaTiO}_3$  sintered with  $\text{Bi}_2\text{O}_3$ ", Communicated to J. Am. Cer. Soc.
- [3] Cabot Patent.

# **THIN FILM-FERROELECTRICS**

**APPENDIX 48.**

# DIELECTRIC BEHAVIOR OF FERROELECTRIC THIN FILMS AT HIGH FREQUENCIES

J. Chen, K. R. Udayakumar, K. G. Brooks, and L. E. Cross  
Materials Research Laboratory  
Pennsylvania State University  
University Park, PA 16802

## Abstract

The high frequency dielectric response of sol-gel derived lead zirconate titanate (PZT) thin films has been investigated. Conceptualizing the presence of interface layers was critical in explaining the dielectric measurements. By a careful control of the processing parameters, aided by rapid thermal annealing, the low frequency dielectric characteristics could be sustained upto a GHz range.  $\text{Ba}_0.5\text{Sr}_0.5\text{TiO}_3$  which is paraelectric at room temperature appears to be a potential candidate material for high frequency applications.

## Introduction

In these modern times, many and varied are the applications of high frequency dielectrics; in high resolution/ digital communication devices encompassing cellular phone and satellite communications, in microelectronics and packaging for high speed switching mode power supply, in frequency sensors for microwave detection, to plainly list but a few. Dielectrics qualifying for such applications must possess high dielectric permittivity, low dissipation loss, and low temperature coefficient of electrophysical properties. Ferroelectric materials, which constitute a unique subclass of dielectrics, while very promising in satisfying these general attributes, suffer from a drop in the dielectric constant at a characteristic frequency, ascribed to the piezoelectric resonance of the crystallites as well as the inertia of the domain boundaries; other plausible explanations advanced for the phenomenon include the existence of interface layers at the film-electrode boundary, impurities in the film, and grain imperfections as also grain boundaries. At still higher frequencies, an additional drop in the relative permittivity may occur, assigned generally to dielectric relaxation. In paraelectric materials, no piezoelectric resonance can occur if the phase is centrosymmetric; the clamped and free dielectric constant, which refer to the dielectric constant at frequencies above and below piezoelectric resonance respectively, are equal to one another. At a given high frequency, dielectric relaxation can still cause a fall in the dielectric permittivity in this non-polar phase.

Shifting the focus from the confines of the bulk materials to the dielectric behavior of ferroelectric thin films at low-amplitude a.c. field of high frequencies, as in the present study, the dominant factors that influence relaxation appear to be connected to the presence of interface layers, and grain imperfections. For, first, these films have been characterized by very small grain sizes, in the 0.1-0.2  $\mu\text{m}$  range [1,2], that has the effect of displacing the threshold frequency due to the piezoelectric clamping of grains or domains to higher levels; and second, fabrication of the films through the sol-gel process ensures maximal chemical purity. This study will, consequently, argue that the dielectric dispersion in the 1 MHz to several GHz range stems from the presence of barrier layers and grain imperfections, both of which can be squarely linked to the film processing.

## Results and Discussion

The PZT films used in the study were of the morphotropic phase boundary composition (with a Zr/Ti mole ratio of 52/48), fabricated by the sol-gel spin-on technique. The details of the film fabrication as well as the structural and electrophysical characterization of these films have been outlined in Refs. 1 and 2; the dielectric and ferroelectric property measurements were limited to the radio frequency range in these earlier studies. For dielectric measurements in this study, a high frequency impedance analyser (HP 4191A) was used. All the films were rapid thermally annealed at temperatures and times as specified.

Fig. 1 is a plot of the dielectric permittivity as a function of frequency for a 0.385  $\mu\text{m}$  thick PZT film, rapid thermally annealed in the temperature range of 600-800°C for 60 seconds. It is patent from the figure that with increasing annealing temperature, the relaxation frequency decreases systematically; of greater import is the precipitous tumble in permittivity to almost a cipher at this frequency. While this latter point is seemingly baffling at first glance, the frequency response of the measured dielectric constant and the corresponding impedance spectrum from the equivalent circuit model, based on properties of the

film core, the electrode, and a series resistance [3], lends a modicum of understanding to the anomalous dielectric behavior. Sayer et al. [3] postulated the formation of an interface layer at the top electrode-film boundary and the film-substrate boundary; by varying the internal barrier layer thickness from 0.01  $\mu\text{m}$  to 0.5  $\mu\text{m}$  (the disturbed layer at both the interfaces are lumped) on a film of 1  $\mu\text{m}$  total thickness, the dielectric constant was computed, which has been reproduced here as Figure 2. Scrutiny of this figure, and its juxtaposition with Fig. 1, reveals a striking similarity, tempting the speculation of the presence of interface layers of increasing thickness with increasing severity of annealing of the films. As observed by the authors [3], the calculated higher dielectric constant for films with thicker barrier layers might be related to the assumption of the full thickness of the film in the computations, when in

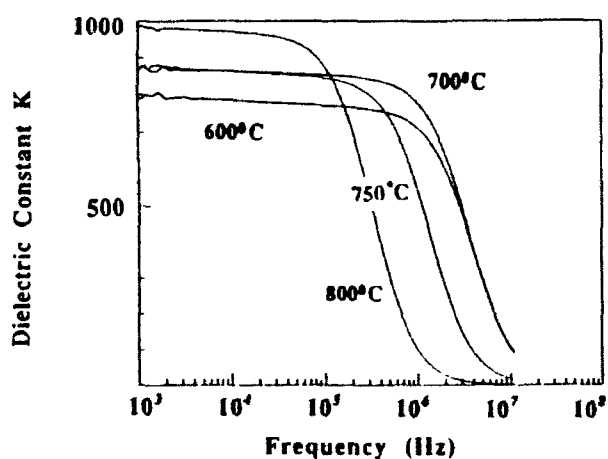


Fig. 1 High frequency dielectric response of PZT thin films, annealed 600-800°C at a constant dwell time of 60 seconds. Note the systematic change in the relaxation frequency with annealing temperature.

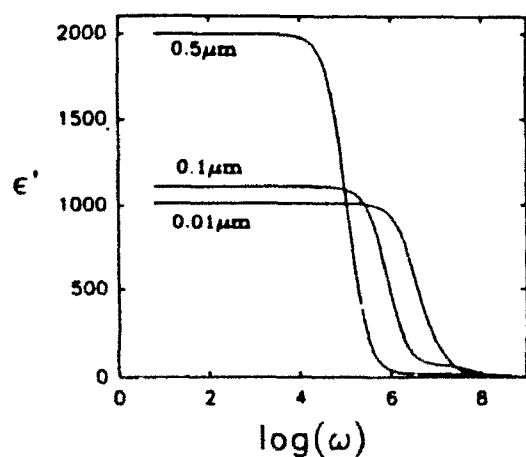


Fig. 2 Computed dielectric constant of a 1  $\mu\text{m}$  film with varying internal barrier thickness; the true value of  $\epsilon' = 1000$  (reproduced from Sayer et al. [3])

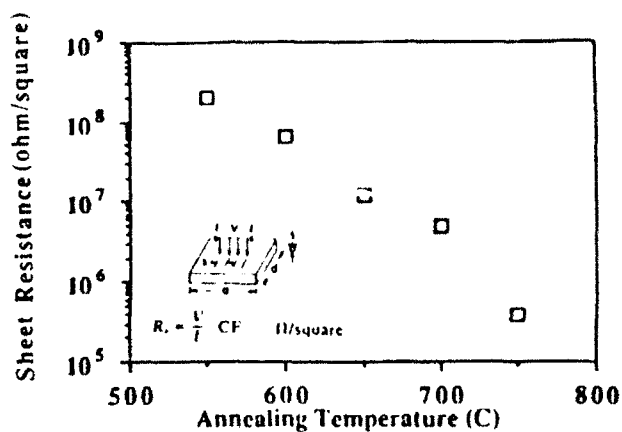


Fig. 3 Resistivity plotted as a function of annealing temperature.

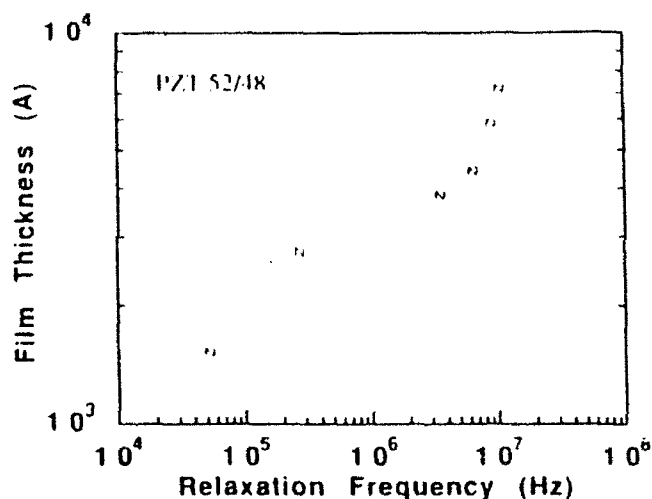


Fig. 4 Relaxation frequencies determined for films of varying thickness shows a drop for thinner films.

reality, it should be smaller by a thickness equal to that of the disturbed layers. In our earlier study [1], the high frequency dielectric relaxation was alluded to the formation of low resistivity surface layers whose resistivity changes with the annealing conditions; from Fig. 3, it is apparent that higher annealing temperature results in lower resistivity of this anomalous layer. Maintaining the same processing parameters, dielectric relaxation frequencies of films varying in thickness from 0.15  $\mu\text{m}$  to 0.75  $\mu\text{m}$  were determined (Fig. 4); thinner films are privy to lower relaxation frequencies, indicating heightened sensitivity to the interface layer formation. When the thermal budget was reduced during annealing by lowering the dwell time from 60 seconds to 10 seconds, there was no

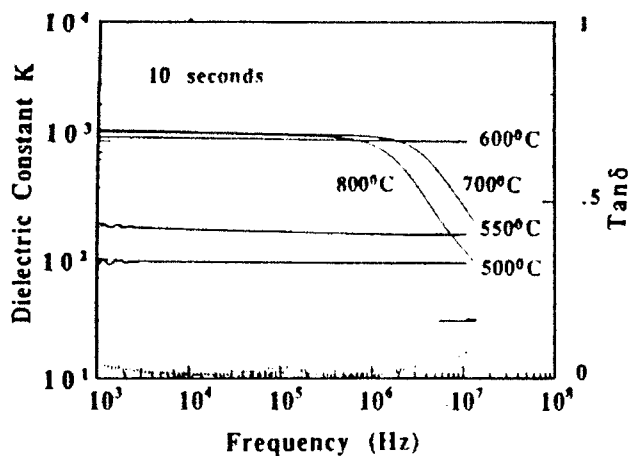


Fig. 5 Dielectric permittivity plotted as a function of frequency for various annealing temperatures but with a reduced dwell time of 10 seconds.

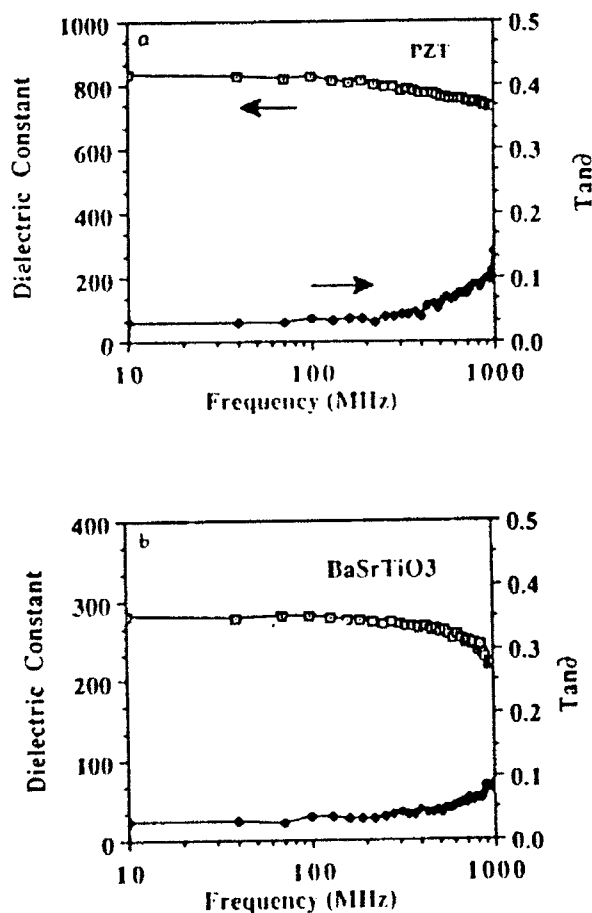


Fig. 6 The frequency characteristics of ferroelectric PZT films (a), and paraelectric BST films (b); note the non-dispersive behavior upto the measured frequency of 1 GHz by a careful control of the growth of the interface layer.

evidence of relaxation in films annealed at 500 to 600°C (Fig. 5); interface layer growth may thus be controlled to eliminate low frequency dielectric dispersion. Extending this theme, by manipulating the processing parameters, the low frequency dielectric permittivity and loss of the PZT films could be sustained upto a GHz, as shown in Fig. 6a. A solid solution system embracing compositions that is paraelectric at room temperature is the (Ba, Sr)TiO<sub>3</sub> (BST) system; specifically, thin films in the BST system, of composition corresponding to a Ba/Sr mole ratio of 50/50, fabricated by the sol-gel chemical technique, revealed dispersion-free dielectric characteristics (Fig. 6b) for measurements upto a GHz.

### Summary

Earlier studies of both bulk ceramics and thin films has shown that the utility of ferroelectrics for high frequency applications is limited on account of the dielectric dispersion at 1 MHz to a few hundred MHz depending on the specific material. The present endeavor has shown that by a deliberate interplay of the processing parameters, dielectric relaxation in the PZT films can be prevented upto a GHz. Films that are ferroelectric at room temperature are *intrinsically* subjected to relaxation due to the piezoelectric clamping of grains or domains, and the inertial response of domain wall movement. It would therefore appear prudent to examine the feasibility of films that are paraelectric at room temperature for high frequency applications; Ba<sub>0.5</sub>Sr<sub>0.5</sub>TiO<sub>3</sub> falls in this category, and the first results are indeed promising.

### References:

- [1] J. Chen, K. R. Udayakumar, K. G. Brooks, and L. E. Cross, "Rapid thermal annealing of sol-gel derived PZT thin films", *J. Appl. Phys.*, pp. 4465-69, May 1992
- [2] K. R. Udayakumar, J. Chen, S. B. Krupanidhi, and L. E. Cross, "Sol-gel derived PZT thin films for switching applications", *Proc. Seventh Intl. Symp. Appl. Ferroelectrics*, 1990, pp. 741-43
- [3] M. Sayer, A. Mansingh, A. K. Atora, and A. Lo, "Dielectric response of ferroelectric thin films on non-metallic electrodes", *Integrated Ferroelectrics*, vol. 1, pp. 129-146, 1992.

**APPENDIX 49**

# Changes in the Crystal Structure of RF-Magnetron Sputtered BaTiO<sub>3</sub> Thin Films

Kenji UCHINO, Nam-Yang LEE, Tamaki TOBA, Narikazu USUKI, Hideaki ABURATANI and Yukio ITO

Department of Physics, Sophia University, 7-1, Kioi-cho, Chiyoda-ku, Tokyo 102

## RF-マグネトロンスパッタ法による BaTiO<sub>3</sub> 薄膜の結晶構造の変化

内野研二・李 南良・鳥羽・環・臼木成和・油谷英明・伊藤由喜男

上智大学理工学部物理学科, 102 東京都千代田区紀尾井町 7-1

[Received December 11, 1991; Accepted May 21, 1992]

The crystal structure of BaTiO<sub>3</sub> thin films fabricated by RF-magnetron sputtering has been investigated. As-sputtered films exhibited a cubic structure with a small grain size of about 6-8nm. After annealing at a temperature above 1100°C, the crystal structure changed from cubic to tetragonal, because the annealing process caused grain growth. The critical grain size of the thin films which provided the cubic structure existed in the range of 0.1-0.2 μm. This value agreed well with the critical grain size of BaTiO<sub>3</sub> fine particles, 0.12 μm.

**Key-words** : RF-magnetron sputtering, BaTiO<sub>3</sub> thin film, Annealing process, Critical grain size, Phase transition

### 1. Introduction

With increasing the demand for ferroelectric thin films for the applications to optical wave guides, non-volatile memories and so on, many studies have been attempted using RF-sputtering and other thin film fabrication techniques.<sup>1)-4)</sup> However, ferroelectric films fabricated by these methods frequently have not shown so good ferroelectricity as seen in bulk sintered ceramics or single crystals. Although many researchers have attempted to give explanations to this phenomenon, they have been insufficient so far.

Nagatomo et al. have reported that the ferroelectric BaTiO<sub>3</sub> thin film could be prepared at a relatively low substrate temperature of 700°C by using RF-planar-magnetron sputtering, however, the ferroelectricity of those films was weak or absent for the fine-grained film, and it was necessary to anneal at 1000°C in order to obtain ferroelectric BaTiO<sub>3</sub> films with high quality.<sup>1),4)</sup> They have explained these phenomena by the 90° domain model suggested by Arlt et al.<sup>5)</sup> However, the reason why the fine-grained film exhibits cubic symmetry and non-ferroelectric properties has not been discussed.

The purpose of this study is to clarify why the as-grown BaTiO<sub>3</sub> thin films do not show ferroelectricity. Our discussion is based upon the "critical grain size" model.

We have reported the particle/grain size dependence of ferroelectricity for powder and polycrystal-

line samples of BaTiO<sub>3</sub>, and clarified that both the tetragonality,  $c/a$ , and the Curie temperature,  $T_c$ , are decreased drastically at a particle size of 0.12 μm.<sup>6)</sup> Fine particles less than this critical grain size will not exhibit ferroelectricity because the crystal lattice becomes a cubic structure.

In order to explain this phenomenon, we have proposed an "effective surface tension" model.<sup>6),7)</sup> A fine particle with  $R$  in radius experiences a hydrostatic pressure of  $2\gamma/R$  ( $\gamma$ : surface tension), and this hydrostatic pressure decreases the Curie temperature of the particle down below room temperature and changes the structure into cubic. It is interesting that the revealed in perovskite ferroelectrics ((Pb, Ba)TiO<sub>3</sub>, (Ba, Sr)TiO<sub>3</sub>) shows an almost constant value of 50 N/m. This extraordinarily large value has not been explained yet, however, it may be attributed to the surface layer generated by the permanent dipoles.

### 2. Experiments

#### 2.1 Sample preparation

The BaTiO<sub>3</sub> film was deposited by using an RF-magnetron sputtering system (Anelva, SPF-430HS). Corning 7059 and fused quartz substrates with 15 mm × 15 mm × 1 mm in size were used. All the substrates were cleaned by using trichloroethane (TCE) and acetone, and then placed in a stainless steel holder by clips prior to film deposition. The target had a stoichiometric composition of BaTiO<sub>3</sub> with purity of 99.9%. The size was 100 mm in diameter and 5 mm in thickness. The sputtering conditions are summarized in Table 1. The thickness of the sputtered films was more than 2 μm, much thicker than the grain size.

In order to control the grain size the as-sputtered

Table 1. Summary of sputtering conditions.

Substrate temperature	room temperature	800°C
RF power	200W	
Target-substrate distance	43 - 70mm	
Gas pressure	0.5 - 2.0Pa	
Sputtering time	3hrs	

thin films were annealed at the temperature range of 600°–1200°C for 12 h. Chemical analysis of the composition was made by the ICPS (Inductively Coupled Plasma Spectroscopy) method and the Ba/Ti ratio was proved to be nearly 1.0.

## 2.2 Measurement

An X-ray diffractometer (JEOL, JDX-11PA) was employed to examine as-grown and annealed thin films. The crystal symmetry and the consequent lattice constants of samples were calculated by averaging the {100} and {200} reflections of the BaTiO<sub>3</sub> perovskite cell. Average grain size in the range of sub-micron was determined from SEM (Hitachi, S-900) micrographs using a line intercept method. In the range of grain size of nano-meter Scherrer's equation<sup>8)</sup> was used for {100} peaks. The grain sizes determined by SEM and X-ray diffraction were almost the same ( $\approx 0.1 \mu\text{m}$ ) for the sample annealed at 1000°C; this suggests that the crystallite size almost corresponds to the grain size.

## 3. Results and discussions

Figure 1 shows the X-ray diffraction patterns of as-grown films sputtered at the gas pressure of 1.0 Pa for various substrate temperatures. The film sputtered at room temperature showed an amorphous phase, but the film fabricated above 500°C showed a crystalline phase. The lattice constant decreased with the substrate temperature from 4.15Å at 500°C down to 4.07Å at 800°C, but it was still larger than that of sintered BaTiO<sub>3</sub> ( $a: 3.989\text{Å}$ ,  $c: 4.029\text{Å}$ ).

Only two peaks due to the preferential orientation along {100} appeared and the preference did not change significantly with the substrate temperature. This result is different from previous researches. It has been reported that if the mobility of atoms during deposition is high (i.e., at a high substrate temperature), the films grow with the orientation of {110} due to its highest occupation density com-

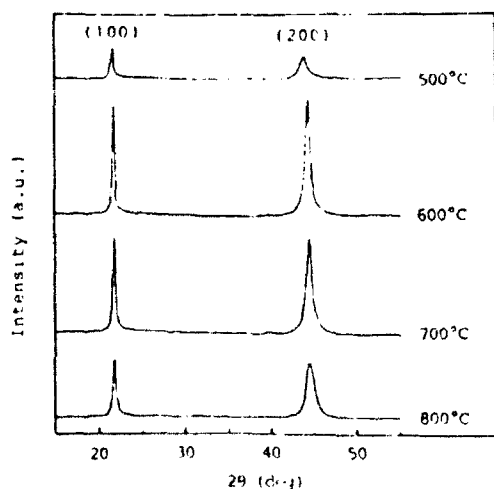


Fig. 1. XRD patterns of films sputtered on the substrate at various temperatures.

pared to the other planes with low indices.<sup>3,4)</sup> The decrease in the X-ray intensity and the peak broadening for the substrate temperature of 800°C seems to be caused by the slight mis-orientation due to higher substrate temperature.

The samples were annealed at various temperatures to increase the grain size so that they were compared to the fine grain ceramic BaTiO<sub>3</sub>. Figure 2 shows the XRD patterns of {200} reflection of films annealed at 1000°, 1100°, and 1200°C. The diffraction pattern of the film annealed at 1000°C shows a symmetrical pattern. On the other hand, the peak of

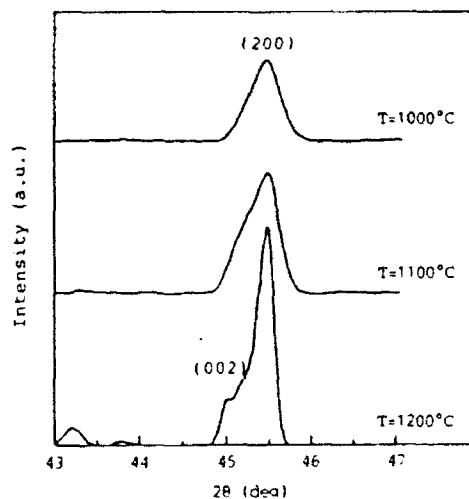


Fig. 2. XRD peaks of the {200} reflections of BaTiO<sub>3</sub> annealed at various temperatures.

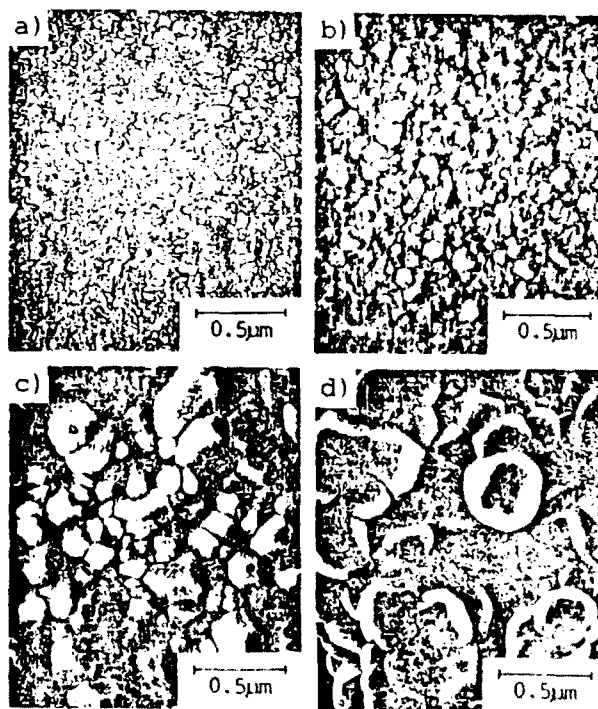


Fig. 3. SEM photographs of BaTiO<sub>3</sub> thin films annealed at various temperatures. (a) 600°C, (b) 1000°C, (c) 1100°C, (d) 1200°C.

the film annealed at 1100°C or 1200°C skews to the right side from the center, revealing an additional peak at a lower angle. This seems to be attributed to the appearance of the (002) peak, although the peak was not entirely separated from the (200) peak. In conclusion, the phase transition from cubic to tetragonal was caused by thermal annealing at the temperature above 1100°C. The microstructure of annealed samples was observed by using SEM and the results are shown in Fig. 3. By the annealing process, the grains grew from about 40nm to 350nm.

Figure 4 plots the relationship between the grain size and the annealing temperature, where the crystal structure is also indicated. The crystal structure was cubic below 0.1  $\mu\text{m}$  in grain size, and tetragonal above 0.2  $\mu\text{m}$ . Therefore, it is shown that the critical grain size might exist between 0.1 and 0.2  $\mu\text{m}$ . This result agrees exactly with that obtained by the study on the particle size dependence of the crystal structure of fine powder  $\text{BaTiO}_3$ ,<sup>6)</sup> where the critical grain size was indicated to be 0.12  $\mu\text{m}$ . The grain size of as-sputtered thin films ranged over 6–8nm in this study. Iijima has reported that the grain size of

evaporated  $\text{BaTiO}_3$  thin films ranges over 35–70nm and the film without heat-treatment did not show any ferroelectric properties.<sup>9)</sup> Although there are some differences among these values due to fabrication methods, both of them are below the critical grain size, 0.12  $\mu\text{m}$ . Accordingly, it can be thought that the cubic structure and non-ferroelectric properties of as-sputtered films are attributed to the small grain size.

#### 4. Conclusions

The results of this study are summarized.

- (1) As-sputtered films prepared on the substrate of 500°–800°C exhibited a cubic crystal structure.
- (2) The crystal structure of sputtered films changed from cubic to tetragonal after annealed at a temperature above 1100°C.
- (3) The critical grain size separating cubic and tetragonal phases existed in the range of 0.1–0.2  $\mu\text{m}$ , and was in good agreement with the critical grain size of 0.12  $\mu\text{m}$  determined from the fine powder of  $\text{BaTiO}_3$ .

#### References

- 1) T. Nagatomo and O. Omoto, *Jpn J Appl Phys.*, 26, Suppl. 26-2, 11-14 (1987).
- 2) K. Sreenivas, M. Sayer and P. Garrett, *Thin Solid Films*, 172, 251-67 (1989).
- 3) C. H. Lee and S. J. Park, *J Mat Sci Mat in Elect.*, 1, 219-24 (1990).
- 4) T. Nagatomo, T. Kosaka, S. Omori and O. Omoto, *Ferroelectrics*, 37, 681-84 (1981).
- 5) G. Arlt, D. Hennings and G. de With, *J Appl Phys.*, 58, 1619-25 (1985).
- 6) K. Uchino, E. Sadanaga and T. Hirose, *J. Am Ceram. Soc.*, 72, 1555-58 (1989).
- 7) T. Yamakawa and K. Uchino, Proc 7th Internation. Symp. on Appl. Ferroelectrics, IEEE, pp. 610-12 (1990, Illinois, USA).
- 8) B. D. Cullity, "Elements of X-Ray Diffractions, Second Edition", Ed. by Addison-Wesley Publishing Co., Inc., Massachusetts (1978) pp. 99-106.
- 9) Y. Iijima, *Jpn J. Appl. Phys.*, 24, Suppl. 24-2, 401-03 (1985).

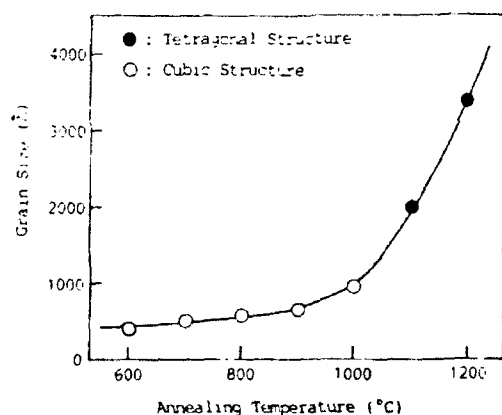


Fig. 4. Relationship between grain size and annealing temperature. The crystal symmetry is also indicated.

**APPENDIX 50**

SIZE EFFECTS IN FERROELECTRIC  
THIN FILMSROBERT E. NEWHAM, K. R. UDAYAKUMAR,  
AND SUSAN TROLIER-McKINSTRY

## INTRODUCTION

Beginning with work on the melting behavior of metals, it has been reported that many phase transitions are susceptible to size effects. The melting point of bulk gold, for example, is 1337.58 K, but this temperature drops rapidly for grain sizes below 100 Å (Fig. 36.1). This decrease in the phase transition temperature has been attributed to the change in the ratio of surface energy to volume energy as a function of particle size. Thus, for spherical particles of radius  $r$ , the melting temperature can be predicted from [Eq. (36.1)]

$$\Delta U dV - \Delta S T_r dV - \sigma dA = 0 \quad (36.1)$$

where  $\Delta U$  and  $\Delta S$  are the changes in internal energy and entropy on melting,  $\sigma$  is the interfacial energy between the liquid and the solid, and  $T_r$  is the melting temperature of the particle. If  $\Delta S$  and  $\Delta U$  are temperature independent, then the difference between the bulk and small particle melting temperatures is inversely proportional to the particle radius according to

$$\frac{T_0 - T_r}{T_0} = \frac{2\sigma}{\rho L r} \quad (36.2)$$

*Chemical Processing of Advanced Materials*,  
Edited by Larry L. Hench and Jon K. West.  
ISBN 0-471-54201-6 © 1992 John Wiley and Sons, Inc.

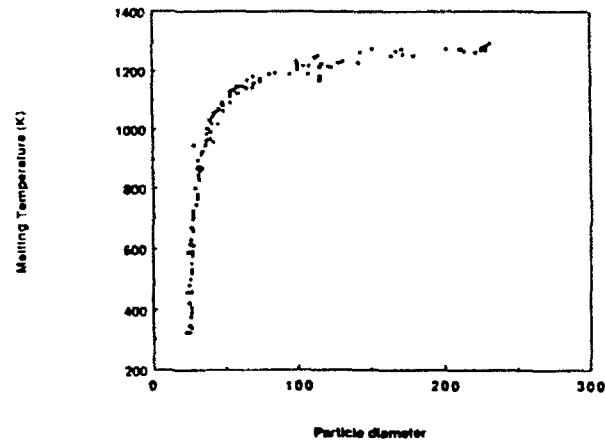


Figure 36.1. Melting temperature of gold particles as a function of size. Taken from Ref. [1].

where  $L$  is the heat of fusion,  $\rho$  the density, and  $T_0$  the bulk melting point.

It is interesting that many types of equilibrium phase transitions display comparable size effects. In addition to the data on gold particles, the melting temperatures of copper [3], tin [4], indium [5], lead, and bismuth [2] particles and thin films have all been shown to be size dependent. Similarly, the superconducting transition depends on size both intrinsically [6, 7] and extrinsically if the stress exerted on the superconducting phase is different at different sizes [8]. Superfluid transitions in He-iii coated powder compacts and thin films also depend on either the film thickness or the size of the pore diameter [9].

In ferroic materials, both the presence of domain walls and the ferroic transition itself are influenced by crystallite size. While this has not previously been critical to most applications, with the growing importance of thin-film- and small-particle-based devices, it is becoming important to understand the size effects expected in ferroic materials.

## REVIEW OF FERROIC SIZE EFFECTS

In brief, we expect four regions in the size dependence of ferroic properties (Fig. 36.2). In large crystallites, multidomain effects accompanied by hysteresis take place. Reductions in size lead to single-domain particles and, at yet smaller sizes, to destabilized ferroics with large property coefficients. Finally, at sufficiently small sizes a reversion to normal behavior is expected at the point where there are simply too few unit cells to sustain cooperative behavior. Similar transitions with size are expected in secondary ferroics. As an introduction to the intrinsic size effects in ferroelectric films, it is instructive to review what is known about the transitions between regions in ferroic particles.

Beginning with the larger end of the size spectrum, it is well known that large-

grained ferroic ceramics exhibit complex domain structures that are bordered by several types of domain walls. As the size of the system decreases, however, the volume free energy necessarily decreases as well, and it becomes increasingly difficult to support the free-energy term associated with domain walls [10]. Consequently, the number of domains is expected to diminish as first one and then the other types of domain walls are eliminated. The transition from polydomain to single-domain behavior is well documented in a number of ferromagnets. Pure iron suspended in mercury, for example, shows a critical size for conversion to single-domain behavior at  $\sim 23$  nm and  $\text{Fe}_{0.4}\text{Co}_{0.6}$  a critical size of  $\sim 28$  nm [11]. This is in good agreement with the calculations of Kittel, who suggested 20 nm as the minimum size for multidomain behavior in magnets [10]. Results for acicular agglomerates of  $\gamma\text{-Fe}_2\text{O}_3$  particles separated by nonmagnetic grain boundaries are also consistent with these estimates; Berkowitz et al. [12] report that the stable single-domain range at room temperature is centered at  $\sim 40$  nm.

Although the loss of multidomain behavior in ferroelectric ceramics is known to occur for much larger grain sizes (approximately several tenths of a micrometer), it is also clear that the stress state in a monolithic body containing domains is considerably more complex than that for isolated particles. Consequently, the changes in ferroic properties as a function of size in ferroelectric powders are expected to follow the ferromagnetic analog more closely. This is born out in experiments on 0-3  $\text{PbTiO}_3$ /polymer composites in which the filler

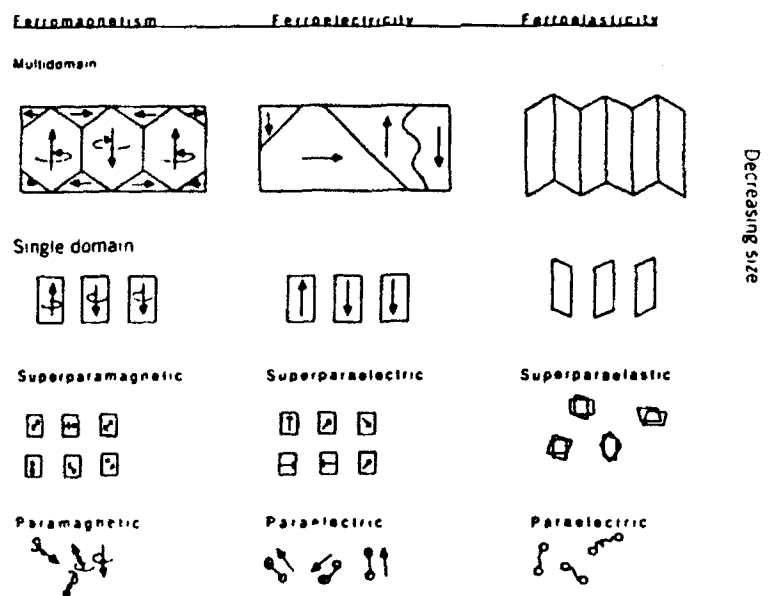


Figure 36.2. Transitions in ferroic behavior as a function of size.

particle size was varied. Lee et al. [13] report that there is a significant drop in the ability to pole such composites for filler particles smaller than  $\sim 200$  nm. Assuming both that the small particles were well crystallized and that the particle size distributions were narrow, this implies that transition from multidomain to single domain occurs in  $\text{PbTiO}_3$  particles near 200 nm.

At still smaller sizes, ferroic materials undergo a phase change to the high-temperature prototype group. In the case of ferromagnetic particles, this has been correlated with the size at which the decrease in volume free energy accompanying magnetization is on the order of the thermal energy [14]. As a result, the spin direction is randomized with time, leading to an unmagnetized but highly orientable single-domain crystal. Thus, a magnet in this size regime is characterized by a zero net magnetization, the disappearance of a magnetic hysteresis loop, extremely high magnetic susceptibilities, and a symmetry that, on average, is higher than that of the ferromagnetic phase. Iron exhibits superparamagnetic behavior at particle sizes near 7 nm [11],  $\gamma\text{-Fe}_2\text{O}_3$  at  $\sim 30$  nm [12] and  $\text{BaFe}_{12-2x}\text{Ti}_x\text{Co}_2\text{O}_{19}$  at 15–35 nm depending on the stoichiometry and the degree of particle shape anisotropy [15]. The loss of the ferroic hysteresis loop coupled with the ability to respond strongly to the presence of a magnetic field has been utilized in a variety of applications, including ferromagnetic fluids and high-frequency transformers where eddy current losses are a problem.

A similar mechanism has been proposed to explain the dielectric and elastic properties of relaxor ferroelectrics [16, 17]. Compositions including many of the  $\Lambda(\text{B}'_{1/2}, \text{B}''_{1/2})\text{O}_3$  and  $\Lambda(\text{B}'_{2/3}, \text{B}''_{1/3})\text{O}_3$  exhibit microdomains (typically 2–30 nm in size) of 1:1 ordering on the B sublattice dispersed in a disordered matrix. It has been suggested that as a result of this nanostructure, the spontaneous polarization in these materials is also subdivided into very small local regions. Thus, a lead magnesium niobate ceramic can be regarded as a collection of disordered but highly orientable dipoles. The result, much like the case of superparamagnetism, is a high dielectric permittivity over a broad temperature range even though the net spontaneous polarization is zero. Because of the long range of the electric fields induced by the local dipoles, however, there is more interaction between the local electric dipoles than was present in the ideal superparamagnet. Consequently, the superparaelectric behavior in relaxor ferroelectrics is modulated by coupling between local moments, so that a spin glass model is necessary to describe the phase transition behavior [17]. Evidence for the importance of the size of the microregions is given in experiments on materials that can be ordered by heat treatment. As the scale of the ordered regions grow beyond a certain size, the material reverts to ordinary ferroelectric (or antiferroelectric) behavior with a well-defined transition temperature and a nondispersive dielectric response.

As yet, direct observation of superparaelectric behavior in particulate ordinary ferroelectrics has not been documented. Recently, however, many investigators have attempted to determine the critical size for reversion to the high-temperature prototype symmetry [18–20]. As in the case of the melting of

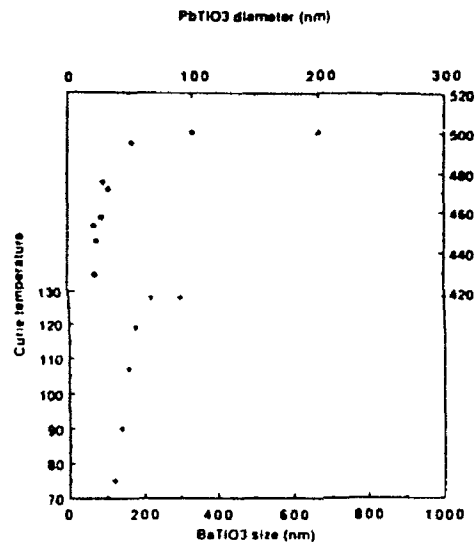


Figure 36.3. Transition temperature for ferroelectric powder. Data from Refs. [18,19].

metal particles, as the particle size is decreased, the transition temperature drops markedly (Fig. 36.3). While at larger sizes the high-symmetry phase is the ordinary paraelectric phase, as the size of the ferroelectric particles becomes small enough that thermal energy can disorder the dipoles, there should be a transition from paraelectric to superparaelectric particles. The reported results indicate that unconstrained  $\text{BaTiO}_3$  particles show the transition to a cubic phase near 80–120 nm [19], whereas  $\text{PbTiO}_3$  is stable in the tetragonal form to  $\sim 10$ –20 nm [13,18]. Because it is difficult to characterize the electrical properties of such small particles, it is not known if and when the high-symmetry particles actually become superparaelectric. On the other hand,  $\text{NaNbO}_3$  shows only some broadening in the differential thermal analysis (DTA) characteristic for the ferroelectric phase transition with no change in the transition temperature for particle sizes down to 5 nm. While it is an order–disorder ferroelectric, and so might have different size dependence for the properties than would a displacive ferroelectric, it is interesting that there is no evidence for superparaelectricity even at particle sizes of 5 nm.

It is also critical to note that it is possible to shift the critical size for reversion to high-temperature symmetry with changes in the processing. Residual strains, in particular, have been shown to drastically affect the properties of  $\text{BaTiO}_3$  [21]. Thus, it is not surprising that heavily milled  $\text{BaTiO}_3$  powders with an average radius of  $\sim 10$  nm have been shown to possess permanent dipole moments [22].

Saegusa et al. [20] examined the solid solution between  $\text{BaTiO}_3$  and  $\text{PbTiO}_3$  to determine the critical size for stabilization of the cubic phase to room

temperature as a function of composition. Assuming that crystallinity and stoichiometry were maintained for the smallest sizes, their data suggest that the critical size is *not* a linear function of composition. It would be interesting to follow the magnitude of the polarization as a function of temperature in such powders to see how its magnitude is affected by particle size.

Although the general outline of size effects expected in films are similar to those demonstrated in ferromagnetic particles, it would not be surprising for the boundaries between different regions to shift along the size axis for different geometries. Kittel was one of the first to explore this possibility in ferromagnetic materials [10]. He calculated that in a film where the preferred magnetization is perpendicular to the major surface, the multidomain to single-domain transition should occur near 300 nm, an order of magnitude larger than the same transition in a particulate material. If, however, there was either no anisotropy or the easy magnetization direction fell in the film plane, new types of domain walls may appear and persist down to very small sizes.

The transition to superparamagnetic behavior is apparently suppressed in comparatively perfect thin films produced in high-vacuum systems, probably because the large two-dimensional area raises the volume energy above the available thermal energy, even for very thin films. Consequently, regular ferromagnetic behavior persists in much thinner films (down to  $\sim 0.5$  nm for Ni films sandwiched between nonmagnetic layers [23]). In such samples, the ferromagnetic transition temperature also drops rapidly for films  $< 15$  nm thick.

Films that grow as discrete islands of magnetic material rather than continuous layers or that consist of magnetic particles isolated from each other by nonmagnetic hydride or oxide layers, on the other hand, should behave like particulate systems (undergoing superparamagnetic transitions appropriate for the primary magnetic particle size). This type of behavior has been confirmed in ferromagnetic films that became superparamagnetic at apparent thicknesses of 2.7 nm (where the film actually consisted of 5–10-nm islands [24]). It is interesting that no change in the Curie temperature was noted before the onset of thermal randomization of the spins.

Given this information, what can be predicted about the behavior of ferroelectric thin films? First, for an unelectroded film it seems likely that ferroelectricity will remain stable at least down to thicknesses of  $\sim 100$  nm for  $\text{BaTiO}_3$  and possibly considerably lower for  $\text{PbTiO}_3$  films. This is in accord with several theoretical predictions for size effects in thin ferroelectric wafers. In that work, it was shown that when space charge effects (which will be considered in the following section) are discounted, the onset of intrinsic size effects is projected to fall in the range of 1–10 nm [25].

Multidomain configurations should also remain stable down to very small sizes. Corroborating evidence for this is suggested by transmission electron microscopy (TEM) studies of thinned ferroelectric ceramics and single crystals where, provided the grain size is large enough, domains can be detected in foils below 100 nm thick [26]. When, however, the grain size in the film falls below

some critical limit, the density of domains will probably decrease in a manner similar to that shown in ceramics [27].

Finally, as in the case of the magnetic films, unless there is some extrinsic mechanism for forming discrete polar microregions, the onset of superparaelectricity should be depressed by the relatively large volume of ferroelectric.

### THIN-FILM SIZE EFFECTS

The experimentally observed size effects reported in the ferroelectric thin-film literature fall into four major categories: an increase in the coercive field, a decrease in the remanent polarization, a depression in the dielectric constant, and a smearing of the paraelectric-ferroelectric transition over values expected from bulk materials of the same composition. Typical data on the first two observations are listed in Table 36.1, the third is depicted in Fig. 36.4, and the fourth point is discussed by Biryukov et al. [28]. One point that is immediately apparent from Table 36.1 and a perusal of literature data is that deviations from bulk properties are nearly universal, but the thickness at which the properties begin to diverge and the magnitude of the disparity are strongly dependent on

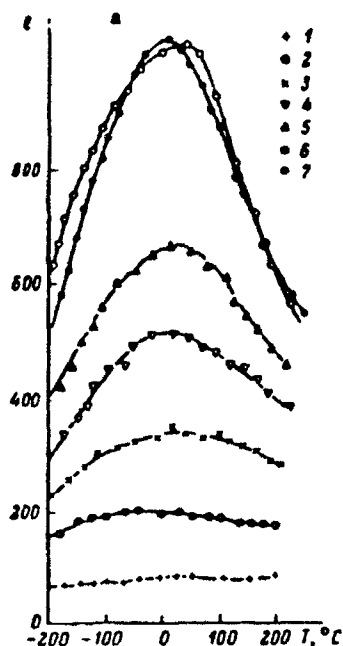


Figure 36.4. Temperature dependences of  $\epsilon$  (a) and  $\tan \delta$  (b) for  $(\text{Ba}, \text{Sr})\text{TiO}_3$  films. Film thickness  $d$  (micrometers): (1) 0.1; (2) 0.33; (3) 0.5; (4) 1.0; (5) 2.0; (6) 5.0; (7) 8.2. Data from Ref. [52].

TABLE 36.1. Remanent Polarization and Coercive Field in a Number of Perovskite Films

Material <sup>a</sup>	$P_r$ ( $\mu\text{C}/\text{cm}^2$ )	$E_c$ (kV/cm)	Reference
Single-crystal $\text{PbTiO}_3$	~ 55-75	6.75	35
Sol-gel $\text{PbTiO}_3$	3.37	54.8	36
Sputtered (001) $\text{PbTiO}_3$	55	75	37
Sputtered (001) $\text{PbTiO}_3$	35	160	38
Sputtered or CVD $\text{PbTiO}_3$	12	250	39
CVD (001) $\text{PbTiO}_3$	14.1	20.16	40
Bulk PZT 58/42	45	17	41
Sol-gel PZT	36		42
Sol-gel PZT 53/47	12	150	43
Sol-gel PZT 52/48	35		34
Sol-gel PZT	18-20	50-60	44
Sol-gel PZT 40/60	6.6	26.7	45
Sputtered PZT 90/10	13.9	60.0	46
Sputtered PZT 58/42	30.0	25	41
Sputtered PZT 65/35, weak (100)	12.5	90	47
Sputtered PZT 65/35	3.6	33	47
Sol-gel PLZT 2/54/46	28.5	190	48
Single-crystal $\text{BaTiO}_3$	26	1	49
Polycrystalline $\text{BaTiO}_3$	8	3	49
Sputtered $\text{BaTiO}_3$	0.8	3	50
Screen-printed $\text{BaTi}_{0.95}\text{Sn}_{0.05}\text{O}_3$	1.7-2.8	25	51
Sputtered (001) $\text{BaTiO}_3$	7	60	33
Sputtered $\text{BaTiO}_3$ , weak (101)	16	20	33

<sup>a</sup>Abbreviations: CVD, chemical vapor deposition; PZT, lead zirconate titanate; PLZT, lead lanthanum zirconate titanate

the preparation conditions. Consequently, films produced at one laboratory may display marked size effects, while others of the same thickness and composition possess bulk properties.

The reasons for this type of discrepancy lie in the variety of mechanisms causing the apparent size effect. Included among these are microstructural heterogeneities, variations in crystalline quality, mechanical stresses imposed on the film by the substrate, space charge effects, and finally intrinsic size effects. It is critical to note that the first two of these, which in the opinion of the authors account for the majority of the "size effects" observed in thin-film properties, are, in fact, size independent. It is fortuitous, then, that many film preparation techniques produce films that are defective and would remain defective even if macroscopic samples could be fabricated.

Inhomogeneity in the film microstructure can take the form of incorporated porosity, surface and interface roughness, or variations in the grain size. In particular, many ferroelectrics grown by vapor deposition processes are columnar and should be expected to have low densities (Fig. 36.5). This, in turn,

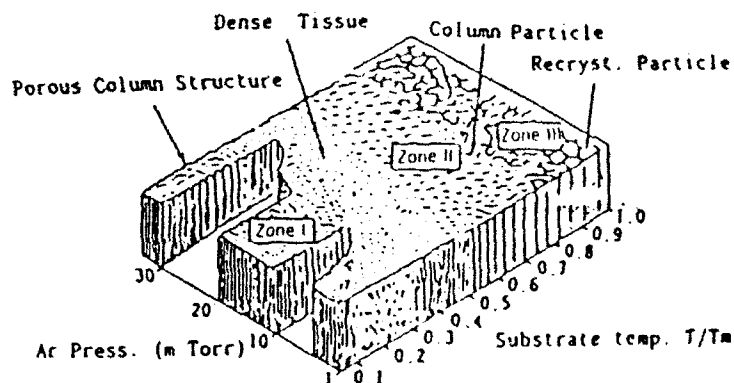


Figure 36.5. Structure of sputtered film as a function of gas pressure and normalized substrate temperature [37].

could appreciably lower the dielectric constant and, if there was poor coupling between the grains, would increase the coercive field as well [29]. Even in films that appear dense, Dudkevich et al. have shown that the microstructure may change continuously as a function of film thickness [30]. Thus, for sputtered  $\text{Ba}_{0.85}\text{Sr}_{0.15}\text{TiO}_3$  films, thinner films tend to be composed of small particles (15 nm for a 4-nm-thick film) where thicker films show a distribution of grain sizes ranging from the very fine particles deposited next to the substrate to larger grains at the film surface (200–300 nm for a film 2000 nm thick). Given this type of microstructural heterogeneity, it is no wonder that many properties appear to depend on film thickness. As the absolute grain size at any given thickness is expected to be a sensitive function of both the deposition conditions and any postannealing, samples prepared at different laboratories should behave differently.

A second significant influence on thin-film properties is the crystalline quality of the ferroelectric material. It is known that the loss of clear X-ray diffraction peaks is coupled to the disappearance of the paraelectric-ferroelectric phase transition. Unfortunately, many film deposition techniques also result in poor crystallinity. During sputtering, for example, the growing film is subjected to bombardment by high-energy ions. While this can be advantageous in terms of providing additional energy to the deposit and increasing the surface mobility, heavy bombardment, particularly at low substrate temperatures, can also introduce high defect concentrations. In chemically prepared thin films, on the other hand, low annealing temperatures can be insufficient to crystallize the ferroelectric phase fully.

Fast neutron irradiation of  $\text{BaTiO}_3$  single crystals (neutron energy  $\geq 50$  keV), for example, eventually introduces sufficient defects that the material transforms into a metastable cubic state with an expanded lattice parameter [31]. Having undergone this transition, no displacive transformation to the tetragonal, ferroelectric, state can be detected at temperatures above 78 K. Although the

bulk still displays some long-range order, the X-ray peaks are broadened by a factor of 5 over the unirradiated crystal, and it is not unlikely that the surface was completely amorphized. Annealing to 1000°C is required before the lattice parameter relaxes back to its initial value. Unfortunately, in many thin films, annealing temperatures are kept as low as possible to minimize changes in stoichiometry. While this may help maintain the perovskite structure, it is probable that 500–700°C is insufficient to crystallize amorphous or badly damaged films fully. Many authors working with either vacuum-deposited or chemically prepared thin films report modifications of the perovskite structure with a slightly expanded cubic unit cell [32].

In characterizing the crystallinity of ferroelectric films, Surowiak et al. [33] measured lattice strains in sputter-deposited BaTiO<sub>3</sub> films. They found that films that experienced heavy bombardment during growth tended to have more heavily deformed crystallites (i.e., the mean microdeformation  $\Delta d/d$  was as large as 0.01–0.005) and small coherent scattering sizes. Larger, less defective crystallites ( $\Delta d/d < 0.005$ ) could be formed when the growth conditions were not as rigorous [33]. Differences between the two types of films were readily apparent in the electrical properties: lower  $\Delta d/d$  values were associated with high remanent polarizations, piezoelectric constants close to single-crystal values, and relatively narrow phase transitions. This last point was examined by Biryukov et al. [28], who demonstrated that films with large lattice strains should be expected to show diffuse phase transitions. Poorly crystallized films from any preparation method will probably display low remanent polarization, lowered dielectric and electromechanical coupling constants, and diffuse phase transitions.

It is not surprising that mechanical stresses should also affect thin-film properties. As in most ferroic materials, the appearance of the order parameter at the transition temperature is accompanied in perovskite ferroelectrics by a spontaneous strain. Domain structure should be influenced by the types of strains present in the film. In a similar way, stresses in heteroepitaxial films have been shown to alter the equilibrium domain structure. Two-dimensional stresses can stabilize the ferroelectric phase to higher temperatures in bulk materials and this mechanism could operate in thin films when there is good cohesion between the substrate and the film.

The primary difference between size effects in ferromagnetic materials and ferroelectric materials is that, in the electrical analog, it is necessary to compensate the polarization at the surface of the material. In a ferroelectric that is slightly conducting or electroded with a material with a low carrier density, tremendous depolarization fields or space charge migration can be generated even in comparatively thick films ( $\sim 1\ \mu\text{m}$ ). These can shift the phase transition temperature, lower the magnitude of the spontaneous polarization, and even destabilize the ferroelectric phase in the film.

Despite all of these opportunities for extrinsic size effects, there is evidence that films that are prepared carefully can display near bulk properties to very

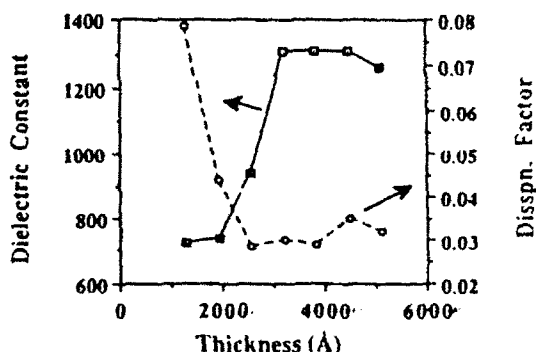


Figure 36.6. Dielectric constant and dispersion factor as a function of film thickness

small thicknesses. In work on sol-gel PZT films, Udayakumar [34], for example, showed that room temperature dielectric constants of ~1300 could be maintained for films exceeding 300 nm thick (Fig. 36.6). The bulk remanent polarization was retained to 450 nm and remained finite, though reduced, in films 190 nm thick (Fig. 36.7). The high breakdown strength of these films (Fig. 37.8) will also be critical in device applications [34].

In work on RF-sputtered BaTiO<sub>3</sub> films, Dudkevich et al. [30] showed that the size of the coherent scattering region, *D*, within their films was more important than the thickness in determining the macroscopic electrical properties. As seen in Fig. 36.9, the dielectric constant increases markedly as the

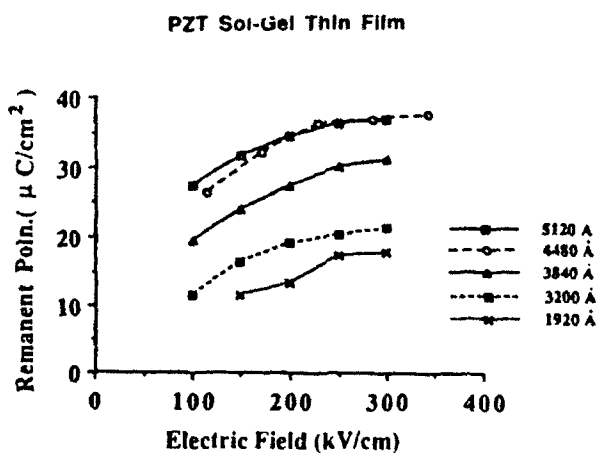


Figure 36.7. Remanent polarization in PZT sol-gel thin films as a function of electric field.

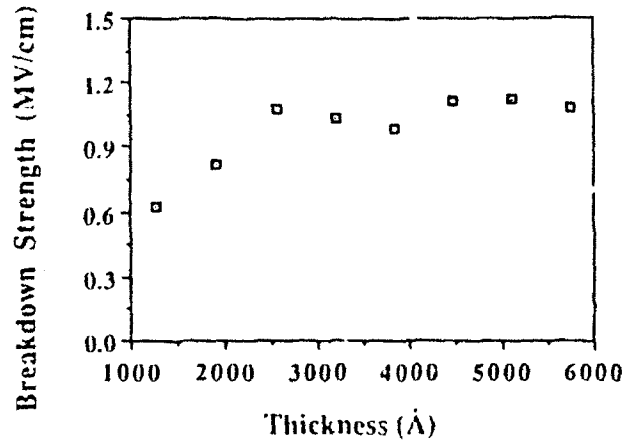


Figure 36.8. Breakdown strength as a function of film thickness.

coherent scattering size grows larger than  $\sim 30$  nm, and when  $D$  reached 50 nm, room temperature dielectric constants exceeding 1000 were achieved, and some indication of a dielectric constant peak could be detected at the Curie temperature [30].

As shown in Table 36.1, several other recent papers have demonstrated that it is possible to achieve bulk or near bulk properties for several members of the perovskite family.

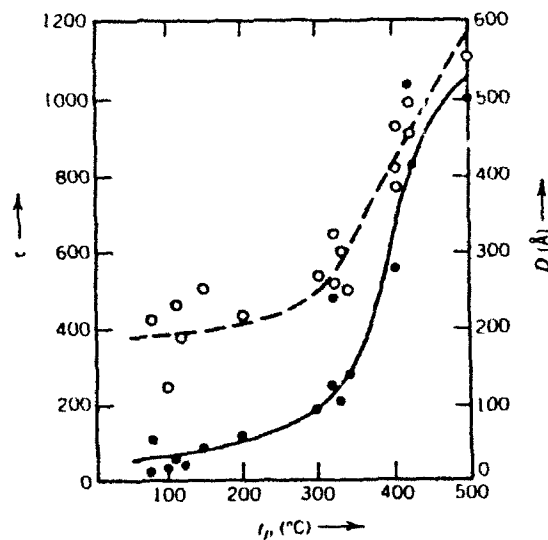


Figure 36.9. Size of the coherent scattering region (curve 1) and the dielectric permittivity (curve 2) of  $\text{BaTiO}_3$  films as a function of substrate temperature. Taken from Ref. [30].

## CONCLUSIONS

As the field of ferroelectric thin films grows, it becomes increasingly important to examine the role of size effects on the expected properties. While intrinsic size effects similar to those demonstrated in ferromagnetic analogs will act as lower limits to the size of ferroelectric devices, in many cases extrinsic, processing-induced contributions overshadow the fundamental size restrictions. Consequently, careful characterization of films to determine the role of extrinsic effects (i.e., internal microstructure, interface layers, and poor crystallinity) are necessary to understand relationships between processing and properties in ferroelectric films.

## REFERENCES

1. Ph. Buffat and J. P. Borel, Size Effect on the Melting Temperature of Gold Particles, *Phys. Rev. A* **13**(6), 2287-2298 (1976).
2. M. Takagi, Electron-Diffraction Study of Liquid-Solid Transition in Thin Metal Films, *J. Phys. Soc. Jpn.*, **9**(3), 359-363 (1954).
3. N. T. Gladkikh, R. Niedermayer, and K. Spiegel, Nachweis großer schmelzpunktserniedrigungen bei dünnen metallschichten, *Phys. Stat. Sol.*, **15**, 181-191 (1966).
4. M. Blackman and A. E. Curzon, On the Size Dependence of the Melting and Solidification Temperatures of Small Particles of Tin, *Structure and Properties of Thin Films*, Wiley, New York (1959).
5. B. T. Boiko, A. T. Pugachev, and Y. M. Bratsykhin, Melting of Subcritically Thin Condensed Films of Indium, *Sov. Phys. Sol. State*, **10**(12), 2832-2834 (1969).
6. M. Ido, Fluctuation Effect on the Knight Shift of Superconducting Al Fine Particles, *J. Phys. Soc. Jpn.*, **41**(2), 412-418 (1976).
7. I. Hlasnik et al., Properties of Superconducting NbTi Superfine Filament Composites with Diameters  $< \sim 0.1 \mu\text{m}$ , *Cryogenics*, **25**, 558-565 (1985).
8. H. P. Watson, Critical Magnetic Field and Transition Temperature of Synthetic High-Field Superconductors, *Phys. Rev.* **148**(1), 223-230 (1966).
9. T. Chainer, Y. Morii, and H. Kojima, Size Effects in Superfluid  $^3\text{He}$ , *Phys. Rev. B*, **21**(9), 3941-3944 (1980).
10. C. Kittel, Theory of the Structure of Ferromagnetic Domains in Films and Small Particles, *Phys. Rev.*, **70**(11, 12), 965-971 (1946).
11. E. F. Kneller and F. E. Luborsky, Particle Size Dependence of Coercivity and Remanence of Single-Domain Particles, *J. Appl. Phys.*, **34**(3), 656-658 (1964).
12. A. E. Berkowitz, W. J. Schuele, and P. J. Flanders, Influence of Crystallite Size on the Magnetic Properties of Acicular  $\gamma\text{-Fe}_2\text{O}_3$  Particles, *J. Appl. Phys.*, **39**(2), 1261-1263 (1968).
13. M. H. Lee, A. Halliyal, and R. E. Newnham, Poling Studies of Piezoelectric Composites Prepared by Coprecipitated  $\text{PbTiO}_3$  Powder, *Ferroelectrics*, **87**, 71-80 (1988).
14. C. P. Bean and L. S. Jacobs, *J. Appl. Phys.*, **27**(12), 1448 (1956).
15. O. Kubo, T. Ido, H. Yokoyama, and Y. Koike, Particle Size Effects on Magnetic Properties of  $\text{BaFe}_{12-2x}\text{Ti}_x\text{Co}_x\text{O}_{19}$  Fine Particles, *J. Appl. Phys.*, **57**(1), 4280-4282 (1985).
16. L. E. Cross, Relaxor Ferroelectrics, *Ferroelectrics*, **76**(3/4), 241-267 (1987).
17. D. Viehland, S. J. Jang, L. E. Cross, and M. Wuttig, Freezing of the Polarization Fluctuations in Lead Magnesium Niobate Relaxors, *J. Appl. Phys.*, **68**(6), 2918-2921 (1990).

18. K. Ishikawa, K. Yoshikawa, and N. Okada, Size Effects on the Ferroelectric Phase Transition in  $\text{PbTiO}_3$  Ultrathin Particles, *Phys. Rev. B*, **37**(10), 5852-5855 (1988)
19. K. Uchino, preprint, American Ceramic Society annual meeting (1989)
20. K. Saegusa, W. E. White, and H. K. Bowen, Preparation of  $\text{Pb}_x\text{Ba}_{1-x}\text{TiO}_3$  and the effect of Composition and the Size of the Crystallite on the Crystal Phase, preprint, American Ceramic Society annual meeting (1989)
21. S. Iyomura, I. Matsuyama, and G. Toda, Effects of the Lapped Surface Layers on the Dielectric Properties of Ferroelectric Ceramics, *J. Appl. Phys.*, **51**(11), 5838-5844 (1980)
22. R. Bachmann and K. Barner, Stable Suspensions of Ferroelectric  $\text{BaTiO}_3$  Particles, *Sol. State Commun.*, **68**(9), 865-869 (1988)
23. P. Beauvillain, C. Chapert, J. P. Renard, C. Marbère, and D. Renard, Magnetic Interaction Between Ultrathin Nickel Films Through a Gold Interlayer, in *Magnetic Thin Films*, 1986, R. Krishnan ed., les editions de physique, France (1986)
24. M. Prutlon, *Thin Ferromagnetic Films*, Butterworth and Co. Ltd, Washington (1964)
25. K. Binder, Surface effects on Phase Transitions in Ferroelectrics and Antiferroelectrics, *Ferroelectrics* **35**, 99-104 (1981)
26. M. Tanaka and G. Honjo, Electron Optical Studies of Barium Titanate Single Crystal Films, *J. Phys. Soc. Jpn.*, **19**(C), 954-970 (1964)
27. G. Arlt, D. Hennings, and G. de With, Dielectric Properties of Fine-Grained Barium Titanate Ceramics, *J. Appl. Phys.*, **58**(4), 1619-1625 (1985)
28. S. V. Biryukov, V. M. Mukhortov, A. M. Margolin, Yu. I. Golovko, I. N. Zakharchenko, V. P. Dudkevich, and E. G. Fesenko, Phase Transitions in Polycrystalline and Heteroepitaxial Ferroelectric Films, *Ferroelectrics*, **56**, 115-118 (1984)
29. Q. Jiang, The Pennsylvania State University private communication (1990)
30. V. P. Dudkevich, V. A. Bukreev, V. M. Mukhortov, Yu. I. Golovko, Yu. G. Smedev, V. M. Mukhortov, and E. G. Fesenko, Internal Size Effect in Condensed  $\text{BaTiO}_3$  Ferroelectric Films, *Phys. Stat. Sol. (a)*, **65**, 463-467 (1981)
31. M. C. Wittels and J. A. Sherrill, Fast Neutron Effects in Tetragonal Barium Titanate, *J. Appl. Phys.*, **28**(5), 606-609 (1957)
32. S. Naka, I. Nakakita, Y. Suwa, and M. Inagaki, Change from Metastable Cubic to Stable Tetragonal Form of Submicron Barium Titanate, *Bull. Chem. Soc. Jpn.*, **47**(5), 1168-1171 (1974)
33. Z. Surowiak, A. M. Margolin, I. N. Zakharchenko, and S. V. Biryukov, The Influence of Structure on the Piezoelectric Properties of  $\text{BaTiO}_3$  and  $(\text{BaSr})\text{TiO}_3$  Thin Films with a Diffuse Phase Transition, *Thin Solid Films*, **176**, 227-246 (1989)
34. K. R. Udayakumar, J. Chen, S. B. Krupanidhi, and L. E. Cross, Sol-Gel Derived PZT Thin Films for Switching Applications, paper presented at the International Symposium on Applications of Ferroelectrics 1990 (1990)
35. V. G. Gavrilyachenko, R. I. Spinko, M. A. Martynenko, and E. G. Desenki, Spontaneous Polarization and Coercive Fields of Lead Titanate, *Sov. Phys. Sol. State*, **12**(5), 1203-1204 (1970)
36. A. X. Kuang, L. S. Wu, and Q. F. Zhou,  $\text{PbTiO}_3$  Thin Film Prepared by Sol-Gel Process, *ISAF 1990 Abstr.*, X.34 (1990)
37. E. Yamaka, H. Watanabe, H. Kimura, H. Kanaya, and H. Okhuma, Structural, Ferroelectric, and Pyroelectric Properties of Highly *c*-Axis Oriented  $\text{Pb}_{1-x}\text{Ca}_x\text{TiO}_3$  Thin Film Grown by Radio-frequency Magnetron Sputtering, *J. Vac. Sci. Technol. A*, **6**(5), 2921-2928 (1988)
38. K. Iijima, Y. Tomita, R. Takayama, I. Ueda, Preparation of *c*-Axis Oriented  $\text{PbTiO}_3$  Thin Films and Their Crystallographic, Dielectric, and Pyroelectric Properties, *J. Appl. Phys.*, **60**(1), 361-367 (1986)
39. M. Okuyama and Y. Hamakawa, Preparation and Basic Properties of  $\text{PbTiO}_3$  Ferroelectric Thin Films and Their Device Applications, *Ferroelectrics*, **63**, 243-252 (1985)

- 40 S-G Yoon, H Y Lee, and H G Kim, Compositional Analysis of Lead Titanate Thin Films by Auger Electron Spectroscopy and Their Electrical Properties, *Thin Solid Films*, **171**, 251-262 (1989)
- 41 K. Sreenivas and M. Sayer, Characterization of  $\text{Pb}(\text{Zr}, \text{Ti})\text{O}_3$  Thin Films Deposited from Multi-element Metal Targets, *J. Appl. Phys.*, **64**(3), 1484-1493 (1988)
- 42 D. A. Payne, Integration of Ferroelectric Materials on Semiconductors by Sol-Gel Methods, *ISAF 1991 Abstr.*, 12.1 (1990)
- 43 H. Nagata, M. Watanabe, H. Sakai, and I.Y. Kubota, Thin Film Ferroelectrics of PZT System by Sol-Gel Processing, *ISAF 1990 Abstr.*, X.1 (1990)
- 44 S. K. Dey and R. Zuleeg, Sol-Gel Ferroelectric Thin Films Merged with GaAs JFET Memory Technology, *ISAF 1990 Abstr.*, 12.2 (1990)
- 45 G. Yi, Z. Wu, and M. Sayer, Preparation of  $\text{Pb}(\text{Zr}, \text{Ti})\text{O}_3$  Thin Films by Sol-Gel Processing: Electrical, Optical, and Electro-optic Properties, *J. Appl. Phys.*, **64**(5), 2717-2724 (1988)
- 46 T. Okamura, M. Adachi, T. Shosaki, and A. Kawabata, Epitaxial Growth of Ferroelectric  $\text{Pb}(\text{Zr}_{0.4}\text{Ti}_{0.6})\text{O}_3$  Films by Reactive Sputtering of Multi-Metal Target, *ISAF 1990 Abstr.*, X.5 (1990)
- 47 A. Croteau, S. Matsubara, Y. Miyasaka, and N. Shohata, Ferroelectric  $\text{Pb}(\text{Zr}, \text{Ti})\text{O}_3$  Thin Films Prepared by Metal Target Sputtering, *Jpn. J. Appl. Phys.*, **26**(Suppl. 26-2), 18-21 (1987)
- 48 Z. Wu and M. Sayer, Properties of Sol-Gel Processed PLZT (2/54/46) Thin Films, *ISAF 1990 Abstr.*, X.6 (1990)
- 49 B. Jaffe, W. R. Cook, Jr., and H. Jaffe, *Piezoelectric Ceramics*, Academic, India (1971)
- 50 T. Nagatomo and O. Omoto, Preparation of  $\text{BaTiO}_3$  Films by rf Sputtering and Their Crystallographic, Dielectric, and Optical Properties, *Jpn. J. Appl. Phys.*, **26**(Suppl. 26-2), 11-14 (1987)
- 51 M. Loposzko, M. Pawelczyk, M. Urbanska, and Z. Surowiak, Diffuse Phase Transitions in Thick Ferroelectric  $\text{Ba}(\text{Ti}_x\text{Sn}_{1-x})\text{O}_3$  Films of Perovskite-Type Structure, *Thin Solid Films*, **69**, 339-345 (1980)
- 52 A. A. Gitel'son, A. M. Lerer, V. S. Mikhalevskii, V. M. Mukhortov, and S. V. Orlov, Physical Properties of  $(\text{Ba}, \text{Sr})\text{TiO}_3$  Ferroelectric Thin Films in Weak Electric Fields, *Sov. Phys. Solid State*, **19**(7), 1121-1124 (1977)

**APPENDIX 51.**

SPECTROSCOPIC ELLIPSOMETRY STUDIES ON ION BEAM SPUTTER DEPOSITED  
Pb(Zr,Ti)O<sub>3</sub> FILMS ON SAPPHIRE AND PT-COATED SILICON SUBSTRATES

S. Trolier-McKinstry, H. Hu, S. B. Krupanidhi,  
P. Chindaudom\*, K. Vedam, and R. E. Newnham

Materials Research Laboratory  
The Pennsylvania State University  
University Park, PA 16802

\*P Chindaudom is now with NECTECH, Ministry of Science, Bangkok, Thailand

Abstract

Spectroscopic ellipsometry has been utilized to non-destructively depth profile multi-ion-beam reactively sputtered lead zirconate titanate films. Some degree of inhomogeneity (in the form of low density layers or surface roughness) was found in all of the films examined. The evolution in the structure and microstructure of such films during post-deposition annealing was investigated with *in-situ* spectroscopic ellipsometry. It was found that the onset of microstructural inhomogeneities was associated with the crystallization of the perovskite phase, and that the final film microstructure was dependent on the details of the annealing process.

A model was developed to approximate the effect that local density variations play in determining the net electrical properties of ferroelectric films. Depending on the configuration of the embedded porosity, it was demonstrated that microstructural inhomogeneities can significantly change the net dielectric constant, coercive field, and remanent polarization of ferroelectric films. It has also been shown that low density regions near the film/substrate interface can result in apparent size effects in ferroelectric films.

## Introduction

Ferroelectric thin films are potentially useful as pyroelectric sensors, ferroelectric memory elements, electrooptic switches, and miniature electromechanical transducers. For these applications, high quality films with reproducible electrical, optical, and electromechanical properties are required. Several growth techniques have emerged in the recent past for the deposition of multi-cation oxide films. In all cases, the final properties seem to be closely connected to the nature of the deposition process [1]. For this study, multi-ion-beam reactive sputtering (MIBERS) was chosen for the growth of optical quality perovskite films. Films for optical applications should have a uniform smooth surface, should be free from defects or inclusions, and should possess minimal absorption and low scattering over the wavelengths of interest. With the MIBERS technique the composition, microstructure, and physical morphology of the films can be controlled by careful choice of the growth conditions [2,3].

Unfortunately, as is the case for transparent films used in optical coatings, non-destructive characterization of the film (including any variations in the microstructure with depth in the sample) has in the past been difficult to perform. To alleviate this problem, this paper describes spectroscopic ellipsometry (SE) as a non-destructive, non-invasive tool for depth profiling ferroelectric thin films on both transparent and absorbing substrates.

The success of SE for depth-profiling samples was demonstrated in the 1970's (e. g. [4]). Following the initial demonstration, careful studies were undertaken to demonstrate that the SE results are consistent with other characterization tools [5-8]. SE has since become widely used for characterizing thin film systems where at least one component is strongly absorbing. Transfer of the process to either monolithic transparent samples or transparent films on transparent substrates, however, has been hindered by inherent difficulties in obtaining accurate SE data for such samples. This difficulty has recently been overcome via the development of a series of systematic

calibrations for a rotating analyzer spectroscopic ellipsometer [9,10]. The information derived from this technique is particularly useful in correlating the role of the processing procedure in controlling the physical structure and net electrical properties of ferroelectric thin films.

### Film Preparation

Pb(Zr,Ti)O<sub>3</sub> (PZT) films with a Zr/Ti ratio of about 50/50 were deposited by multi-ion-beam reactive sputtering [2]. This technique, as established earlier, offers a highly controllable, reproducible deposition process with excellent uniformity in composition and thickness for large surface area samples. As substrates for the deposition of oriented films, both (1 $\bar{1}$ 02) and (0001) sapphire were used (One side polished, Union Carbide). The interest in (1 $\bar{1}$ 02) sapphire stems from the fact that this orientation can be grown epitaxially on silicon, leading to the possibility of integrating a PZT electrooptic component on to a silicon substrate prepared with a sapphire intermediate layer [11]. In addition, platinum-coated silicon wafers were also utilized as substrates for some films. These latter substrates had a thick SiO<sub>2</sub> barrier layer to prevent reaction between platinum and silicon at elevated temperatures, and a thin Ti film between the SiO<sub>2</sub> and Pt to improve adhesion.

The depositions were carried out on unheated substrates without low energy ion assistance. It was observed that the substrate temperature rose to about 100°C during deposition due to intrinsic bombardment by the sputtered species. While the films on sapphire were deposited with a Pb content very close to the stoichiometric composition of the perovskite phase, the films on Pt-coated silicon were deposited with 3 - 6% excess Pb to promote crystallization of the correct phase on annealing [2]. Some films were reserved for *in-situ* ellipsometric studies. The remaining films were heated *ex-situ* at 10°C/min to 650°C and soaked at this temperature for 2 hrs. This procedure yields well-crystallized perovskite films. All films deposited on sapphire showed highly

oriented X-ray diffraction patterns after annealing. Films on  $(\bar{1}102)$  substrates, as seen in Fig. 1, were almost exclusively (101) oriented. Similarly, with (0001) substrates, the films were also (101) orientated, although to a lesser degree. Films on Pt-coated silicon had a random polycrystalline orientation. Ferroelectricity was established by measuring hysteresis loops for the films on Pt-coated silicon substrates.

### Ellipsometer configuration and calibration

A schematic of the rotating-analyzer spectroscopic ellipsometer used in these experiments is shown in Figure 2. In addition to standard calibrations to eliminate first order errors in the optics [12], two additional steps were required to achieve accurate data for transparent samples. First, the problem of detector non-linearity was minimized by calibrating the polarization detection system both for the presence of ambient light and for variations in the gain of ac and dc components of the signal with changes in the overall signal level [13]. Secondly, inherent difficulties in accurately measuring the near  $0^\circ$  (or  $180^\circ$ ) phase change on reflection from a transparent sample [14] were overcome through the use of an achromatic compensator.

In contrast to the standard Babinet-Soleil compensator, the three-reflection achromatic compensator [15] used in these experiments produces approximately a  $90^\circ$  phase retardation for all wavelengths between 300 and 800 nm. To correct for the remaining wavelength dependent errors introduced by the compensator, a two-measurement, "effective source" calibration was utilized. With this technique, the polarization state of the light emerging from the compensator is first measured at each wavelength with the ellipsometer detection arm in the straight-through position. Then, the sample is aligned at the desired angle of incidence and measured over the same wavelength range to obtain a spectrum containing lumped information on the sample properties and the source polarization. The change in the light polarization due to reflection from the sample itself, the quantity of interest, can then be calculated.

With these calibrations in place, the ellipsometric parameters  $\Delta$  and  $\Psi$  can be measured for transparent samples to within  $0.03^\circ$  and  $0.01^\circ$ , respectively, over the spectral range 300 - 800 nm. This corresponds to an accuracy in the real and imaginary parts of the refractive index of 0.001 [9,13] for a bulk specimen of vitreous silica [16]. As shown in Figure 3, this is an order of magnitude improvement over the accuracy which can be obtained without these data correction procedures. It should be noted that the additional procedures utilized constitute a calibration of the polarization detection system, and as such are sample independent.

Measurements made as a function of temperature were performed in a windowless electrical resistance furnace. As shown in Figure 4, a kanthal-wire wrapped alumina tube was used as the heat source. The temperature was monitored by a thermocouple placed within half an inch of the sample, and controlled by computer. The outer shell of the chamber consisted of a capped, monolithic brass cylinder machined with two  $1/2" \times 1/4"$  holes for the entrance and exit beams. Both the cylinder and the baseplate were subsequently electroplated with nickel to minimize oxidation of the copper and vaporization of the zinc at elevated temperatures. Because the chamber is windowless, no additional corrections for the ellipsometer optics were required.

### Experimental Procedure

Measurements were made on films on sapphire substrates at an incidence angle of  $80^\circ$  using the compensator and the effective source calibration described above. For films on Pt-coated Si, measurements were performed at an angle of incidence of  $70^\circ$  without the compensator. SE data were collected both on films which had been annealed at  $650^\circ\text{C}$  for 2 hours and on as-deposited films which were heat-treated *in-situ* in the ellipsometer. For the *in-situ* experiments, data were taken at different annealing temperatures in  $50^\circ\text{C}$  intervals between 25 and  $60^\circ\text{C}$ . Between room temperature and  $350^\circ\text{C}$ , data were collected at the annealing temperature. Above  $400^\circ\text{C}$ , however, the

film was heated to the desired temperature, soaked for half an hour, and cooled below 300°C for measurement to eliminate errors associated with glow from the furnace. In all cases, the film was heated to the previous annealing temperature at 5°C/min, and then raised from there to the new annealing temperature at 2°C/min. Cooling was done at 5°C/min until the furnace could no longer follow. After this treatment, the same film was annealed in a conventional furnace at 650°C for 2 hr in order to match the maximum annealing temperature experienced by the *ex-situ* annealed samples. Following data collection, the SE data were modelled in order to analyze the film thickness, optical properties and the degree of inhomogeneity present within the film.

Modelling of the experimental data was done under the assumption of planar interfaces between layers with all layers parallel to the surface of the film. Inhomogeneities in the film density were described by subdividing the film into a series of layers with different volume fractions of air present in each. Bruggeman effective medium theory was used to calculate the effective dielectric functions of two phase mixtures. Variables in the fitting procedure included all of the layer thicknesses, the volume fraction of air present at any depth in the film, and the dispersion relation describing the optical properties of the film itself. The equation used to describe the film refractive index was:

$$(n + ik)^2 = 1 + \frac{A(1)\lambda^2}{\lambda^2 - \lambda_0^2 - i2\lambda A(2)} \quad (\text{eq. 1})$$

where  $(n + ik)$  is the complex refractive index,  $\lambda$  is the wavelength in nm,  $\lambda_0$  is the oscillator position, and  $A(1)$  and  $A(2)$  are constants. Both  $\lambda_0$  and the  $A(j)$  were determined during the fitting. To reduce the number of variables, the optical properties of the film were assumed to be isotropic.

Reference optical property data were used to describe the substrate dielectric functions. For sapphire, reference data were taken from Malitson [17] and Jeppesen

[18] for the ordinary and extraordinary indices, respectively. Because the literature values for  $dn/dT$  are so small (on the order of  $10^{-5}/^{\circ}\text{C}$ ), room temperature data for the refractive indices of sapphire were used at all temperatures. For the Pt-coated silicon substrates, ellipsometric spectra were collected for the bare substrate, and were directly inverted to provide an effective dielectric function for the exposed metal. Modelling of the data for these substrates showed that the surfaces consisted of roughened platinum. Unfortunately, the degree of roughness was found to change as the substrates were heated, so there is considerable residual uncertainty in the effective dielectric functions for the Pt-coated silicon substrates.

For the modelling, the data sets were truncated to between 400 and 800 nm in order to eliminate the onset of the absorption edge in PZT. Output from the fitting program included values for the "best-fit" parameters, 90% confidence limits for each variable, a correlation coefficient matrix describing the interrelatedness between variables, the unbiased estimator,  $\sigma$  [4], of the goodness of fit, and calculated  $\Delta$  and  $\Psi$  spectra for the final model. All of these factors were examined to determine the appropriateness of a given model.

With the exception of the films on (0001) sapphire, all of the fitting was done assuming that both film and substrate could be treated as isotropic materials. The routine which handled the propagation of light through anisotropic materials was written by Parikh and Allara [19] following the  $4 \times 4$  matrix formalism of Yeh [20,21]. An anisotropic substrate model was not used for the film on ( $\bar{1}102$ ) sapphire as the angle between the inclined optic axis of the alumina and the plane of incidence of the light could not be determined accurately.

#### Analysis of Crystallized MIBERS Films on Sapphire and Pt-coated Silicon

Results from the ellipsometric modelling of the SE data for the films annealed at  $650^{\circ}\text{C}$  for 2 hr are shown in Table 1. All of the films were determined to be between

400 and 600 nm thick, which is consistent with profilometry measurements on the same films. In most cases, a low density interfacial layer between the substrate and the film was essential to properly match the peak heights in both the  $\Delta$  and  $\Psi$  spectra. In addition, layer of surface roughness improved the fit for some films. As seen in Figure 5, the final fits resulted in very good matches to the experimental data.

The high refractive indices obtained for the middle layer of the films suggest that this region is reasonably dense. Figure 6 shows the modelled refractive indices for several films on sapphire (determined with  $A(2)$  from eq. 1 assigned to zero) in comparison with reference data for 2/65/35 and 16/40/60 PLZT ceramics [22]. As the refractive index of PLZT ceramics is largely controlled by the Zr/Ti ratio [22], the film on (0001) sapphire in particular shows excellent agreement with the values which would be expected for a dense PZT 50/50 material. The lower  $n$  values for the films on ( $\bar{1}102$ ) sapphire could be due either to the presence of residual porosity distributed throughout the densest portion of the film or the assumption of isotropic behavior for both the film and the substrate. When these films were modelled with reference data from the film on (0001) sapphire, 5.7% additional residual porosity was required in each layer of the film to fit the experimental data.

Unless the restriction  $A(2) = 0$  was imposed during the fitting, however, finite values for the imaginary part of the refractive index in the films were obtained in the SE modelling. In part, the larger  $k$  values may reflect the fact that transparency in lead-based perovskites decreases as the lanthanum content is reduced. The opacity of dense, bulk PZT ceramics has been attributed to light scattering at refractive index discontinuities such as domain walls and grain boundaries consisting of a second phase [23]. It is likely that the same mechanisms are present in the films. In addition, there are probably "microstructural" contributions to the effective  $k$  which arise from inhomogeneities in the film not accounted for in the modelling (i.e. scattering from distributed porosity in the bulk of the film, the presence of a lossy layer associated with

either space charge formation or lead loss during firing, or the presence of additional porosity in the film not properly accounted for in the modelling). It was also found that a non-zero value of  $A(2)$  resulted in an increase in the dispersion found for the film refractive indices and a somewhat improved fit for the SE data on the films. The reason for this additional dispersion is unknown. The values reported in Table 1 are for fits with a non-zero  $A(2)$ . Because of the uncertainties in the optical properties of the Pt-coated silicon substrates, it was not possible to determine the exact refractive indices for PZT films on such substrates.

Figure 7 shows a comparison of the *ex-situ* annealed PZT films on Pt-coated Si and (0001) sapphire substrates. Both are densest throughout the bulk of the films, with low density layers near the substrate and some surface roughness. This type of depth profile is common in films with a columnar or cluster morphology [24]. It is also consistent with SEM observations on the same films [2].

For the same annealing conditions, films on Pt-coated silicon possess a much thicker surface roughness layer than those on sapphire. That could be a result either of the higher degree of roughness of the sputtered Pt substrate or the higher initial PbO content in the film on platinum. As discussed by Yang et al. [25], the roughness of a film with a columnar microstructure is dependent on the smoothness of the substrate: with rougher substrates leading to rougher films. Fox et al. [3] also suggest that crystallization of the perovskite phase and PbO vaporization are important in determining the microstructural features of annealed lead lanthanum titanate films.

#### Evolution of Structure During *In-Situ* Annealing

Films deposited at room temperature on  $(\bar{1}\bar{1}02)$  sapphire and Pt-coated Si substrates were annealed *in-situ* in the ellipsometer to determine whether the inhomogeneities seen in films crystallized conventionally were created during the deposition, or whether they were generated during the annealing. For these studies,

sapphire substrates were preferable as all changes in the spectra with temperature could be attributed unambiguously to the film. For the films on Pt-coated silicon, temperature-dependent changes in the effective substrate optical properties obscured interpretation of the SE data. Nevertheless, the results for the film on Pt-coated silicon seem consistent with those reported for the sapphire substrates.

Figure 8 shows the ellipsometric spectra collected during the annealing of the film on sapphire. The data can visually be divided into three regimes. At low temperatures the interference oscillations are damped strongly at short wavelengths. As shown in Figure 9, however, this additional damping disappears between 450° and 500°C. Little change occurs from this temperature until 600°C, which appears to mark a transition between the second and third regions. The latter, as illustrated with the data after the 650°C anneal, is characterized by higher  $\Psi$  values (See Fig. 8).

It was not possible to model the full spectra at low temperatures with a single oscillator, as that did not mimic the abrupt decrease in damping below 500nm. A much better fit could be achieved by mixing the contribution of the oscillator with reference data for rf sputtered lead oxide [26]. For all low temperature data, reference data for rf sputtered PbO provided a better fit than did data for evaporated PbO, largely because the band gap was shifted 0.6 eV lower in energy. No explanation for the disparity in the dielectric functions of the two was given by Harris et al. [26], though one possibility would be the presence of mixed valence states in the sputtered Pb [27]. Fits to as-deposited films on sapphire substrates were not improved significantly by the addition of surface roughness or a gradient in the PbO content to the model. Due to the strong correlation between the void volume fraction and the PbO content, it was not possible to achieve reproducible fits with low density regions near the film-substrate interface. No evidence for low density regions near the substrate were found in Fox's work on as-deposited MIBERS lead lanthanum titanate films [3].

The volume fraction of PbO remained approximately constant at lower temperatures, but beginning at 450°C, successively less PbO was required to match the ellipsometric spectra. Figure 10 shows the best-fit models for 450 and 500°C; the modelling is improved by allowing the lead "loss" to begin at the film surface and move progressively through the film thickness. Over the same temperature range, the film changed from an orange color to pale yellow.

Two possibilities would account for these changes. First, following composition analysis of as-deposited and annealed films, Fox et al. [3] concluded that as-deposited MIBERS lead lanthanum titanate thin films contain excess PbO which is removed during high temperature annealing. Comparable results were obtained on PZT films [2]. The onset temperature at which this was projected to occur was  $490 \pm 50^\circ\text{C}$  [3]. While this temperature is lower than that reported for PbO loss from bulk  $\text{PbTiO}_3$  samples [28], it is in good agreement with the SE experiments. Secondly, the lead oxide could at  $\sim 450^\circ\text{C}$  revert to a less lossy species. Thus, the increase in transparency at low wavelengths could be associated either with a homogenization of the lead oxidation state or with the incorporation of the lead species in to a more transparent phase (like that of evaporated PbO, the perovskite, or a pyrochlore phase). It is not possible to distinguish between these two mechanisms on the basis of the SE data and both may be operative. Similarly, although it is likely that a pyrochlore phase was formed during these lower temperature anneals (at least for the film on Pt-coated Si), this could not be unambiguously identified on the basis of the SE modelling.

At 550°C the experimental data were fit well with a two layer model consisting of a "dense" underlayer with a thin layer of surface roughness. As shown in Figure 11, the extent of the inhomogeneities becomes more pronounced for anneals above 550°C. In contrast to the samples annealed only at 650°C for 2 hrs (i.e. those not exposed to extended periods at intermediate temperatures), no low-density layer near the film/substrate interface was required to model the ellipsometric spectra.

Between the 500 and 550°C anneals, the film refractive index also increased markedly (see Figure 12). This is most likely associated with the crystallization of the perovskite phase. X-ray diffraction patterns following the 600 and 650°C anneals confirmed that the films on sapphire had converted to the perovskite structure with a very high degree of <110> orientation. Figure 12 also shows that the refractive index remains reasonably constant for all fits above 550°C; there is a slight drop at 650°C (not shown) that is probably associated with the fact that the "dense" bottom layer of the PZT contains some residual porosity. In summary, Figure 13 shows the proposed reaction scheme for changes occurring during the annealing of a MIBERS film deposited at room temperature.

#### Role of Annealing Profile in Controlling Inhomogeneities in MIBERS Films

In comparing the microstructures of films annealed in different ways, it is clear that while the inhomogeneity profiles are consistent for samples given identical annealing schedules, they are strongly dependent on variations in the heating cycle. This is apparent in Figure 14, which shows the SE-determined depth profiles for films annealed at 650°C for 2 hrs with and without extended lower temperature soaks. It is interesting that for samples annealed *in-situ* in the ellipsometer the major changes in the film inhomogeneities were coincident with the crystallization of the perovskite phase. This suggests that while the initial microstructure of a vapor-deposited film is controlled by factors such as substrate temperature, gas pressure, and adatom mobility [29], the final appearance is also a function of any post-deposition processes involving diffusion. Thus, in ferroelectric films elimination of excess PbO, reaction with the substrate, crystallization of either the pyrochlore or perovskite phases, and grain growth could successively alter the film microstructure. Additional support for this hypothesis is given by Fox et al. [3], who used scanning electron microscopy to follow the microstructural evolution of MIBERS lead lanthanum titanate films.

It is demonstrated in the following section that inhomogeneities in the microstructure, especially those associated with low density regions, alter the net coercive field, dielectric constant and remanent polarization of ferroelectric films. Given the dependence of the microstructure on the details of the post-deposition annealing profile observed here, it is clear that two films of the same composition, crystal structure, and thickness, which were annealed at the same peak temperature, could nevertheless still possess considerably different electrical properties. Consequently, post-deposition annealing should be considered an important variable in both the microstructure and property development of ferroelectric films.

It is also clear that the reasons for the discrepancies between the properties of the two films in Figure 14 would not be detected by X-ray diffraction. This clearly establishes the need for microstructure-sensitive characterization techniques in the study of ferroelectric films for device applications. Both spectroscopic ellipsometry and electron microscopy should be useful in this regard.

#### Influence of Inhomogeneities on the Electrical Properties of Films

Some ferroelectric films grown with the MIBERS technique possess low density regions near the film/substrate interface which are consistent with the appearance of either clustering or columns in the annealed film. Such a low density layer should be expected to alter the net electrical properties of the film. Indications of this can be seen experimentally in the hysteresis loop of a film which was shown to have an inhomogeneous depth profile by spectroscopic ellipsometry. The coercive field and net dielectric constant of the film was 75 kV/cm and ~850, respectively. By contrast, a homogeneous film of the same composition and the same grain size (chemically prepared) had a lower coercive field (~40 kV/cm) and a higher net dielectric constant. Both films have higher  $E_c$  values than would be expected for bulk ceramics of the same composition, probably as a result, in part, of the fine grain size of the films and stress

exerted on the film by the substrate [30]. Nevertheless, the inhomogeneous vapor-deposited films possess a higher coercive field and a more severe tilt to the "vertical" sides of the loop than do the homogeneous films. An attempt was made to model the hysteresis loop of the films to determine whether these differences could be attributed to the ellipsometrically characterized inhomogeneities.

To model the effect that embedded porosity of this type would have on the apparent electrical properties of the film, the following approximation was considered. If a representation of a columnar microstructure is subdivided into elements vertically, then most segments contain dense PZT in series with a low dielectric constant layer (see Fig. 15). It is assumed here that the upper electrode is conformal, so that the surface roughness does not strongly influence the net electrical properties of the film. Given these conditions, the net capacitance of one element can be expressed as

$$\frac{1}{C} \propto \frac{\epsilon_2 (d-x) + \epsilon_1 x}{\epsilon_1 \epsilon_2}$$

where  $\epsilon_1$  and  $\epsilon_2$  denote the dielectric constants of the dense and the defective regions respectively,  $d$  is the total film thickness, and  $x$  is the thickness of the low density material. For this geometry, the ratio of the actual coercive field of the dense PZT to the apparent coercive field of the element is

$$\frac{E_{c(1)}}{E_c} = \frac{V_1}{\frac{V}{d}} = \frac{\epsilon_2 d}{\epsilon_2 (d-x) + \epsilon_1 x}$$

It is also assumed that there are no forces (such as stress) acting to depole the film. While some depolarization will occur in actual samples, tilting the lines bounding the top and bottom of the hysteresis loops, that will not alter the basic conclusions of this argument.

In vapor-deposited materials, the dielectric constant and the thickness of the defective material would be expected to vary locally as nucleation and growth

commenced, leading to a distribution in the capacitances and coercive fields of the different subelements. The absence of a well-defined coercive field, in turn, leads to a loss in the squareness of the hysteresis loop, which is one of the desired attributes for the model. As a first approximation, the dielectric constant and coercive field for the dense fine-grained PZT were assigned the values from the sol-gel film, i.e.  $\epsilon_1 = 1300$ , and  $E_{c(1)} = 40\text{kV/cm}$  [31]. To mimic the slope of the sides of the hysteresis loop for a 600 nm thick MIBERS film, the coercive fields for the elements were divided into equal steps between 40 and 110kV/cm. This gives the right slope and correctly predicts the average value for  $E_c$  ( $\sim 75\text{kV/cm}$ ). The shape of the derived hysteresis loop is also in reasonable agreement with the experimental data.

To further check the validity of this model, the net dielectric constant for a film 600 nm thick with a 60 nm thick low density layer near the substrate was also calculated using a parallel model to average the capacitance of the individual vertical elements. The coercive field distribution described above requires dielectric constant values for the bottom layer to vary between 70 and 1300. This leads to a net dielectric constant for the film of 770, reasonably close to the experimentally observed value of  $\sim 850$  [2]. The volume fraction of air in the bottom layer of each element needed to cause the assumed coercive field distribution was also calculated using the logarithmic and series approximations for the dielectric constant of a composite. These values bracket the average volume fraction of air derived from the SE determination. This is also reasonable. Consequently, this model provides a good approximation for the observed electrical properties of some types of inhomogeneous ferroelectric films. In all cases heterogeneities within the film should be expected to increase the coercive field value. When a distribution of coercive fields is present, the hysteresis loop should be both significantly broadened and tilted to the right, as is generally observed in reported data on ferroelectric thin films.

Moreover, depending on the distribution of porosity in the film, the coercive field of some regions could be so high as to make them practically unswitchable, lowering the apparent polarization for the film. Thus it is possible that a film of well-crystallized ferroelectric could display apparent remanent polarizations significantly below that expected for the bulk ceramic material. This would occur despite the fact that if the film could be fully switched, the remanent polarization would be 99.2% of the bulk value for the case where the bottom 60 nm (of a film 600 nm thick) was, on average, 92% dense.

Finally, defective regions in the film could serve as pinning sites for domain wall motion. This, in turn, could influence both aging and fatigue in ferroelectric films. Consequently, deposition techniques which facilitate production of films which are highly homogeneous, in addition to being highly crystalline, may be essential in the preparation of optimized films for device applications.

It is clear from the above discussion that inhomogeneities in the microstructure can significantly affect the observed low and high field electrical properties of ferroelectric films. This explains much of the variability reported in the literature for these properties. As the degree and types of inhomogeneities present in the film are controlled by the preparation conditions, it is not surprising that films prepared under different conditions display widely disparate dielectric constants and hysteresis loops. However, the role of inhomogeneities has often been ignored. For vapor deposited films, low-energy ion bombardment during growth and rapid thermal annealing have been shown to be useful in improving the film microstructure [32,33].

#### Role of Inhomogeneities on Apparent Size Effects in Ferroelectric Films

Any film which contains low density regions near the substrate should also be expected to display marked extrinsic size effects. Thus, for the films discussed above, and for other vapor-deposited films grown under low adatom mobility conditions, as the

total film thickness is decreased, the defective layer contributes a larger fraction to the overall properties, and the observed properties demonstrate an extrinsic dependence on film thickness.

Consider, for example, the simplified model for the MIBERS film discussed in the previous section, where the first 60 nm of perovskite has a lower density than the remainder of the film. As before, the dielectric constant of the defective region will be distributed between 70 and 1300, so that the hysteresis loop of the film has the proper shape. If this initial layer is kept constant while the total film thickness of the film is varied, then the hysteresis loops become progressively broader and more tilted as  $d$  is decreased (see Fig. 16). At the same time, the net dielectric constant drops off markedly, even though  $\epsilon$  for the solid phase is assumed to remain unchanged. Thus, an infinitely thick film would be essentially undisturbed by the anomalous layer, and would have a well-defined coercive field and dielectric constant equivalent to the values for a bulk, fine-grained ceramic. For thinner films, however, both  $\epsilon$  and  $E_c$  diverge from the bulk values. The decrease in dielectric constant for thinner films shown in Figure 16 is also in agreement with a variety of experimental studies [31,34].

Figure 16a is drawn with even the thinnest films showing the maximum value for the remanent polarization. If the low density layer is, on average, 92% dense (i.e. the ellipsometrically determined value), this is a good approximation, even for the 100 nm thick film, since the effective remanent polarization is calculated to be 95.2% of the bulk value. As the film thickness increases, the maximum  $P_r$  value rapidly approaches 100% of the bulk value. However, this marks the limiting value for  $P_r$  assuming that full switching of the film could be achieved. In practice, it is more likely that given the presence of high local coercive fields in the thinner films, some areas of the film would become unswitchable, and the measured remanent polarization would be lowered.

The sensitive dependence of the apparent size effects on the initial stages of the film microstructure would also explain why films prepared under different conditions

demonstrate different properties as a function of thickness. Spectroscopic ellipsometry offers one means through which depth profiles of inhomogeneities in thin film samples can be characterized non-destructively, and so should be useful in resolving many of the residual questions about structure-microstructure-property relationships in ferroelectric films.

### Conclusions

It has been shown that spectroscopic ellipsometry can be utilized to characterize the microstructural inhomogeneities in ferroelectric thin films. Some degree of inhomogeneity (in the form of low density layers or surface roughness) was found in each of the films examined; in all cases these were more important in modelling the ellipsometric spectra than were intrinsic changes in the properties of the ferroelectric phase as a function of film thickness. The presence of microstructural inhomogeneities is not necessarily linked to the existence of a poorly crystallized film. As a result, well-crystallized, and even well-oriented films can display poor microstructures.

A model was developed to approximate the effect that such local density variations should have on the net electrical properties of an otherwise perfect film. Depending on the configuration of the embedded porosity, it was demonstrated that microstructural inhomogeneities can profoundly alter the dielectric constant, coercive field, and remanent polarization of ferroelectric films. Effects of this type are expected to be especially pronounced in vapor-deposited films with columnar or cluster microstructures and low density sol-gel films. Therefore, optimization of processing conditions to produce dense, homogeneous microstructures will be critical in the development of high quality devices.

Due to the relationship between the film microstructure and the net electrical properties, any systematic variations in the density with film thickness, like those associated with columnar growth, will cause changes in the net film properties as a

function of thickness. This mechanism is expected to be responsible for the majority of apparent size effects reported in the literature. Consequently, in examining the properties of ferroelectric films, and especially in considering the variation in properties with film thickness, it is imperative that some microstructure-sensitive technique, such as microscopy or spectroscopic ellipsometry, be utilized.

It has also been demonstrated that spectroscopic ellipsometry can track the evolution of crystallinity and structural inhomogeneity during annealing of as-deposited MIBERS films. One of the advantages of performing these studies on transparent materials is that the entire depth of the film can be sampled (and characterized) at once. In this work, crystallization of the perovskite phase was shown to be largely complete after half an hour at 550°C for MIBERS films on sapphire substrates. For the prolonged heating cycles utilized during *in-situ* annealing of the ferroelectric films, roughening of the film surface was coincident with this crystallization, and can probably be attributed to the growth of crystal nuclei. In addition, lower temperature phenomena like changes in the lead species present could be identified.

It was found that the final microstructures of MIBERS PZT films is dependent on the details of the annealing process. Thus, while the depth profile of film inhomogeneities was consistent for films given the same annealing schedule, changes in the annealing resulted in considerable modification of the final density distribution. Even films annealed at the same peak temperature, but which were exposed to intermediate temperatures for different lengths of time displayed this type of behavior. Consequently, while the final film microstructure will be influenced by the as-deposited state, it will not necessarily be controlled only by the deposition parameters.

This has several important consequences in terms of processing ferroelectric films for device applications. First, the post-deposition annealing schedule can be as important as the deposition conditions in controlling the film microstructure, and thus the film properties. Second, evaluation of annealing schedules should be conducted in

light of structural information for the film (i.e. from microscopy or spectroscopic ellipsometry) in addition to X-ray diffraction information. Third, as the net electrical properties depend on the inhomogeneities present in the film, some limited property tuning may be possible given proper control of the annealing process. In particular, porosity profiles could be tailored to permit control or grading of the film properties (i.e. structural or optical) through the thickness. One area in ceramic materials in which this type of control might be interesting is in the preparation of functionally gradient materials or in ceramic membranes.

### References

- 1 S. B. Krupanidhi, *J. Vac. Sci. & Technol. A*, 10 (1992) 1569 .
- 2 S. B. Krupanidhi, H. Hu, and V. Kumar, *J. Appl. Phys.*, 71 (1992) 376.
- 3 G. R. Fox, S. B. Krupanidhi, K. L. More, and L. F. Allard, *J. Mat. Res.*, 7 (1992).
- 4 D. E. Aspnes and J. B. Theeten, *Phys. Rev. Lett.*, 43 (1979) 1046.
- 5 K. Vedam, P. J. McMarr, and J. Narayan, *Appl. Phys. Lett.*, 47 (1985) 339.
- 6 P. J. McMarr, K. Vedam, and J. Narayan, *J. Appl. Phys.*, 59 (1986) 694.
- 7 J. Narayan, S. Y. Kim, K. Vedam, and R. Manukonda, *Appl. Phys. Lett.*, 51 (1987) 343.
- 8 N. V. Nguyen, K. Vedam, and J. Narayan, *J. Appl. Phys.*, 67 (1990) 599.
- 9 P. Chindaudom, *Characterization of Inhomogeneous Transparent Thin Films on Transparent Substrates by Spectroscopic Ellipsometry*, Ph.D. Thesis, The Pennsylvania State University (1991).
- 10 P. Chindaudom and K. Vedam, *Opt. Lett.*, 17 (1992) 538.
- 11 S. Krishnakumar, S. C. Esener, C. Fan, V. H. Ozguz, M. A. Tille, C. Cozzolino, and S. H. Lee, *MRS Symposium Proceedings Vol. 200: Ferroelectric Thin Films* E. R. Myers and A. I. Kingon, eds. MRS: Pittsburgh, PA 1990 91.
- 12 D. E. Aspnes, *J. Opt. Soc. Am.*, 64 (1974) 812.

- 13 P. Chindaudom and K. Vedam, *Appl. Opt.* 1993 (submitted).
- 14 J. M. M. de Nijs and A. van Silfhout, *J. Opt. Soc. Am.*, 5 (1988) 773.
- 15 R. J. King and M. J. Downs, *Surf. Sci.*, 16 (1969) 288.
- 16 I. H. Malitson, *J. Opt. Soc. Am.*, 52 (1962) 1377.
- 17 I. H. Malitson, *Opt. Soc. Am.*, 55 (1965) 1205.
- 18 M. A. Jeppesen, *J. Opt. Soc. Am.*, 48 (1958) 629.
- 19 A. N. Parikh and D. L. Allara, *J. Chem. Phys.*, 96 (1992). 927.
- 20 P. Yeh, *J. Opt. Soc. Am.*, 69 (1979) 742.
- 21 P. Yeh, *Surface Science*, 96 (1980) 41.
- 22 P. D. Thacher, *Appl. Opt.*, 16 (1977) 3210.
- 23 C. E. Land, P. D. Thacher, and G. H. Haertling, in *Applied Solid State Science: Advances in Materials and Device Research Vol. 4*, Ed. by R. Wolfe. Academic Press Inc., New York, 1974.
- 24 B. Yang, *Spectroscopic Ellipsometry and Computer Simulation Studies of Thin Film Morphology Evolution*, Ph.D. Thesis, The Pennsylvania State University, 1988.
- 25 B. Yang, B. L. Walden, R. Messier, and W. B. White, *SPIE Proc. 821: Modelling of Optical Thin Films* (1987) 68.
- 26 E. P. Harris, P. S. Hauge, and C. J. Kircher, *Appl. Phys. Lett.*, 34 (1979) 680.
- 27 A. E. Ennos, *J. Opt. Soc. Am.*, 52 (1962) 261.
- 28 R. L. Holman and R. M. Fulrath, *J. Appl. Phys.*, 44 (1973) 5227.
- 29 R. Messier, A. P. Giri, and R. A. Roy, *J. Vac. Sci. Technol. A2* (1984) 500.
- 30 G. H. Haertling, *J. Vac. Sci. Technol. A*, 9 (1991) 414.
- 31 K. R. Udayakumar, J. Chen, S. B. Krupanidhi, and L. E. Cross, *Proc. 1990 IEEE 7th Int. Symp. Appl. Ferroelec.* (1990) 741.
- 32 H. Hu and S. B. Krupanidhi *Appl. Phys. Lett.* 61 (1992) 1246.
- 33 H. Hu, L. Shi, V. Kumar, and S.B. Krupanidhi, *Ceram. Trans.* 25 ed. by A. S. Bhalla and K. M. Nair, The American Ceramic Society, Westerville, Ohio (1992) 113.

- 34 A. A. Gitel'son, A. M. Lerer, V. S. Mikhalevskii, V. M. Mukhortov, and S. V. Orlov,  
*Sov. Phys. Sol. State*, 19 (1977) 1121.

## List of Figures

- Fig. 1: X-ray diffraction patterns of the PZT films on (a)  $(1\bar{1}02)$  sapphire and (b) Pt-coated Si. Films were annealed at 650°C for 2 hours.
- Fig. 2: Schematic of the rotating analyzer ellipsometer utilized in this work.
- Fig. 3: Comparison of uncorrected and corrected SE data for vitreous silica.
- Fig. 4: Electrical resistance furnace and sample mount (a) Side view. (b) Top view of the baseplate and sample holder. The entire baseplate can be translated along y and rotated about z to permit alignment of the sample at any temperature. Rotation of the sample about the x axis was performed with the worm gear and screw shown in the figure. This could also be adjusted at any temperature.
- Fig. 5: Fit to the film on (0001) sapphire.
- Fig. 6: Comparison between the refractive index of PZT films and PLZT ceramics. (Note: Thacher has demonstrated that the refractive index of PLZT ceramics is largely controlled by the Zr/Ti ratio [22]. Consequently, the film refractive indices should fall between those for the 2/65/35 and 16/40/60 PLZT ceramics).
- Fig. 7: Depth profile of the inhomogeneities in films deposited on (a) Pt-coated silicon and (b) (0001) sapphire.
- Fig. 8: SE data for the *in-situ* annealing of a film on sapphire.
- Fig. 9: Annealing of a film showing a decrease in the high energy damping at 500°C. The lower temperature data was very close to that shown for 450°C.
- Fig. 10: Best fit models for intermediate temperature anneals of an as-deposited film on sapphire. Note that the refractive index of the "a-PZT" changed with annealing temperature as shown in Fig. 12.
- Fig. 11: Evolution of microstructure with temperature during high temperature *in-situ* annealing of an as-deposited film on sapphire. Note that the refractive index of the "PZT" material in the film changed continuously during these anneals as

shown in Fig. 12. These changes are probably associated with the crystallization of the perovskite phase.

Fig. 12: Refractive index of an as-deposited film on sapphire as a function of annealing temperature.

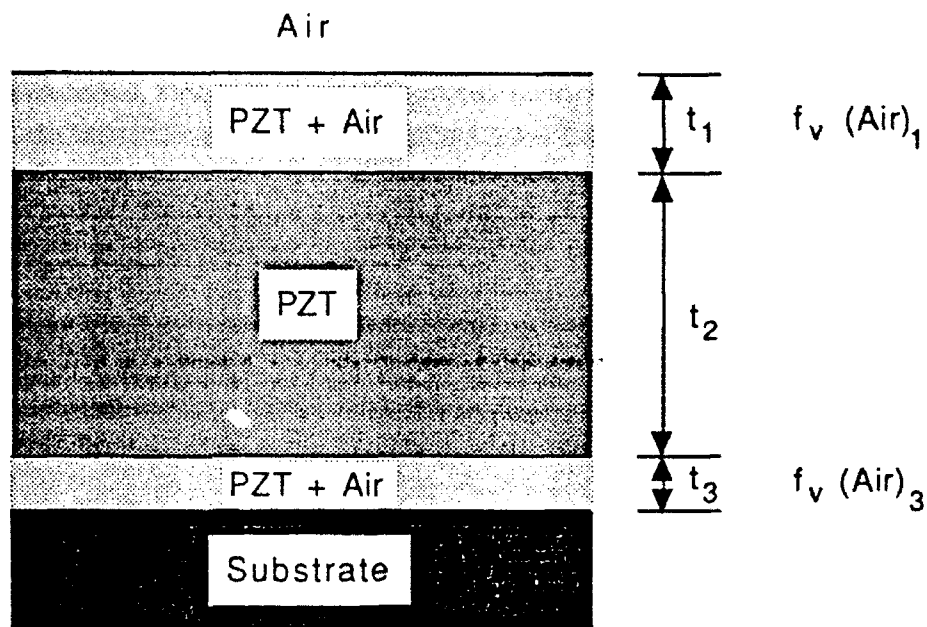
Fig. 13: Reaction scheme for the *in-situ* annealing of a PZT film on sapphire (Note that as a pyrochlore phase could not be identified from the SE data alone, it is not shown on the reaction scheme. It is possible, however, that pyrochlore phase formation is concurrent with the removal of the lossy lead oxide phase).

Fig. 14: Final microstructures of films on sapphire annealed at 650°C (a) with and (b) without extended annealing at lower temperatures. The annealing profile shown for (b) is simplified.

Fig. 15: Geometry used for modelling the effect of inhomogeneities on the electrical properties of an inhomogeneous ferroelectric film. (a) A two-dimensional representation of columnar growth subdivided vertically. (b) One element of the above structure.

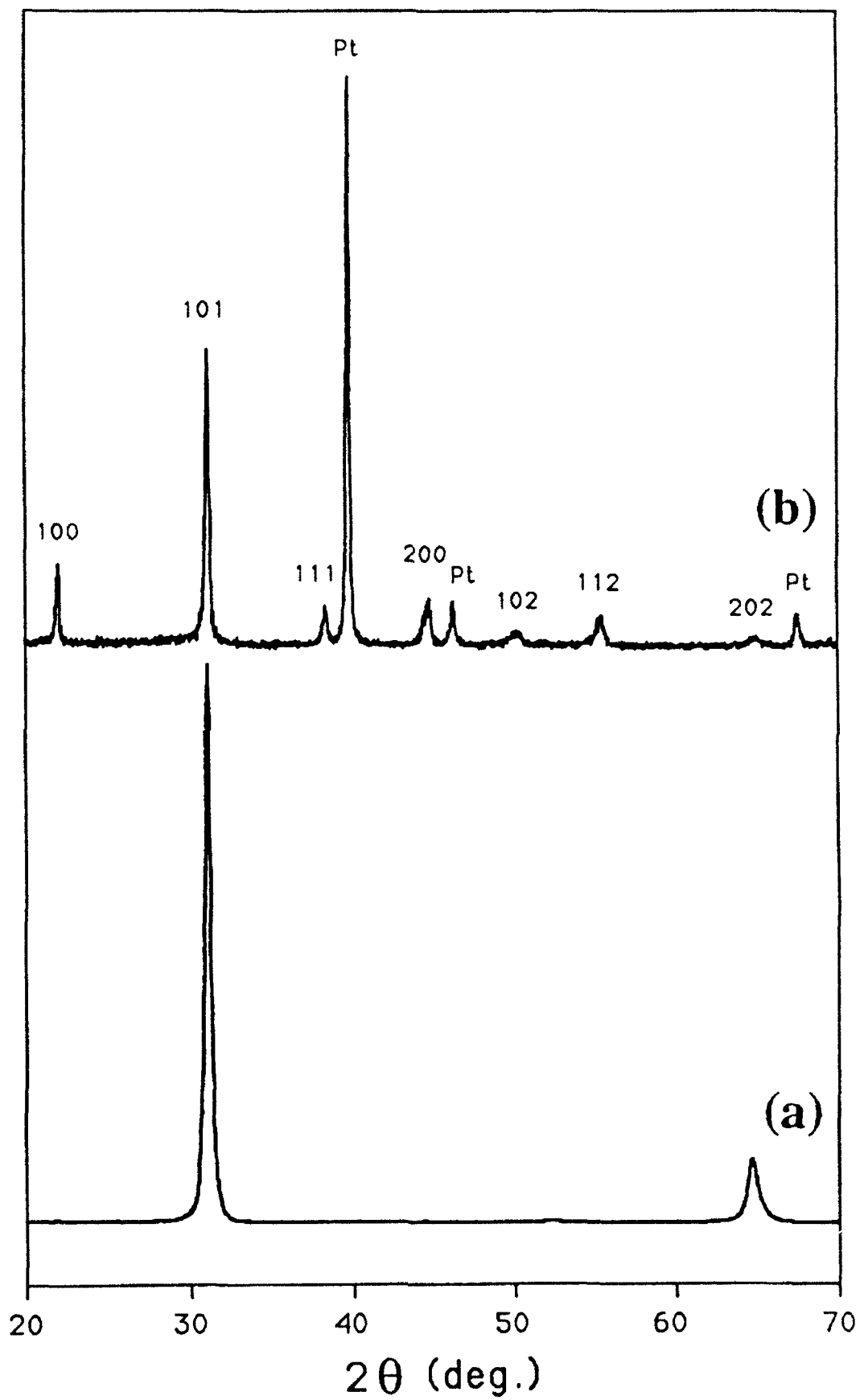
Fig. 16: The effects of a 60 nm thick low density layer near the substrate on the electrical properties of PZT thin films. (a) Variation in the hysteresis loop with the total film thickness. (b) Variation of the dielectric constant and the coercive field with film thickness. Limiting values are  $\epsilon = 1300$  and  $E_c = 40$  kV/cm for a homogeneous fine-grained film on a Pt-coated Si substrate.

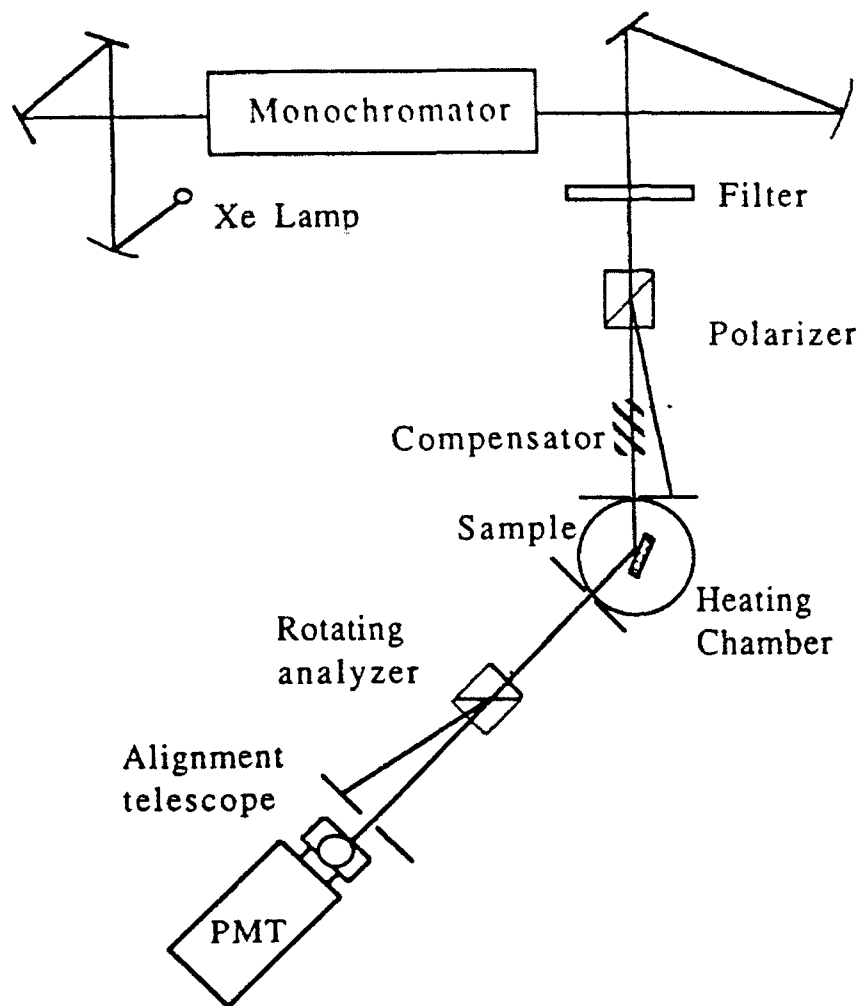
Table 1: Best-fit parameters for the modelling of films annealed at 650°C for 2 hours.

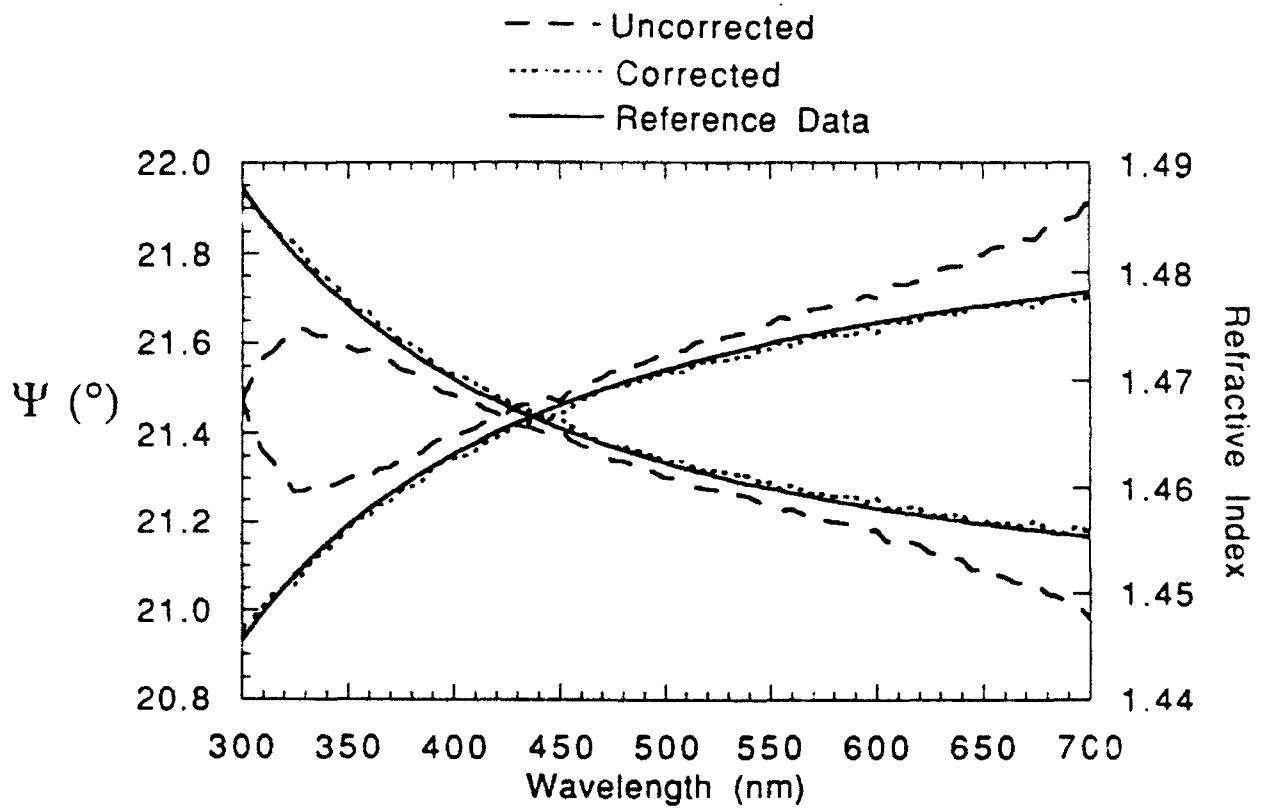


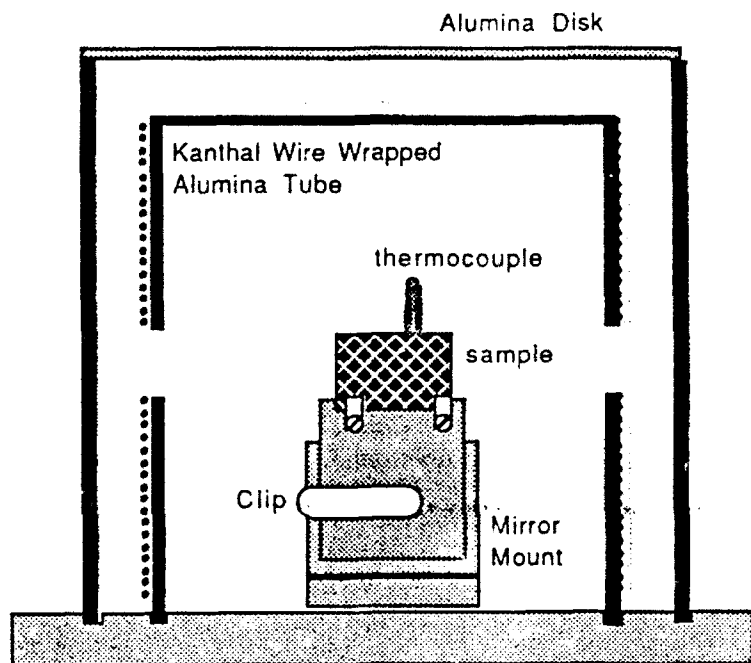
	$f_v(\text{Air})_1$	$t_1$ (nm)	$t_2$ (nm)	$f_v(\text{Air})_3$	$t_3$ (nm)
PZT on (0001) Sapphire	$0.07 \pm 0.02$	$18.3 \pm 5.2$	$478.5 \pm 9.8$	$0.08 \pm 0.01$	$83.9 \pm 3.8$
PZT on ( $\bar{1}102$ ) Sapphire	-----	-----	$548.1 \pm 6.6$	$0.08 \pm 0.01$	$62.4 \pm 4.7$
PZT on ( $\bar{1}102$ ) Sapphire	-----	-----	$580.3 \pm 2.7$	$0.12 \pm 0.01$	$53.8 \pm 1.3$
PZT on Pt- coated Silicon	$0.21 \pm 0.03$	$109.2 \pm 2.6$	$557.5 \pm 18.8$	-----	-----
PZT on Pt- coated Silicon	$0.15 \pm 0.02$	$107.7 \pm 3.9$	$522.0 \pm 25.9$	$0.14 \pm 0.06$	$56.3 \pm 18.5$

Intensity (arb. unit)

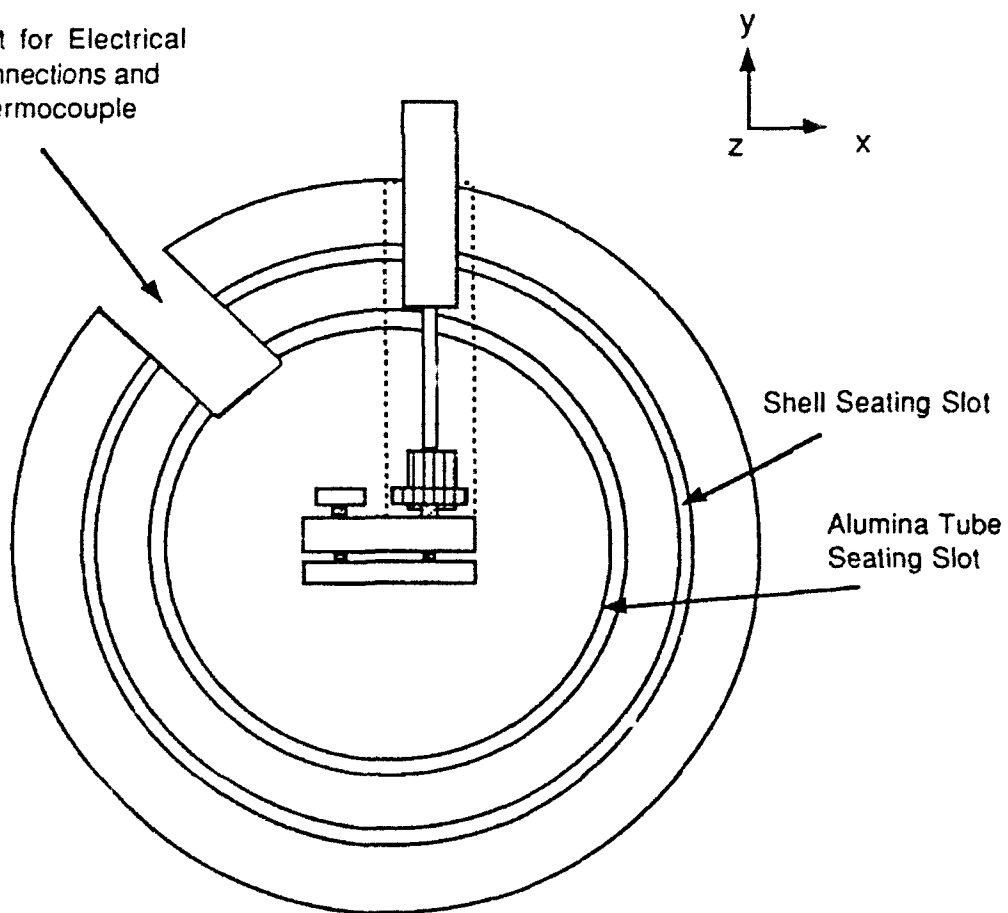


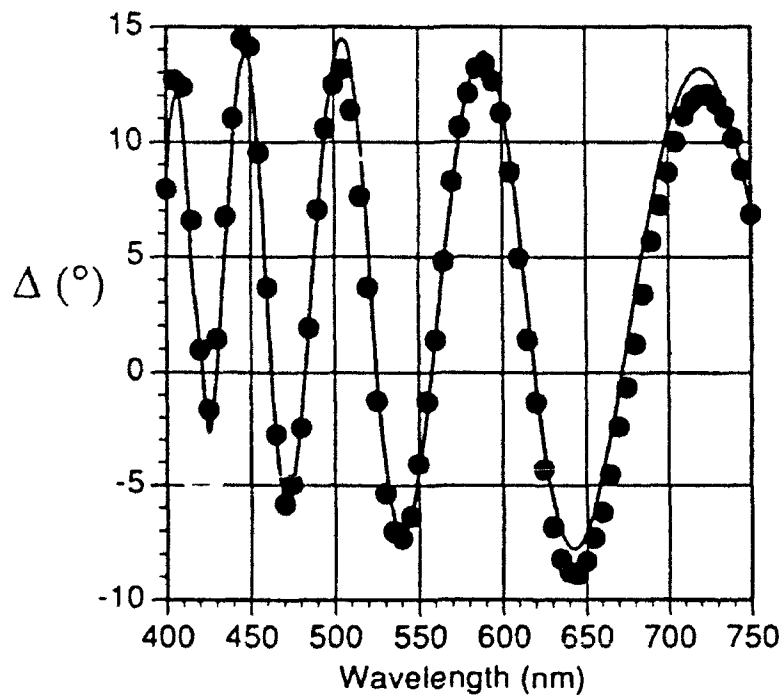
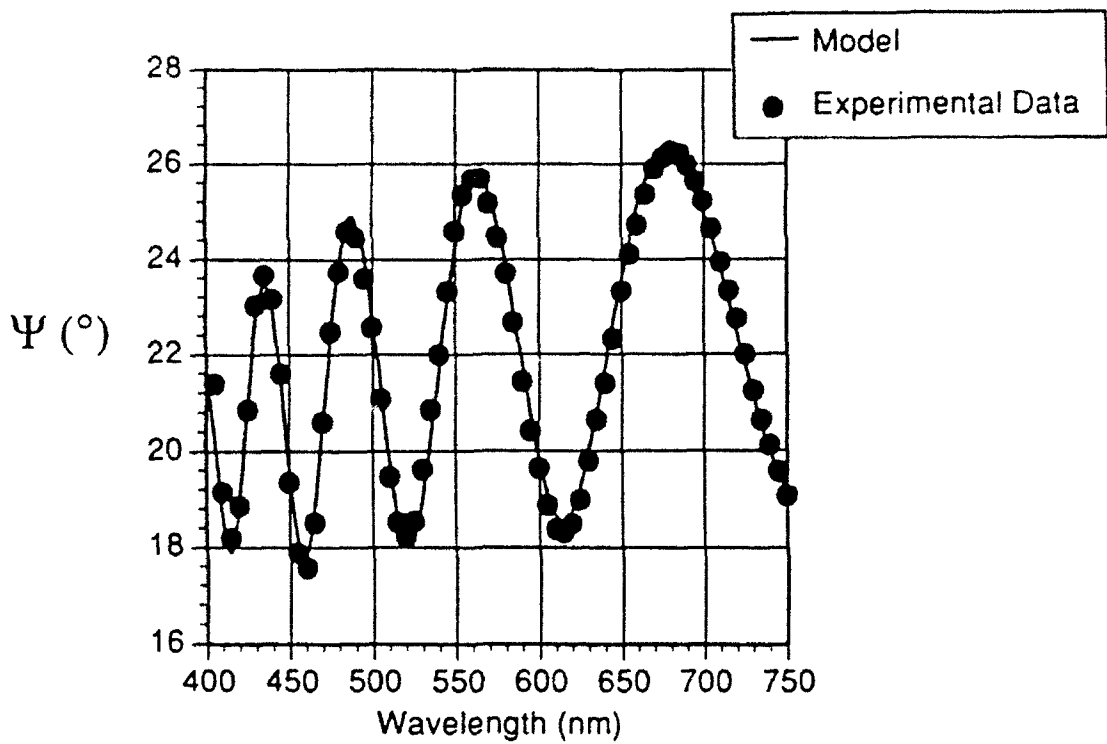


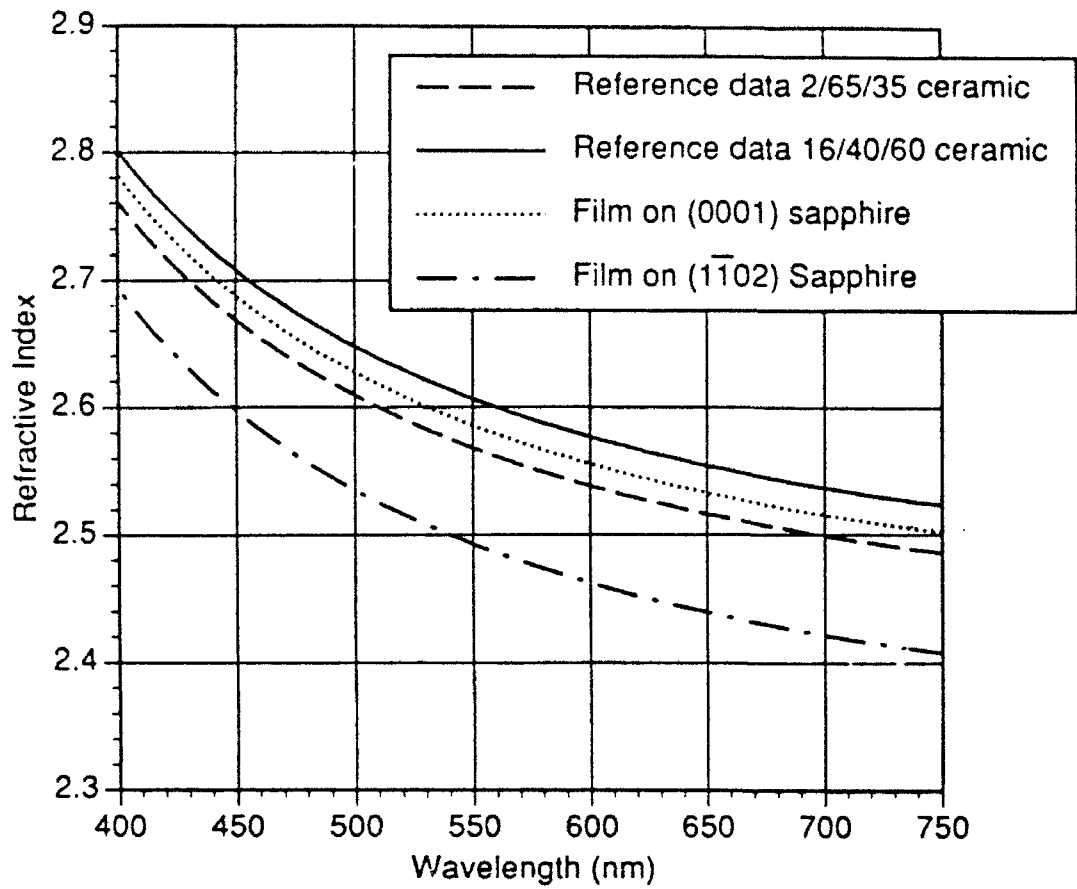


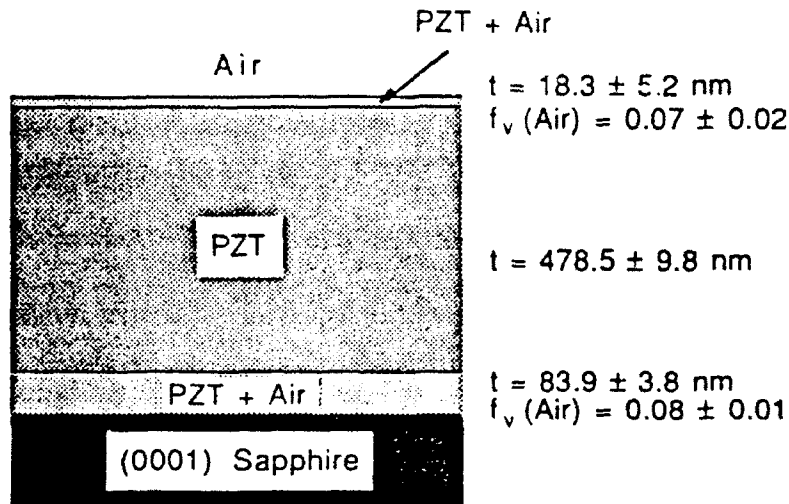
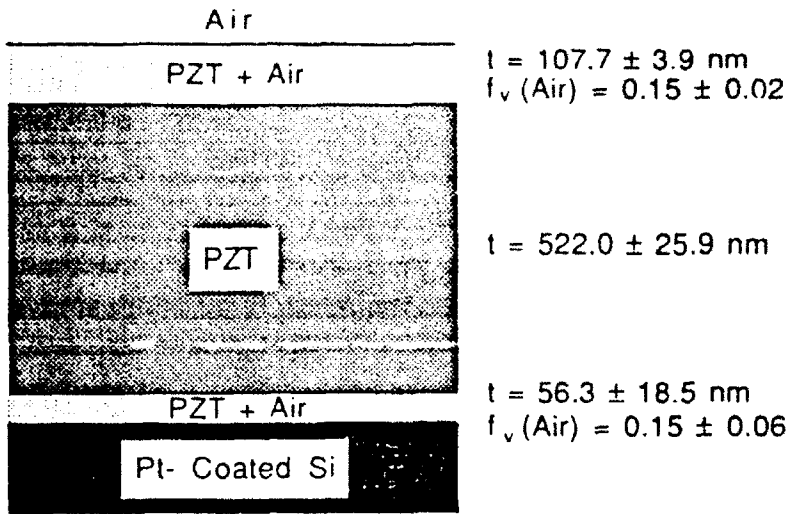


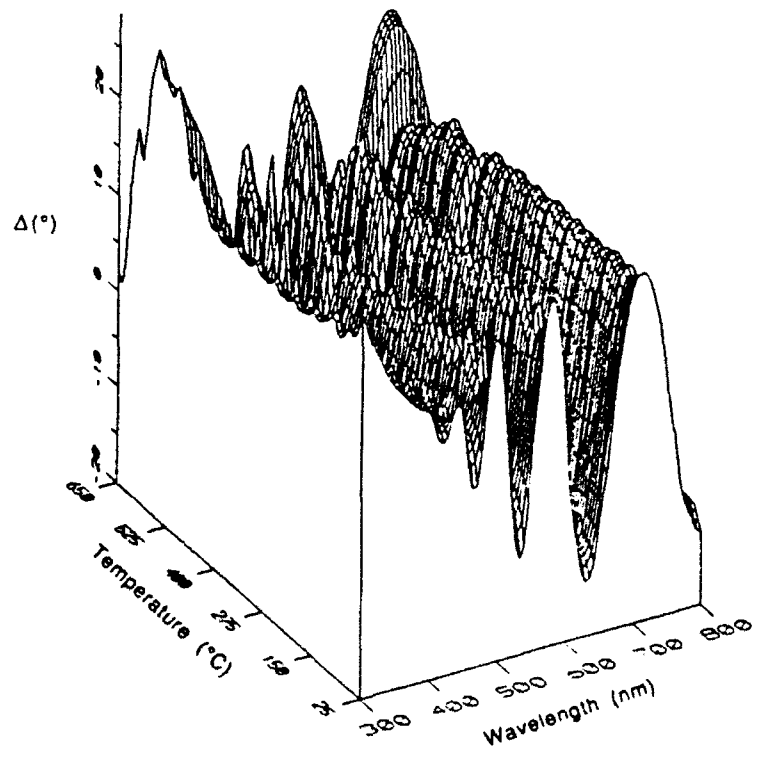
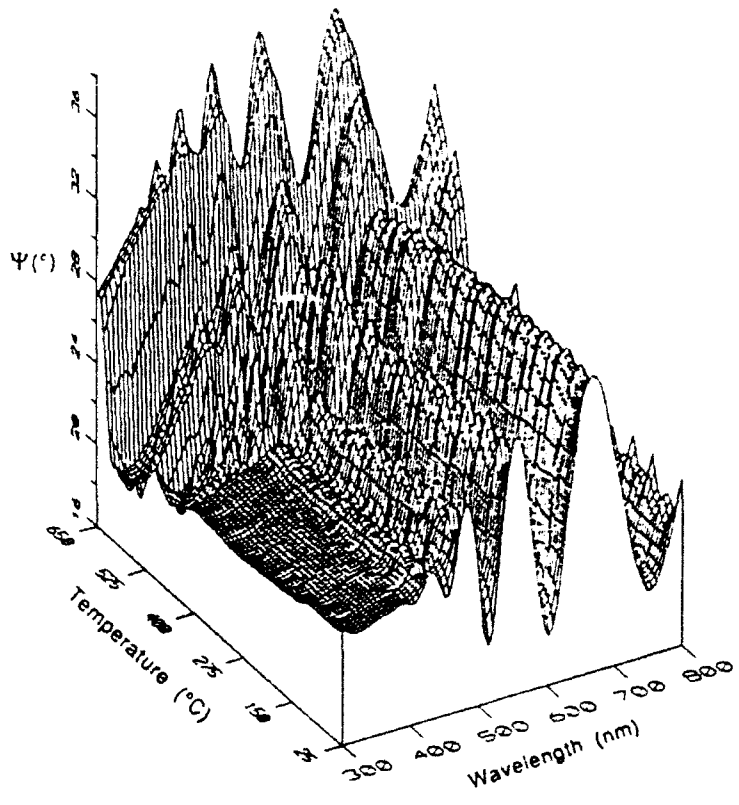
Slot for Electrical  
Connections and  
Thermocouple

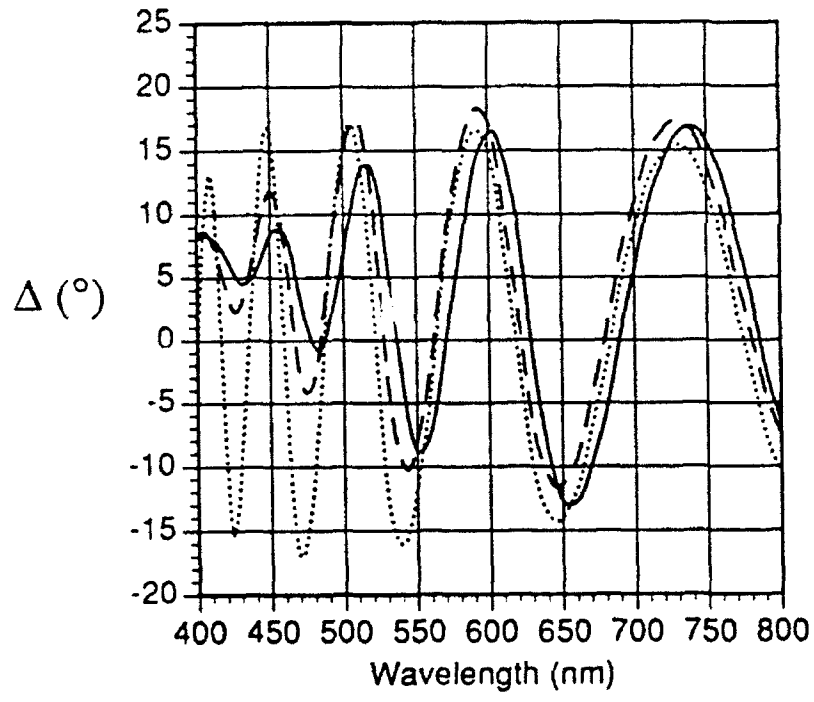
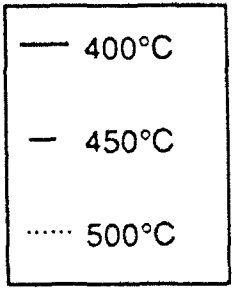
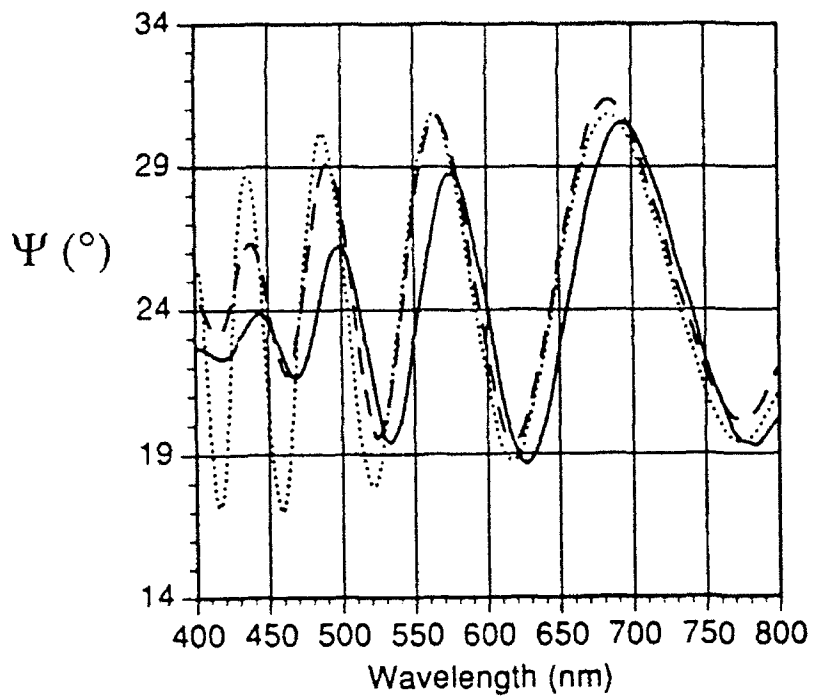


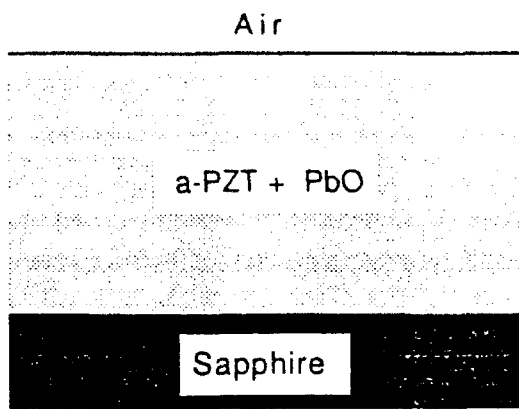




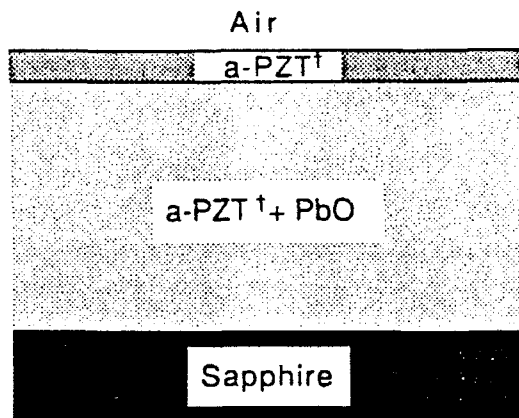




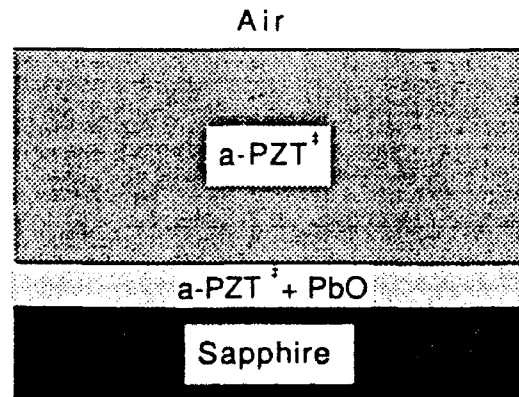




$f_v(\text{PbO}) = 0.26 \pm 0.03$   
 $t = 662.7 \pm 3.8 \text{ nm}$       $400^\circ \text{ C}$



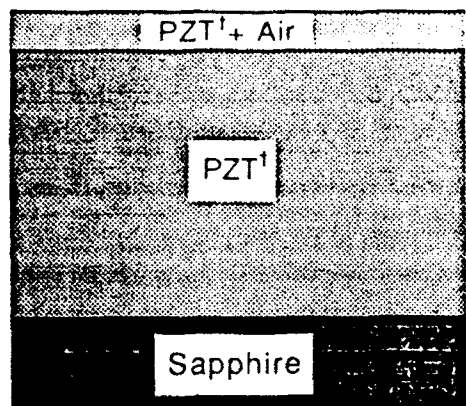
$t = 33.7 \pm 2.6 \text{ nm}$   
 $t = 619.1 \pm 5.8 \text{ nm}$       $450^\circ \text{ C}$   
 $f_v(\text{PbO}) = 0.14 \pm 0.01$



$t = 602.6 \pm 19.4 \text{ nm}$       $500^\circ \text{ C}$   
 $t = 63.0 \pm 22.9 \text{ nm}$   
 $f_v(\text{PbO}) = 0.12 \pm 0.06$

550° C

Air

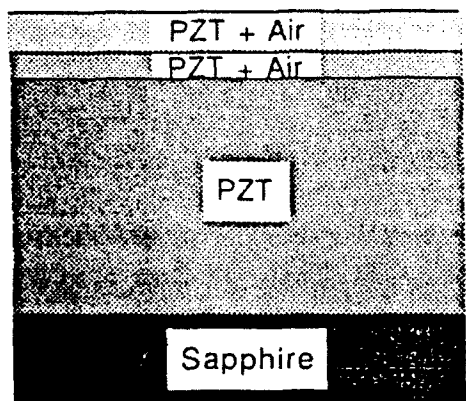


$t = 82.3 \pm 3.4 \text{ nm}$   $f_v(\text{Air}) = 0.06 \pm 0.01$

$t = 492.1 \pm 3.6 \text{ nm}$

600°C

Air



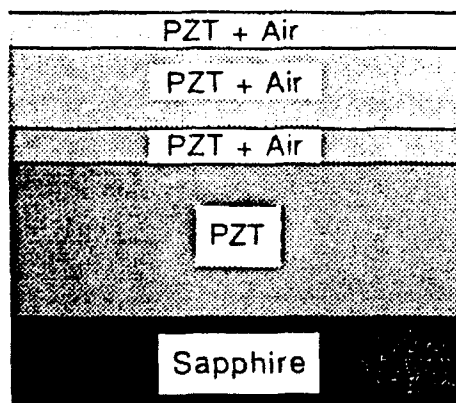
$t = 80.8 \pm 2.3 \text{ nm}$   $f_v(\text{Air}) = 0.26 \pm 0.01$

$t = 47.7 \pm 2.8 \text{ nm}$   $f_v(\text{Air}) = 0.08 \pm 0.01$

$t = 458.9 \pm 8.8 \text{ nm}$

650°C

Air

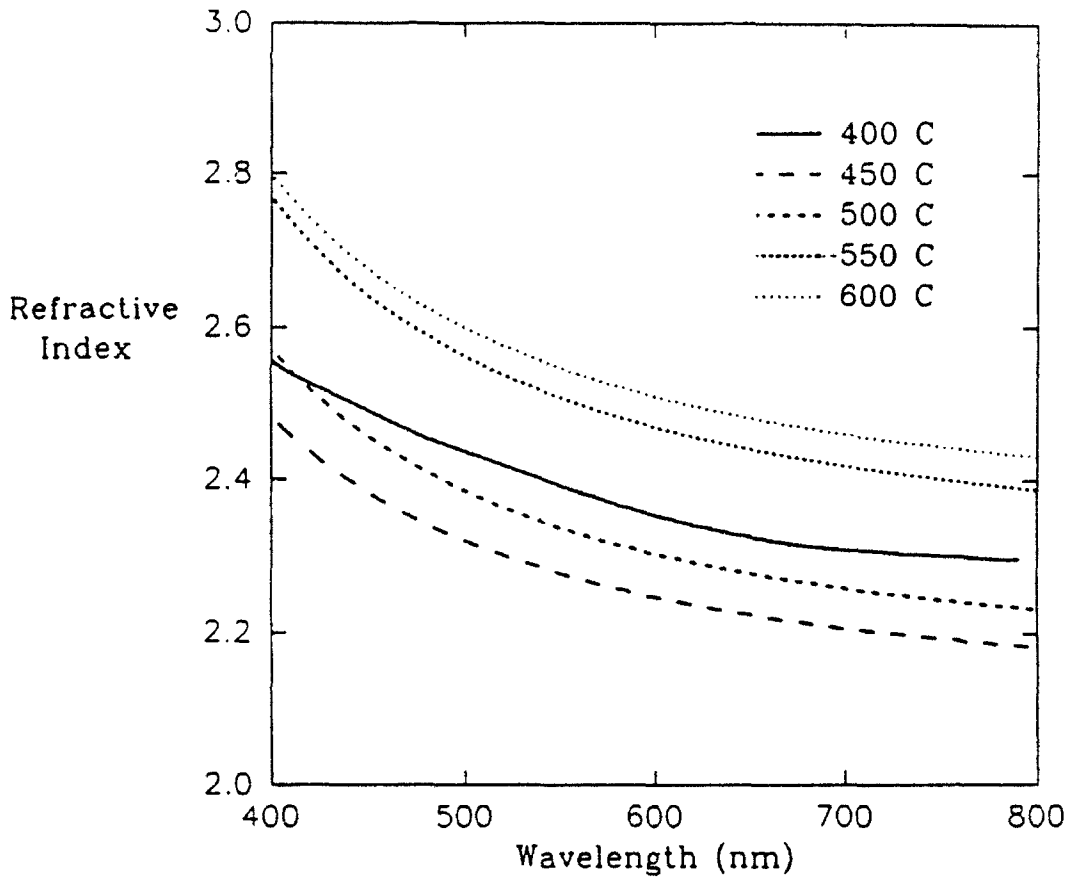


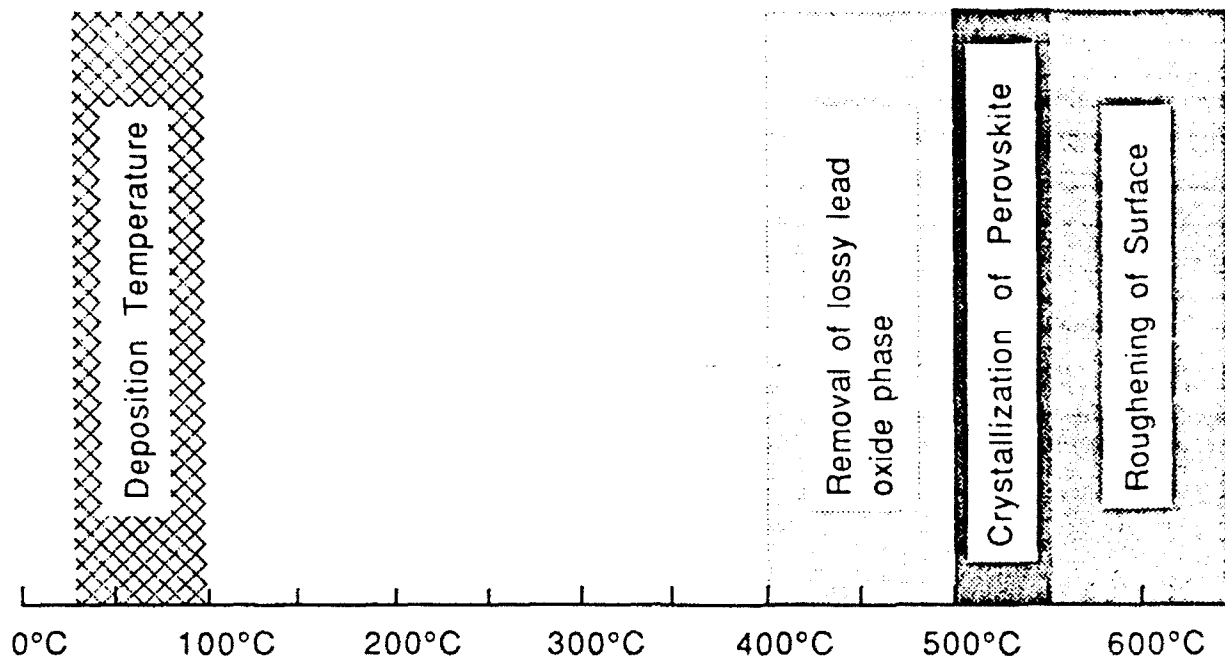
$t = 72.3 \pm 0.4 \text{ nm}$   $f_v(\text{Air}) = 0.56 \pm 0.01$

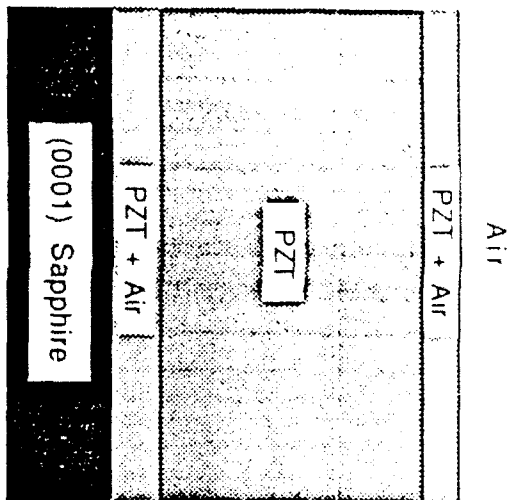
$t = 178.6 \pm 1.9 \text{ nm}$   $f_v(\text{Air}) = 0.15 \pm 0.01$

$t = 57.6 \pm 1.5 \text{ nm}$   $f_v(\text{Air}) = 0.07 \pm 0.01$

$t = 323.7 \pm 5.4 \text{ nm}$

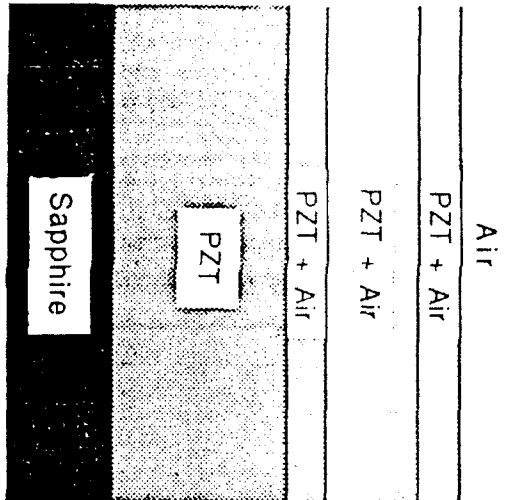
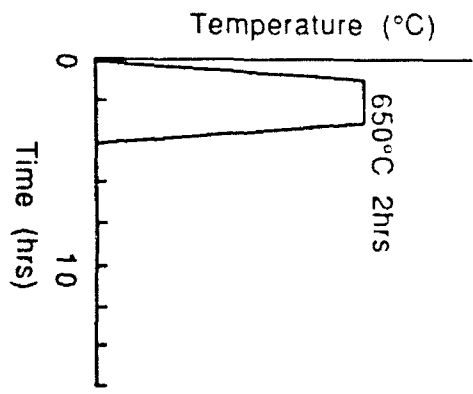






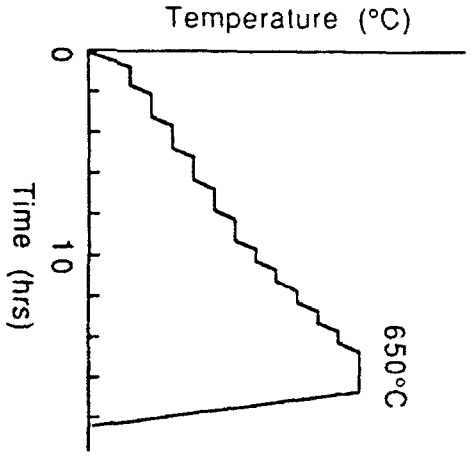
$t = 18.3 \pm 5.2 \text{ nm}$   
 $f_v (\text{Air}) = 0.07 \pm 0.02$   
 $t = 478.5 \pm 9.8 \text{ nm}$   
 $t = 83.9 \pm 3.8 \text{ nm}$   
 $f_v (\text{Air}) = 0.08 \pm 0.01$

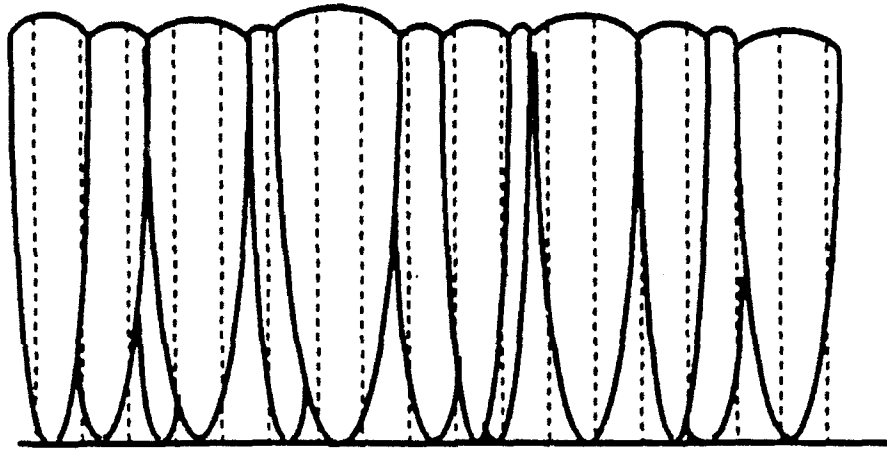
(a)



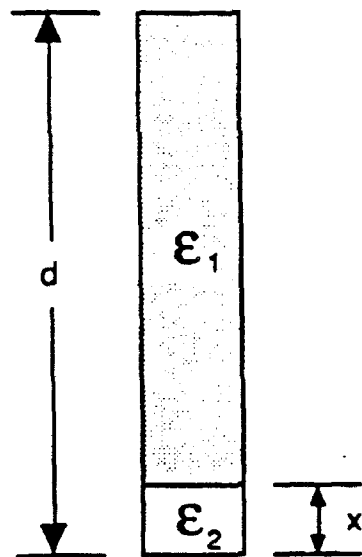
$t = 72.3 \pm 0.4 \text{ nm}$   
 $f_v (\text{Air}) = 0.44 \pm 0.01$   
 $t = 178.6 \pm 1.9 \text{ nm}$   
 $f_v (\text{Air}) = 0.15 \pm 0.01$   
 $t = 57.6 \pm 1.5 \text{ nm}$   
 $f_v (\text{Air}) = 0.07 \pm 0.01$   
 $t = 323.7 \pm 5.4 \text{ nm}$

(b)

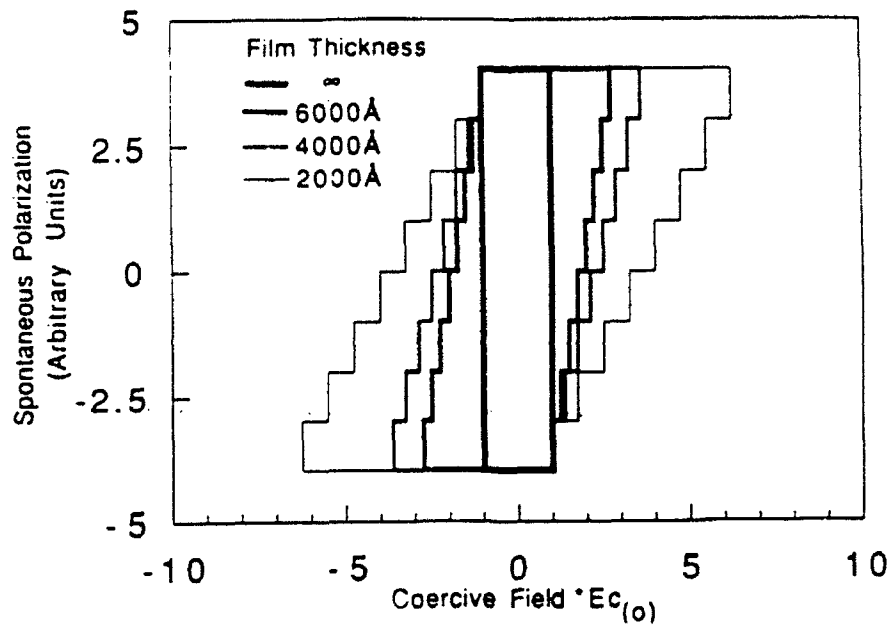




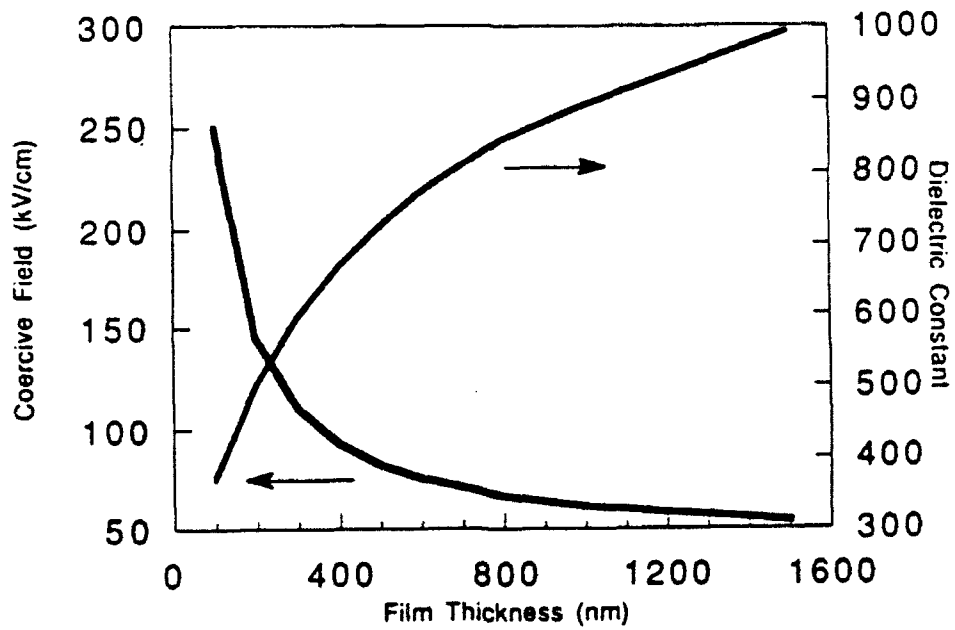
(a)



(b)



(a)



(b)